HEAT TRANSFER BEHAVIOUR OF A DILUTE IMPINGING AIR-WATER MIST JET

Cian Quinn

Department of Mechanical & Manufacturing Engineering

Parsons Building

University of Dublin, Trinity College

Dublin 2

Ireland

September 2015

A thesis submitted to the University of Dublin in partial fulfilment of the requirements for the degree of Ph.D.

Declaration

I declare that this thesis has not been submitted as an exercise for a degree at this or any other university and it is entirely my own work.

I agree to deposit this thesis in the University's open access institutional repository or allow the library to do so on my behalf, subject to Irish Copyright Legislation and Trinity College Library conditions of use and acknowledgement.

Abstract

While the convective heat transfer characteristics of conventional air jets have received a large amount of attention, mist jets remain relatively under-represented within the literature. The mist jet has the potential to offer significant heat transfer enhancement using very small amounts of liquid. However, the mechanisms by which this is accomplished are not fully understood. Thus, an in-depth investigation into the heat transfer phenomena of the dilute mist jet is required.

This work is concerned with the heat transfer behaviour of an air-water mist jet impinging onto a surface held at a temperature below the water saturation temperature. To this end, this study utilises time-averaged heat transfer measurements, as well as simultaneously obtained high-speed shadowgraph imaging flow visualisation and heat transfer measurements. High-speed imagery is also used to characterise the mist jet atomisation and its impingement behaviour.

Several parameters are considered in this study: jet Reynolds number, nozzle-to-surface distance and mist loading fraction. Flow visualisation points towards the aerodynamic Weber number as a key parameter in the atomisation of the dilute mist jet, and a continued influence on the flow structure in terms of droplet sizes and velocities axially downstream from the nozzle. Droplet size and velocity distributions are presented for the above parameters at various locations within the mist jet. It is determined that, subsequent to the chaotic nature of the atomisation process, the mist jet tends towards a uniform structure in terms of droplet size and velocity downstream.

The behaviour of the mist jet liquid that gathers on the impingement surface is investigated. It is determined that surface liquid morphology varies primarily with mist loading fraction, evolving from the case where the behaviour is characterised by the existence of discrete liquid slugs, to partial localised liquid films, before finally a continuous liquid film is established at higher mist loading fractions.

The impingement behaviour is reflected in the heat transfer measurements, with significant fluctuations in the heat transfer signal correlating strongly with simultaneously obtained

droplet detection data from the shadowgraph imagery. Thermal disturbance caused by the impingement of the droplets is identified as the dominant heat transfer mechanism when the mist loading fraction is low. For higher mist loading fraction, evaporation from the liquid film that forms on the surface, as well as convective cooling as it flows outwards, becomes more significant.

Through the use of the different measurement techniques used in this investigation, it is shown that the dilute mist jet heat transfer is influenced by a number of parameters, but the mist loading fraction and associated surface liquid morphology have been identified as being of particular importance.

Acknowledgements

I would first and foremost like to express my eternal gratitude to my supervisor, Professor Darina Murray for her guidance and support throughout this project. Her wealth of experience and knowledge was invaluable in bringing this work to completion. I would also like to thank Dr. Tim Persoons; his enthusiasm for research and dedication was inspiring, and he was always willing to offer his advice and help when I found myself in a tricky situation. My sincerest thanks to Mr. Gerry Bryne, whose help and knowledge of everything practical in the lab is boundless and hugely appreciated. Thanks also to Dr. Tony Robinson for sharing his advice and knowledge. I would also like to express my gratitude to Mr. Mick Reilly, Mr. Gordon O'Brien and everyone in the workshop for their help and expertise over the last few years.

To my friends and colleagues in the research group, thank you for the help, encouragement, distractions and coffee, without which I would not have made it to the end of this project. Thanks to Eoin, Kate, Maurice, David, Rudi, Diarmuid, Michael, Stephen, Seamus, Rayhaan, and Karl.

To my family, your continued support and encouragement throughout all my studies has been unwavering, and I would not be who and where I am today without you. Thank you for everything.

To Rachel, for your limitless patience, and your support and belief, thank you.

Finally I would like to acknowledge the Irish Research Council who provided the funding for this project.

Contents

List of Figures

List of Tables

Nomenclature

Symbol	Description	Units
A	Area	[m^2]
c	Speed of sound	[m/s]
c_p	Specific heat capacity	[J/kgK]
d	Liquid jet diameter	[m]
D_L	Liquid jet diameter	[m]
d	Annular jet diameter	[m]
D_o	Annular jet outer diameter	[m]
D_h	Annular jet hydraulic diameter	[m]
D_i/D_o	Annular jet diameter ratio	[–]
d	Droplet diameter	[m]
D	Droplet diameter	[m]
D_σ	Droplet diameter standard deviation	[m]
$D_{0.5}$	Mass median droplet diameter	[m]
$D_{0.9}$	90 % total volume droplet diameter	[m]
$D_{1,0}$	Arithmetic mean droplet diameter	[m]
$D_{3,0}$	Volume mean droplet diameter	[m]
$D_{3,2}$	Sauter mean droplet diameter	[m]
E	Senflex® hot film sensor voltage	[V]
f	Mist loading fraction	[–]
G	Surface droplet mass flux	[kg/m^2s]
h	Heat transfer coefficient	[W/m^2K]
h	Surface liquid film thickness	[m]
$h*$	Dimensionless surface liquid film thickness	[–]
H	Nozzle height above surface	[m]
H	Enthalpy	[J]

k	Thermal conductivity	[W/mK]
k	Ratio of specific heats	[–]
l_0	Characteristic length	[m]
L	Liquid jet core length	[m]
L	Length of flow meter element	[m]
M	Momentum flux ratio	[–]
$\dot{m}$	Mass flow rate	[kg/s]
$\dot{M}$	Mass flow rate	[kg/s]
n	Number of droplets	[–]
n	Number of samples	[–]
P	Pressure	[Pa]
q''	Heat flux	[W/m^2]
$\dot{Q}$	Heat flux	[W/m^2]
Q	Volumetric flow rate	[ml/min]
Q''	Volumetric flow rate	[m^3/s]
r	Radial displacement from geometric centre	[m]
r	Radius of flow meter element	[m]
R	Resistance	[Ω]
R	Universal gas constant	[J/kgK]
t	Time	[s]
t_0	Droplet relaxation time	[s]
T	Temperature	[K]
ΔT	Temperature difference	[K]
u_0	Flow velocity	[m/s]
U	Velocity	[m/s]
V	Velocity	[m/s]
X	Axial distance from nozzle exit	[m]
y	Axial distance from nozzle exit	[m]
z	Axial distance from nozzle exit	[m]

Greek Symbols

Symbol	Description	Units
α	Temperature coefficient of resistance	$[K^{-1}]$
α	Thermal diffusivity	$[m^2/s]$
δ	Micro-Foil® sensor thickness	[m]
ϵ	Dimensionless temperature	[–]
λ	Liquid jet disturbance wavelength	[m]
λ	Evaporation constant	$[m^2/s]$
μ	Dynamic viscosity	[kg/ms]
ν	Kinematic viscosity	$[m^2/s]$
ρ	Density	$[kg/m^3]$
σ	Surface tension	[N/m]
τ	Droplet response time, $\rho_L D^2/18\mu_g$	[s]
τ	Shear stress	$[N/m^2]$

Subscripts

Symbol	Description
a	Air
atm	Atmosphere
bub, s	Secondary bubble
bub, w	Nucleation bubble
c	Critical
c	Cable
$cond$	Conduction
$decade$	Decade resistance
$drop$	Droplet
$envi$	Environment
$evap$	Evaporation
f	Fluid
$film$	Liquid film

g	Gas
h	Hydraulic diameter
$hot, film$	Hot film sensor
i	Inner
j	Jet
Jet	Jet
L	Liquid
$MicroFoil$	Micro-Foil® sensor
o	Outer
o	Absolute conditions in temperature or pressure
opt	Optimal conditions for liquid jet break-up
r/D	Radial component
s	Sensor
s	Standard conditions in temperature or pressure
s	Surface
sat	Saturation conditions
$surf$	Surface
t	Top
w	Water
wet	Surface wetting conditions
x	Radial distance
y/D	Axial component

Dimensionless Numbers

Symbol	Description
K	Splashing threshold on a wet surface, $K = We Oh^{-0.4}$
K_d	Splashing threshold on a dry surface, $K_d = We^{0.5} Re^{0.25}$
Ma	Mach number, $Ma = V/c$
Nu	Nusselt number, $Nu = hD/k$
$Nu_{D_{3,2}}$	Nusselt number with characteristic length $D_{3,2}$, $Nu_{D_{3,2}} = hD_{3,2}/k$
$\overline{Nu}$	Average Nusselt number, $\overline{Nu} = \overline{h}L/k$
Oh	Ohnesorge number, $Oh = \mu_L/(\rho_L \sigma d)^{0.5} = We^{0.5}/Re$
Pr	Prandtl number, $Pr = \nu/\alpha$
Re	Mist jet Reynolds number, $Re = UD_h/\nu$
Re_a	Air jet Reynolds number, $Re_a = U_a D_a/\nu_a$
$Re_{D_{3,2}}$	Reynolds number with characteristic length $D_{3,2}$, $Re_{D_{3,2}} = UD_{3,2}/nu$
Re_{eff}	Effective Reynolds number, $Re_{eff} = (U_a D_a/\nu_a)[(1 - D_L^2/D_a^2) + D_L^2/(MD_a^2)]$
Re_L	Liquid jet Reynolds number, $Re_L = U_L D_L/\nu_L$
Stk	Stokes number, $Stk = t_0 u_0/l_0$
We	Aerodynamic Weber number, $We = \rho(U_a - U_w)^2 D_w/\sigma$
We	Droplet Weber number, $We = \rho U^2 D_{1,0}/\sigma$
We_{crit}	Critical Weber number for splashing
We_{shear}	Shear atomisation Weber number, $We_{shear} = \rho_a(U_a - U_L)^2 d/\sigma$
We_{spray}	Spray Weber number, $We_{spray} = \rho_L U_L^2 d_L/\sigma$
We_{turb}	Turbulent Weber number, $We = \rho_g u(\bar{d})^2 d/\sigma$

Chapter 1

Introduction

This research explores the flow structure and convective heat transfer characteristics of an impinging dilute air-water mist jet. The heat transfer mechanisms and flow structures of impinging air jets have been extensively studied. Air jets have been shown to offer high heat transfer performance and are widely used in engineering applications such as the cooling of turbine blades and the thermal management of electronics. However, a flow of liquid droplets in the form of a mist jet or a spray has been shown to offer even higher heat transfer levels than a single phase air jet. While a substantial body of work exists for single phase jet impingement cooling, mist jets and sprays have not received the same levels of interest, with sprays attracting significantly more attention than mist jets. A mist jet is differentiated from a spray by how it is generated; a spray is formed by forcing liquid through a small nozzle, whereas the droplets in a mist jet are produced from a liquid jet via shear driven atomisation caused by a co-flowing annular air jet; this is discussed in detail in section 2.1. Thus, mist jets are inherently complex two-phase flows, and both the nature of the flow structure and the dominant heat transfer mechanisms are not fully understood.

1.1 Background

The use of single phase jets for surface cooling is a well established practice; they have been used in numerous applications where high heat transfer levels are required. O'Donovan et al. [1] examined the use of an impinging air jet to cool a grinding process and Hollworth and Durbin [2] used a jet array to cool a simulated electronic circuit. The effects of jet Reynolds number, nozzle-to-plate spacing, angle of impingement and a number of other parameters on heat transfer have been reported on extensively, for example by Lytle and Webb [3] and O'Donovan and Murray [4]. In addition to this, methods of enhancing the heat transfer of a single phase jet have been explored; Zhou and Lee [5] examined the effect of placing a

mesh screen in front of the impinging jet and Goldstein and Behbahani [6] investigated the influence of cross flow on impinging jet heat transfer.

An improvement in jet impingement heat transfer can be obtained by using a fluid other than air. Water is a popular choice as it is non-toxic, environmentally sound and does not require much pre-treatment. Studies such as that of Vader et al. [7] have shown water jets to offer superior heat transfer characteristics to those of an impinging air jet, while Garimella and Rice [8] reported on the high heat transfer performance available from a FC-77 dielectric liquid jet. One reason for these elevated heat transfer levels is that a liquid jet in ambient air is a free surface jet; the ambient air imposes minimal shear resistance to the liquid flow, allowing the jet momentum to impinge on a surface more efficiently than an air jet in ambient air. The configuration of an air jet in stagnant air is termed a submerged jet, and undergoes extensive momentum exchange with the ambient air, resulting in a reduction in velocity and turbulence. As well as this, water has a higher thermal conductivity, Prandtl number and specific heat than air, further enhancing the heat transfer capabilities of the water jet. However, practical issues arise, such as the removal of large amounts of water, pumping pressure requirements, storage issues and the environmental cost of potentially inefficient use of water. Therefore, attention turns to a flow of water droplets in the form of a mist jet or a spray as a possible compromise between the benefits of water and air jets.

1.2 Research Motivation and Objectives

Interest in the cooling possibilities of droplets entrained within an air flow has motivated studies back as far as the 1960s. Hodgson and Sunderland [9] and Mednick and Colver [10] performed analytical and experimental work respectively on the heat transfer from a heated cyinder in air-water mist flows, with results pointing to the potential heat transfer enhancements available. Historically, there is a much greater body of work for sprays than for mist jets. These studies have focussed mainly on the effect on heat flux of a spray impinging on a heated surface [11, 12], on the behaviour of droplets within sprays [13] and on the relationship between droplet behaviour and heat transfer [14, 15]. Until relatively recently, work on impinging spray heat transfer has almost exclusively examined surface temperatures above the spray liquid saturation temperature. However, spray cooling has been identified as a potential

means of dissipating high heat fluxes at surface temperatures below the liquid saturation temperature, for example in computer electronics [16–18].

While significant progress has been made recently for non-boiling impinging spray heat transfer, the case for mist jets remains poorly represented. Chang and Su [19], Graham and Ramadhyani [20] and Oliphant et al. [21] have reported on parameters such as the liquid and air flow rate and the nozzle-to-surface spacing. However the range of these parameters remains very limited; there is disagreement also over the effect of flow rates, with a general lack of data at the lower end of the range of liquid fractions, i.e. for a dilute mist jet. The potential for significant heat transfer enhancement at very low liquid flow rates is an appealing prospect, and therefore a main objective of this study is to explore this potential by examining the non-boiling heat transfer of a mist jet for very low liquid flow rates. Both time-averaged and fluctuating heat transfer data are presented to characterise the heat transfer behaviour.

Two important flow characteristics that influence the heat transfer enhancement of impinging mist jets have been identified: the behaviour of the liquid that gathers on the impingement surface and the behaviour of the droplets and their quantity within the flow. However, no study to date has reported on the link between the structure of the mist jet and its heat transfer characteristics, nor has there been an investigation into the local behaviour of the surface liquid. Indeed, what work has been done on the structure of a mist jet has been typically for very high liquid flow rates, as in Engelbert et al. [22] or Lasheras et al. [23]. Thus, another primary objective of this study is to investigate the dilute mist jet structure in terms of its atomisation and subsequent droplet properties, and to examine how this structure affects the surface liquid behaviour by using the shadowgraph imaging flow visualisation technique. This is done with a view to providing a better understanding of the heat transfer phenomena of the mist jet, with simultaneous heat transfer and flow visualisation being performed to this end.

Main objectives:

- Investigate the dilute mist jet structure in terms of its atomisation, droplet properties and impingement behaviour.
- Examine the non-boiling heat transfer of a dilute mist jet for very low liquid flow rates.
- Combine flow visualisation and heat transfer data to obtain a better understanding of

the mist jet heat transfer phenomena.

This thesis is therefore divided as follows:

- chapter 2 describes the atomisation process of sprays and mist jets, as well as a review of the flow visualisation data available.
- Chapter 3 presents a review of both the boiling and non-boiling heat transfer studies for mist jets and sprays.
- Chapters 4 and 5 discuss the experimental set-ups used in this investigation and the calibration procedures respectively.
- Chapter 6 presents results obtained on the mist jet atomisation, structure and surface liquid behaviour.
- Chapter 7 discusses the heat transfer results obtained, as well as the simultaneous heat transfer and flow visualisation measurements made in an attempt to link the two.
- Conclusions and future work are presented in chapter 8.

Chapter 2

Mist Jet Structure

At its most basic, an impinging mist jet can be considered as a flow of droplets carried by an air flow striking a surface. Several different types of liquid droplet flows have been considered, from individual droplets or streams of droplets impinging on a surface, to ensemble flows like mist jets and sprays. Though appearing similar, mists and sprays have fundamental differences, and a thorough understanding of the mist jet is necessary as the primary objective of this work is to investigate the convective heat transfer of the mist jet.

The structure of the mist jet can be viewed as having three aspects: the mist jet formation, which also provides the definition for the mist jet, the flow of the liquid droplets and the impingement of the droplets on a surface. Therefore this chapter examines these three aspects.

2.1 Mist Jet Formation

The process by which a liquid is broken up into droplets is known as atomisation. There are several methods of atomisation, and the different way in which liquid is atomised is what separates a spray from a mist. Therefore the formation of a spray is first considered, before moving on to that of a mist jet.

The formation of a spray is essentially the atomisation of a liquid jet issuing from a nozzle. The spray can therefore be thought of as the most fundamental form of liquid jet atomisation, as the mist jet involves an additional co-flowing air jet, as will be discussed below.

2.1.1 Atomisation of a Liquid Jet to Form a Spray

The surface of a liquid jet emerging from a nozzle will undergo oscillations as the surface tension and disruptive forces arising from the jet's kinetic energy compete. These oscillations cause the disintegration of the liquid jet. This has been the subject of investigation for over 100 years. The first work was done by Plateau [25] who proposed that the break-up of a liquid

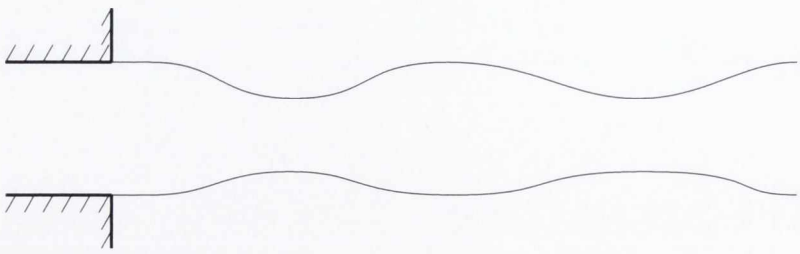

Figure 2.1: Example of a Rayleigh instability, or dilational wave, in a liquid jet emerging into stagnant air; based on a sketch originally by Lefebvre [24]

jet emerging into stagnant air would occur due to instabilities if the jet was longer than it was wide; these instabilities are described "dilational waves" by Lefebvre [24] and consist of pinched and expanded regions of fluid as shown in figure 2.1. It was then Rayleigh [26] who showed these instabilities to be the cause of the break-up and that they were related to the liquid surface tension. He determined that the liquid jet would become unstable if subjected to a disturbance whose wavelength, λ, is:

$$\lambda > \pi d \tag{2.1}$$

where d is the jet diameter. This analysis was done for low Reynolds numbers, i.e. laminar jets, and the analysis neglected viscous effects. This form of disintegration results in a stream of droplets. Rayleigh also determined mathematically the optimum disturbance wavelength for break-up:

$$\lambda_{opt} = 4.51d \tag{2.2}$$

and from this, calculated that the droplet size, D, for optimal break-up conditions would be

$$D = 1.89d \tag{2.3}$$

So the average droplet size in the stream is almost twice the diameter of the original jet.

Weber [27] provided a more general analysis, including the effect of viscosity for low velocity jets. He showed that the effect of viscosity was to stabilise the jet; Weber proposed that any disturbances caused symmetrical oscillations in the jet and if these oscillations were less than the wavelength in Rayleigh's inequality, equation 2.1, the viscosity would tend to dampen these disturbances. The effect of viscosity served to increase the optimum wavelength

required to produce an instability as per his equation:

$$\lambda_{opt} = \sqrt{2}\pi d\left(1 + \frac{3\mu_L}{\sqrt{\rho_L \sigma d}}\right)^{0.5} \tag{2.4}$$

Weber also found that increasing the relative velocity between the liquid jet and the air shortened the optimum break-up distance to

$$\lambda_{opt} = 2.8d \tag{2.5}$$

and would result in correspondingly smaller diameters. Thus the Weber number is a significant parameter for the disintegration of liquid jet. Representing the ratio of the fluid's inertia to surface tension, the spray Weber number, We_{spray}, is defined as

$$\mathrm{We}_{spray} = \frac{\rho_L U_L^2 d}{\sigma} \tag{2.6}$$

where U_L is the jet velocity.

Ohnesorge [28] proposed criteria for classifying the disintegration of a liquid jet issuing into stagnant gas. He classed the different criteria by Reynolds number and a then unnamed dimensionless number, now termed the Ohnesorge number, Oh, which relates the viscous forces to inertial and surface tension forces.

$$\mathrm{Oh} = \frac{\mu_L}{(\rho_L \sigma d)^{0.5}} \tag{2.7}$$

where μ_L is the liquid viscosity, ρ_L is the liquid density, σ is the liquid surface tension and d is the original jet diameter. For a constant Ohnesorge number, Ohnesorge's criteria are as follows:

1. For lower Reynolds numbers, the jet breaks into large drops of uniform size, as per Rayleigh's mechanism.

2. For intermediate Reynolds numbers, oscillations cause the break-up of the jet; the magnitude of these oscillations increases with air resistance.

3. For high Reynolds numbers, the break-up of the jet is complete very close to the nozzle

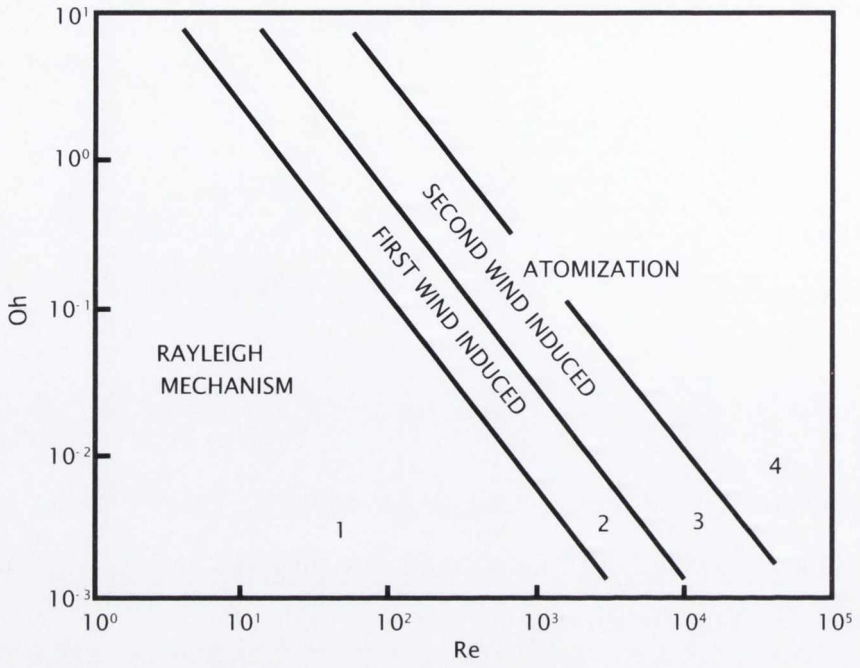

Figure 2.2: Classification of modes of liquid jet disintegration, Reitz [29]

exit and results in complete atomisation of the jet.

This was expanded upon by Reitz [29], who refined Weber's model of classification as follows:

1. Rayleigh jet break-up for lower Reynolds numbers
2. First wind-induced break-up for intermediate Reynolds numbers. Here the surface tension is augmented by the relative velocity between the jet and the air. This results in a static pressure distribution across the jet and accelerates the breaking up of the jet.
3. Second wind-induced break-up for slightly higher intermediate Reynolds numbers. Here the unstable growth of short surface waves is caused by the relative velocity, producing drops that are smaller than the jet and first two regimes.
4. Atomisation; for higher Reynolds numbers the jet is completely disrupted at the nozzle exit and the average droplet size is much less than the jet diameter.

The fourth regime described above is a spray, while the first three regimes represent a liquid jet breaking into large drops of liquid of a comparable diameter to the initial jet. The modes of disintegration as per Reitz [29] are shown graphically in figure 2.2. Sprays are by far the

most common type of droplet flow, and are generated by applying a high pressure to a liquid to force it through a small nozzle at high relative velocity to the stagnant air, thus achieving the atomisation discussed above, as described by Lefebvre [24].

2.1.2 Atomisation of a Liquid Jet to Form a Mist Jet

As stated above in section 2.1.1, a spray relies solely on the conversion of pressure to kinetic energy to atomise a liquid jet. In contrast, a mist jet is produced when a co-flowing axial air jet is used to provide the necessary energy to atomise the liquid jet. This process has been referred to as coaxial airblast atomization by several authors [23, 24, 30, 31]. Essentially, there is a transfer of momentum between the inner water jet and the co-flowing annular air jet as a result of the air jet shearing the water jet. Lefebvre [24] describes airblast atomisation as resulting in finer liquid droplets and requiring lower liquid pumping pressures. As well as this, the presence of the air stream provides good mixing of the air and liquid, which Lefebvre [24] cites as an important reason that airblast atomisers are commonly used in fuel injection.

The earliest work on airblast atomisation was carried out by Nukiyama [32] who considered droplet size. However it was not until the advent of high-speed imaging that the break-up mechanisms could be fully explored. Several studies have examined the liquid jet atomisation phenomena [22, 23, 30, 31, 33] using high-speed imagery and particle sizing techniques like phase Doppler anemometry, with a thorough review provided by Lasheras and Hopfinger [30], and a comprehensive analysis of airblast atomisation provided by Marmottant and Villermaux [33].

Lasheras and Hopfinger [30] attempted to classify the different regimes of airblast atomisation in terms of the aerodynamic Weber number, defined as

$$\mathrm{We} = \frac{\rho_a U_a^2 D_L}{\sigma} \tag{2.8}$$

where ρ_a is the air density, U_a is the air jet velocity, D_L is the liquid jet diameter and σ is the water surface tension.

The four regimes are shown in figure 2.3. In figure 2.3 (a) for small Weber numbers (We = 38) the surface tension forces dominate the flow, preventing the visible instabilities from developing and thus droplets from forming. In figure 2.3 (b) for a slightly larger Weber

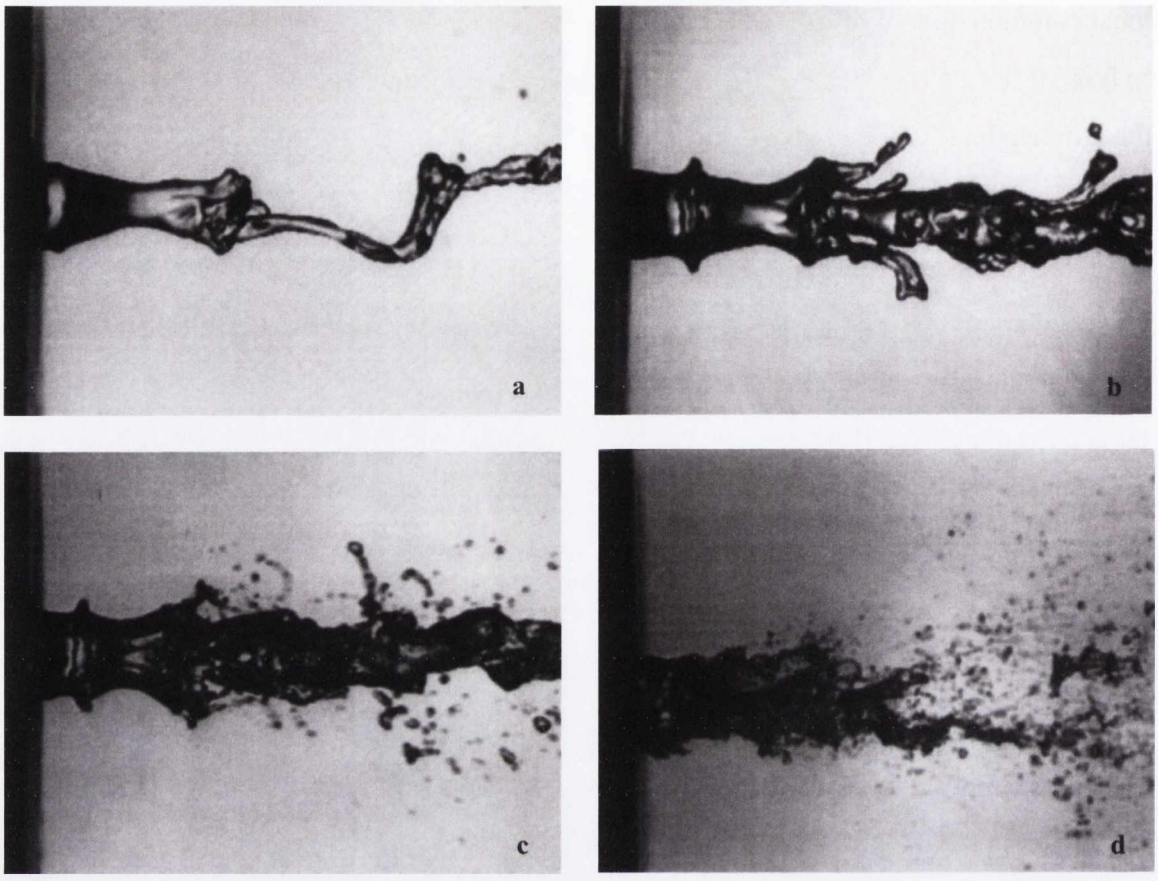

Figure 2.3: Breakup regimes due to airblast atomisation [30]. (a) We = 38, (b) We = 58, (c) We = 118 and (d) We = 318

number of We = 58 the formation of ligaments is visible. These ligaments can then be forced into a membrane shape by the pressure exerted by the air flow, which may then break off. The authors [30] term this the membrane break-up regime. Figure 2.3 (c) shows the scenario when the Weber number is We = 118, resulting in smaller ligaments, resulting in a higher rate of atomisation of the ligaments. For We = 318 in figure 2.3 a fine mist is seen owing to the formation of thinner liquid fibers [23]. Chigier and Farago [34] presented a similar classification, with the inclusion of a Rayleigh break-up regime for We < 25.

Lasheras and Hopfinger [30] also attempted to produce a regime diagram, similar to that for pressure nozzles shown in figure 2.2, though given the complex nature of airblast atomisation this regime diagram is more unwieldy, and a lack of experimental data means that boundaries are not well-defined. Nevertheless, the regime diagram is reproduced in figure 2.4 The diagram considers the break-up in terms of liquid jet Reynolds number, Re = $U_L D_L / \nu_L$, and aerodynamic Weber number. Here the subscripts L and a denote liquid and air jet

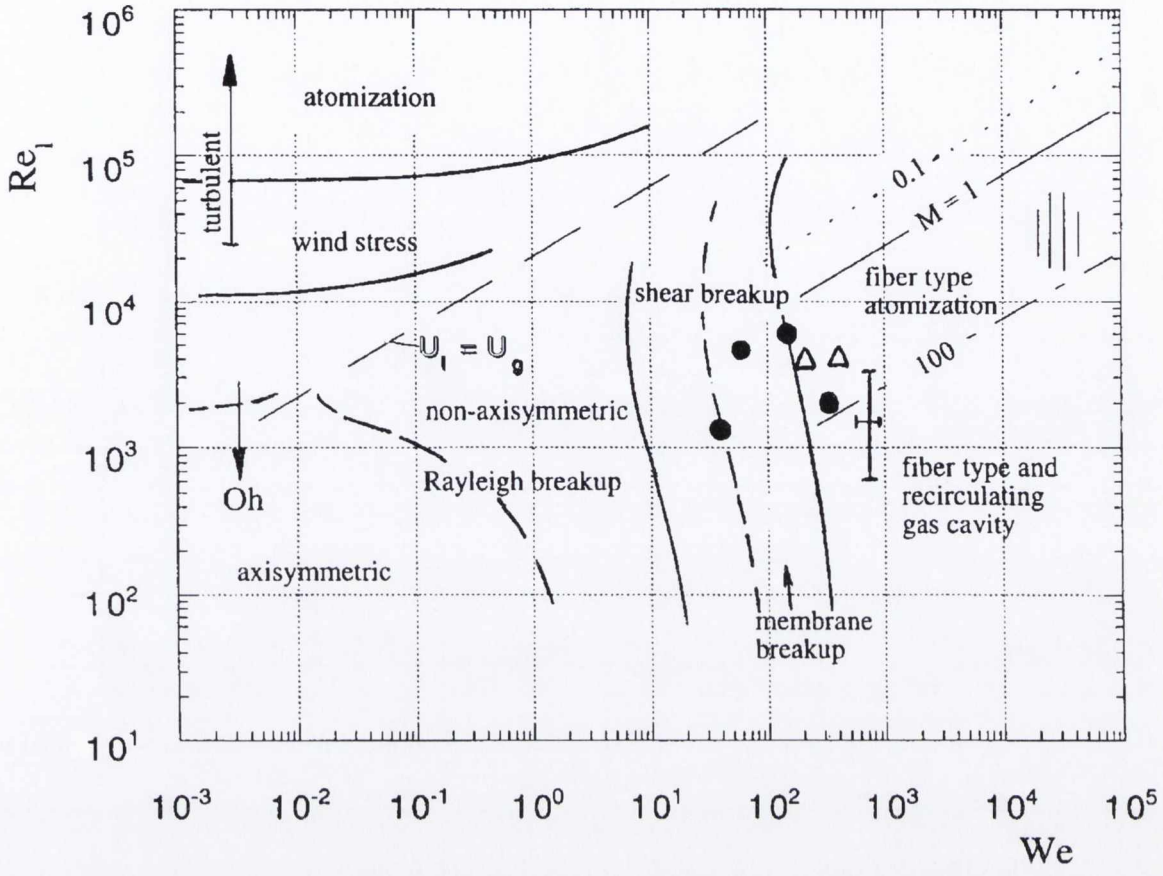

Figure 2.4: Airblast atomisation regime diagram [30]

properties respectively. Though this diagram is complex, the main point is that a fine, uniform mist exists in the far right region or above, i.e. for higher aerodynamic We and liquid Re.

In terms of the break-up mechanisms, airblast atomisation has been described as a two-part process [23, 30], described as atomisation in the near-field region, close to the nozzle exit, and atomisation in the far-field region, further from the nozzle exit. The logic behind this is clear when considering images of the atomisation process as seen in figure 2.3. Considering these images, there exists an initial state where the liquid jet forms what is termed a liquid core; the near-field, or primary, atomisation constitutes droplets that initially atomise from this liquid core. At the end of the core, further atomisation occurs, as can be seen clearly in figure 2.3 (d); this is the far-field, or secondary, atomisation and is the method by which the liquid core disintegrates and a mist jet proper is formed. Therefore the length of the liquid jet core determines the fraction of near- and far-field atomisation that occurs.

The length of the initial liquid core is mainly determined by the ratio of the momentum

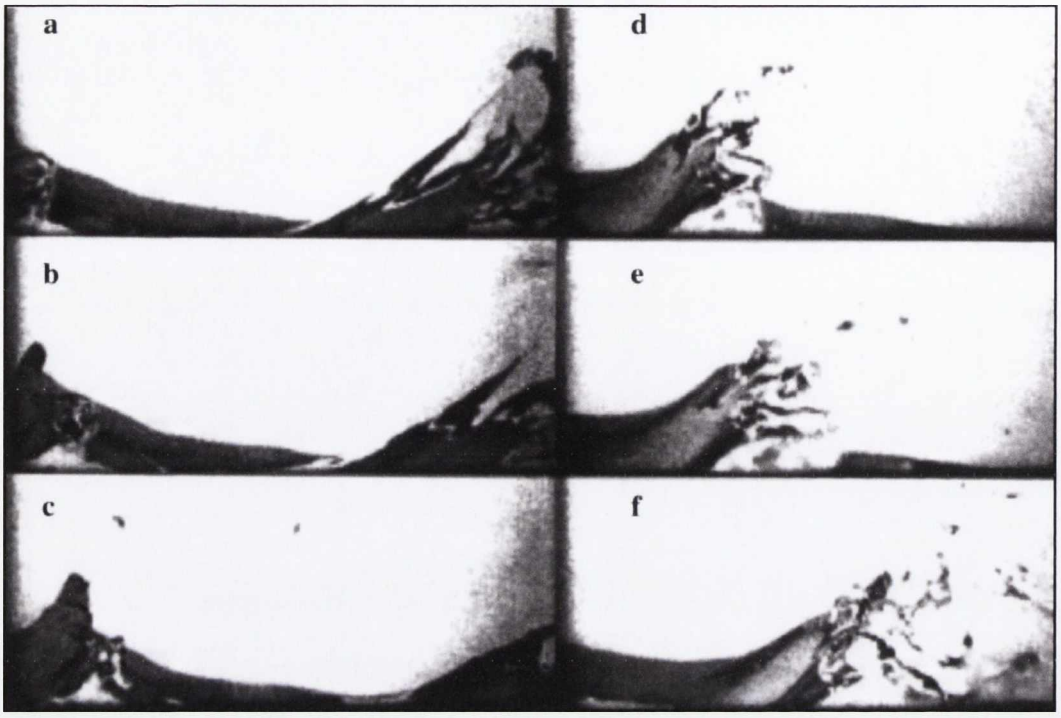

Figure 2.5: Photographs of the growth of instabilities at the liquid-air jet interface which lead to near-field break-up under airblast atomisation [30]

fluxes, or the dynamic pressure ratio, of the two jets, M, defined as:

$$M = \frac{\rho_g U_g^2}{\rho_L U_L^2} \tag{2.9}$$

When M is much less than 1, the liquid jet determines the length of the core, whereas for values much greater than 1 it is the air jet that determines the length of the core [23]. For large M, the liquid core is seen to be very short. Lasheras et al. [23] determined an approximate expression for the liquid core length by arguing that, for their experiments, the largest instability wavelengths were large, and as such the restoring force of the interfacial surface tension was insignificant when the Weber number was large. This allowed them to estimate that the ratio of the core length, L and liquid jet diameter, D_L could be given as

$$\frac{L}{D_L} \approx \frac{6}{\sqrt{M}} \left(\left| 1 - \frac{U_L}{U_a} \right| \right)^{-1} \tag{2.10}$$

It should be noted that while several authors have examined this atomisation [22, 23, 30, 31, 33, 35], there is a lack of information for the cases when the momentum flux ratio is very

Table 2.1: Mist loading fractions, f, and momentum flux ratios, M, considered within the literature

Author	f	M
Engelbert et al. [22]	0.37–2.7	5–175
Lasheras et al. [23]	> 5	2.05–40
Varga et al. [31]	> 0.07	< 11.1
Liu et al. [35]	0.137–15.6	0.03–36550

large. This corresponds to low ratios of the liquid to air mass flow rates, f, defined as

$$f = \frac{\dot{m}_w}{\dot{m}_a} \tag{2.11}$$

where $\dot{m}_w$ and $\dot{m}_a$ are the mass flow rates of water and air. Table 2.1 illustrates the range of M and f that has been previously considered within the literature.

Near-Field Atomisation

Atomisation along the liquid core comes about when perturbations of the liquid jet at the interface between it and the air jet are amplified and the liquid is drawn out into a sheet. Figure 2.5 shows the process. The initial instabilities grow away from the centreline and become thinner as they move through the jet, shown in figure 2.5 (a) – (d). The edge of the sheet is disturbed by the aerodynamic force of the air jet and Rayleigh instabilities. Beyond the instability, a membrane is formed which atomises into droplets, as seen in figure 2.5 (e) and (f), [30]. This form of atomisation is mainly associated with low Weber number flows; the Weber number here is defined as per equation 2.8.

Far-Field Atomisation

In contrast to near-field atomisation where ligaments separate from the liquid jet and atomise into droplets, far-field atomisation is characterised by the detachment from the end of the liquid jet, causing its disintegration. For large aerodynamic Weber numbers, or large momentum flux ratios, this far-field atomisation accounts for the majority of the liquid droplets in the mist jet [23]. This corresponds to the situation when the liquid core length is small, as seen in figure 2.6. According to Lasheras and Hopfinger [30] this regime is dominated by unsteadiness

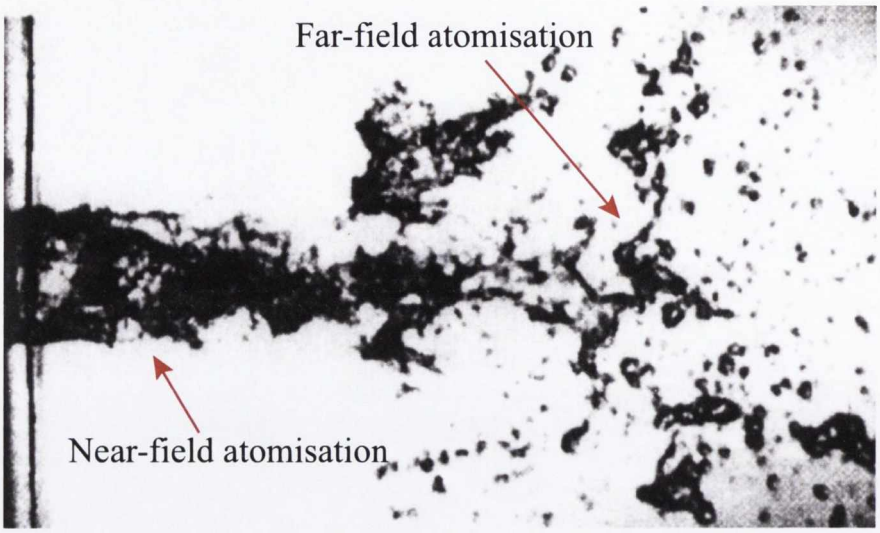

Figure 2.6: Photograph of the airblast atomisation of a liquid jet where far-field atomisation is dominant [30]

in the liquid and the dynamics of large-scale eddies. It is termed the "superpulsating mode" by Chigier and Farago [34].

Far-field atomisation is further divided into two processes: shear break-up and turbulent break-up [23, 30]. In shear break-up the forces acting are due to the mean relative velocity between the droplet and air jet, whereas in turbulent break-up the force acting is due to the turbulent fluctuations of the air.

Considering first the shear break-up, if a droplet shear Weber number is greater than a critical value of approximately $We_{shear} = 12$ as per Lasheras and Hopfinger [30], the droplet will atomise. The shear Weber number is defined based on the relative velocity between the air and the liquid structure undergoing secondary atomisation, termed the slip velocity, $U_a - U_L$:

$$We_{shear} = \frac{\rho_a (U_a - U_L)^2 d}{\sigma} \tag{2.12}$$

A droplet that is exposed suddenly to a stream of gas can undergo disintegration that ranges with increasing We from stretching into a membrane and bursting to having ligaments stripped off and eventually to disintegrating when exposed to a sever shock wave [36]. However, in airblast atomisation liquid droplets are not exposed suddenly to a gas flow but rather to an air jet that has slowed somewhat since the nozzle exit. The explosive disintegration of droplets is unlikely. Nevertheless, droplets shed from ligaments are exposed to the co-flowing air jet and if their Weber numbers are sufficiently high, will further atomise.

For the turbulent break-up, if the turbulent stresses acting on a droplet in a turbulent gas field are greater than the confinement stresses of surface tension and viscosity, the droplet will disintegrate into smaller droplets [37]. For a droplet in a turbulent gas, the turbulent Weber number is defined as

$$\mathrm{We}_{turb} = \frac{\rho_g \overline{u(d)^2} d}{\sigma} \tag{2.13}$$

Here, $\overline{u(d)^2}$ is the mean square of the relative fluctuations in velocity between two points on opposite sides of the droplet and is a function of the droplet diameter. Thus, when We_{turb} is greater than a critical value, which Lasheras and Hopfinger [30] give as being of O(1), the liquid droplet will atomise as the dynamic pressure forces from the turbulent motion are sufficiently large to overcome the surface tension restoring forces.

Thus in the far-field atomisation regime, ligaments that are stripped from the end of the liquid core due to instabilities on the core interface are further atomised into smaller droplets by the action of the above shear and turbulent break-up. This is shown in figure 2.6.

2.1.3 Summary of atomisation parameters

The liquid properties of the fluid in the mist jet affect its atomisation [22, 24]. The surface tension of the liquid influences the readiness of a liquid to undergo atomisation. Liquids with higher surface tension result in larger droplet sizes after atomisation as the surface tension represents a liquid's ability to resist external forces and the formation of new surface areas.

Liquid viscosity also affects atomisation via both the size of the droplets produced and the rate at which atomisation occurs when a liquid is subjected to shear forces imparted from a co-flowing air jet. Low viscosity liquids are atomised almost immediately whereas the atomisation of liquids with larger viscosities tends to increase the length of the liquid jet core. This is because the viscosity of the fluid determines its ability to resist deformation, and therefore delays the growth of interfacial instabilities that cause coaxial airblast atomisation [24]. Similarly, an increase in density delays the growth of instabilities by resisting the acceleration of the instabilities.

The use of dimensionless numbers provides a convenient way to examine the relative effects of viscous, surface tension and inertial forces on atomisation. This has already been examined above, but is summarised here for clarity.

Reynolds Number

For co-flowing air and liquid jets, the Reynolds number can be defined separately for the liquid and air jets. Consider first the liquid jet Reynolds number, Re_L, defined as

$$\mathrm{Re}_L = \frac{U_L D_L}{\nu_L} \tag{2.14}$$

where ν represents the kinematic viscosity of the fluid under consideration [23].

For a liquid jet issuing from a nozzle in stagnant air, the case for pressure sprays, the liquid Reynolds number is the dominant parameter for determining the mechanism of atomisation, as seen from figure 2.2. As Re_L increases, atomisation eventually occurs as short-wavelength instabilities arising from shear effects occur. Thus as the liquid jet velocity increases so too does the tendency of the jet to atomise as the inertial forces come to dominate the resistive viscous forces. The liquid Reynolds number also determines the length of the liquid core [30, 38], with the length increasing to a local maximum in the Rayleigh regime, described in section 2.1.1, before decreasing again in the transition region from a laminar to a turbulent flow; it increases to a second local maximum in the wind induced regime, before decreasing once more asymptotically for further increases in Re_L.

For the case of the coaxial airblast atomisation that forms the mist jet, increasing the liquid jet Reynolds number has a similar effect, increasing the rate of instabilities in the liquid jet and hence enhancing atomisation [23]. However, for most airblast atomisation nozzles, the liquid jet Reynolds number is low as the air jet is used to provide the break-up energy to the system.

When considering the air Reynolds number, different authors have used different definitions. Lasheras et al. [23] define Re using the outer annular air jet diameter as the characteristic length:

$$\mathrm{Re}_a = \frac{U_a D_a}{\nu_a} \tag{2.15}$$

whereas for their review paper, Lasheras and Hopfinger define it using the difference between the two jet diameters, $D_a - D_L$ as

$$\mathrm{Re}_a = \frac{U_a (D_a - D_L)}{\nu_a} \tag{2.16}$$

The use of the momentum flux ratio, or dynamic pressure ratio, captures the effect of varying the jet velocities on the atomisation process in a clearer manner than using the Reynolds numbers as it contains jet velocities.

$$M = \frac{\rho_a U_a^2}{\rho_L U_L^2} \tag{2.17}$$

Increases in M lead to a "finer" mist [30] and decrease the length of the liquid jet core [39], as the higher momentum flux increases the rate of instabilities due to more kinetic energy being available to shear the liquid jet. The ratio of mass flow rates, also termed the mist or mass loading fraction and denoted here as f, is also used [22, 23] and decreases as the momentum flux ratio, M, increases. It is defined as

$$f = \frac{\dot{m}_w}{\dot{m}_a} \tag{2.18}$$

where $\dot{m}_w$ and $\dot{m}_a$ are the water and air mass flow rates respectively.

Defining the Reynolds number for the overall mist jet is a complex task given the two phase nature of the flow. Lasheras et al. [23] define an effective Reynolds number they claim characterises the total flow as

$$\mathrm{Re}_{eff} = \left(\frac{U_a D_a}{\nu_a}\right)\left[\left(1 - \frac{D_L^2}{D_a^2}\right) + \frac{D_L^2}{M D_a^2}\right] \tag{2.19}$$

though the authors [23] do not appear to use this effective Reynolds number, but rather consider M to be a more relevant parameter when reviewing airblast atomisation. Sozbir et al. [40] define the Reynolds number based on the liquid mass flux, G, and used the outer nozzle diameter, D, as the characteristic length as the airblast nozzle used in their study atomises the liquid internally before it is ejected from the nozzle. The dynamic viscosity used was the liquid viscosity, μ_L:

$$\mathrm{Re} = \frac{GD}{\mu_L} \tag{2.20}$$

This definition is frequently used for pressure sprays, which do not have an air jet phase to consider, e.g. Zhang et al. [41]. For pressure sprays, some authors do not use the Reynolds number at all; Choi and Yao [42] used the liquid mass flux while Chen et al. [15] presented

their results in terms of the droplet velocity. An issue arising with these methods is that the Reynolds number can only be determined once some detection method is employed, for example by collection of droplets as was the case for Sozbir et al. [40]. In the work of Chang and Su [19], the air properties alone and the air jet diameter are used when calculating the Reynolds number in order to facilitate comparisons between the mist jet and air jet. Though the mist jet nozzle used by Chang and Su [19] consists of a circular air jet surrounded by an annular water jet, the opposite of the nozzle configuration in the present study. Previous work on mist jets within the research group [43, 44] has also used the air properties and the annular jet hydraulic diameter, D_h, when calculating the Reynolds number.

$$\mathrm{Re} = \frac{U_a D_h}{\nu_a} \tag{2.21}$$

The droplets in a mist jet can be viewed as being carried by the air jet, and tend to be accelerated up towards the air jet velocity and follow the air jet motion [23]. This choice of characteristic length is similar to that found in studies on the annular jet, where the hydraulic diameter, defined as the difference between the outer and inner diameters of the annulus, is typically used as the jet Reynolds number characteristic length [45, 46]. Thus the air Reynolds number is considered an adequate indicator of flow conditions within the mist and is used in the present study.

Weber Number

As with the Reynolds number, the Weber number has been defined differently by different authors. Engelbert et al. [22], Lasheras et al. [23] and Liu et al. [35] defined it based on the initial velocity difference between the gas and liquid jets, as the authors believed this best captured the aerodynamic deformation pressure force

$$\mathrm{We} = \frac{\rho_a (U_a - U_l)^2 D_L}{\sigma} \tag{2.22}$$

This is also how Weber initially defined it [27]. However, Lasheras and Hopfinger [30] define it using the air jet velocity, the logic being that the air velocity is significantly higher than the

liquid jet velocity.

$$\mathrm{We} = \frac{\rho_a U_a^2 D_L}{\sigma} \tag{2.23}$$

This is the definition used in the break-up regime diagram shown in figure 2.4.

The break-up regime diagram in figure 2.4 shows the influence of the Weber number; for a constant liquid Reynolds number, with increasing We the mist jet becomes finer, or more atomised as a result of the increasing momentum flux ratio. Thus as the inertial forces increase, the surface tension restoring forces will have less of an influence. The Weber number also determines the liquid core length; Lasheras et al. [23] argued that as it increases, the surface tension no longer has an effect on the interfacial instabilities between the air and the liquid. As We increases, the length of the liquid jet core decreases. This behaviour is characteristic of the near-field break-up regime, as discussed above.

The Weber number also influences the far-field break-up mechanisms. Described above as consisting of shear break-up and turbulent break-up, the different Weber numbers define the type of atomisation that occurs. For shear break-up, as the shear Weber number, discussed previously in section 2.1.2 and based on the slip velocity between the air and liquid jets, increases, the influence of surface tension on droplets decreases under increasing inertial forces of the gas jet and the droplet disintegration mode shifts from the stretching and rupturing characterised by low We_{shear}, to the explosive shattering of high We_{shear}. Droplets formed by this method quickly accelerate to the gas jet velocity and their Weber numbers become small [30]. For the turbulent break-up regime, when the turbulent Weber number is above a critical value, ~O(1) [30], the dynamic pressure forces due to the air jet turbulence are greater than the surface tension forces and the droplet is atomised.

Ohnesorge Number

Defined as the ratio of viscous to inertial and surface tension forces and given as

$$\mathrm{Oh} = \frac{\mu_L}{\sqrt{\rho_L D_L \sigma}} \tag{2.24}$$

the Ohnesorge number is sometimes referred to as the stability group [24], and is more important for spray formation than mist jet formation; it has generally been replaced by the Weber number in classification of droplet break-up regimes for airblast atomisation. An

increase in Oh will lead to a corresponding increase in liquid core length as the increase in the influence of viscosity reduces the rate of growth of instabilities. In general, liquids used in airblast atomisation are such that their value of Oh is sufficiently low, generally << 1, that the viscous forces do not prevent initial break-up [31, 39]. The Ohnesorge number is related to the Weber and Reynolds numbers as:

$$\mathrm{Oh} = \frac{\sqrt{We}}{\mathrm{Re}} \tag{2.25}$$

2.2 Mean Droplet Size

Before discussing the structure of the mist jet, it is important to draw attention to some the different methods of defining the mean droplet size of a mist jet.

The most commonly used way of presenting the average droplet diameter within a mist or spray is the Sauter mean diameter, sometimes written as SMD, D[3,2] or $D_{3,2}$. The Sauter mean diameter is the diameter of the droplet whose ratio of volume to surface area is the same as that of the entire mist jet [24]. In other words, the smaller the Sauter mean diameter is, the higher the concentration of smaller droplets within the mist. In this way, the Sauter mean diameter can be thought of as indicating the fineness of the mist or spray. This is particularly important for heat and mass transfer or reaction applications. The Sauter mean diameter is defined mathematically as

$$\mathrm{D}_{3,2} = \frac{\sum n_i d_i^3}{\sum n_i d_i^2} \tag{2.26}$$

where d_i represents the diameter of individual droplets that are summed to the total number of droplets, n.

Another important measure of droplet size is the mass median diameter (MMD), which represents the drop diameter such that 50% of the total liquid volume is in drops smaller than the mass median diameter. It is usually given by $D_{0.5}$. This is an example of what is known as a representative diameter; these are used in distributions of the droplet sizes to help show the range of droplet diameters measured. Another useful representative diameter is $D_{0.9}$ which is the diameter such that 90% of the total liquid volume is in droplets with a smaller diameter. It often serves as an upper bound on droplet size, as droplets larger than

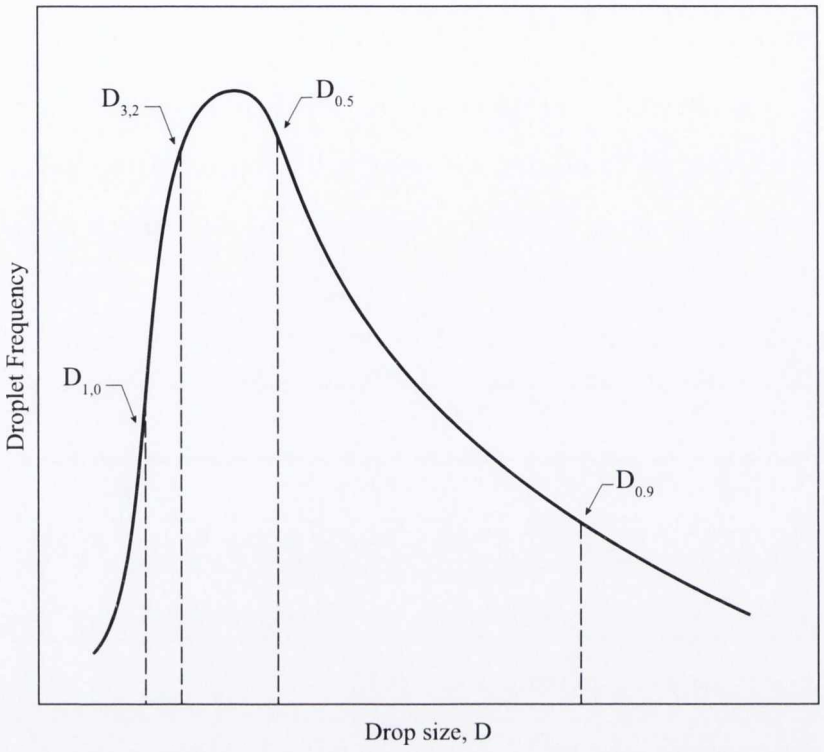

Figure 2.7: Locations of representative and mean diameters on a pressure spray droplet distribution curve [47]

this are usually very infrequent. A sample distribution from Chin and Lefebvre [47] for a pressure spray as reported by Lefebvre [24] is shown in figure 2.7. The positions of different representative and mean diameters are shown.

The arithmetic mean droplet diameter, $D_{1,0}$ is also used.

$$D_{1,0} = \frac{\sum n_i d_i}{\sum n_i} \tag{2.27}$$

The volume mean is another measure of average droplet size, $D_{3,0}$. Calculated based on the droplet volume, multiplying it by the total number of droplets gives an estimate for the total volume of liquid contained within the droplets detected.

$$D_{3,0} = \left(\frac{\sum n_i d_i^3}{\sum n_i} \right)^{1/3} \tag{2.28}$$

2.3 Mist Jet Flow Structure

Once the liquid jet has been atomised and the mist jet has been formed, the next aspects to consider are the structure of the mist jet, the behaviour of the droplets within the jet and the effect the droplets have on the jet structure. While within the literature there is substantial coverage on the distribution of droplets within a spray, the structure of mist jets has received less attention. Where possible, this section focuses on results for mist jets formed using airblast atomisation.

As the formation of a mist jet from airblast atomisation involves annular air jet flow, this section first examines the structure of the annular air jet before moving onto that of the mist jet.

2.3.1 Structure of an Annular Air Jet

Standard round jet impingement has received significant attention; many studies have been reported on the fluid flow and heat transfer characteristics of the impinging round jet, see for example Liu and Sullivan [48], Lytle and Webb [3] or O'Donovan and Murray [4]. Annular air jets have not been as extensively studied. However, within the literature there is sufficient information to provide a description of the annular jet structure.

The structure of an annular jet was divided into three regions by Ko and Chan [49–51]; this has been summarised by Patte-Rouland et al. [52], who presented a schematic to represent the different regions, as shown in figure 2.8. The first region is the initial merging zone, just beyond the nozzle exit, shown as zone 1 in figure 2.8; this is characterised by a recirculation zone, potential core and stagnation point where the jet is undisturbed by interactions with the surrounding fluid. The second region is the intermediate merging zone, which is at the end of the potential core, identified as zone 2 in figure 2.8. In this region the annular jet is seen to reattach to the axis of the jet, at point 8 in figure 2.8; beyond this point the jet is fully developed and merges into the third region, namely the fully developed region, zone 3 in figure 2.8. The overall pattern in this region is similar to that of a round jet [46].

Patte-Rouland et al. [52] examined the flow structure of the annular jet using particle image velocimetry (PIV) for a Reynolds number of 7680. Figure 2.9 shows the time-averaged

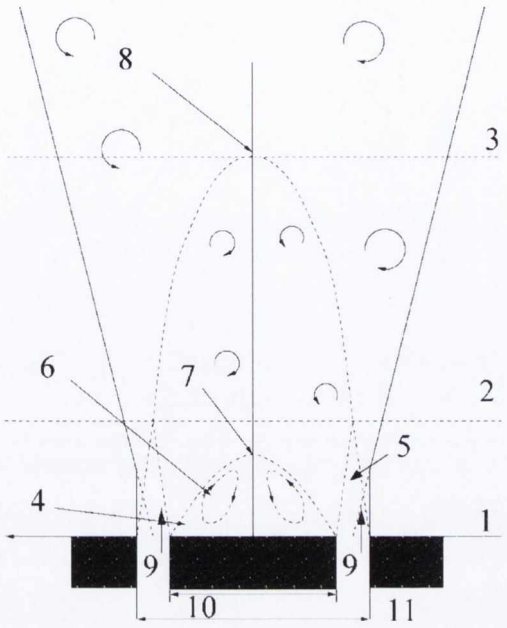

Figure 2.8: Schematic showing the structure of an annular air jet [52]. 1, 2, 3 are the initial, intermediate and fully developed merging zones; 4 is the recirculation zone; 5 is the potential core; 6 is a circulating flow; 7 is the stagnation point; 8 is the reattachment point; 9 is the nozzle exit; 10 and 11 are the inner and outer diameters

velocity field for an upward facing annular jet, the same configuration as in figure 2.8. The recirculation within the initial mixing zone can be clearly seen, with the stagnation zone located at $X/D_o \approx 0.5$. Beyond the stagnation zone in the intermediate zone the jet is seen to contract towards the jet axis and flow downstream at $X/D_o \approx 0.7$. Downstream from $X/D_o \approx 0.7$ represents the fully developed region.

Yang et al. [46] also performed PIV measurements on an annular jet with Re = 7000, this time examining the flow field for an impinging jet. They examined three nozzle-to-plate spacings, H/d = 0.5, 2.1 and 4.1. The different velocity fields are shown in figure 2.10. The solid black lines represent streamlines of the flow and are included for illustration purposes. The different flow structure with varying z/d is clear from these results. At the low separation of 0.5, figure 2.10 (c), the exit flow is deflected towards the jet axis by the presence of the plate, forming a strong reverse stagnation point. As the separation increases to 2.1, 2.10 (b), the plate still causes a relatively strong reverse motion of the jet towards the nozzle exit. For the relatively large separation distance of 4.1, figure 2.10 (a), the flow impinges on the plate in a similar manner to a round jet, with a peak region in pressure noted by Yang et al. [46].

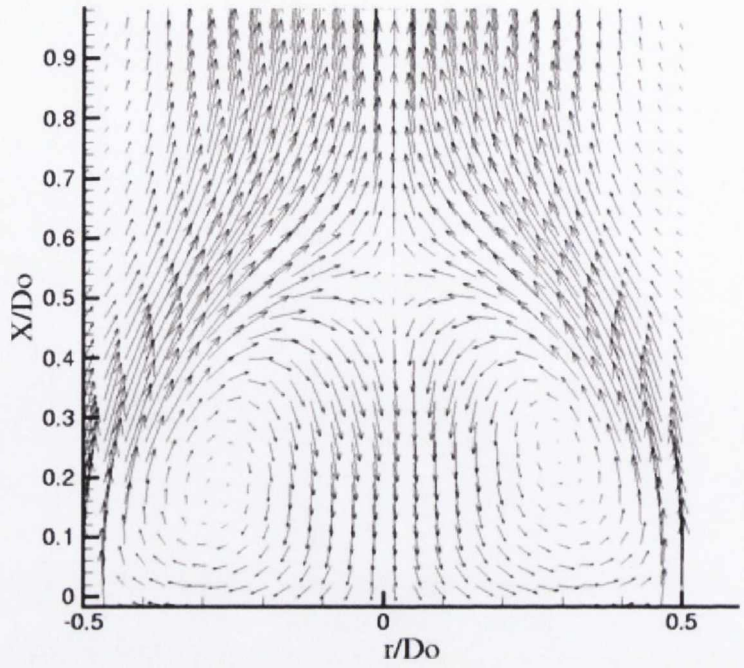

Figure 2.9: Average velocity field for an upward facing annular jet, with $X/D_o = 1$ and Re = 7680, [52]. The outer walls of the annular nozzle are at $r/D_o = 0.5$ and $r/D_o = -0.5$

Recirculation towards the nozzle exit is still visible just beyond the nozzle exit in the initial zone, as described by Patte-Rouland et al. [52].

An impinging annular jet structure may experience hysteresis and bistability, as reported by Trávníček and Tesař [53–55]. These authors have reported that the structure of the annular jet can take on one of two forms, as demonstrated in figure 2.11. The pattern in figure 2.11 (a) is characterised by the small recirculation zone just downstream of the nozzle exit and a central stagnation point on the wall. The pattern in figure 2.11 (b) shows a larger recirculation zone that reaches the wall and a stagnation circle. In figure 2.11 (a), the flow reverses upstream of the wall, whereas in the alternate pattern shown in figure 2.11 (b) this reversal happens on the wall, so the entire space between the nozzle exit and the impingement wall has recirculating fluid.

Trávníček and Tesař [55] determined that either of the two flow structures can occur for specific conditions. This bistable behaviour was observed for values around $H/D = 1$. The authors [55] determined that Reynolds number is a key parameter; for Re = 5000 this behaviour was observed, but not for Re = 10000. From this it was concluded that the bistability is promoted by the fluid viscosity as increasing the Reynolds number caused the

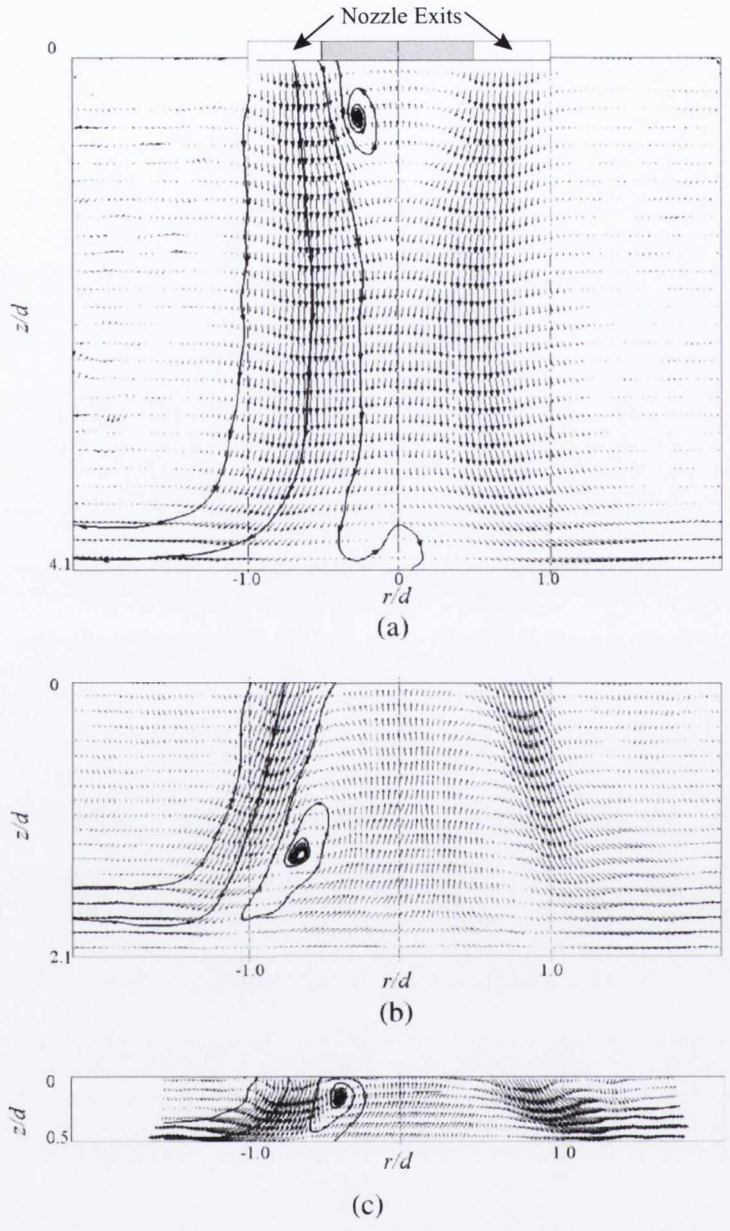

Figure 2.10: Velocity fields for an impinging annular air jet with Re = 7000 and for (a) $z/d = 4.1$, (b) $z/d = 2.1$ and (c) $z/d = 0.5$, [46]

cessation of the bistable behaviour. It was speculated that turbulent eddies in the flow at higher Reynolds numbers prevent the bistability from occurring. The centre-body of the annular jet was seen to also affect this behaviour, if it extended beyond the jet exit. Extension of the centre-body tended to promote the hysteretic behaviour, as per Trávníček et al. [55]. The authors attribute this to the Coanda affect, which causes the flow to cling to the centre-body extension and affect the recirculation behaviour. The effect of the diameter ratio, D_i/D_o was

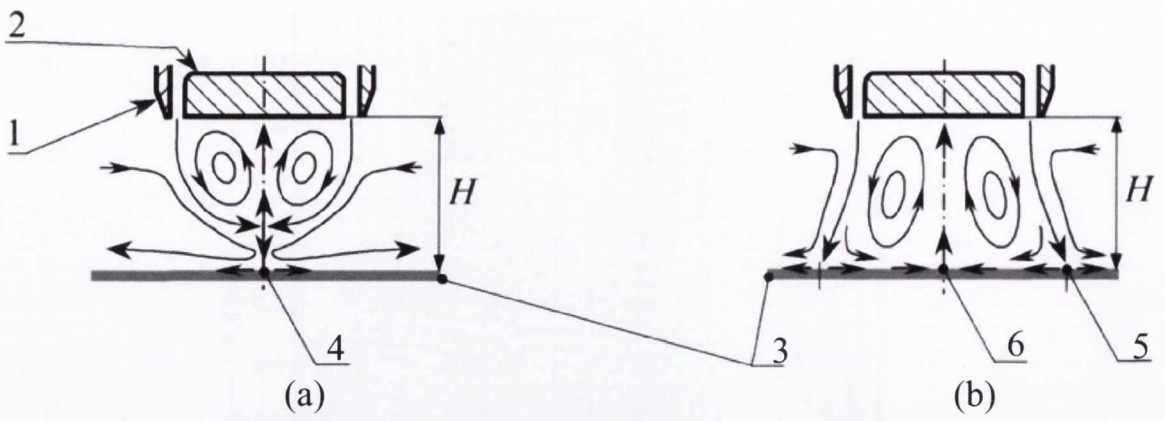

Figure 2.11: Bistable impinging annular air jet for Re = 5030, D_i/D_o = 0.947; H/D_o = 1.067. 1: outer nozzle body, 2: nozzle centre-body, 3: wall, 4: central stagnation point, 5: stagnation circle, 6: reverse stagnation point [55]

also examined and it was found that while for $D_i/D_o = 0.947$ two different flow structures were observed for the same Reynolds number, for $D_i/D_o = 0.767$ the annular jet flow structure did not exhibit any hysteresis. The authors surmised that this bistability was linked to very small annular jet widths, i.e. large diameter ratios, though no explanation is provided.

The annular nozzle exit affects the choice of characteristic length when considering parameters such as the Reynolds number, as discussed in section 2.1.3, and the dimensionless nozzle-to-surface, H/D, and radial, r/D, spacings. Ichimiya [45] used the outer diameter of the annulus for the calculation of H/D and r/D as the author asserts this better represents the spread of the annular jet. For this study the same approach is taken, while the hydraulic diameter of the annular jet is used for the Reynolds number characteristic length, again as per section 2.1.3.

2.4 Mist Jet Structure

Due to the complex nature of the co-flowing jets of different densities, the general structure of the mist jet is not well understood. To date, the flow structure has been examined in terms of the liquid droplet properties only, as to the best of the author's knowledge, the air structure has not been visualised. However, the mist jet may resemble an annular air jet, with a recirculation zone close to the nozzle exit and a gradual evolution towards a structure similar to that of a circular jet at high H/D.

With the advent of particle sizing techniques, particularly phase Doppler anemometry, information has been obtained on the structure of the mist jet in terms of its droplet properties. Early work using this technique by Hardalupas and Whitelaw [56], as reported by Engelbert et al. [22], suggested that the mist jet produced by coaxial airblast atomisation was symmetric, and the work of Engelbert et al. [22] produced the same result using the same nozzle. Engelbert et al. [22] demonstrated that the Sauter and arithmetic mean droplet diameters were largest at the liquid jet axis, and decreased with increasing radial distance. The larger centreline droplets were attributed to the atomisation of "liquid clusters" that sheared off the liquid jet in the far-field, while the smaller droplets on the edge were viewed as having been stripped from the liquid jet core in the near-field. For their study, [22], the Weber and Reynolds numbers were such that a relatively long liquid jet core existed. It was also seen that with increasing distance from the nozzle, z/D_L where D_L is the liquid jet inner diameter, the proportion of large droplets increased as the smaller drops are more readily dispersed, and the spreading of the jet increased with increasing z/D_L. The radial mean droplet diameter distributions of Engelbert et al. [22] can be seen in figure 2.12 (a).

The axial velocity profiles obtained by Engelbert et al. [22] can be seen in figure 2.12 (b) for different mean droplet sizes. It can be seen that for the smallest z/D_L the centreline velocity is lower than the higher z/D_L cases; this was attributed to delayed acceleration of the droplets as momentum is transferred to them from the air stream. With increasing z/D_L the centreline velocity increases as the droplets accelerate to their maximum velocity. Further downstream again, at $z/D_L = 91$, the larger droplets have higher centreline velocity than smaller droplets as they maintain their velocity while the air velocity decreases due to their larger inertia. The centreline velocity for the three different droplet sizes are closest for the

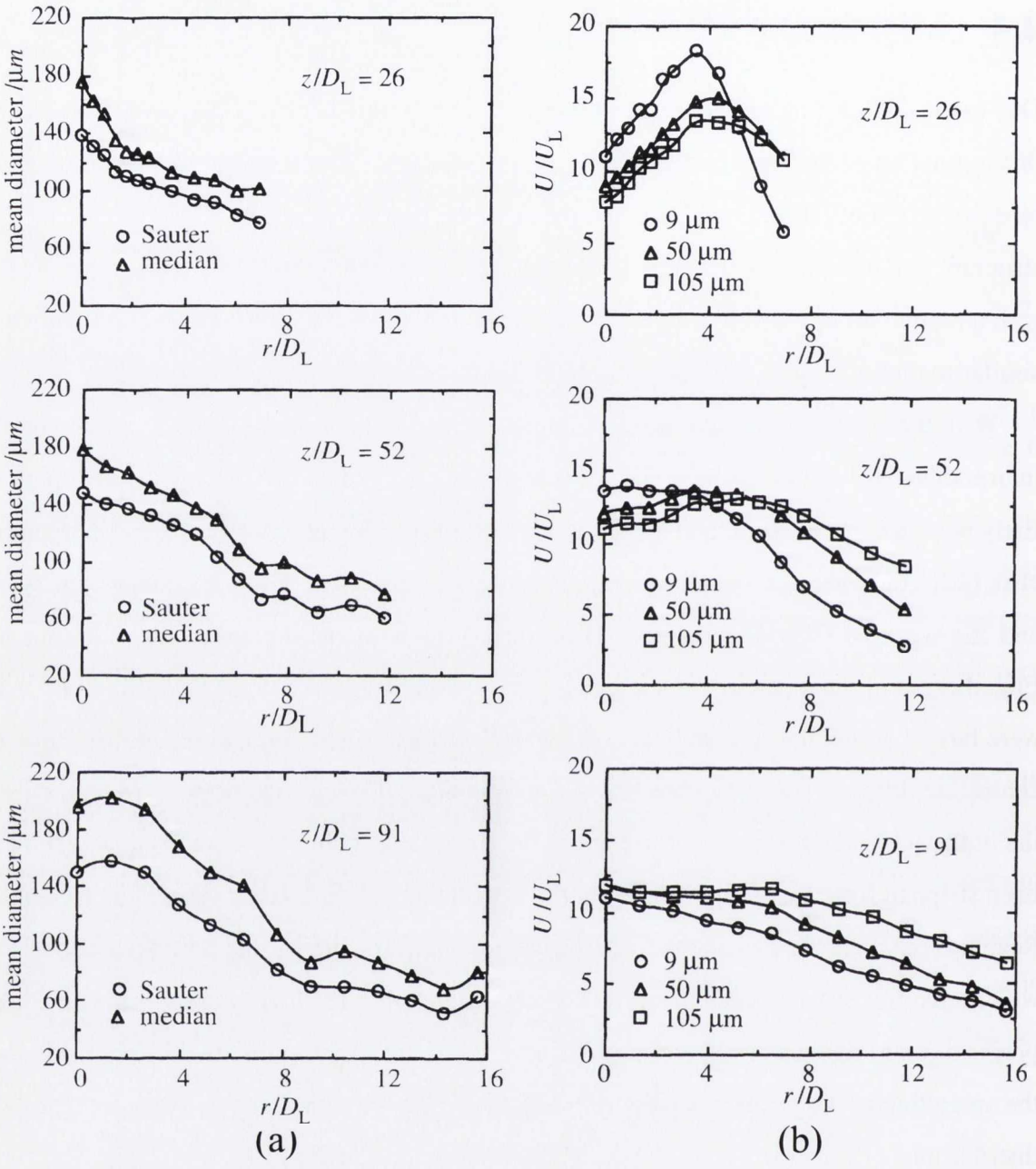

Figure 2.12: Droplet (a) diameter and (b) velocity radial profiles for airblast atomisation with increasing distance from liquid jet nozzle [22].

largest z/D_L indicating that the mist jet is becoming more uniform. Nearest the nozzle exit, the droplet velocities initially increase with radial distance; this was attributed to higher air velocity at this location. As the jet moves downstream the droplets on the jet axis accelerate and the local minimum at $r/D = 0$ has disappeared by $z/D_L = 91$. At the edge of the mist jet, the larger droplets have higher velocities as they maintain their velocity as the air jet

decelerates due again to their larger inertia.

The authors [22] also found that with increasing air flow rates at constant liquid flow rate the mean droplet size decreased, and the rate at which the droplets spread was seen to decrease with increasing air velocity. This behaviour was unexpected, as larger air velocity meant smaller droplets; these were expected to spread more than larger droplets. The authors attributed the behaviour to larger droplets being atomised from the edge of the liquid core with higher air velocities, which in turn act to prevent the smaller droplets from being ejected radially.

The jet conditions in the study by Engelbert et al. [22] were such that near-field atomisation was the primary factor in generating the droplet flow. This was also the case in the work of Marmottant and Villermaux [33], who produced probability density function maps of the droplet sizes that were stripped from near-field atomisation ligaments, showing a distribution weighted towards smaller droplet sizes in a gamma shape distribution.

Lasheras et al. [23] reported a different droplet distribution for the case when the liquid core was estimated as $L_b \approx 0$. Their droplet distributions are shown in figure 2.13. The distribution shows a minimum in droplet Sauter mean diameter at the jet centreline, which increases gradually until $r/D_g = 3$, after which point the droplet size increased sharply. The authors [23] do not explicitly state the reason for this behaviour, but suggest that the liquid jet is being atomised at the nozzle and the larger droplets are being thrown outwards as the break-up regime is "more efficient at the edge of the jet".

Lasheras et al. [23] also measured the mean droplet diameter for increasing downstream distance at the jex axis. It was reported that the Sauter mean diameter initially decreased to a local minimum at a downstream distance of between 15 and 30 diameters, depending on the flow conditions. For constant air velocity the local minimum occurred further downstream with increasing liquid velocity. For a constant liquid velocity and varying air velocity the local minimum moved slightly downstream with increasing air velocity. Beyond this minimum, the droplet size was seen to increase and continued to do so monotonically as far downstream as measurements were taken. This behaviour was attributed to coalescence in the mist jet, which occurred given a large enough distance from the nozzle exit when the turbulent kinetic energy had decreased until it was no longer able to provide strong enough pressure deformation forces to overcome the surface tension restorative forces. As with Engelbert et al. [22], Lasheras et

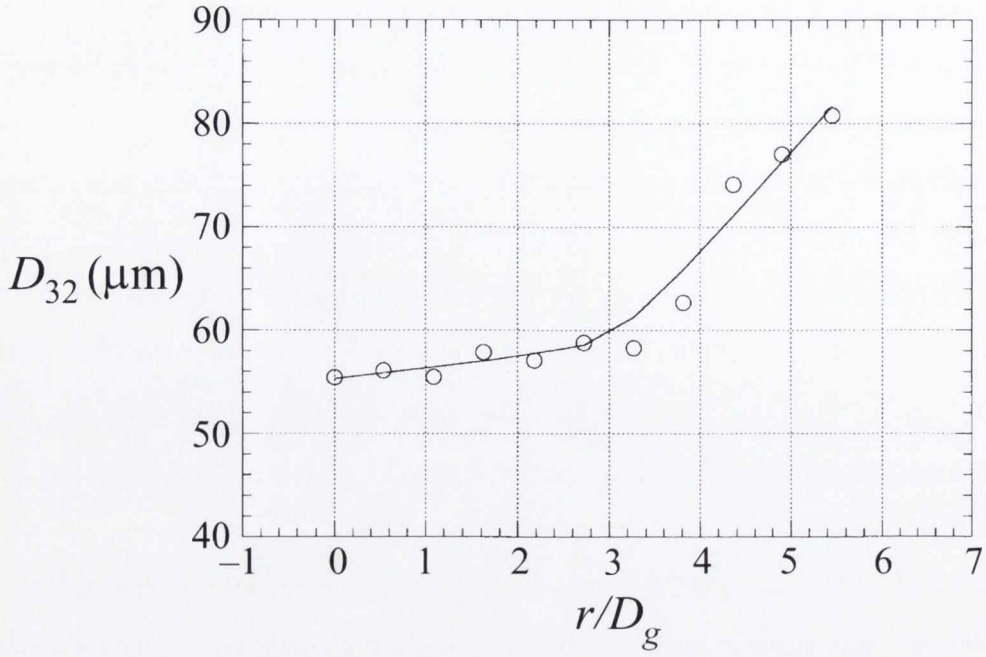

Figure 2.13: Droplet diameter radial distribution at 30 diameters downstream, [23]

al. [23] reported that larger droplets were slower to accelerate, but also slower to decelerate once they were far downstream, than smaller droplets.

The droplet size behaviour observed by Lasheras et al. [23] as liquid and air velocities were varied was much the same as that reported by Engelbert et al. [22]. For a constant air velocity, the Sauter mean diameter of the flow at the centreline was seen to increase with increasing liquid flow rate. With a constant liquid velocity and increasing air velocity, the Sauter mean diameter decreased, as more kinetic turbulent energy was available to atomise the jet. This behaviour has also been recorded in work by members of the research group using a similar nozzle [43].

Neither of these studies reported on the droplet intensity throughout the flow, however Engelbert et al. [22] demonstrated that the liquid flux is at a maximum at the jet centreline before decreasing with increasing radial distance. As the flow moves downstream, the liquid flux tends to spread out, indicating again the spread in the liquid droplets downstream. Lyons et al. [43] reported that droplet intensity increased with axial distance from the nozzle exit, and that droplet intensity decreases radially outwards towards the edge of the spray.

Liu et al. [35] studied the effect of the liquid jet diameter on airblast atomisation. For a constant air velocity, the liquid flow rate was varied for different liquid jet diameters. It was

seen that, in general, increasing the liquid jet diameter initially led to a decrease in droplet diameter to a local minimum before increasing again with further increases in liquid jet diameter. The local minimum in droplet diameter tended to correspond to larger jet diameters as the liquid flow rate increased. This behaviour was not as noticeable for low liquid flow rates though, for which the droplet diameter tended to remain constant. The authors attribute this decrease followed by an increase to competing influences on atomisation. As reported by Lasheras and Hopfinger [30], the droplet size is proportional to the liquid jet diameter. However as well as this, the relative velocity increases with liquid jet diameter, which results in a decrease in droplet size. Also, the mean spacing of Rayleigh-Taylor instability ligaments decreases as the liquid jet diameter decreases [30, 31]. The droplet size is proportional to this mean spacing and as such decreases. The results of Liu et al. [35] indicate that when the liquid jet is large its effect is dominant, and when it is small the relative velocity between the liquid and the gas dominates.

Droplet size affects the path of the droplets in the mist jet. This can be examined using the droplet Stokes number, which quantifies responsiveness of the droplet to turbulent fluctuations in the air flow and represents the ratio of the mean air flow timescale, T_m, to the droplet response time, τ. The mean flow timescale is defined as the ratio of the air jet diameter to the air velocity, while the droplet response time is the time it takes the droplets to accelerate to 66% of the air velocity. This is given by

$$\tau = \frac{\rho_L d^2}{18\mu_g} \tag{2.29}$$

where d is the droplet diameter under consideration. Engelbert et al. [22] found that for water droplets, the Stokes number was of the order of 1 for droplet diameters of 9 μm, the smallest diameter they considered. This implies that the droplets only follow the mean flow, rather than every turbulent flow structure. For bigger droplets, the Stokes number was always less than 1, so it was concluded that the droplet response to turbulent structures was mostly small. However, for different fluids this is not always the case. Nijdam et al. [13] reported that for organic droplets generated using a slightly different type of nozzle known as air-assist atomisation, the smallest droplets, of the order of 5 μm did follow most of the turbulent structures, possibly due to their smaller densities relative to water.

For a different type of droplet flow in an air jet, where droplets are injected into the flow rather than being atomised from a liquid jet, Ferrand et al. [57] and Mostafa and Mongia [58] found that the presence of droplets increased the centreline velocity of the air jet. This was attributed to a combined effect of momentum transfer from the droplets to the gas and a decrease in turbulent diffusion intensity. This decrease in turbulence intensity decreased as measurements were taken further downstream from the nozzle where the droplet concentration was lower. Increasing the liquid mass loading, which increases the droplet concentration, was seen to further increase the centreline velocity. This has not been demonstrated for the airblast atomisation process used to generate the mist jet in this study.

2.5 Mist Jet Impingement

As this work concerns the impingement heat transfer of a mist jet, it is important to consider the physical processes that take place when a mist jet impacts on a solid surface. The impingement of a droplet laden flow on a surface has been simplified by some authors as consisting of a large number of individual droplets [59, 60], particularly when considering spray impact models for heat transfer studies. In reality, these droplets will interfere with each other and this approach has been shown to be invalid for an ensemble droplet flow, for example in Kalantari and Tropea [61, 62] and Roisman and Tropea [63]. However, it is useful to examine the impact behaviour of a single droplet as it shows the different outcomes that can occur when a droplet hits a solid surface.

2.5.1 Single Droplet Impingement

Engel [64] presented an early study on the behaviour of water droplets impinging on a solid surface, using early high-speed Schlieren imagery to track the droplet impact; the results from this study were included in comprehensive reviews by Chandra and Avedisian [65] and Rein [66]. Rein et al. [66] described how droplets may rebound, spread or splash upon impact, as shown in figure 2.14 (a). In a more recent review of single droplet impingement, Yarin [67] discussed the work of Rioboo et al. [68] who expanded on the impact morphology, describing how a droplet can undergo deposition, a prompt splash or a corona splash, as shown in figure 2.14 (b).

The particular droplet impact behaviour that occurs was described by both Rein [66] and Rioboo et al. [68] as being dependent on the droplet impact kinetic energy, or velocity, although the dependence is not straightforward. This is generally expressed using the Weber number, defined for droplet impacts as

$$\mathrm{We} = \frac{\rho U^2 D}{\sigma} \tag{2.30}$$

where U and D are the droplet velocity and diameter respectively and the density, ρ, and surface tension, σ, are those of the liquid. Rein et al. [66] described that for low We the droplets rebound, and as We increases, the behaviour changes to spreading and then to splashing. Yarin [67] also describes the behaviour evolving from deposition to corona splashing with increasing Weber number. However, there is disagreement, on the thresholds for different impact morphologies. For example, Rein [66] presented the following experimental correlation of Walzel [69] relating the critical Weber number for splashing to occur, We_c, and the Ohnesorge number, Oh.

$$\mathrm{We}_c = 7.9 \times 10^{10} \mathrm{Oh}^{2.8} \tag{2.31}$$

However, this correlation was not in agreement with the experimental study of Stow and Hadfield [70], who reported that the correlation predicts a critical Weber number that is an order of magnitude too large.

More recently, Mundo et al. [71] presented a new dimensionless parameter, $\mathrm{K_d}$ with the subscript referring to the fact that the surface is dry, to characterise the transition from spreading to splashing. Defined in terms of the Weber and Ohnesorge number as

$$\mathrm{K_d} = \mathrm{We}^{1/2} \mathrm{Re}^{1/4} \tag{2.32}$$

Mundo et al. [71] gave a threshold of $\mathrm{K_d} > 57.7$ for splashing to occur. This correlation produces critical Weber numbers orders of magnitude smaller than that of Walzel [69] in equation 2.31. However, disagreement exists over this correlation also, as reported by Yarin [67]; Rioboo et al. [68] asserted that the splashing threshold could not be determined by the dimensionless groups of We, Re, Oh and K, as they do not account for surface roughness effects and wettability, which they state are of "the utmost importance" when determining the

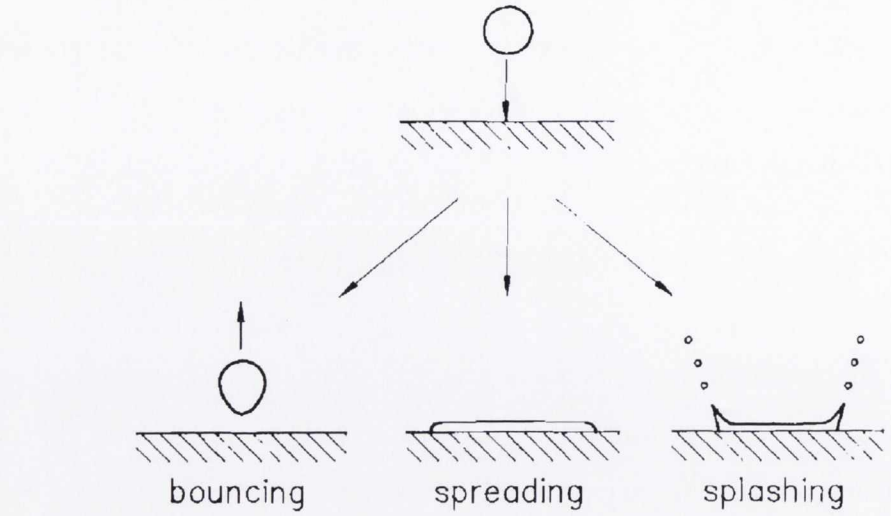

(a)

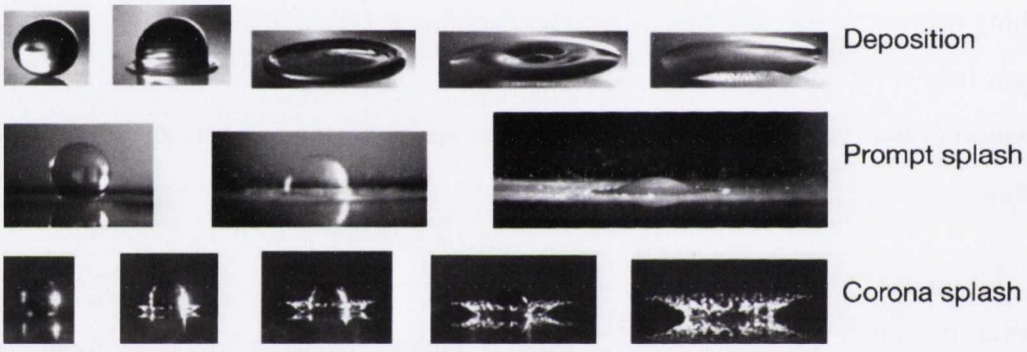

(b)

Figure 2.14: Impact of a droplet on a solid surface; (a) Rein et al. [66] and (b) Rioboo et al. [68]

droplet impact behaviour. As such, the correlation for K is essentially specific to the case of Mundo et al. [71]. No correlation accounting for these surface parameters was produced by Rioboo et al. [68].

For an impinging mist jet, the case of a droplet hitting a liquid film is important, since during mist impingement a liquid film can accumulate under the repeated impacts of droplets. As in the case of a droplet hitting a dry surface, different behaviour may occur when a droplet strikes a liquid surface. Rein [66] showed that a droplet can float, bounce, coalesce or splash, as shown in figure 2.15. Yarin and Weiss [72] identified the splashing of a droplet on a liquid film as being the result of a "kinematic discontinuity" in the film. Thus, when a droplet strikes a film, the liquid that was at the point of impact, as well as liquid in the droplet, flows radially outwards from the impingement zone. However, this local flow of liquid is prevented from

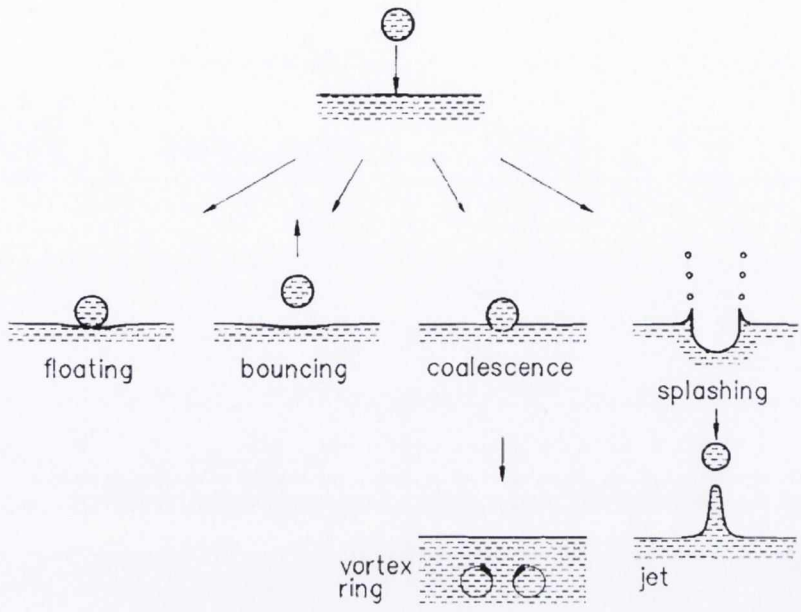

Figure 2.15: Impact of a droplet on a liquid surface [66]

flowing freely by the surrounding liquid film. Therefore, the flow of liquid caused by the splash is forced to move "virtually normal" [72] to the film, under capillary action, resulting in a splash.

Several authors have examined the behaviour of a droplet impinging on a liquid film; the work is usually linked to an attempt to model spray impingement as it has been recognised that a spray will often not be impinging on a dry surface. The majority of these studies have considered the case when the liquid film is thick, usually of the order of the droplet size and bigger, for example see [73–77]. These works are concerned in particular with the splashing case, and the subsequent liquid film behaviour as it is an important area of study for the development of spray impact models.

Figure 2.16 shows the different stages of a high energy droplet impact [77], and Figure 2.17 shows the same but for the case where a central jet is seen. After initial impact, a film of liquid flared outwards is ejected upwards from the edge of the collision region. This ejected film contains both liquid from the impinging droplet and the layer of liquid on the surface [78]. The crater expands into the liquid layer until either the viscous forces of the liquid decelerate the cavity to a stop, or the action of the wall forces the cavity to stop expanding down and rather forces it outwards. As the film expands upwards it thins and a crown shape is formed with secondary droplets being thrown from the rim. Surface tension and downward motion

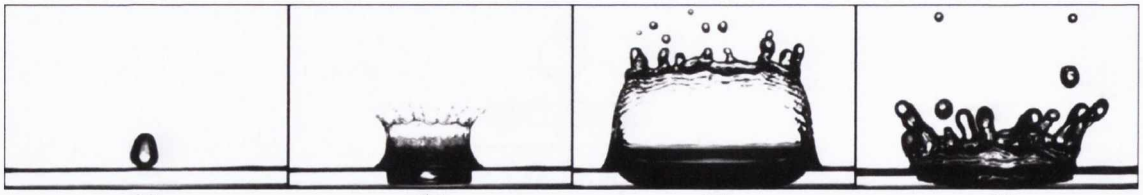

Figure 2.16: Photographs of the behaviour of a droplet impinging on a relatively thick liquid surface [77]

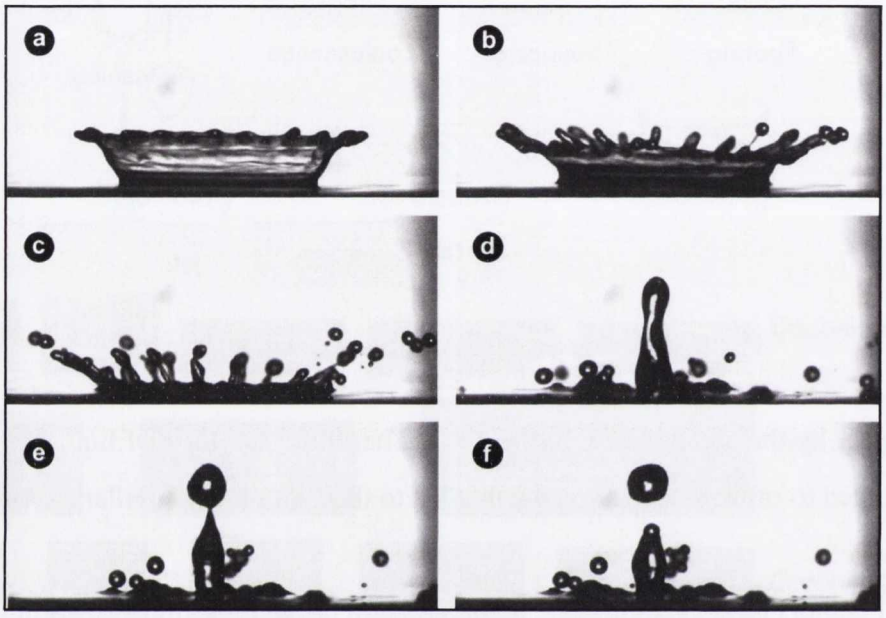

Figure 2.17: Photographs of the behaviour of a droplet impinging on a relatively thick liquid surface with a central jet [63]. (a) Creation of crown; (b) formation of outward jets from crown rim; (c) break-up of jets and onset of secondary droplets; (d) emergence of central jet; (e) deformation of central jet and (f) break-up of central jet

of capillary waves on the inner side of the cavity become dominant, leading to the waves converging concentrically at the bottom of the cavity and driving the crown down to the film. Within the cavity, the residual film begins to fluctuate under the action of the capillary waves. If the film is thick enough, a central jet is ejected from the cavity as it refills.

The work of van Hinsberg et al. [76] examined the dynamics of the cavity of the film under different conditions and reported that increasing the droplet velocity did not affect the propagation velocity of the liquid cavity. Instead, increasing the droplet impact energy led to a wider cavity being formed and increased the likelihood of the formation of a central jet. For liquid films thin enough for the wall to affect the flow, the residual film thickness under the cavity decreased asymptotically; this was attributed to viscous forces decelerating the flow and the incompressible nature of water.

A study on the impact of droplets on thick liquid films that is relevant to the current investigation is that of Samenfink et al. [73], who examined droplet impact on a shear driven flow, which resembles the film under a mist jet which is subject to the shear action of the wall air jet. Samenfink et al. [73] reported that the air flow that provides the shear energy forced secondary droplets outwards away from the impact location. Another important observation was that the momentum of droplets impinging obliquely mostly transferred downstream; little difference existed between the radial velocity of the impinging droplet and the secondary droplets. It should be stressed that this was for a relatively thick, wavy film, thicker than is encountered in the current study.

The case when the liquid film under the droplet is very thin has also been considered by some authors [78–80]; as the flow rates in the current work result in thin liquid films this case is of particular relevance. The film thickness is usually presented in the non-dimensional form as

$$h^* = \frac{h}{D} \tag{2.33}$$

where h is the actual film thickness and D is the droplet diameter. Van Hinsberg et al. [76] included in their analysis the case when $h^* < 1$. It was reported that changing the liquid film thickness in the range of $h^* << 1$ had little effect on how the residual thickness under the cavity changed with time, and that for constant droplet Weber number the cavity depth did not vary in any meaningful way for different thin films. Wang and Chen [79] also considered the case when $h^* < 0.1$. Figure 2.18 shows their work (a) for $h^* = 0.05$ (b) for $h^* = 0.5$, with the same Weber number of 2010 in both. It can be seen that for the thinner film, the crown shape is wider than the thick film case, and that the crown completely disintegrates into secondary droplets and ligaments rather than retracting back into the film. The small secondary droplets are spread widely after the break-up of the crown, wider than in the thick film case. No central jet is seen here, which was the case for all Weber numbers examined; this was attributed to the dissipation of kinetic energy to the crown which subsequently broke apart rather than collapse back into the film.

As in the case of droplet impact on a dry surface, the threshold for splashing to occur when a droplet impacts a liquid film has also been considered. Yarin [67] described a similar dimensionless grouping, K, to that for a dry surface as shown in equation 2.32, for impact on

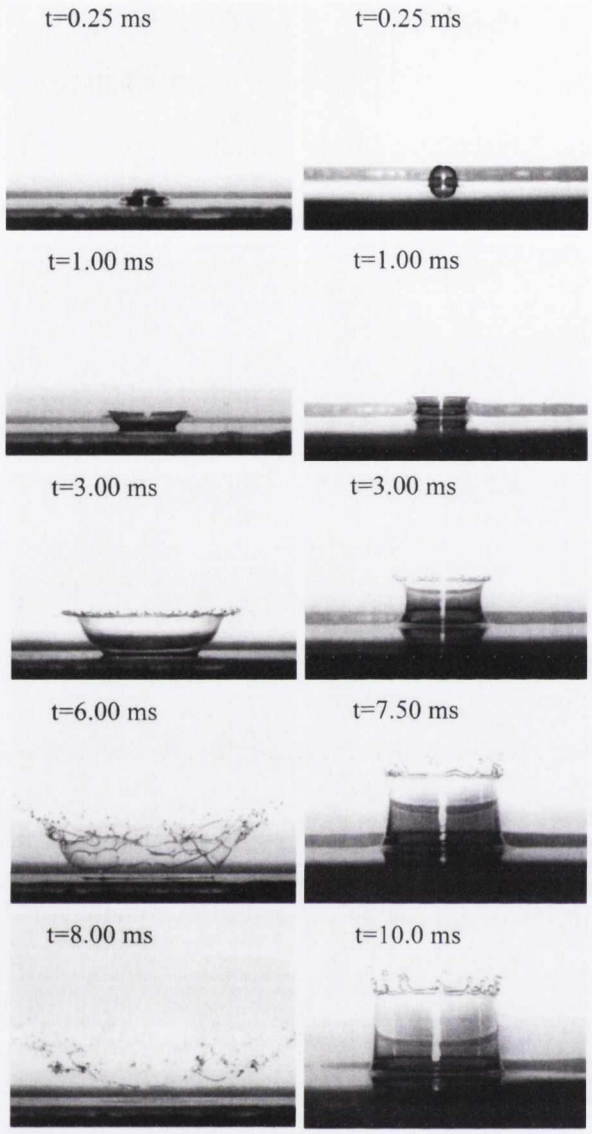

Figure 2.18: Impact of a liquid on a thin liquid film; (a) $h^* = 0.05$, (b) $h^* = 0.5$; We = 2010, Re = 1168 for a 70% glycerol-water solution [79].

a liquid film.

$$K = WeOh^{-2/5} \tag{2.34}$$

This parameter can be related to K_d by

$$K = K_d^{8/5} \tag{2.35}$$

Cossali et al. [81] produced an experimental correlation for the threshold of the onset of

splashing for a liquid film with a dimensionless thickness $0.1 < h^* < 1$.

$$K > 2100 + 5880h^* \tag{2.36}$$

This correlation was in reasonable agreement with Wang and Chen [79] for the same range of h^*. Again however, Yarin [67] suggests that the surface roughness will influence this threshold. Wang and Chen [79] also demonstrated that for $h^* < 0.1$ the critical Weber number for splashing to occur when $h^* < 0.1$ is very insensitive to changing film thickness. When their data is considered, the onset of splashing occurred at lower K than the correlation of Cossali et al. [81] in equation 2.36. Wang and Chen [79] suggested that surface roughness may be responsible for this, but did not elaborate further. They suggested a critical Weber number for splashing of $We_c \approx 400$ for similar Ohnesorge numbers as this study; this gives a K of ~2000.

While thresholds for the onset of splashing from droplet impact on dry and wetted surfaces have been produced, the conclusion of reviews of single droplet impingement behaviour such as Rein [66] and Yarin [67] is that this is a complex hydrodynamic process. Experimental correlations that have been produced are unlikely to predict the impact morphology for different experiments owing to surface roughness affects which have not been accounted for fully. Thus, while the thresholds offer a guideline for splashing behaviour, they are not strict boundaries.

2.5.2 Spray Impingement

No work has been reported on droplet impingement and film interactions for a mist jet generated using airblast atomisation. However some work has been reported on the behaviour of impinging sprays. These are discussed in this section as a reasonable approximation of an impinging mist jet, though without the annular air jet component of the mist jet. Work on spray impingement behaviour has focussed on two areas: droplet and cavity behaviour and the generation of secondary droplets [62, 82], and the flow of the film under the influence of the impinging droplets [61, 63, 83]; again the majority of work has focussed on relatively thick films.

In these studies on spray impingement, it is reported that the interactions between droplet

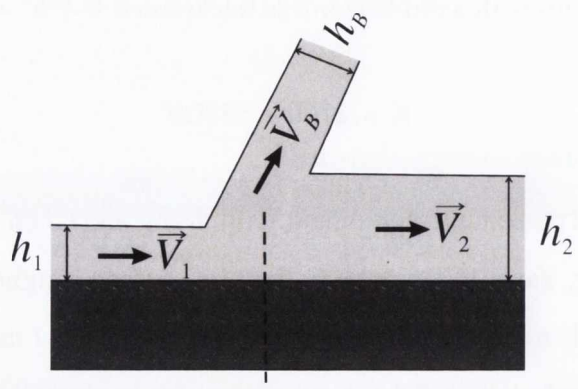

Figure 2.19: Flow of the liquid film under a droplet impact. h_1 is the liquid thickness under the cavity, h_2 is the mean thickness of the film and h_B is the thickness of the uprising sheet; V_1 is the film velocity under the cavity, V_2 is the velocity of the rest of the film and V_B is the uprising sheet velocity [63].

impacts will affect how the droplets behave on impingement [84]. As reported by Sivakumar and Tropea [85], Tropea and Roisman [84] characterised the interactions as direct due to collisions or indirect due to fluctuations in the film on the surface; this work was concerned with dense sprays. It was seen that these interactions manifested themselves as disruptions in the spray crowns and critical splashing Weber number. In another study on a dense spray, Roisman and Tropea [83] demonstrated that for the thick film generated from a dense spray, the interactions were seen to enhance the size of droplet splashes. This was attributed to fluctuations in the pressure of the film due to the repeated impacts of the droplets. Kalantari and Tropea [61] reported that for a spray, the non-dimensional crown height after splashing and its radius did not depend on the Weber number, unlike the case of a single droplet where a strong dependence is seen.

Kalantari and Tropea [61] also discussed the generation of secondary droplets from spray impact. The authors [61] discussed how larger impinging droplets resulted in relatively larger secondary droplets being shed from splashes; it was also observed that faster impinging droplets resulted in smaller secondary droplets as the increased kinetic energy of the splashes was better able to overcome the surface tension. It was also reported that normal impacts resulted in significant velocity decay between the initial and secondary droplets. However for oblique impacts, tangential velocity was preserved. This led the authors [61] to conclude that tangential momentum was conserved, while the normal momentum was dissipated or else diverted into tangential momentum, causing the film to flow outwards. The observation that the film was thinner for higher nozzle pressures, and therefore higher liquid flow rates,

would back up this behaviour. For some oblique impacts, more liquid mass was observed being ejected from the film than was incident with the intial drop. This points to significant disturbance in the liquid film as it is the only source for this extra liquid mass.

While most of the literature is concerned with dense sprays, Roisman and Tropea [63] considered a sparse spray, and how its impingement behaviour compares to that of a denser spray. In their paper, the authors contend that for a sparse spray the secondary droplets are produced by the splashing of impinging droplets in a manner similar to single droplet impingement, and that in dense sprays the secondary droplets are mainly produced by fluctuations in the liquid film as the splashes are disrupted by further impinging droplets. It was also observed that since the liquid film is flowing outwards from the centre, even normal droplet impacts are locally oblique, thereby affecting the splashing behaviour in a spray. Figure 2.19 shows the flow of the liquid after a droplet impact. The authors [63] conclude that even for sparse sprays, the presence of other impacts mean the spray impingement behaviour cannot be treated as the superposition of individual impacts due to the flow of the film. Therefore even in sparse sprays, similar to this study, the presence of many droplets will affect each other, even if the droplets and their splashes never come in direct contact.

2.6 Summary

This chapter has outlined the processes involved in the formation of both a spray and a mist jet, and the parameters that affect their generation. The structure of a mist jet and spray is also presented, as well as the behaviour of individual droplets and sprays upon impingement. A thorough understanding of these issues is important before moving onto a review of mist jet and spray heat transfer as their cooling performance is inherently linked to their structures and what happens on impingement.

Chapter 3

Mist Jet Heat Transfer

As discussed in the introduction in section 1.1, mist jets have been shown to offer significant heat transfer enhancement over that of conventional gas jets [19], and work has also been reported showing that spray cooling compares favourably with liquid jet cooling, particularly in terms of the efficiency of liquid usage [21]. However the convective heat transfer mechanisms associated with the flow of droplets in a jet is complex; interdependence of mist parameters makes it difficult to isolate individual parameters for study and leads to competing heat transfer influences.

Historically within the literature, far greater attention has been paid to the heat transfer behaviour of impinging sprays than mist jets, and even for sprays heat transfer studies until very recently have almost exclusively dealt with boiling heat transfer; very few studies have been identified that explore heat transfer of a mist jet, particularly in the absence of boiling. Thus for clarity this literature review is structured as follows: first the issue of heat transfer between the phases within the mist jet flow is examined; then, as in section 2.5, the heat transfer due to a single droplet impinging on a heated surface is briefly examined. Next an overview of boiling regime spray and mist jet heat transfer is provided; this is followed by a review of spray cooling heat transfer without boiling. Finally the limited studies to date for mist jet heat transfer without boiling are discussed.

3.1 Heat Transfer Within the Mist Jet Flow

The addition of liquid droplets to an air jet in the form of a mist adds an additional heat transfer mechanism that does not exist within a single-phase jet: the vaporisation of droplets within the flow. Studies on evaporation have focussed on organic liquid sprays such as isopropyl alochol [86] or methanol [87], or on refrigerant sprays [87] rather than water sprays or mist jets. Indeed, Lefebvre [24] considers the evaporation of liquid hydrocarbon fuels in

combustion devices at elevated temperatures to be the main area where evaporation within the flow is relevant.

For the case of a solvent spray in a room temperature environment, Ferrand et al. [88] made the assumption that no vaporisation occurs as the droplet vaporisation time was estimated to be greater than the droplet transit time. Lefebvre [24] quantified the droplet vaporisation rate according to the relationship referred to as the "D^2 Law"

$$D_0^2 - D^2 = \lambda t \tag{3.1}$$

where D_0^2 is the initial droplet diameter, D is the drop diameter after evaporation over some time, t, and λ is the evaporation constant which depends on the relative velocity between the droplet and the gas, local gas properties, vapour pressure, liquid vapour mass fraction and mass diffusivity [24]. Ferrand et al. [88] considered the case when a droplet is completely evaporated, which gives

$$t \approx \frac{D_0^2}{\lambda} \tag{3.2}$$

and estimated that for a 50 μm drop diameter, a typical Sauter mean diameter, the minimum droplet evaporation time was 1.45 s; the corresponding transit time was significantly shorter, being measured as approximately 35 ms. Therefore it was decided that the evaporation within the flow was negligible. This assumption is also generally made when the droplet liquid is water, as per Lasheras et al.[23], though the authors caution that this assumption is not valid for large transit times. As the water droplets in this study are entrained within a high velocity air jet, the assumption that negligible evaporation is occurring is made. However, smaller droplets are more readily vaporised, as shown by Mostafa and Elghobashi [87], and a two-component two-phase flow will undergo some level of evaporation [89]. Thus, it is prudent to examine the heat transfer process briefly.

Both numerical [87, 90] and experimental [13, 86] studies into the phenomenon of droplet evaporation in a flow have been performed. Mostafa and Elghobashi [87] described the driving force behind the evaporation of a droplet in a gas flow as being the concentration gradient within the flow; this is defined as the ratio of the mass of the evaporated material within a control volume to the mass of the carrier phase in the same volume. Different parameters have

been identified as impacting droplet evaporation. Berlemont et al. [90] examined numerically the effect of turbulent fluctuations in the carrier flow, as well as fluctuations in temperature and vapour mass fraction, on droplet evaporation. Turbulent fluctuations were seen to have little effect on droplet evaporation. Again, this was attributed to the small interaction time between the droplet and the gas, relative to the transit time. High temperature fluctuations were also seen to increase the evaporation rate, whereas the variations in vapour mass fraction were not seen to influence the mean droplet diameter.

Sommerfeld and Qiu [86] found that decreasing the air velocity led to lower droplet velocities and hence higher droplet transit times; this resulted in increased droplet evaporation as the droplets are exposed to the air stream for longer. It was also reported that increasing the air temperature resulted in an increase in evaporation rates. However, the authors noted that this effect was less marked than that of decreasing the air velocity.

Nijdam et al. [13] examined experimentally the evaporation of droplets at different locations in a jet flow. It was seen that close to the nozzle exit and in the potential core of the jet, little evaporation occurred. However downstream and in the shear layer at the edge of the potential core, the turbulence levels were higher and more evaporation was observed. It was suggested that the air that is entrained into the flow dilutes the evaporated vapour and hence causes an enhancement in evaporation. It was also seen that the evaporation level was higher at the edge of the jet due to the fact that smaller droplets gather at the edge due to higher dispersion because of their smaller inertia; these droplets evaporate more readily, thereby increasing the level of evaporation. Nijdam et al. [13] used two different fluids, turpentine and acetone, and the spreading of droplets was shown to be independent of the fluid. The authors therefore concluded that evaporation does not affect jet spreading as the different fluids had different evaporation rates.

The evaporation of droplets within a mist jet is relevant to the heat transfer enhancement offered by a mist jet; due to the evaporation the air temperature will be lowered, resulting in an improvement in the convective cooling ability of the air jet, and hence the total mist jet enhancement [91]. As stated above, however, evaporation is unlikely to occur for an air-water mist jet at an appreciable rate for all but the very smallest droplets, due to the vaporisation time being greater than the transit time. Therefore the level of enhancement due to evaporation within the jet will be relatively small when compared with the mechanisms described below.

3.2 Impinging Single Droplet Heat Transfer

While it has been shown that a spray cannot be modelled as the superposition of undisturbed individual droplet impacts [63, 85], examining the heat transfer behaviour of an individual droplet impinging on a heated surface provides a useful starting point. This has been the motivation behind several studies conducted, for example the work of Senda et al. [92] and Cossali et al. [93]. As for mist and spray studies, the majority of work reported has been for surface temperatures above the boiling point of the droplet liquid. Chandra and Avedisian [65] conducted a study where the surface temperature was below the boiling point, however this was concerned only with the fluid dynamics associated with a droplet hitting a heated surface and did not report on the heat transfer.

Healy and Hartley [94] described how when a droplet impacts on a heated surface, it is first assumed to spread adiabatically over the surface, as demonstrated by Chandra and Avedisian [65], giving rise to a film shape. After the film has spread to its maximum area, the heat transfer to the film from the surface is assumed to begin as the liquid begins to evaporate. The authors [94] numerically examined this assumption for a water droplet and the case when the surface temperature was at the saturation temperature; they discovered that the adiabatic assumption is valid at the start of the impact, but the surface temperature may start to have an influence as the spreading goes on by affecting the liquid properties. Evaporation from the droplet is coupled with the relatively high momentum of the droplet impinging on the surface to account for the heat transfer performance of the impinging droplet.

The collision of a droplet with a surface heated to different temperatures is shown in figure 3.1 as presented originally by Chandra and Avedisian [65]. As the film spreads, it becomes thinner, facilitating evaporation. The authors [65] reported that increasing surface temperature led to the liquid film becoming thinner in places, further enhancing the evaporation rate in these locations. The ligament like structures seen in figure 3.1 were also observed to facilitate evaporation.

The effect of droplet parameters such as velocity and size is not discussed here for the single droplet impingement case as even for sparse sprays the interaction of droplets is likely to significantly alter these affects [63]; the influence of these parameters is discussed for the ensemble flow instead.

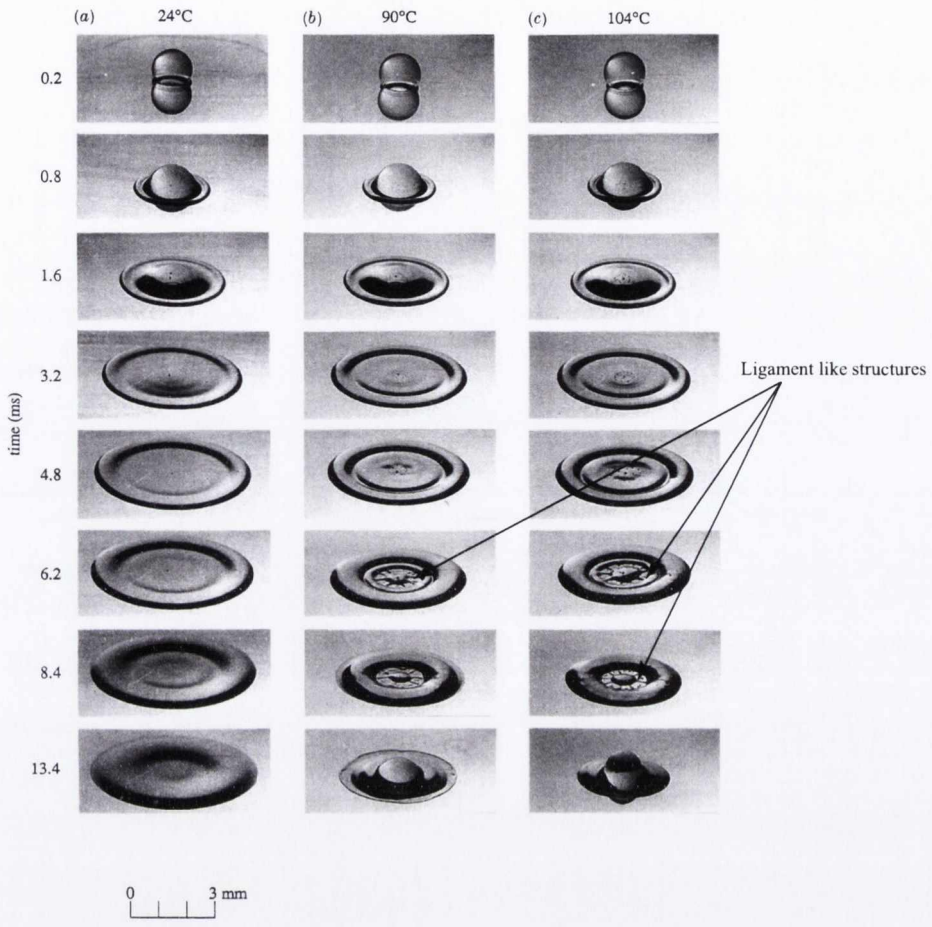

Figure 3.1: Impact of a heptane droplet on a heated stainless steel surface at increasing surface temperatures [65]. The saturation temperature of heptane was given as 98 °C

3.3 Characterising Spray and Mist Jet Heat Transfer

Before discussing the heat transfer behaviour of sprays and mist jets, it is important to note that quantifying heat transfer for such flows is not straightforward, and the same approach cannot necessarily be used for both cases. The Nusselt number, Nu, is the usual choice for presenting convective heat transfer for a single-phase jet, O'Donovan and Murray [4], Vader et al. [7], and is typically used for convective heat transfer correlations. Representing the ratio of convective to conductive heat transfer, for an impinging jet, the Nusselt number is given by

$$\mathrm{Nu} = \frac{hD}{k_f} \tag{3.3}$$

where h is the heat transfer coefficient, D is the characteristic length scale, generally the jet diameter for impinging jets, and k_f is the thermal conductivity of the fluid.

In the case of sprays generated by pressurising the fluid across the nozzle exit, most authors have chosen to express the heat transfer with the Nusselt number, using the thermal conductivity of the liquid in the spray and the nozzle diameter (e.g. Fabbri et al. [16] and Tao et al. [95]). Thus, the spray is treated as a single-phase liquid flow. Spray heat transfer has also been quantified in terms of the heat flux from a surface. For example Rybicki and Mudawar [17] and Wang et al. [96] use this approach for spray studies in the non-boiling regime. Typically this is also the case for boiling studies, especially those concerned with the critical heat flux, such as Hernández-Bocanegra et al. [12].

For a mist jet, which is a two-phase air and water flow, an issue arises with respect to the value of the thermal conductivity to be used in determining the Nusselt number. To avoid this problem, the heat transfer coefficient, h, is commonly used to characterise the mist jet heat transfer. This was the approach used in the work of Chang and Su [19] and Tay et al. [97]. The heat transfer coefficient is defined as

$$h = \frac{q''}{T_s - T_j} \tag{3.4}$$

where q'' is the surface heat flux, T_s is the surface temperature and T_j is the jet temperature. The adiabatic surface temperature is often used as the reference temperature for complicated flows, as per Li et al. [98]. However, when a constant temperature boundary condition is used, as in this study, this can result in negative heat transfer coefficients, particularly when the driving temperature difference is low. For mist jets, there exists the further issue of which reference fluid temperature to use: the water temperature, as in Fabbri et al. [16] or the air temperature as per Tay et al. [97]. The air temperature has been chosen for this study for consistency with previous departmental work and with comparable work within the literature [97]. The water and air temperatures are similar levels, and for the very small liquid flow rates considered in this investigation the water temperature will have a very small influence on the overall temperature.

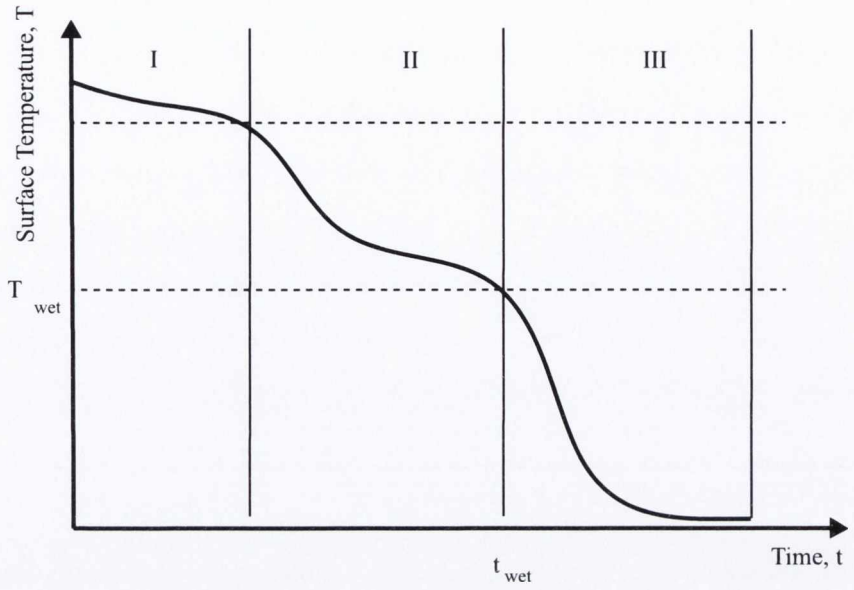

Figure 3.2: Transient mist cooling curve under boiling conditions, split into three regimes: regime I is radiation dominated; regime II is convection dominated; regime III is the case when the surface temperature is close to the saturation temperature of the droplets [100]

3.4 Boiling Regime Spray and Mist Jet Heat Transfer

Boiling heat transfer studies for mist jets and sprays have been reported on extensively, again with more attention being paid to sprays than mists. Although this study is focussed on the non-boiling regime, a brief overview of spray and mist jet boiling heat transfer is appropriate. Kim [99] reported a thorough review of spray cooling, focussing particularly on the boiling regime and methods of further enhancing spray cooling.

Lee et al. [100] examined the boiling heat transfer for a mist jet. The authors [100] described mist jet boiling as consisting of three regimes, as shown in figure 3.2: regimes I and II correspond to film boiling and regime III to transition and nucleate boiling. The wetting temperature, T_{wet}, refers to the surface temperature excess relative to the saturation temperature below which a liquid film begins to form due to the impinging mist jet; above this temperature the mist droplets are vaporised before impacting on the surface. The wetting time, t_{wet}, is the length of time it takes for this wetting to occur once a heated plate is subjected to an impinging mist jet.

In regime I, as reported by Lee et al. [100], Buckingham and Haji-Sheikh [101] described the heat transfer as being radiation dominated. The surface temperature is so high that

virtually all droplets evaporate before hitting the surface. Regime II was identified as a convection-dominated region [101]. Here, the vast majority of droplets are evaporated within the thermal boundary layer as radiation is not sufficiently high to vaporise the droplets before they reach the boundary layer; convective heat transfer to the air-water vapour mixture is therefore the dominant mechanism. In regime III, the surface temperature is just above the liquid saturation temperature and as such most of the droplets impinge upon the surface. In this regime, Lee et al. [100] described the heat transfer as being driven by "wetting phenomena", with evaporation of the liquid film being suggested as the dominant parameter, though no quantitative analysis was performed. Horacek et al. [11] described how for surface temperature corresponding to regime III, droplet impingement on the liquid film that forms under spray impingement is seen to disturb the film significantly, enhancing heat transfer.

3.4.1 Boiling Heat Transfer Parameters

Several parameters have been identified as affecting boiling regime heat transfer of mist jets and sprays. However, as concluded by Kim [99], there remains disagreement over the effect these parameters have and their relative contributions to boiling heat flux.

Significant attention has been afforded to examining the effect of liquid mass flow rate, or flux, for sprays in the boiling regime. Several authors [15, 40, 42, 102–104] have reported that increasing the liquid mass flow rate, or droplet flux, increases cooling performance; Deb [102] and Choi and Yao [42] went so far as to label it the dominant parameter for film boiling in sprays. However, Jia and Qiu [14] reported that while heat flux increased with increasing liquid mass flux, the trend was not uniform across the range of surface temperatures considered in the study. Ma and Tian [105] found that stagnation zone heat flux increased with liquid mass flow rate but only up to a point, before decreasing again. Competing influences of different parameters and variation in film thickness, which could serve as a thermal barrier, are often given as an explanation for disagreements [15].

The effect of droplet size and velocity has also received attention in boiling regime studies, particularly in terms of the critical heat flux of the spray. Again, however, there is disagreement of the relative importance of these parameters. Increases in droplet velocity have been found in some cases to lead to an increase in heat flux [12, 15, 42], particularly

when considering the maximum critical heat flux, although Choi and Yao [42] reported that this was only the case for dilute sprays rather than dense sprays. The increase was attributed to an increase in droplet energy [12] which enabled the droplets to spread more widely across the heated surface, and also to increased disturbance in the liquid film (when a film is present). However, Sozbir et al. [40] reported that droplet velocity did not have an appreciable effect on heat transfer for their spray. It was postulated that an increase in droplet velocity may increase droplet deformation upon impact and decrease the duration of droplet interaction with the surface. With regards to droplet size Chen et al. [15] reported, in a study on optimising the critical heat flux, that small droplets with a high velocity were desirable for optimum liquid usage efficiency, while a film boiling heat flux correlation reported by Hernández-Bocanegra et al. [12] also showed a slight increase in heat flux with decreasing droplet size. Lee et al. [106] reported, that droplet size had an appreciable effect; the wall temperature initially decreased with increasing Sauter mean diameter, $d_{3,2}$, for values of $d_{3,2} < 30$ μm, then remained constant in the range of 30 μm to 80 μm before increasing with further increases in $d_{3,2}$. This was attributed to changing liquid film behaviour, with very little film existing for the smallest diameters. As the diameter increased, the film spread over the surface, decreasing the temperature until the film completely covered the surface. Then as the droplet diameter further increased, the authors [106] concluded that the film was thickening and providing additional resistance to heat transfer, leading to the increase in wall temperature.

3.5 Spray Heat Transfer in the Non-Boiling Regime

Though there has been an increase in the number of studies in the last few years, spray cooling in the non-boiling regime has received much less attention in the literature than spray studies with boiling. Authors have recently identified spray cooling as a potential means to cool computer electronics and other systems, such as laser diode arrays, which require the dissipation of high heat fluxes at relatively low surface temperatures [16–18]. Studies have been reported on single-nozzle spray cooling, for example Karwa et al. [107] and Cheng et al. [108], and on multi-nozzle spray arrays, such as the work of Fabbri et al. [16] and Tao et al. [95]. Fluids other than water, as in Liu et al. [109], have been considered; for example R-134a refrigerant was investigated by Hsieh and Tien [110] and polyalphaolefin by Sleiti

and Kapat [111]. A broad range of parameters has also been considered, as will be discussed below.

This section outlines the mechanisms of spray heat transfer in the non-boiling regime, as well as the different parameters that have been identified as affecting the spray heat transfer.

3.5.1 Heat Transfer Mechanisms

The heat transfer mechanisms in spray cooling without boiling have been discussed by several authors. Hsieh and Tien [110] described the heat transfer mechanisms as consisting of three main aspects: sensible heating of the thermal boundary layer within the liquid film which was moving rapidly outward as more droplets arrived; a convective component caused by random droplet impacts on the film creating disturbances in the boundary layer; and evaporative cooling from the unsteady liquid film to the air. Karwa et al. [107] also described heat transfer by sensible heating of the liquid film and evaporation of the liquid film. However, the authors concluded that evaporation was not a significant contributor in the non-boiling regime, and that single-phase convection to the liquid film was the dominant parameter. This was echoed by Cheng et al. [108]. It was hypothesised that the discrete and random mixing of the liquid film under droplet impacts introduced turbulence into the liquid film, as well as thermal disturbances in the film. Wang et al. [96] described the heat transfer as being due to the heated liquid film being "swept away" by incoming droplets supplying fresh liquid and the evaporation of the liquid film, particularly at the edges which were described as turbulent in nature. Several other works [95, 99, 109, 112–114] have all described the heat transfer mechanisms in similar terms.

Xie et al. [115] developed an analytical model for non-boiling spray cooling for the case when the liquid film is relatively thin. Figure 3.3 shows the schematic of the analytical model, along with element analysis of the heat transfer model. Here, Q_i and $T_{film,i}$ are the mass flow rate of the liquid and mean temperature of the film in the control element, while Q_{i-1} and $T_{film,i-1}$ are the corresponding upstream values. The local heat flux from the heated surface is given by q_i'' and $Q_{drop,i}$ and T_{drop} are the impinging droplet mass flow rate and temperature respectively. The authors gave the energy conservation for the control volume as

$$c_p Q_{i-1} T_{film,i-1} + q_i'' A_i + c_p Q_{drop,i} T_{drop} = c_p Q_i T_{film,i} \tag{3.5}$$

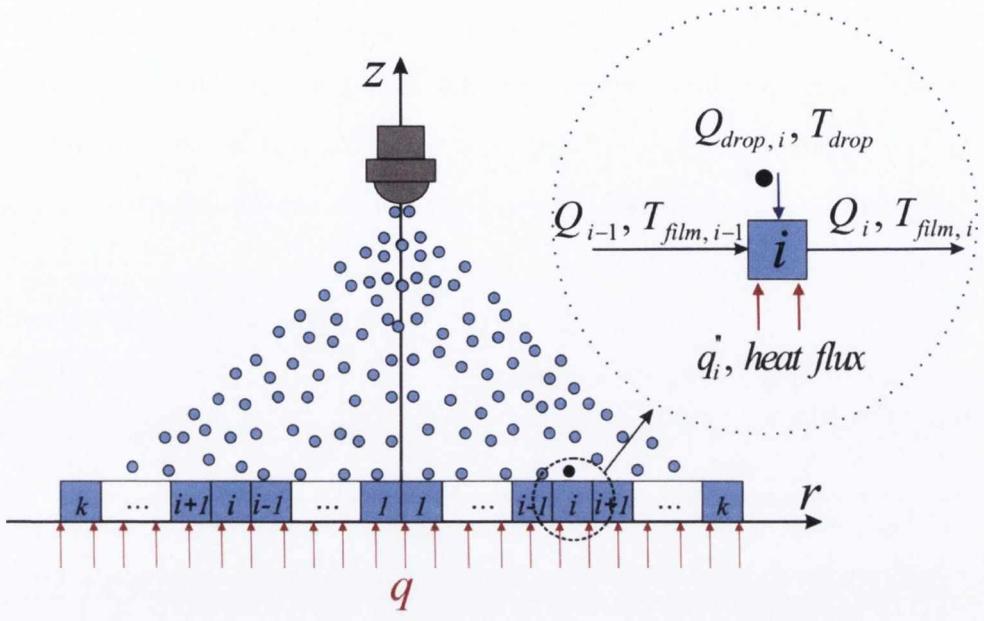

Figure 3.3: Schematic of the anaytical model of Xie et al. [115]

where c_p is the specific heat capacity of the liquid and A_i is the element surface area. For this model, the authors have assumed there is negligible heat loss from the film to the ambient air, i.e. no evaporation or convection is present. Thus the authors attribute the cooling to only droplet impingement cooling and thin film convection. Therefore

$$q_i'' A_i = q_{drop,i} + q_{film,i}. \tag{3.6}$$

The droplet heat transfer was represented as the sum of contributions from individual droplets by using a correlation derived by Issa and Yao [116] in a study that examined a stream of water droplets. The thin film convection was modelled as laminar boundary layer flow as it was suggested by Zhao et al. [117] that the thin film under a spray was similar. The authors reported reasonable agreement between their model and experimental data, though the model underpredicted significantly when the nozzle height above the surface increased. The authors [115] inferred from their model that the droplet impingement cooling was the dominant mechanism. However the model was not able to capture the heat transfer behaviour when the droplet impact energy was lower, such as when the nozzle height increased. It should be reiterated that in studies that examine the fluid dynamics of liquid films, it has been reported that summing the effect of individual droplets does not capture the true hydrodynamic

behaviour of the liquid film [63, 85]; it is entirely possible that this limitation applies to this heat transfer model also. In addition, it is worth noting that the study by Zhao et al. [117], cited by Xie et al. [115] as justification for treating the liquid film as a laminar flowing boundary layer, was a boiling study, with different heat transfer behaviour as discussed in section 3.4.

Cheng et al. [59] also presented a spray cooling model intended to be used both with and without boiling. Their [59] model is similar in concept to that of Xie et al. [115] although modified to apply for a wider range of surface temperatures. Thus, the energy conservation equation is given as

$$\dot{Q}_{in} = \dot{Q}_{drop} + \dot{Q}_{film} + \dot{Q}_{envi.} + \dot{Q}_{bub,w} + \dot{Q}_{bub,s} \tag{3.7}$$

where $\dot{Q}_{in}$ is the surface heat flux, $\dot{Q}_{drop}$ is the droplet heat transfer, $\dot{Q}_{film}$ is the liquid film convective heat transfer, $\dot{Q}_{envi.}$ is the heat transfer to the environment and $\dot{Q}_{bub,w}$ and $\dot{Q}_{bub,s}$ are the nucleation bubble and secondary bubble heat transfer respectively. The last two terms are specific to boiling heat transfer and are not considered here. The authors split the droplet heat transfer into two parts: droplets impinging on the film and droplets impinging on the surface. Again, the film convection is assumed to be that of a laminar boundary layer while the environmental heat transfer consists of convection to the air and radiation from the surface of the liquid film. It was assumed that the air was not moving, and as such an empirical correlation for natural convection was used for the convection component. It should be noted, however, that Deb and Yao [102] and Yoshida et al. [118] reported that a spray will entrain some air into the flow. While this model was seen to compare reasonably well with the experimental results, the study [59] was concerned with a thick film, and the best agreement was found for the boiling regime.

3.5.2 Heat Transfer Parameters

The heat transfer characteristics of an impinging spray in the non-boiling regime depend on a complex combination of different parameters. In this section, these parameters are discussed.

Reynolds Number and Liquid Flow Rate

For sprays, when the Reynolds number is reported it is usually calculated using the nozzle exit diameter and the liquid flow rate in some form. Commonly, the liquid mass flux, G, is used [41, 96, 107, 113]; this is the mass flow rate per unit area of the impingement surface and is used because many spray studies are concerned with the total heat flux removal from a surface under a spray. Some authors have used alternative definitions, still based on the flow rate of the liquid in the spray; Sleiti and Kapat [111] use the liquid jet velocity, calculated from the mass flow rate, while Cheng et al. [108] used the droplet velocity as measured using phase Doppler anemometry. Rybicki and Mudawar [17] based the Reynolds number on the liquid volumetric surface flux, defined as the volumetric flow rate impinging on an infinitesimal surface area divided by the same area (Q'' [m^3/sm^2]), and used the Sauter mean diameter of the spray as the characteristic length and Tao et al. [95] used simply the volume flow rate. Thus the Reynolds number for a spray can be thought of as describing the flow rate of the liquid.

The effect of Reynolds number, or liquid flow rate, on heat transfer has been widely investigated, both for single-nozzle studies, as reported by Karwa et al. [107], and nozzle arrays, as in Sleiti and Kapat [111]. For sprays in the non-boiling regime it has been reported that increasing Reynolds number, or liquid flow rate, leads to an increase in heat transfer [17, 18, 96, 107–110, 114, 119] for both single and multi-nozzle set-ups. This has been attributed to an increase in the velocity of the liquid film that forms on the surface, increasing the convective heat transfer to the film. Increased flow rate leading to an increase in droplet flux also leads to an increase in the disturbance to the liquid film and local thermal boundary layer. Hsieh and Tien [110] suggest that increasing the liquid flow rate would also increase the film thickness thereby leading to a decrease in the evaporative heat transfer from the film, even as the convective heat transfer to the film was increasing. Their measured increase in heat transfer with increasing flow rate led them to infer that convective heat transfer is more significant than the evaporative component when boiling does not take place. A similar finding was reported by Karwa et al. [107], however Xie et al. [115] found that the thin liquid film on the surface remains constant with increasing liquid flow rate. This led Xie et al. [120] to deduce that the film velocity increases, allowing for the spray to "flush away"

the liquid film at a higher rate, improving heat transfer. The work of Zhang et al. [41] was consistent with the findings of Hsieh and Tien [110], identifying a thicker liquid film for an increased liquid flow rate. Indeed, Zhang et al. [41] reported that there would be an optimal flow rate, balancing the competing influences of the increased convective heating to the film with the loss of evaporative cooling. Cheng et al. [114] reported that, for a multi-nozzle array, increasing the liquid flow rate only led to an increase in the liquid film velocity up to a certain point, after which increasing the flow rate resulted in the film thickening more rapidly than it could flow outwards. One other result of note was that of Cheng et al. [108]; it was reported that for temperature differences between the surface and the spray of less than 25 °C there was little increase in heat flux as the liquid flow rate was increased from 3.6 litres/hour to 5.2 litres/hour. No explanation is given for this behaviour.

It is clear from the discussion above that no consensus exists regarding the influence of the Reynolds number and liquid mass flow rate on spray impingement heat transfer without boiling.

Nozzle-to-Surface Distance

The effect of nozzle to surface distance, H, has also received attention. Often non-dimensionalised by the nozzle diameter, D, as H/D, it has been identified as an important parameter in spray cooling without boiling. As with the liquid flow rate, authors have reported on an optimal H/D [41, 95], but again this varies depending on the specific spray set-up used in the study. In the main, it has been found that the heat transfer decreases with increasing H/D [95], with the exception of the low H/D range [120]. Different explanations for this behaviour have been proposed: Mudawar and Estes [121] reported that if the nozzle height was too great, some of the droplets would not strike the impingement surface, reducing the heat transfer, and that an optimal critical heat flux was found for the case when the nozzle-to-surface distance was such that the spread of the spray just covered the impingement surface. Thus, Tao et al. [95] attributed their finding that the heat transfer initially increased with increasing H/D to this behaviour, with the heat transfer increasing until the surface was completely covered, and thereafter decreasing as the spread became greater than the surface. A similar situation was reported by Karwa et al. [107].

Xie et al. [120] offered a different explanation, considering instead how the droplet impact

energy would change with changing H/D. The authors reported that the droplet impact energy decreased with increasing H/D, and as the energy decreased the spreading of the liquid film also decreased. They also proposed that the lower droplet energy would mean that droplets would not penetrate through the film to the heated surface, again decreasing the heat transfer. However the authors [120] do note that for lower H/D, the heat transfer initially increases as the coverage of the impingement surfaces increases, before decreasing with further increases in H/D. Cheng et al. [108] also observed a decrease in heat transfer with increasing nozzle-to-surface distance; for the spray set-up in question [108], a decrease in spray height led to an increase in droplet Sauter mean diameter. The authors [108] therefore concluded that the heat flux was higher for lower H/D as the larger droplets were observed to undergo greater splashing upon impingement, thereby promoting disturbance to the liquid film and improving the draining of the film. Zhang et al. [41] noted that droplet velocities and droplet numbers at impingement increased with lower H/D, which were said to lead to "stronger and more frequent impacts" and hence to improve heat transfer. However, they also reported on the existence of an optimal H/D, as at very low nozzle-to-surface spacings the liquid film was deemed too thick to effectively remove heat, because of the high droplet number density.

Surface Temperature and Non-Uniformities in the Surface Temperature

In the non-boiling regime, surface temperature has been observed to affect the heat transfer behaviour of impinging sprays. Though Karwa et al. [107] did not report data on the effect of varying the surface temperature, the authors [107] drew attention to the fact that as the surface temperature came closer to the saturation temperature, the rate of evaporation of the liquid film would be higher. Wang et al. [96] performed a more detailed study; it was seen that increasing the surface temperature for a constant liquid temperature and flow rate led to an increase in heat transfer coefficient, unlike other convective heat transfer processes. The authors [96] concluded that the added evaporative cooling was the reason for this behaviour. As the surface temperature approached the liquid saturation temperature, the heat transfer coefficient increased rapidly with increasing surface temperature while still remaining below the liquid boiling point; this was attributed to the local onset of boiling in the stagnation zone. Liu et al. [109] and Cheng et al. [108] also reported the same behaviour, both attributing the

increase in heat transfer coefficient with surface temperature to increased evaporation.

The surface temperature has also been reported to affect the morphology of the spray. Xie et al. [120] reported that increasing the surface temperature led to the spreading of the spray cone though this was only observed for surface temperatures close to the liquid boiling temperature. In a further study, Xie et al. [122] examined in more detail the effect of surface temperature on a spray. Again, the spray cone was seen to expand when the surface temperature was close to the liquid boiling temperature. Rising vapour from the evaporating liquid film on the surface was given as the explanation for the changing spray behaviour as it was deemed to cause flow resistance, leading to the expansion. The impinging droplet velocity was seen to decrease for these raised surface temperatures, again attributed to increased drag from the vapour plume. The authors [122] also reported that increased surface temperature led to an increase in Sauter mean diameter of the droplets. It was suggested that this arose from an increase in the number of secondary droplets which were deemed to be buoyed upwards by the vapour plume to collide with the impinging droplets, leading to larger droplets being detected. It was also speculated that because of the vapour plume, the smaller droplets were being evaporated before the plane on which droplet size measurements were taken, thus increasing the mean droplet diameter. In addition, Xie et al. [122] reported that the increased spreading in the spray for higher surface temperatures led to a decrease in the heat transfer as the concentration of droplets impinging on the surface decreased. However, it should be noted that this behaviour was only significant once the surface temperature was at or had exceeded the liquid boiling point.

Non-uniformity in the surface temperature under spray cooling was investigated by Cheng et al. [59], who reported that the non-uniformities depend on the droplet behaviour. When the droplet impact energy is high, such as at lower H/D and higher spray flow rates, the non-uniformities in temperature were lower. This was hypothesised as being a result of the liquid film being effectively and rapidly drained away. Non-uniformities were seen to increase with increasing surface temperature though no explanation for this was provided.

Liquid Temperature

The effect of varying the temperature of the spray has also been investigated. In the work of Hsieh and Tien [110] it was observed that decreasing the liquid temperature resulted in an

increase in heat flux.

Droplet Parameters

Until relatively recently, no studies had been reported on the effect of droplet parameters on spray heat transfer in the non-boiling regime; instead work had focussed on the boiling regime and even then there was disagreement within the literature on the relative importance of droplet properties such as velocity, size and flux. This has already been discussed in section 3.4.1. However, some recent studies have explored the effect on heat transfer of spray droplet properties in the non-boiling regime for a spray; this work is discussed in this section.

For a R-134a spray, Hsieh and Tien [110] developed a correlation that showed the average Nusselt number as increasing with both droplet Sauter mean diameter, $d_{3,2}$, and Weber number. The authors [110] reported that the Weber number was more influential than $d_{3,2}$ and attributed this to the dense spray and thick liquid film that results from the higher volumetric flux associated with increasing Weber number. Contrary to this, Karwa et al. [107] reported that the effect of Weber number was marginal when compared with the liquid mass flow rate. The authors [107] reported that droplets with higher Weber numbers resulted in more splashing, and in expulsion of secondary droplets from the liquid film that were larger than the impinging droplets. It was concluded that while this would enhance heat transfer, it also led to poor liquid utilisation. The authors concluded that for dense sprays with high Weber numbers, the effect of Weber number on heat transfer was marginal. This was echoed by Wang et al. [96] in their study on the effect of the inclination angle of a dense spray.

Cheng et al. [108] also reported on the effect of droplet velocity and size on heat transfer. They [108] observed an increase in heat flux with liquid flow rate and attributed the increase to the observation that droplet velocity increased with liquid flow rate. It was concluded that the higher droplet velocities led to greater splashing upon impact with the liquid film, and hence enhanced the film discharge. The decrease in heat flux with increasing H/D was reported to be related to the droplet $d_{3,2}$. For decreasing H/D, $d_{3,2}$ was seen to increase; the authors [108] concluded that this led to enhancement in droplet splashing and thus increased draining of the liquid film, resulting in the observed heat transfer behaviour. It should be noted however that a decrease in $d_{3,2}$ was also reported for increasing flow rate, and hence increasing droplet axial velocity. Thus it would seem that the relative influence of the droplet

size and velocity varied throughout the tests, though this is not discussed by the authors [108]; this points to the complex effect of the droplet parameters on the heat transfer.

Xie et al. [120] determined that the surface temperature distributions under a spray were influenced by the droplet flux, with regions of high flux corresponding to lower surface temperatures. From this result, the authors [120] concluded that droplet impingement cooling was the primary heat transfer mechanism in the non-boiling regime, rather than convective heat transfer to the liquid film. This finding had previously been inferred in a theoretical study by the same authors [115].

Abbasi and Kim [112] proposed that the non-boiling spray heat transfer depends primarily on droplet kinetic energy, i.e. the droplet velocity as opposed to the liquid flow rate. It should be noted, however, that droplet velocity is linked to the liquid flow rate for a spray [108, 120]. Abbasi and Kim [112] considered that the kinetic energy of the droplets is transferred to the liquid film by increased agitation of the film, leading to decreased boundary layer thickness. They [112] conclude that the dynamic pressure of the impinging droplets is the dominant heat transfer mechanism as the largest heat flux was measured in the same location as the largest dynamic pressure on the surface. This hypothesis did not hold well for larger radial distances; here Abbasi and Kim [112] concluded that it was the radial flow of the film that was the dominant heat transfer mechanism.

It is clear that there is still disagreement as to the influence on heat transfer of the droplet parameters in non-boiling spray cooling. However, for a spray, the literature seems to point towards the conclusion that improving the rate at which the liquid film flows outwards enhances the heat transfer; which droplet characteristics contribute to this motion is not definitively known.

Spray Inclination Angle and Surface Roughness

Wang et al. [96] considered the effect of spray inclination angle in the non-boiling regime. It was observed that increasing the inclination angle from the normal axis resulted in an improvement in heat transfer performance. This heat transfer enhancement was attributed to increased efficiency in the draining away of the liquid film with increasing spray inclination angle. This again implies that the draining of the liquid film is a key heat transfer mechanism for impinging sprays in the non-boiling regime.

Wang et al. [96] also reported, however, that this was in contrast with similar studies by Li et al. [123] and Visaria and Mudawar [124] both of which reported little difference in heat flux until the inclination angle was greater than 40° in the case of Li et al. [123] and greater than 55° for Visaria and Mudawar [124]. Wang et al. [96] account for the discrepancy with Li et al. [123] by explaining that in their study, the nozzle-to-surface height was decreased as the spray inclination angle increased to ensure that the test surface was completely inscribed by the spray; this was not the case in the work of Li et al. [123]. The disagreement with Visaria and Mudawar [124] was attributed to a difference in nozzle geometry. Wang et al. [96] used a nozzle that had a recirculation zone of droplets in the spray cone centre which resulted in liquid pooling in an unsteady manner in a central stagnation zone. This is important as it indicates the variability in heat transfer results arising from the complex nature of spray flows issuing from different types of nozzle.

As with boiling heat transfer studies [125], Zhang et al. [41] reported that increasing surface roughness resulted in an increase in impinging spray heat transfer. The enhancement is attributed to the micro- and nano-scale structures accelerating the spread of the liquid film. This is different from the boiling study of Pais et al. [125], in which the increase in nucleation sites with increased roughness is given as the reason for the heat transfer enhancement of rough surfaces.

3.5.3 Heat Transfer Correlations

Within the literature, different authors have produced correlations for their specific spray heat transfer in the non-boiling regime. However there is significant variation between these correlations, with many of them seeming to only suit the specific application considered. This section presents some of the correlations reported to give an indication of the variance that exists.

Rybicki and Mudawar [17] produced the following correlation, in which the spray Sauter mean diameter, $d_{3,2}$, is used as the characteristic length and k_f is based on the spray fluid. The Reynolds number range was approximately 0.5 to 70 and was defined by $d_{3,2}$ and the volumetric spray flux.

$$\mathrm{Nu}_{d_{3,2}} = 4.7\mathrm{Re}_{d_{3,2}}^{0.61}\mathrm{Pr}_f^{0.32} \tag{3.8}$$

where Pr_f is the spray liquid Prandtl number. Karwa et al. [107] presented a Nusselt number correlation with a similar Reynolds number exponent for a Reynolds number range of 65 – 285 with the Reynolds number being defined by the nozzle exit diameter and the liquid mass flux; their correlation did not contain a Prandtl number dependence.

$$Nu = 20.344Re^{0.659} \tag{3.9}$$

Wang et al. [96] related Nu to the Reynolds number and also the dimensionless temperature, ζ, introduced to account for variations in surface temperature with respect to the liquid boiling temperature. This correlation developed was for Re $\approx$ 150 to Re $\approx$ 250.

$$Nu = 7.144Re^{0.438}\zeta^{0.9016} \tag{3.10}$$

Cheng et al. [108] developed a correlation that took the droplet properties into account, using the Weber number and the Reynolds number calculated using the spray nozzle diameter and flow rate. A range was not presented for these parameters, but it was stated that the correlation was valid for liquid Prandtl numbers of 2.1 to 6.8.

$$Nu = 0.036Re^{1.04}We^{0.28}Pr^{0.51}(3.02 + \epsilon^{1.53}) \tag{3.11}$$

Here, ϵ is the dimensionless temperature, defined as

$$\epsilon = \frac{T_{surf} - T_f}{T_{sat}} \tag{3.12}$$

where T_{surf} and T_f are the surface and spray liquid temperatures respectively, and T_{sat} is the liquid saturation temperature.

A unique correlation was proposed by Abbasi and Kim [112], following on from their previous work [119]. In it, the heat transfer coefficient, h, is correlated against measured spray local impingement pressure, P. The basis for this is that the heat transfer can be calculated without reference to the droplet properties expressed via the Weber and Reynolds numbers,

and is based on the spray liquid properties of density, ρ, specific heat, c_p, and Prandtl number.

$$h = 0.042\rho^{0.5}c_p\mathrm{Pr}^{-0.33}P^{0.5} \tag{3.13}$$

In many of the studies reported here, the authors have reported good agreement between their correlation and their experiments, and even with the experiments of others, however the existence of a wide range of correlations, and the different ways in which they are formulated, is indicative of the complex nature of impinging spray heat transfer in the absence of boiling.

3.6 Mist Jet Heat Transfer in the Non-Boiling Regime

While spray cooling in the non-boiling regime has received relatively little attention, especially when compared with the boiling regime, the topic of non-boiling mist jet heat transfer has been the focus of even fewer studies. Yet it is an important topic in its own right; the addition of the air jet differentiates it from the spray and adds another dimension to the already complex heat transfer behaviour. This section presents a review of the limited work on the subject of non-boiling mist jet heat transfer.

3.6.1 Heat Transfer Behaviour

Chang and Su [19] reported that the heat transfer profiles for a dense impinging mist jet in the non-boiling regime are similar to that of a conventional air jet. The same bell-shaped curve was found with a maximum at the stagnation point and a gradual reduction in heat transfer with increasing radial distance. Example of the heat transfer profiles presented by Chang and Su [19] are shown in figure 3.4. Note that these profiles are for high water flow rates, ranging from 0.0222 to 0.0813 kgs^{-1}, significantly higher than those used in this investigation as discussed below in section 3.6.2.

Graham and Ramadhyani [20] summarised the heat transfer mechanisms for a mist jet as having three components: evaporative cooling at the liquid film and air interface; convective heat transfer from the liquid film to the airflow; and sensible heating of the liquid film as it flows outwards from the stagnation point. Chang and Su [19] described the mechanisms in similar terms, referring to the sensible heating of the liquid film as "laminar-like" convection

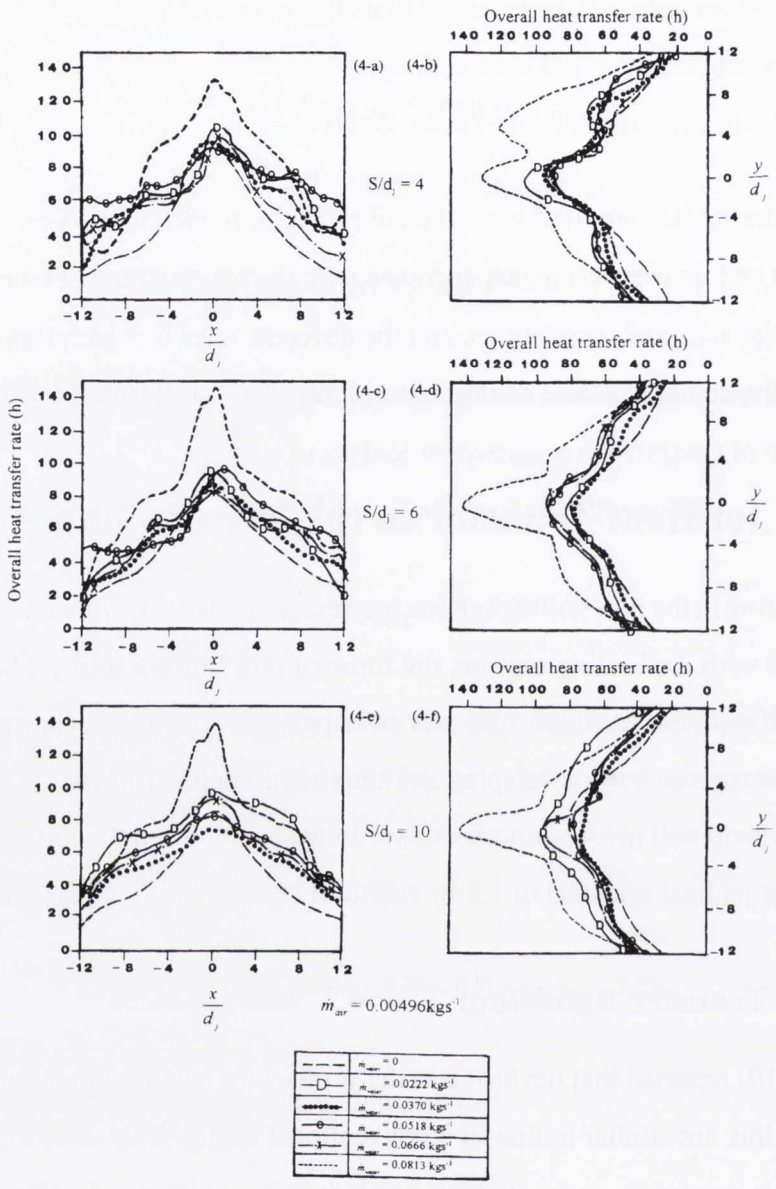

Figure 3.4: Heat transfer coefficient profiles for an air-water mist jet with constant Reynolds number of 15000 and varying water flow rates and H/D of 4, 6 and 10 [19].

of the film flow away from the impingement zone. Oliphant et al. [21] added that, as with a spray, droplet impacts will cause an unsteady boundary layer in the liquid film, adding to the heat transfer of the mist jet. Oliphant et al. [21] also attributed the heat transfer of the mist jet primarily to evaporative cooling from a large surface area.

Graham and Ramadhyani [20] presented an analytical model of the mist jet heat transfer and film flow without boiling, the schematic for which is reproduced in figure 3.5. The model

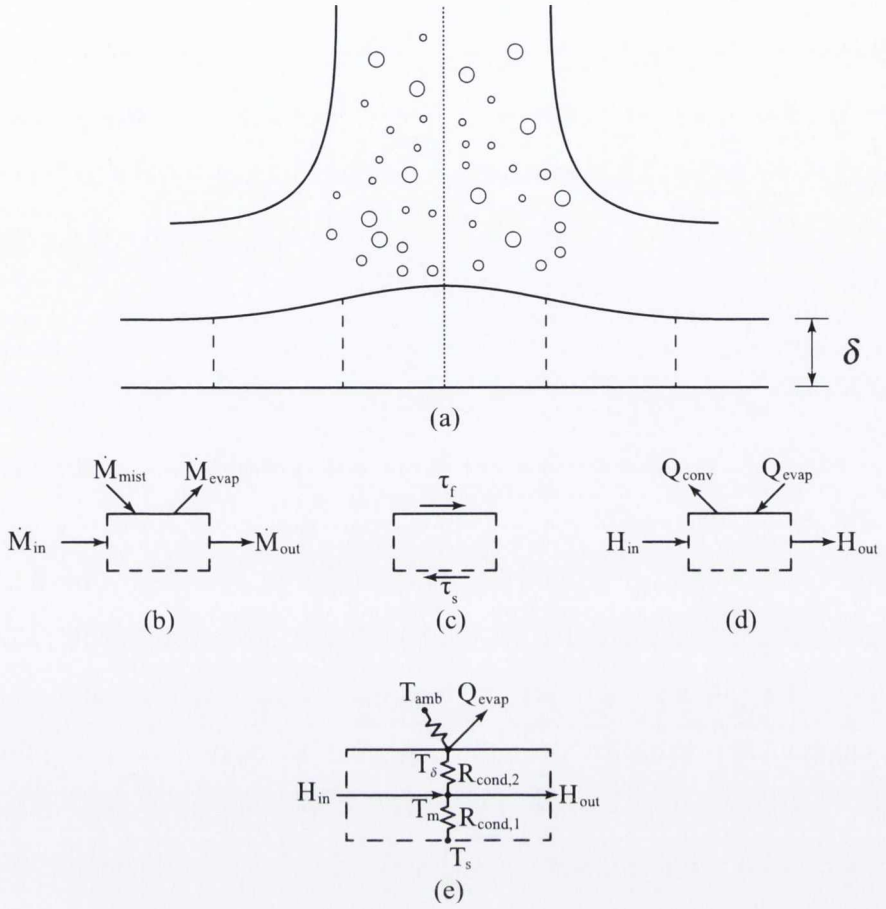

Figure 3.5: Schematic of the analytical model used by Graham and Ramadhyani [20]; (a) control volume schematic; (b) mass flows; (c) film shear stresses; (d) heat transfer components; (e) resistance network

describes the mass balance for a control volume as

$$\dot{M}_{mist,x} + \dot{M}_{in,x} = \dot{M}_{evap,x} + \dot{M}_{out,x} \tag{3.14}$$

where $\dot{M}_{mist,x}$ is the mass flow rate from the mist jet droplets, $\dot{M}_{in,x}$ and $\dot{M}_{out,x}$ are the laminar flow rates into and out of the control volume of the liquid film and $\dot{M}_{evap,x}$ is the mass flow rate of the liquid that evaporates from the film and was computed from the heat transfer model. In the heat transfer model the energy balance was given as

$$Q_{cond,x} = Q_{conv,x} + Q_{evap,x} + (H_{out,x} - H_{in,x}) \tag{3.15}$$

Here, $Q_{cond,x}$ is the heat conducted from the surface to the liquid film within the control

volume; $Q_{conv,x}$ is the convection to the flowing air; $Q_{evap,x}$ is the evaporation from the control volume; and $H_{in,x}$ and $H_{out,x}$ represent the change in enthalpy of the liquid within the film between where it enters and exits the control volume. In the resistance network, (e) in figure 3.5, $R_{cond,1}$ is for the conduction from the heated surface to the middle of the liquid film and $R_{cond,2}$ is for the conduction from the middle of the film to the top, where it is exposed to the mist jet and ambient conditions.

Several assumptions are made in this model. Firstly, the velocity within the liquid film is taken to have a linear velocity profile, allowing the surface shear stress to be calculated. As the droplet impact on the surface will result in agitation of the film, this assumption may not be valid. The shear stress on the surface is approximated as the shear of a laminar gas jet impinging on a solid surface. The convective heat transfer is assumed to be that of an air jet, while the assumption of constant specific heats is also made for the enthalpy flows.

For a methanol mist jet, the model predicts that the liquid film is at its thickest in the stagnation region. This is attributed to the mass flux of the droplets being highest in this region. This result is contrary to that which was observed for some spray studies [60, 115]. The film surface temperature and film thickness were predicted to be coupled; thus, when the thickness decreased the film surface temperature was predicted to decrease and vice versa, indicating that a thicker film offers more thermal resistance than a thinner one. As a result of this, the model predicted a local heat transfer minimum in the stagnation region; this was not reproduced in the experiments of Chang and Su [19] as shown in figure 3.4.

While the model does a reasonable job of matching the heat transfer experiments for a methanol mist jet, it fails to capture the behaviour of a water mist jet. The authors [20] speculate that the difference in surface tension between water and methanol may be significant in this; it is not accounted for in the model and it is suggested that it may contribute to the film thickness. In addition, the above assumptions concerning the film thickness discussed in the previous paragraph may contribute to the failure to model the water mist jet heat transfer. It is also noted by the author [20] that the model does not work for liquid flow rates that are low enough that some or all of the liquid film has evaporated completely and the surface is exposed. This also occurs if the wall temperature is sufficiently high that boiling begins.

3.6.2 Heat Transfer Parameters

In a similar fashion to section 3.5.2, this section examines the parameters that have been reported to affect mist jet heat transfer in the non-boiling regime.

Reynolds Number and Air and Liquid Flow Rates

In a study comparing the heat transfer performance of liquid jet arrays with a mist jet, Oliphant et al. [21] defined the Reynolds number in terms of the liquid mass flux on the impingement surface, G, and the impingement surface diameter, D, as $\mathrm{Re} = GD/\mu$. This is the same definition as used in several non-boiling spray studies as outlined in section 3.5.2. It was reported [21] that the heat transfer coefficient increased, approximately exponentially, with liquid mass flux, and hence Reynolds number, in most cases; indeed the authors speculated that the dependence on mass flux is stronger than that of a liquid jet. However, in some cases h increased with decreasing liquid mass flux; this was observed for the largest nozzle-to-plate spacing examined. It was speculated that this may be caused by changes in the droplet parameters, however as no testing of this nature was done the authors [21] do not provide any details beyond reasserting that the heat transfer behaviour is "a complex function" of the mist jet parameters. Significant scatter in the data was also reported, which could affect the heat transfer results. The authors [21] do not report on variations the air flow rate.

In their study, Chang and Su [19] defined the Reynolds number based on the air jet velocity and nozzle exit diameter. This was done to facilitate comparison between the mist jet and an air only jet. In general, the mist jet heat transfer was seen to increase with increasing jet Reynolds number when the liquid flow rate was kept constant. The authors speculated that the increased air flow may be "squeezing" the liquid film, reducing the conductive resistance and enhancing the film velocity. It is implied that this improves the evaporation and the liquid flow convection. It is also speculated that the radial air flow results in a lower partial vapour pressure at the interface between the film and the air, which enhances the evaporation from the film. However, the behaviour was not straightforward; the effect of Reynolds number on the heat transfer was seen to depend on the water-to-air mass flow ratio. Thus more attention was focussed on this ratio than on the mist Reynolds number.

The water-to-air mass flow ratio, also referred to as the liquid mass or mist loading

fraction, f, is defined as

$$f = \frac{\dot{m}_w}{\dot{m}_a} \tag{3.16}$$

where $\dot{m}_w$ and $\dot{m}_a$ are the water and air mass flow rates respectively. As well as Chang and Su [19], this definition was used in a study of a mist flow over a surface by Kumari et al. [126] and also by Su et al. [127] in a boiling study on an air and liquid nitrogen impinging mist jet.

When Chang and Su [19] considered the effect of increasing water-to-air mass flow ratio, it was found that for all Reynolds numbers and separation distances from the surface, the spatially averaged heat transfer rate reached a local maximum before decreasing again. Subsequently, the heat transfer could undergo further increases, and decreases, with increasing water-to-air ratios. The behaviour was far from uniform, with the pattern of increases and decreases varying for different Reynolds numbers and separation distances. For illustration purposes, figure 3.6 is a reproduction from Chang and Su [19]. Clearly visible are what Chang and Su [19] refer to as "critical points", or local maxima in the heat transfer. This behaviour is speculated to be caused by non-linear flow phenomena between the mist jet, water droplets and the flow of the liquid film over the surface, though no further details are discussed and no local analysis of the effect of this mist loading fraction on the liquid film are reported . The authors also speculate that increasing the water flow rate did not necessarily lead to an increase in heat transfer because of thickening of the liquid film, resulting in an increase in the conductive thermal resistance. This complex behaviour illustrates that the water-to-air mass flow rate may be a key parameter in non-boiling mist jet heat transfer.

Graham and Ramadhyani [20] did not present results in terms of the Reynolds number, but did report on the effect of varying the liquid flow rate. In their work, a consistent trend was not seen for increasing liquid flow rate, with lower flow rates sometimes performing better than higher flow rates. It was again speculated that this behaviour was due to competing heat transfer influences; higher liquid flow rates were thought to lead to thicker surface films which led to a decrease in evaporation and convective heat transfer from the film to the air flow as the conductive resistance of the film is increased. However, the thickening of the film also means that convective heat transfer to the film flowing along the surface could increase at the same time. The effect of increasing air flow rate for constant liquid flow rate was also presented. Higher air flow rates were seen to dissipate more heat for both methanol-air and

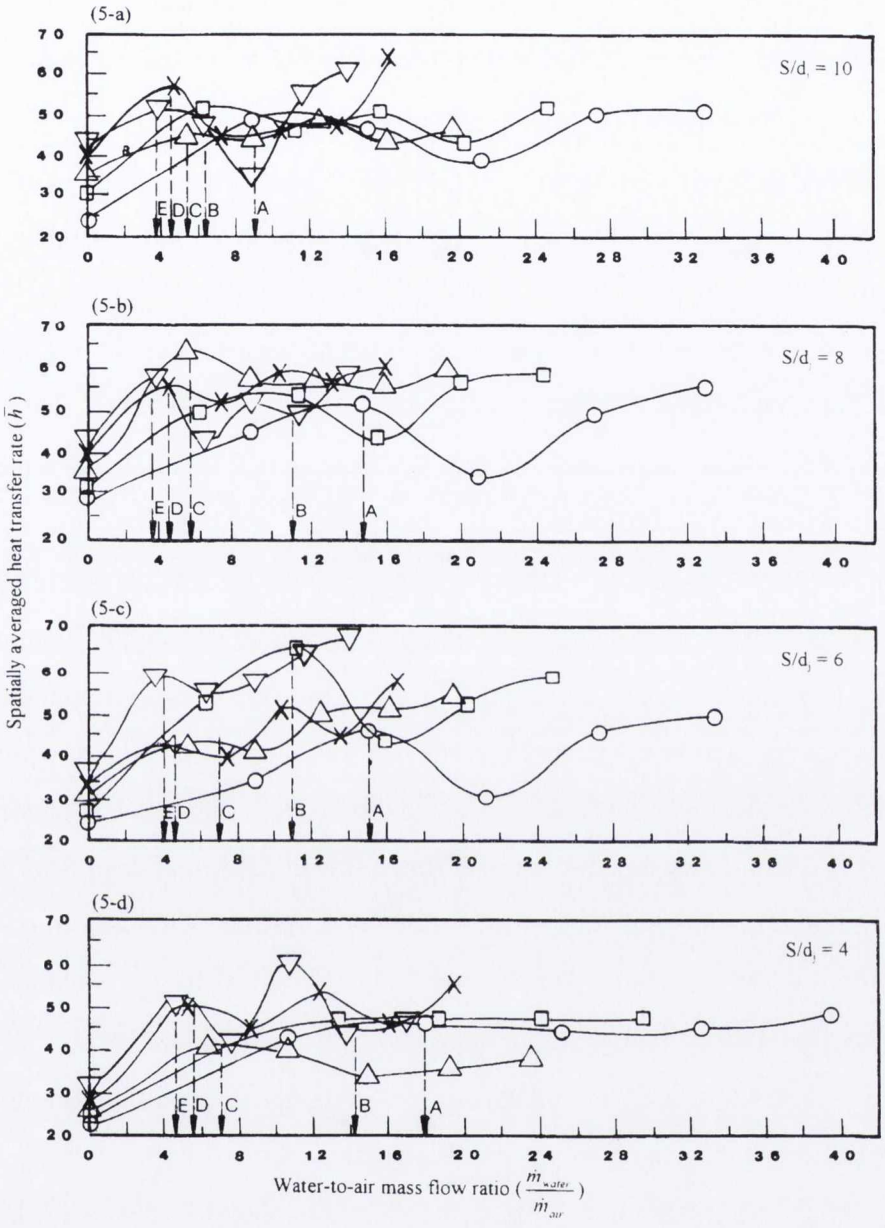

Figure 3.6: Spatially averaged heat transfer behaviour for varying water-to-air mass flow ratios for different Reynolds numbers and nozzle-to-plate distances [19]

water-air mist jets, though this finding was not explored further.

In their analytical model, the authors [20] identified evaporation of the liquid film as the largest contributor to the heat transfer, so increasing the film thickness could indeed decrease the heat transfer. The model predicted that evaporation and convective flow in the film were the dominant heat transfer mechanisms, with evaporation vastly outweighing convective heat transfer. This is in contrast to spray studies, some of whom [107] neglected evaporation as it

was deemed to play an insignificant role, as discussed in detail in section 3.5.1. As discussed in section 3.6.1 there are several issues with the model of Graham and Ramadhyani [20], not least that it did not predict water-air mist jet heat transfer.

In a more recent study, Tay et al. [97] reported on a comparison of slot-jet and mist jet cooling of micro-channels. As with Graham and Ramadhyani [20], no definition of the Reynolds number was provided. However, it was reported that increasing the air flow rate for constant water flow rate resulted in an increase in heat transfer, as did increasing the liquid flow rate for constant air flow. However, these observations were not expanded on.

The liquid flow rate and mist mass fraction is clearly an important parameter, the effect of which is not fully understood for non-boiling mist jet heat transfer. The range of liquid flow rates investigated in studies to date and the corresponding mass fractions, where available, are presented in table 3.1. There are a few issues to note concerning this summary information. In the case of Graham and Ramadhyani [20] the air mass flow rate is an approximate calculation based on information within the paper; also the water flow rate was varied, within a narrow range, for only one air flow rate. The case when the air flow rate was varied for a constant water flow rate in the work of Graham and Ramadhyani [20] is also shown. Oliphant et al. [21] did not provide information on the air flow rates used in their study so no assessment of mist loading fraction is possible. In the case of Chang and Su [19] the water mass flow rate was higher than the air flow rate, resulting in a very dense mist jet. Tay et al. [97] considered a constant water and varying air flow rates, and also considered two different water flow rates at the same air flow rate; both cases are shown in table 3.1.

The lowest mist loading fraction considered by Graham and Ramadhyani [20], $f = 0.17$ is reasonably comparable to the highest f in the work of Tay et al. [97], $f = 0.15$. However, in the work of Graham and Ramadhyani [20], this mist loading fraction gave rise to a heat transfer coefficient of ~6700 W/m^{2}K, while Tay et al. [97] reported that $h = 3824$ W/m^{2}K for only a slight reduction in f from the study of Graham and Ramadhyani. The driving temperature differences were comparable in the two specific instances considered here: $\Delta T \approx 13$ K for Graham and Ramadhyani [20] and $\Delta T = 14.1$ K for Tay et al. [97]. The clear discrepancy in the heat transfer coefficients for similar test conditions highlights the lack of clarity that exists regarding the effect of mist loading fraction on mist jet non-boiling heat transfer.

It is clear from this table that while there is a lack of information on mist jet non-boiling

Table 3.1: Mist jet flow rates examined within the literature

Author	Water flow rate Q_w [ml/min]	Water mass flow rate $\dot{m}_w$ [kg/s]	Air mass flow rate $\dot{m}_a$ [kg/s]	Mist loading fraction f
Graham and Ramadhyani [20]	2.4 to 6.9	4×10^{-5} to 1.15×10^{-4}	2.4×10^{-4}	0.17 to 0.48
Graham and Ramadhyani [20]	3.3	5.5×10^{-5}	2×10^{-4} to 3.1×10^{-4}	0.28 to 0.18
Oliphant et al. [21]	800 to 1800	0.013 to 0.03	NA	NA
Chang and Su [19]	1330 to 4880	0.0222 to 0.0813	0.0025 to 0.0058	3.8 to 33
Tay et al. [97]	1.998	3.33×10^{-5}	2.8×10^{-4} 3.8×10^{-4} 4.1×10^{-4}	0.12 0.1 0.08
Tay et al. [97]	1.998 and 3.798	3.33×10^{-5} and 6.33×10^{-5}	4.1×10^{-4}	0.08 and 0.15

heat transfer generally, there is a particular paucity of data regarding the effect of liquid flow rate and mist loading fraction on the heat transfer; only a small range has thus far been reported and the results obtained from different studies, where comparable, lack consistency. No results have been reported for water flow rates less than 2 ml/min and for mist loading fractions less than $f < 0.08$. This aspect of mist jet heat transfer is completely under-represented in the literature and is of huge interest as the behaviour of the liquid film is potentially different in this region. Thus, Graham and Ramadhyani [20] identified that for very small flow rates the film may not be uniform across the surface. This would represent a very different heat transfer situation from that which has been reported to date, with different dominant heat transfer mechanisms expected.

Nozzle-to-Surface Distance

As with non-boiling spray cooling, the nozzle-to-surface distance, or H/D, is an important heat transfer parameter. As there are very few studies available for mist jet heat transfer, there is little information on the effect of nozzle-to-surface distance available. Oliphant et al. [21] reported a slight increase in heat transfer for the same mass flux as the nozzle-to-surface distance increased from 1.5 cm to 2.3 cm, though the authors [21] caution that there was considerable scatter in the data. It was suggested that variations in droplet parameters might be responsible, but no evidence for this was gathered.

In their study on a very dense mist jet, Chang and Su [19] considered the effect of nozzle-to-surface distance in more detail. Termed the separation distance, normalised by the outside jet diameter and denoted by S/d, it was seen to have a complex effect that varied with mist loading fraction and air Reynolds number. Figure 3.6, which shows the spatially averaged heat transfer for varying mist loading fraction, demonstrates the complex separation distance behaviour, with no clear pattern emerging. It can be seen that the local maxima in heat transfer for changing mist loading fractions and Reynolds number varied with S/d. For the baseline air only tests, the heat transfer increased as S/d varied from 4 to 8 before decreasing with further increases in S/d, but this was not necessarily the case for the mist jet. For some Reynolds numbers and water flow rates the maximum heat transfer was observed at $S/d = 6$ and in some cases there was no real change with varying S/d. The authors [19] offer no explanation for this behaviour beyond speculating that complex non-linear and interacting phenomena are affecting the heat transfer. However, they do comment that choosing optimal operational parameters for the use of a mist jet requires consideration of not only the air and water flow rates, but also the separation distance.

Surface and Liquid Temperatures

The work of Graham and Ramadhyani [20] reported that heat flux increased with increasing surface temperature for constant air and liquid flow rates. Tay et al. [97] reported that the heat transfer coefficient increased with increasing surface temperature for a reference mist jet temperature that was constant to within 0.5 K; this was attributed to higher temperatures tending to promote evaporation. However the increase in surface temperature is small, from

299.2 K to 305.5 K while the mist jet reference temperature remained at ~289.5 K, with large differences in reported heat transfer coefficient.

Oliphant et al. [21] indicated that a decrease in liquid temperature resulted in an increase in the heat transfer coefficient. This was speculated to be due to increasing surface tension at lower surface temperatures giving rise to larger but fewer droplets.

Droplet Parameters

To date, no study has been reported that links the droplet parameters to heat transfer for the non-boiling regime mist jet. Graham and Ramadhyani [20] reported a droplet range of 3 to 400 μm and $d_{3,2}$ = 100 μm for a water mist jet; they claimed to use radial droplet distributions for their analytical model, but did not show the distributions, nor report how the distributions affected heat transfer. No information on droplet velocity was given. Similarly, Oliphant et al. [21] reported a value of $d_{3,2}$ = 50 μm for their water mist jet. It was also reported that the manufacturers specified droplet mean velocity was 3 m/s, although no verification of this was done. Oliphant et al. [21] considered the droplet parameters to be important in understanding mist jet heat transfer, but no measurement of droplet size or velocity was carried out. Chang and Su [19] also speculated that the droplet parameters would affect the heat transfer but no data of this nature were reported.

3.6.3 Heat Transfer Correlations

To date, only Oliphant et al. [21] have attempted to correlate the heat transfer of a mist jet in the non-boiling regime. The Reynolds number is defined based on the target surface diameter, D, and mass flux, G, as

$$\mathrm{Re} = \frac{GD}{\mu} \tag{3.17}$$

where μ is the dynamic viscosity of water. The use of the mass flux implies that the mist jet covers the entire impingement surface. Using this definition for the Reynolds number, the following correlation was produced.

$$\overline{\mathrm{Nu}} = 32.5\mathrm{Re}^{0.51} \tag{3.18}$$

where $\overline{Nu}$ represents the mean Nusselt number with the characteristic length being the square root of the heater surface area. The authors [21] used the properties of water calculated at its inlet temperature in the calculation of $\overline{Nu}$ as is the case for a spray. Thus, the issue that arises as the mist jet is a two-phase air and water flow, as discussed in section 3.3, was neglected when choosing the correct fluid thermal conductivity. It was noted by the authors [21] that the droplet properties would be needed to provide a more accurate heat transfer correlation.

3.6.4 Nozzle Geometry

One final parameter of relevance for mist jet heat transfer is the nozzle geometry used to generate the mist. Both Graham and Ramadhyani [20] and Tay et al. [97] used a nozzle in which the air and liquid streams mix internally before leaving through a single exit orifice. A schematic of this type of nozzle is reproduced from the work of Graham and Ramadhyani [20] in figure 3.7 (a). The nozzle manufacturer and type specified by Oliphant et al. [21] appears to be of the same construction, although no schematic is included in that paper. Uniquely, in non-boiling mist jet heat transfer, Chang and Su [19] used a nozzle which is the inverse of a typical airblast atomiser in that a circular air jet is surrounded by an annular water jet. This could explain why their mist jet had higher water mass flow rates than air, as shown in table 3.1. A cross-sectional view of their nozzle geometry is reproduced in figure 3.7 (b). Preliminary work reported from within the research group by Lyons et al. [43] used a nozzle in which both the air and the water jets were annuli with a solid centrebody extrusion, as shown in figure 3.7 (c) while a later study also from within the research group [44] used a mist jet nozzle in which the liquid jet protruded from the centre of the air jet, a schematic of which is shown in figure 3.8.

To the best of the author's knowledge, the work reported by Lyons et al. [44] represents the only case of a mist jet with a protruding liquid jet thus far within the literature. In this work, a similar nozzle configuration is used, with the liquid jet emerging from the annular air jet.

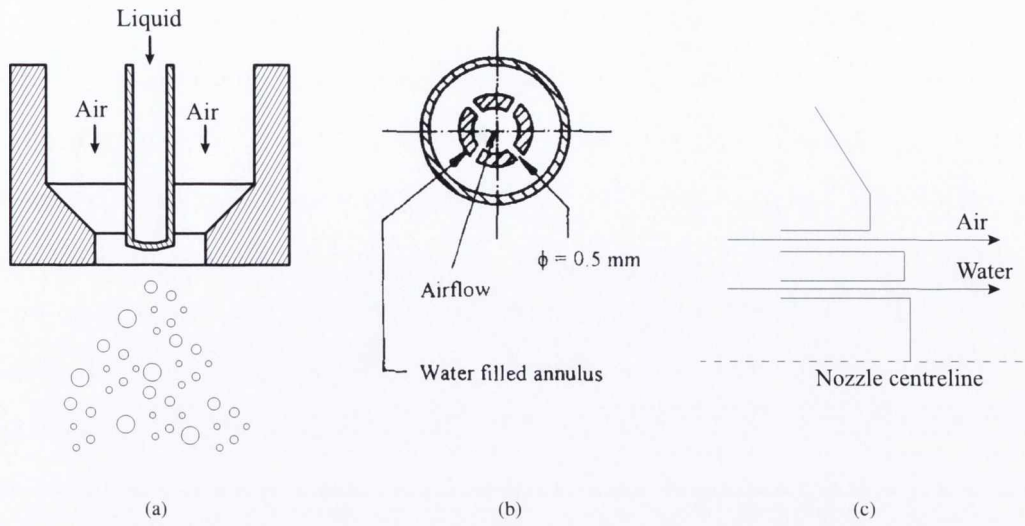

Figure 3.7: Schematics of different mist jet geometries: (a) internal atomisation nozzle [20]; (b) cross section of mist jet nozzle with an internal air jet surrounded by an annular water jet [19]; (c) mist jet nozzle where both jets are annuli [43]

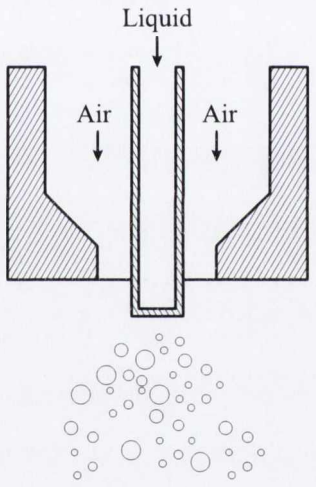

Figure 3.8: Schematic of an the mist jet nozzle geometry for external atomisation, as used in Lyons et al. [43]

3.7 Summary and Objectives

This literature review has explored the flow characteristics and heat transfer associated with impinging sprays and mist jets in both the boiling and non-boiling regimes. The heat transfer mechanisms reported and their associated parameters have been presented, where available. It is clear that while there is a comprehensive body of work on the subject of boiling spray and mist jet heat transfer, and a contribution on non-boiling spray heat transfer, the subject of

mist jet heat transfer without boiling has received very little attention.

In particular, it is clear that for the mist jet there is a lack of understanding on the effect of mist loading fraction on the heat transfer mechanisms. The number of studies in which this parameter has been explored is tiny, as summarised in table 3.1, and there are no data reported for small liquid mist loading fractions below $f = 0.08$. The possibility of achieving significant heat transfer enhancement using very small water flow levels is an important prospect for study and would deliver significant practical and environmental benefits if the level of understanding was such that optimisation could be achieved. It is also evident that there is no clear understanding of the effect of such parameters as nozzle-to-surface distance and air flow Reynolds number for different liquid flow rates.

It has been demonstrated that these are complex issues [19] that merit further work, particularly for the case when the air mass flow rate is larger than the liquid flow rate. One of the main objectives of this study is to address this paucity of information in an attempt to develop a more comprehensive understanding of the mist jet behaviour, in particular for low liquid flow rates. This will be done by examining both the time-averaged and fluctuating heat transfer components of the mist jet.

To date, there has been no attempt to examine the effect that droplet properties have on the heat transfer of a mist jet in the non-boiling regime. While some authors have reported [20, 21] on the Sauter mean diameter and droplet velocity, there has been no assessment of how these parameters vary for different liquid flow rates, air flow rates or distances from the nozzle exit. Nor has the influence they might have on the impinging mist jet heat transfer been investigated. This is an important gap in the literature as such information is crucial for developing an understanding of the convective heat transfer mechanisms in dilute mist jets. Thus, another aim of this study is to examine the droplet properties in dilute mist jets by the use of shadowgraph imaging.

As well as this, no attempt has been made to date to examine the local behaviour of the liquid film that forms on the surface under an impinging mist jet. The studies reported on mist jet heat transfer without boiling have assumed laminar flow of a continuous film, with the model of Graham and Ramadhyani [20] being based on this assumption. However, for the small f considered here, the film produced may not exhibit this behaviour. The final aim, therefore, is to link the droplet properties to the film behaviour, and to combine this

information with the simultaneous high-speed heat transfer measurements, with a view to elucidating the convective heat transfer mechanisms in dilute impinging mist jets.

Chapter 4

Experimental Set-up and Instrumentation

This chapter describes the two experimental set-ups used in this study, one for examining the heat transfer due to a mist jet with various flow and positional parameters, and a second for performing simultaneous heat transfer and shadowgraph flow visualisation. The measurement techniques employed are also described.

A separate rig was designed and constructed for the visualisation experiments as it was not possible to perform shadowgraph imaging on the original heat transfer rig, the reasons for which are described below. Both set-ups consist of a heated instrumented surface, with a different surface used in each case, and the mist jet nozzle, which is common to both set-ups.

4.1 Mist Jet Nozzle

As described in section 2.1.2, the mist jet is generated by the shear driven atomisation of a liquid jet by a co-flowing air jet. Thus, the mist jet nozzle consists of an annular air jet wrapped around an internal water jet as illustrated in figure 4.1. The nozzle is a Spraying Systems B1/4 VMAU-316 SS nozzle and is shown in figure 4.2.

The main features of the mist jet nozzle can be seen in figure 4.1. Here, D_o and D_i refer to the outer and inner annular air jet diameters respectively, and D_w is the water jet internal diameter. The outer diameter of the annular air jet is 1.7251 mm, and the inner diameter is 1.2851 mm. Thus the hydraulic diameter, which for an annulus is the difference between the outer and inner diameters of the annulus, is 0.44 mm. The water jet internal diameter is 0.3805 mm. As discussed in section 2.3.1 the outer diameter is used for non-dimensionalising physical distances whereas the hydraulic diameter is used for calculating Reynolds numbers. The nozzle supplied by Spraying Systems has been modified to allow low H/D values to be examined. Thus, two protrusions that were originally on the end of the nozzle have been machined off; this can be seen in figure 4.3. Here the nozzle after machining is on the left,

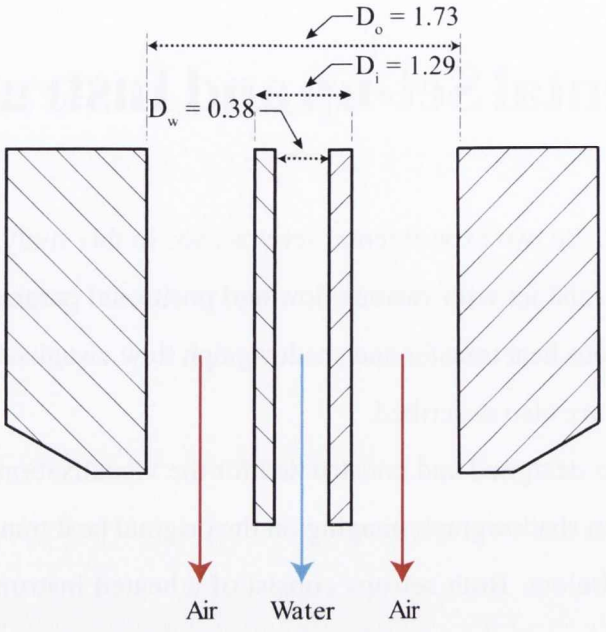

Figure 4.1: Cross-sectional schematic of the mist jet used in this study; all dimensions in millimetres

Figure 4.2: Mist jet nozzle

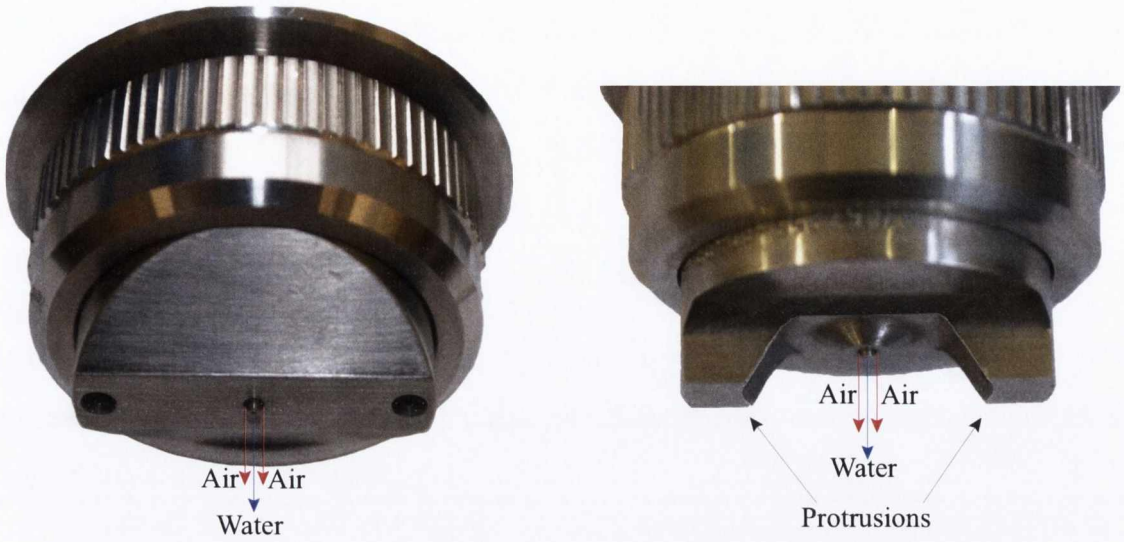

Figure 4.3: Magnified view of (a) the machined mist jet nozzle and (b) the original mist jet nozzle

and a nozzle from the same manufacturers with the protrusions still present is shown on the right. The nozzle on the right is not the identical model used in this investigation; it is included here for illustrative purposes.

4.1.1 Jet Flow Parameters

Air flow control

The air flow for the mist jet is regulated using a flow control needle valve connected to a buffer vessel, fed off the laboratory compressed air grid. The flow rate is measured using an Alicat Scientific M-500SLPM-D air flow meter which has an accuracy of ±1% over a range of 0–500 SLPM.

The air is forced through a streamline flow element within the flow meter designed to produce laminar flow. The meter measures the pressure drop, $P_i - P_o$, and uses the Poiseuille equation for laminar flow to determine the volumetric flow rate:

$$Q = \frac{(P_i - P_o)\pi r^4}{8\mu L} \tag{4.1}$$

where r and L are the radius and length of the pipe in the flow element respectively and μ is the dynamic viscosity. The viscosity is calculated within the flow meter using a discrete

temperature sensor and a microprocessor. The volumetric flow rate is then used to find the mass flow rate, $\dot{m}$, which is more appropriate for the flow through the small annular air jet nozzle. The mass flow rate is related to the volumetric flow rate as per

$$\dot{m} = \rho Q \tag{4.2}$$

where ρ is the density of the gas. As per the ideal gas law, the density of a gas is affected by its pressure and temperature. Therefore, the meter applies a correction factor to the density in equation 4.2. The density of the actual gas flow, ρ_o, can be related to the density of the gas at standard conditions of temperature and pressure, ρ_s, as

$$\frac{\rho_o}{\rho_s} = \frac{T_s P_o}{T_o P_s} \tag{4.3}$$

where T_o and T_s are the absolute temperatures in Kelvin of the actual flow and at standard conditions respectively, and P_o and P_s are the absolute pressures of the flow and at standard conditions. Therefore, in addition to the temperature sensor, the flow meter contains an absolute pressure sensor, allowing the mass flow rate to be calculated.

The flow meter expresses the mass flow rate in terms of standard litres per minute, SLPM, which is the flow rate at standard atmospheric pressure, P_{atm}, and temperature, T_s, as per the National Institute of Standards and Technology. The SLPM flow rate is calculated therefore as per

$$SLPM = \frac{\dot{m} \times 60}{10^{-3}} \times \frac{RT_s}{P_{atm}} \tag{4.4}$$

where R is the universal gas constant equal to 287 J/kgK.

Owing to the small diameter of the annular nozzle exit, the flow exiting the air jet is compressible. Thus compressibility flow analysis must be used to find the air jet velocity and hence to calculate the jet Reynolds number. In order to find the jet velocity, the Mach number, Ma, of the flow must be determined. Ma is defined as

$$\text{Ma} = \frac{V}{c} \tag{4.5}$$

where V is the jet velocity and c is the speed of sound at the jet exit. The Mach number is

calculated by solving equation 4.6, the compressible flow relationship between the Mach number and the mass flow rate, iteratively.

$$\dot{m} = \frac{A_e \mathrm{Ma} P_0 \sqrt{\frac{k}{RT_0}}}{\left[1 + \frac{(k-1)\mathrm{Ma}^2}{2}\right]^{\frac{k+1}{2(k-1)}}} \tag{4.6}$$

where A_e is the annular exit area of the nozzle, R is the specific gas constant, k is the ratio of specific heats and P_0 and T_0 are the pressure and temperature measurements in the flow meter. The speed of sound at the nozzle exit, c is calculated as

$$c = \sqrt{kRT} \tag{4.7}$$

where T is the temperature of the flow at the nozzle exit. This is calculated using the compressible flow relationship of

$$\frac{T_0}{T} = 1 + \frac{k-1}{2}\mathrm{Ma}^2 \tag{4.8}$$

The jet velocity, V, can now be calculated, and hence the jet Reynolds number.

$$\mathrm{Re} = \frac{V D_h}{\nu} \tag{4.9}$$

where ν is the kinematic viscosity of air calculated at T and D_h is the hydraulic diameter of the annular air jet, as discussed in section 2.1.3.

The uncertainty in Reynolds number depends on the uncertainty in the flow meter, as well as the uncertainties in the measurement of the hydraulic diameter and fluid properties. Thus, by propagating the different uncertainties through the equations used to calculate the air flow rate, as per Coleman and Steele [128], the uncertainty in the SLPM registered by the flow meter was calculated to be 2.8 %, which results in an uncertainty in the jet Reynolds number of 3.9 %.

Figure 4.4: Watson-Marlow 120 U/DV Auto/Manual Control peristaltic pump

Figure 4.5: Avery Berkel TSA 3001 weighing scales

Water flow control

A Watson-Marlow 120 U/DV Auto/Manual Control peristaltic pump, shown in figure 4.4, was used as the water delivery system for the mist jet. The flow rate is set by varying the rate of revolution of the rollers of the pump that drive the water through the tubing which connects the water reservoir to the nozzle; the speed of the rollers can be changed in steps of 0.1 rpm. The flow rate obtained depends on the size of the tubing used. Tubing of 0.8 mm bore was used here, which provides a nominal flow rate ranging from 0.004 ml/min at the lowest pump speed of 0.1 rpm up to 8 ml/min. In practice the flow would be too unstable at the very low speeds. Thus the lowest flow rate used in this investigation is 0.032 ml/min. Measurement of the water flow rate was performed by placing the water reservoir on a high sensitivity Avery Berkel TSA 3001 weighing scales, shown in figure 4.5, to determine the mass of water leaving the reservoir over a given interval of time. From this the water mass flow rate was calculated.

4.2 Experimental Set-Up for Heat Transfer Measurements

4.2.1 Impingement surface

An image of the experimental set-up used for the heat transfer measurements is shown in figure 4.6, while figure 4.7 shows a schematic of the rig. The mist jet nozzle is positioned above an instrumented isothermally heated copper plate, 0.55 m $\times$ 0.425 m in area and 0.006 m in thickness. A heater mat is attached to the entire underside of the plate in order to obtain the nominally uniform wall temperature boundary condition of the upper plate surface. This mat is powered by a Kikusui PWR1600L 1600 W DC power supply, shown in figure 4.8. The underside of the mat is insulated to minimise heat losses through the base. The plate, heater mat and insulation are mounted on a carriage driven by a stepper motor and lead screw actuator which allows the impingement surface to traverse relative to the mist jet. This allows for heat transfer measurements to be undertaken at different radial positions relative to the jet impingement zone. A Micro-Foil® heat flux sensor is embedded in the upper surface for heat transfer measurements; this sensor also contains a thermocouple. The heat transfer instrumentation is described in detail in section 4.4.

4.3 Experimental Set-Up for Simultaneous Heat Transfer Measurements and Shadowgraph Imaging

The experimental set-up used for simultaneous heat transfer and shadowgraph imaging, or shadowgraphy, is shown in figure 4.9, with a schematic presented in figure 4.10. As in section 4.2 this set-up consists of a heated impingement surface, but with the addition of the shadowgraphy apparatus.

4.3.1 Impingement Surface

The impingement surface in this case consists of a copper block with two 535 W cartridge heaters contained within machined-out holes in the middle of the block. The block is 0.1 m $\times$ 0.05 m in area and 0.025 m thick. A different impingement surface was required for the shadowgraph imaging set-up, as the large size of the plate used in the heat transfer

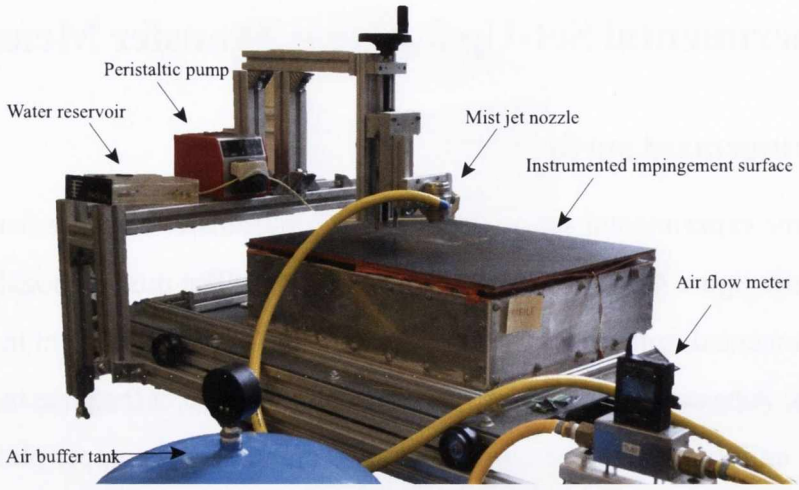

Figure 4.6: Mist jet nozzle and impingement plate

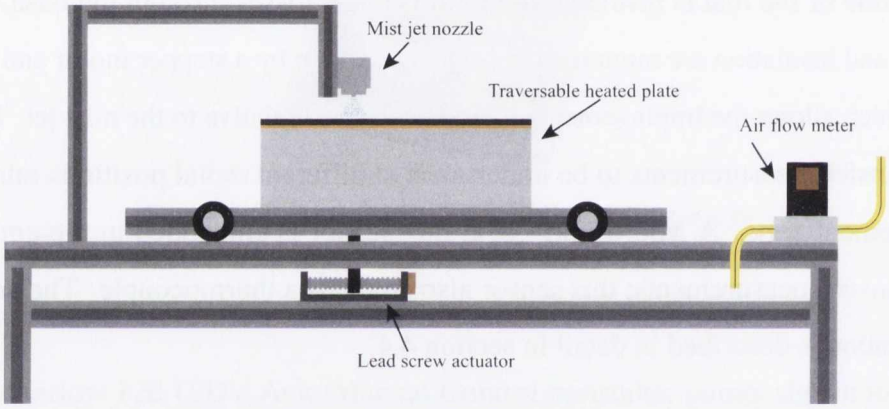

Figure 4.7: Schematic of heat transfer rig

Figure 4.8: Kikusui PWR1600L 1600 W DC power supply used to heat impingement surface

measurements, as described in section 4.2, prevented the shadowgraph imaging camera from being positioned close enough to the mist jet and its local impingement zone. As the simultaneous heat transfer and flow visualisation measurements were only taken for the stagnation region of the jet, the copper block was fixed in position on a platform with adjustable height. The cartridge heaters are connected to the mains via a Variac resistance

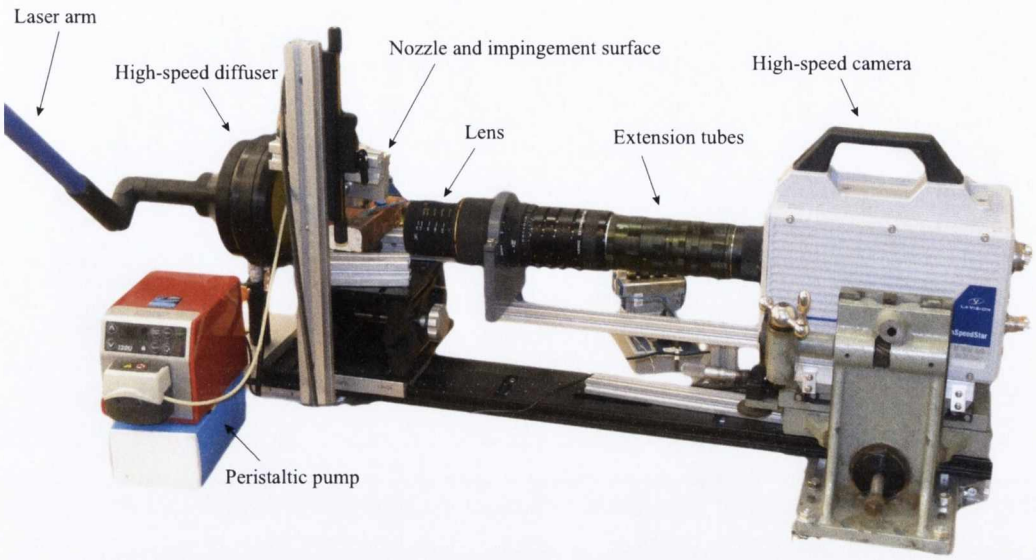

Figure 4.9: Simultaneous shadowgraphy and heat transfer rig

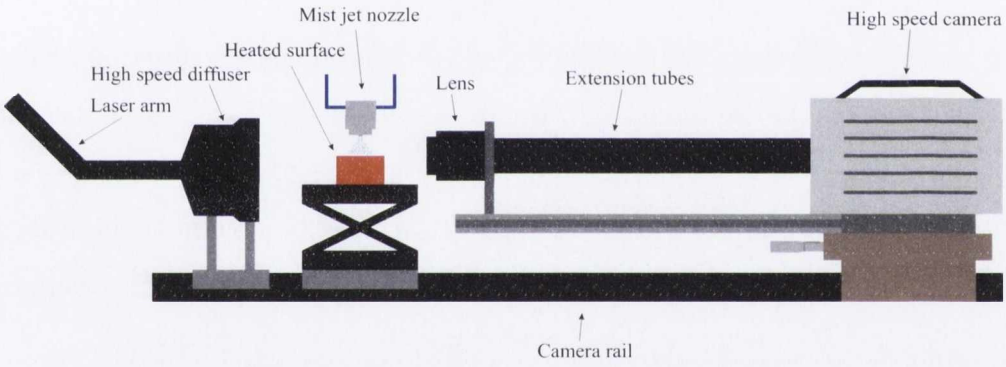

Figure 4.10: Schematic of the simultaneous shadowgraphy and heat transfer rig

power unit which allows for controllability of the cartridge heaters' power.

A hot film sensor was attached to the face of the copper block. This choice of sensor was made as the hot film sensor has the high temporal resolution required to perform the simultaneous high-speed heat transfer and shadowgraphy measurements. A thermocouple was embedded within the block below the hot film sensor.

4.3.2 Shadowgraph Imaging Set-up

This section describes the equipment used in shadowgraph imaging, or shadowgraphy. Shadowgraphy is a particle visualisation technique whereby a uniform light source is placed behind the particles of interest, in this case the mist jet water droplets, while a high-speed

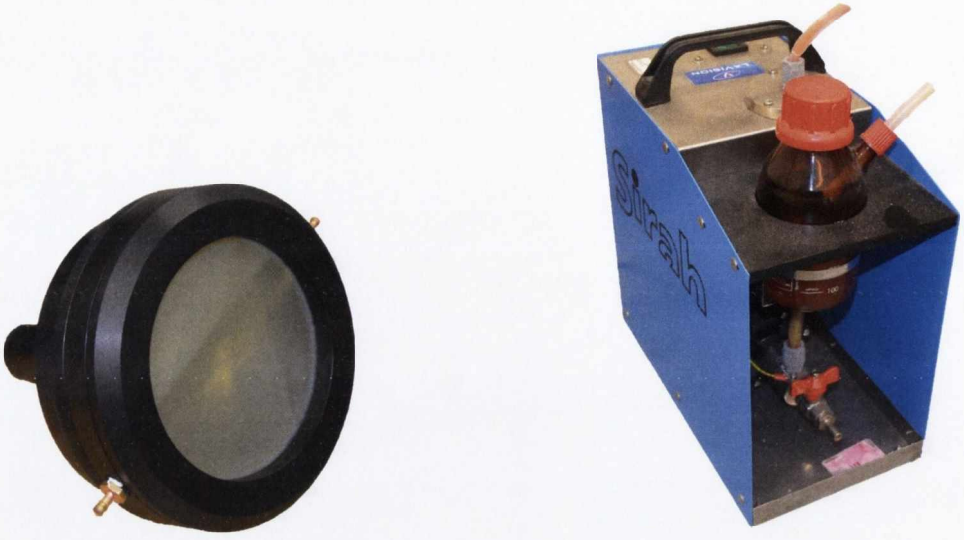

(a) (b)

Figure 4.11: (a) DaVis High Speed diffuser and (b) dye pump

camera is positioned focussed on the droplets with the uniform light source in the background. The particles show up as shadows in the images taken of the flow, and from these shadows measurements can be obtained of their size, position and velocity. The procedure used in this investigation is similar to that of Berg et al. [129], and is discussed in detail in section 4.5. The background illumination, optical system, mist jet nozzle and impingement surface are all mounted on the same camera rail. This ensures they are in line and stable.

High Speed Diffuser

A LaVision High Speed Diffuser, shown in figure 4.11 (a) is used to provide the uniform background illumination required for shadowgraphy. The diffuser consists of a diverging lens and a cuvette that is filled with Rhodamine 6G dye dissolved in ethanol. The diffuser is mounted to the guide arm of a high-speed Quantronix Darwin-Duo Nd:YLF double pulse laser. The laser light causes the dye to fluoresce mono-chromatically, providing the uniform illumination required. The laser dye is delivered to and returned from the cuvette continually via a DaVis dye pump, shown in figure 4.11 (b). This is to ensure the dye doesn't heat up under the laser light, which could occur under high laser powers.

Detection system

A LaVision HighSpeedStar 6 CMOS camera with 1024 × 1024 resolution is used to obtain the shadowgraph images. A Sigma DG Macro 105 mm lens is attached to the camera via a series of extension tubes with a total length of 214 mm. The purpose of the extension tubes is to act as a long distance microscope. The use of extension tubes results in the loss of some light. As such, a suitable lens aperture was identified; too small an aperture would result in insufficient light reaching the camera sensor, whereas too wide an aperture reduces the depth of field of the lens. Using this set-up the field of view was approximately 5 mm × 5 mm, with a depth of field of approximately 0.7 mm.

The camera is mounted on a movable plate that is adjusted using a micrometer controlled actuator. The resolution of the micrometer is 0.025 inches, or 0.635 mm. This allows for the camera to move towards and away from the mist jet, as well as from side to side. Therefore the position of the mist jet and impingement surface could be fixed, and the camera adjusted independently so that the mist jet was in the centre of the image obtained as well as in sharpest focus.

4.3.3 Simultaneous Measurements

To perform simultaneous measurements, the heat transfer measurements and shadowgraph imaging are triggered at the same time. To do this, a TTL (Transistor-Transistor Logic) signal is used. It is generated using National Instruments LabVIEW^{TM} software on the PC used to obtain the heat transfer measurements. The DaVis software used to run the shadowgraphy measurements is set-up to start recording upon receiving a TTL signal at the same rate of 1000 Hz as the hot film sensor. The high-speed camera is constantly storing and overwriting images until it receives the TTL. However, because of hardware limitations within the computer and DAQ chassis used to generate the TTL, a slight delay exists between the beginning of the hot film sensor voltage measurement and the shadowgraph recording. The signals can be re-synchronised by performing a cross-correlation between the temporal signals of the hot film sensor voltage and the detection of droplets in a shadowgraph frame, as the heat transfer of a mist jet is expected to depend significantly on the presence of droplets, as discussed in detail in chapter 7. An example of this cross-correlation is shown in figure 4.12 for the mist

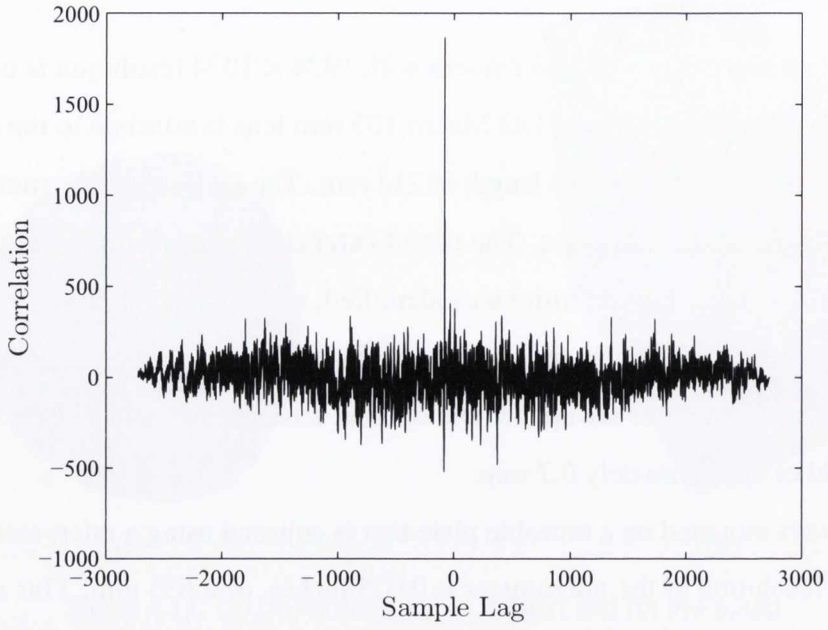

Figure 4.12: Example of the cross-correlation between the hot film sensor voltage and detection of droplets using shadowgraph imaging

jet with a mist loading fraction of $f = 0.006$ at Re = 4500. The clear spike in figure 4.12 is indicative of the very strong correlation between the hot film sensor voltage signal and the detection of droplets in the shadowgraph images. Across the range of flow parameters studied, there was very little deviation of the lag between the signals, less than 5 samples at most. With further investment in a higher specification National Instruments DAQ card, or potentially a high-speed, high-precision oscillating device that could trigger both devices, the need for this cross-correlation may be removed. However, for the current set-up, this method provided a repeatable method of synchronising the simultaneous measurements.

4.4 Heat Transfer Measurements

In this investigation, the nominal thermal boundary condition is a constant surface temperature, and as discussed in section 3.3, the local heat transfer coefficient, h, is determined using Newton's law of cooling.

$$q'' = h(T_s - T_j) \tag{4.10}$$

Thus, measurements of the heat flux, q'', from the heated impingement surface, the surface temperature, T_s, and the jet temperature, T_j, are required to calculate h. Two different sensors are required for the two experimental set-ups; one to measure the time-averaged q'' in the measurement of the heat transfer in the set-up described in section 4.2, and a second to measure the time resolved q'' for the simultaneous heat transfer and shadowgraph imaging experiments described in section 4.3. This section outlines the heat transfer measurement techniques used in this investigation.

4.4.1 Thermocouples

T-Type thermocouples are used in this study; these are suitable across a range of −200 to 300 °C. This thermocouple type consists of a copper positive wire and a negative constantan (an alloy of copper and nickel) wire junction. A voltage is measured across the junction of the two wires which is proportional to the temperature difference between the thermocouple junction, T_h, and the temperature of the cold junction, T_c:

$$V \propto (T_h - T_c) \tag{4.11}$$

The typical sensitivity of this type of thermocouple is approximately 43 μV/°C.

4.4.2 RdF Micro-Foil® Heat Flux Sensor

A RdF Micro-Foil® heat flux sensor is used for obtaining time-averaged local heat flux measurements. It uses a differential thermopile contained within the sensor to calculate heat flux from Fourier's law for heat transfer by conduction. The sensor also contains a thermocouple, used to measure local surface temperature; this thermocouple is located 4.5 mm from the thermopile for heat flux measurements, and this positioning difference must be taken into account in the processing of data from the sensor. The sensor is mounted flush to the copper plate. A schematic of the sensor is shown in figure 4.13 (a), which illustrates the positioning of the thermopile and thermocouple within the sensor.

The thermopile sensor consists of three thin layers of Kapton with T-type thermocouples on either side of the central layer. The thermal conductivity and thickness, k and δ respectively, of the central Kapton layer are known and the heat flux, q'', through the sensor can be

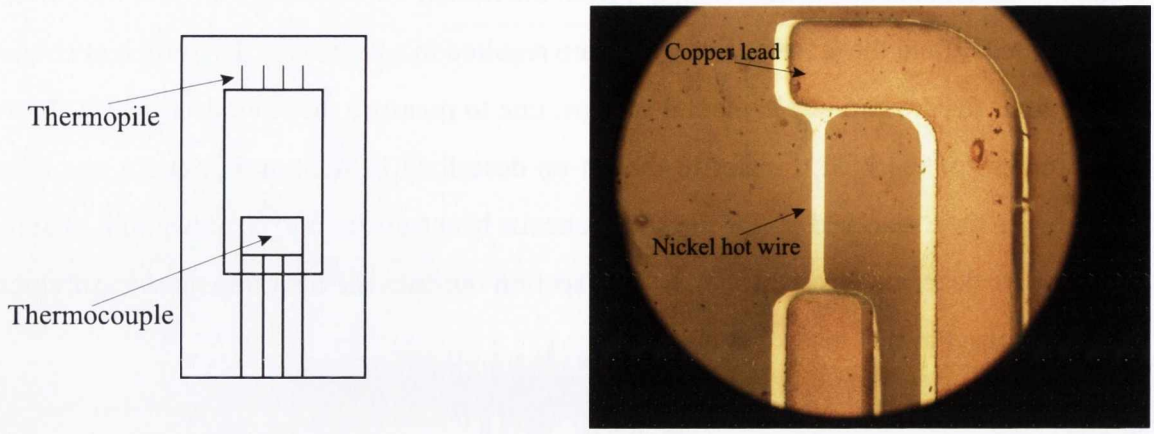

(a) (b)

Figure 4.13: (a) Schematic of a Micro-Foil® heat flux sensor and (b) a magnified view of the Senflex® hot film sensor

calculated using the temperature difference, ΔT , determined from the the thermopile readings as per equation 4.12:

$$q'' = k\frac{\Delta T}{\delta} \tag{4.12}$$

Five thermocouple junction pairs are used within the thermopile to improve signal magnitude and resolution. The voltage signal from the heat flux sensor is amplified by a factor of 1000 to improve signal to noise ratio. The heat flux measurement region of the sensor has dimensions of 4 mm × 0.5 mm. As per the manufacturers, this sensor has a characteristic 62 % response time to a step function of 0.02 s.

4.4.3 Senflex® Hot Film Sensor

A Senflex® SF9902 coated hot film sensor is used in conjunction with a constant temperature anemometer (CTA) to obtain fluctuating, or real time, heat flux measurements. The sensor is made of a nickel film element electron beam deposited onto a Upilex S polymide film. Copper leads are also deposited on the polymide film to act as terminals to connect wires to the CTA module. The nickel element has a thickness of < 2 μm and has an area of approximately 0.1 mm × 1.4 mm as specified by the manufacturer. The sensor cold resistance is nominally between 6 – 8 Ω. Figure 4.13 (b) shows a magnified image of the nickel film element of the hot film sensor, outlining the different components.

A Dantec Dynamics 90C10 CTA Module housed in a StreamLine 90N10 Frame, shown

Figure 4.14: Dantec Dynamics 90C10 CTA Module housed in a Streamline 90N10Frame

in figure 4.14, is used to set and maintain the temperature of the nickel film to a slight overheat above the surface temperature, typically ~7 °C. The power required to maintain this overheat temperature can be assumed to be equal to the heat dissipated from the nickel film to the impinging jet, once the appropriate correction factors have been applied as outlined in section 5.1.3.

Since a relationship exists between the electrical resistance of the nickel film and the temperature of the film, changing the resistance of the film will change the temperature. In essence, the CTA is a Wheatstone bridge with the hot film sensor forming one arm of the bridge. By controlling the decade resistance of the other arm of the bridge, and applying a voltage to the hot film sensor arm of the bridge such that the two resistance arms of the bridge are balanced, the overheat temperature can be set and maintained. Thus, the heat flux from the film is proportional to the voltage applied to the hot film sensor to maintain the overheat under a forced convection condition, as per equation 4.13:

$$q'' \propto \frac{E_{out}^2}{R} \tag{4.13}$$

where E_{out} is the voltage across the CTA bridge arm containing the hot film sensor and R is the resistance of the same bridge arm. The CTA decade resistance has a resolution of 0.1 Ω and the bridge ratio is 1 : 20. The calibration of this sensor is a complex process, and issues surrounding its use in this investigation of the high heat flux mist jet meant that the sensor voltage was used as an indicator of the temporal variations in heat flux, without a calculation of the heat transfer coefficient being performed. This is discussed in detail in chapter 5

4.5 Shadowgraph Imaging

Shadowgraph imaging, or shadowgraphy, is a spatial technique for visualising flows containing droplets or particles [130]. As with other established techniques, such as Phase Doppler Anemometry (PDA), shadowgraphy is used to obtain particle size distribution and, if used in conjunction with a double-pulsed light source, velocity information. Unlike PDA, shadowgraphy is able to measure directly flow information such as droplet shape and spray morphology, as shadowgraphy uses high-speed greyscale images as opposed to the phase shift information used in PDA. Thus it is possible to use the shadowgraph images to perform direct high-speed imaging analysis of features of interest within the mist flow. This includes aspects such as the break-up region of the jet, as well as the impingement of droplets on the surface and the spread of liquid on the impingement surface. Shadowgraphy also allows for size and velocity measurements to be made for non-spherical droplets, which is more difficult to do in other particle visualisation techniques. Berg et al. [129] applied a number of different particle imaging techniques, including shadowgraphy, to the study of a spray. A similar procedure is used in this investigation to the shadowgraph imaging technique implemented by Berg et al. The authors [129] reported that, although shadowgraphy was not as proficient at detecting particles smaller than 5 μm, it provided results that matched well with the other imaging techniques for particles above 10 μm. Also, unlike the other techniques, shadowgraphy did not have an upper limit on the size of droplets that could be detected.

The shadowgraphy technique has become more established in recent years. Pavlova et al. [131, 132] used it in their studies on the controllability of a spray by means of a synthetic jet. Zhang et al. [41] characterised a spray in a non-boiling heat transfer study with the help of shadowgraph images, while Castanet et al. [133] examined secondary droplets produced by drop impact on a heated surface using the technique. It has also been used to characterise droplet properties in dense diesel sprays by Blaisot and Yon [134], while Klinner and Willert [135] even presented early work into using the shadowgraphy process to reconstruct a 3D distribution of spray droplet sizes. More researchers are turning to the technique for its non-intrusive measurements and ability to capture non-uniform morphologies.

4.5.1 Shadowgraph Imaging Process

Obtaining shadowgraph images

As outlined in section 4.3, shadowgraph imaging uses background illumination to produce shadows of the water droplets on an image taken by the detection system. A Sigma 105 mm 1:2.8 DG Macro lens is mounted on extension tubes totalling 214 mm in length and attached to the high-speed camera; this allows the lens to act as a long-distance microscope with a magnification factor of 3 and a resolution of 4.9 μm per pixel. The field of view using this set-up is 5×5 mm. The depth of focus of the imaging system is about 0.7 mm. Using the double-pulse high-speed laser to fluoresce the dye in the diffuser, the high-speed camera is triggered at the same time as the pulses to record two frames with a separation of 5 μs at a frequency of 1000 Hz. An example of a shadowgraph image is shown in figure 4.15 (a). The number of double images that can be obtained is limited by the RAM of the camera and the resolution; for the set-up used in this investigation 2728 double-pulse images could be obtained. The maximum number was recorded for each test in order to provide a sufficiently large sample size of detected droplets.

Image processing and droplet detection

Before processing the shadowgraph images, it is necessary to calibrate the images for distance in micrometres per pixel. This is because the droplet detection algorithm determines the droplet sizes in pixels. This calibration is conducted as recommended in the LaVision shadowgraphy manual [130] and is straightforward: first an image of a known distance is taken; in this investigation an image was taken of the nozzle exit. As the diameter of the nozzle exit is known, the DaVis shadowgraph software can be used to select the nozzle diameter in the image and then calculate the pixel to micrometer scale.

Rather than using the DaVis software to detect droplets, Matlab® code was written to process the images. A potential issue arising with shadowgraphy is the capture of droplets away from the focal plane, i.e. the detection of defocussed droplets [133, 136]. An out of focus droplet will show on an image as a blur, the size of which would be different from the actual droplet size. Thus, it is important to account for droplets outside the focal plane. This can be done in different ways: one solution is to set a contrast limit between the detected droplet and the illuminated background as per Malot and Blaisot [137]. Another approach,

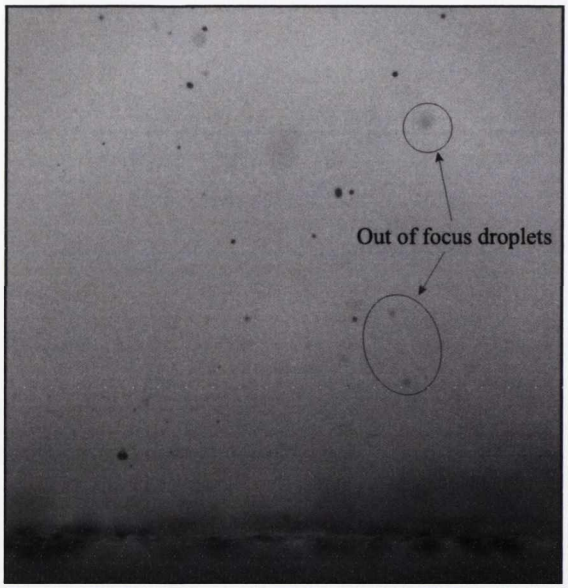

(a) Raw shadowgraphy image bitmap

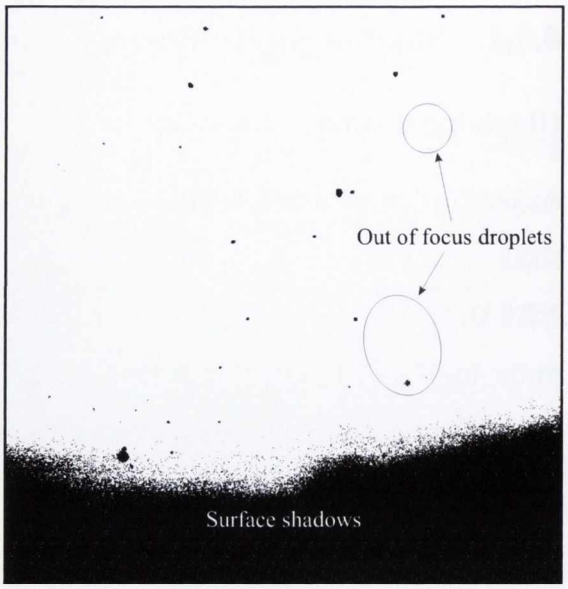

(b) Binary shadowgraphy image

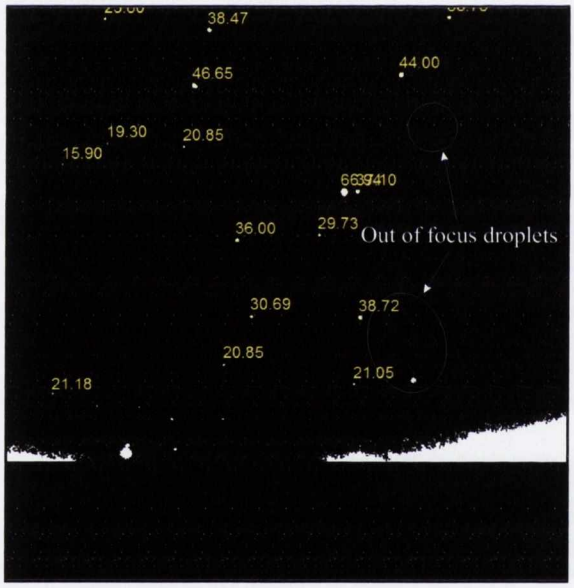

(c) Droplet detection

Figure 4.15: Shadowgraph imagery processing

for greyscale images, is to set a limit on the gradient of the grey-level at a detected droplet boundary; if the gradient is small, the droplet will be blurry and hence out of focus. This is the technique used by Castanet et al.[133]. In this study, the contrast method is used. Castanet et al. [133] described how Koh et al. [138] reported that the contrast method is more appropriate for sprays containing a large fraction of smaller droplets, with an approximate value of 30 μm given as a threshold between large and small droplets. However, Koh et al. [138] caution

that this value is specific to their optical arrangement and cannot be generalised. Castanet et al. [133] noted that the error using the gradient method for these smaller droplets was significant. However as the droplet sizes in their study tended to be much larger than this threshold, they deemed the gradient method appropriate for their work. As a large fraction of the droplets in the mist jet in this investigation are smaller than the droplet sizes found in the work of Castanet et al. [133], who examined the impact of large droplets on a heated surface, the contrast method is selected as the more appropriate technique. The use of Matlab® code rather than DaVis shadowgraph software allows for better controllability of the contrast limits, as well as subsequent filtration as discussed next.

An example of the droplet detection process is shown in figure 4.15. The raw greyscale bitmap image, a sample of which is shown in figure 4.15 (a), was first read into Matlab® . Droplets that are out of focus are marked clearly in figure 4.15. The greyscale image is then converted into a binary black and white image as shown in figure 4.15 (b). It is at this stage that the contrast limit discussed above is applied to the image. The contrast limit is based on the overall greyscale intensity of the image, which can be thought of as the background brightness. This application of the contrast limit has resulted in the rejection of almost all of the droplets that are out of focus, though some do remain; one of these remaining droplets can be seen in the lower circled area in figure 4.15 (b). Therefore further filtration is required to remove as many of the defocussed droplets as possible. This is primarily done by examining the solidity of a detected droplet using a built-in function within Matlab® . Out-of-focus droplets have lower solidity values than in-focus droplets; setting an appropriate threshold results in better rejection of defocussed droplets. The blurry droplet that remained after the contrast limit was applied in figure 4.15 (b) has not been included in the sizing calculation, the results of which are shown in figure 4.15 (c). The droplet sizes shown in figure 4.15 (c) are given in microns, and are the result of the mean of three different shape sizing functions within Matlab® . The presence of the impingement surface in the images casts shadows on the image that are unavoidable with impingement zone shadowgraph imaging. They contribute significantly to noise at the bottom of the image, as identified in figure 4.15 (b). A set area close to the surface was therefore masked out before droplet detection, as seen in figure 4.15 (c). This does not completely remove the surface shadows, which means that any droplets that are detected within a certain distance of the surface are subject to a stricter solidity limit

to prevent noise generated by the shadows from being included in the droplet list. As can be seen in figure 4.15 (c), this results in the rejection of some valid droplets near the surface but is unavoidable to ensure accurate results in most of the field of view.

The droplet velocities are calculated using a similar method to that used in the commercial DaVis software [130]. Droplets detected in the first pulse image are compared with those in the second pulse. This is done by setting up a detection window in the second image for each droplet detected in the first image; the size of the window and its location relative to the droplet in the first image is initially based on an estimation of the general path of the droplets. The results of this estimation are examined for a selection of the droplet double-pulse images, and the estimations of the window size and location are revised appropriately. As an added reliability measure to ensure the droplets are correctly matched, the sizes of the two droplets are compared and if there is more than a 20% difference the droplet in the second image is rejected and the algorithm attempts to locate the correct droplet. This again is similar to the approach used in the DaVis software [130]. The final droplet size is determined to be the mean of the sizes in the two pulses; this again is the recommended approach [130].

4.6 Data Acquisition

Separate data acquisition systems were used for the two separate experimental set-ups. These are described in this section.

4.6.1 DAQ Hardware

Heat transfer set-up

A National Instruments cDAQ-9172 chassis is used to house the different input and output modules. The thermocouple readings are obtained using an NI 9211 module. The stepper motor used to move the heated plate is driven by a controller box which uses digital 5 V inputs to control the direction of the stepper motor and the number of steps moved, i.e. the distance the plate travels. A digital input-output high-speed NI 9401 module provides these voltage inputs. The voltage signals from the Micro-Foil® and the hot film sensors are obtained using an NI 9215 module. The Micro-Foil® signal is read via a Fylde FE-351-UA amplifier to

apply the desired gain of 1000.

Simultaneous heat transfer and shadowgraphy set-up

A National Instruments cDAQ-9174 chassis is used to house the input and output modules. Again, an NI 9211 module is used for thermocouple measurements. The NI 9401 high-speed digital module provides the TTL signal to the DaVis software to trigger the shadowgraph image recording. The NI 9215 module is used for the hot film sensor voltage measurements once again.

4.6.2 DAQ Software

LabVIEW^{TM} software is used to acquire and display signals for both set-ups. The software allows for real-time signal acquisition as well as setting and running automated tests. When temperatures and flow rates have stabilised, the software can be triggered to obtain and save the various signals, and to trigger a TTL in the case of the simultaneous heat transfer and shadowgraphy tests. For time-averaged heat transfer measurements, data acquisition is performed for approximately 10 seconds per radial location at a rate of 1000 Hz. Normally, the plate traversed in steps of 0.25 mm.

For the shadowgraphy tests, the hot film sensor signal is recorded at rate of 1000 Hz, the same as the camera frame rate. The RAM of the camera limited the number of frames that could be recorded to 2728. The signal from the hot film sensor was recorded for 5 seconds per test, with recording beginning at the same time as the camera and continuing on afterwards.

4.6.3 Experimental Procedure

Heat transfer set-up

For the heat transfer set-up, the experimental procedure is as follows: the copper impingement plate is heated and the mist jet set to the desired air and liquid flow rates and positioned with the jet stagnation point above the thermocouple embedded in the Micro-Foil® heat flux sensor. Once the surface temperature in the stagnation zone has stabilised to the desired value, ~40 °C regardless of flow conditions, the test is started. During a test, at each radial location there is a delay before the measurements of the various signals are taken to allow conditions

to stabilise. Once the measurements are taken, the plate moves to the next radial location and the process restarts. At the end of the test, the data are saved to a text file for external processing using Matlab®.

Simultaneous heat transfer and shadowgraphy set-up

For the simultaneous heat transfer and shadowgraphy tests, the impingement surface was fixed in place, with the centreline of the mist jet positioned over the hot film sensor. The impingement surface was heated and the temperature allowed to stabilise under the mist jet, again to ~40 °C for all flow conditions. When conditions are stable, the shadowgraph imaging system is set to begin recording when it receives a TTL signal, and the heat transfer measurement is started. This involves several steps: firstly, the resistance of the hot film sensor probe is measured when no overheat is applied to it; this is to determine the temperature of the sensor under the mist jet. After the measurement is performed, a delay is applied to allow the probe to stabilise after the resistance measurement. Next, the CTA sets the overheat temperature of the hot film sensor, typically to ~7 °C. After another delay, again required to allow the sensor to stabilise at the desired overheat, the TTL is sent to the computer controlling the shadowgraphy set-up to trigger the recording of the images and the hot film sensor voltage measurement begins. As discussed in section 4.3.3, hardware limitations result in a delay between the triggering of the hot film sensor voltage and shadowgraph measurements; this is compensated for in post-processing by correlating the voltage to the detection of droplets, again as described in section 4.3.3. Once the high-speed camera recording is finished, the images are checked to ensure they have been obtained correctly and stored. At the end of the heat flux signal measurement, the CTA stops applying the overheat to the hot film sensor, and the probe is once more allowed to stabilise before the process can be started again. The hot film sensor voltage signal is saved at the end of the test for external processing.

Chapter 5

Data Processing and Calibration of Measurement Systems

This chapter describes the calibration of the measurement systems discussed in chapter 4, as well as the data processing needed to obtain time-averaged heat transfer coefficients and fluctuating heat transfer signals. Experimental uncertainty is also addressed here.

5.1 Calibration of Heat Transfer Measurements

As introduced in chapter 4, three different measurement techniques are used in determining local heat transfer characteristics; T-type thermocouples, the RdF Micro-Foil® sensor and the Senflex hot film sensor. This section details the calibration of these devices. Uncertainty calculations are performed as per Bendat and Piersol [139] and Chang and Mills [140].

5.1.1 Thermocouple Calibration

A Resistance Temperature Detector (RTD) probe was used as the reference temperature when performing the thermocouple calibrations as it has been calibrated and certified by the manufacturers (the calibration certificate is included in appendix B). As per the manufacturers, the uncertainty of the RTD probe is 0.2 °C at 100 °C. Four thermocouples were used: one for the jet air temperature, one contained within the Micro-Foil® sensor one in the water reservoir and a final thermocouple embedded within the copper block under the hot film sensor used for the simultaneous heat transfer and flow visualisation tests. The Micro-Foil® and jet air thermocouples were calibrated simultaneously using the heated copper imgingement plate. The Micro-Foil® was embedded within the plate and the jet thermocouple and RTD reference probe were positioned on the heated plate, coated with thermally conductive heat sink compound and covered with several layers of insulation covering the plate and thermocouples

to ensure a constant temperature. The plate was then heated in increments from 20 to 75 °C and the temperatures recorded once the plate reached a steady temperature value for each step. The calibration results are plotted in figures 5.1 and 5.2. A linear regression fit was applied to the data to find the calibration equation for each thermocouple. The water reservoir and copper block thermocouples were calibrated separately using an Omega Thermoregulator water bath. In each case, the thermocouple and the RTD probe were placed together in the water bath, which was heated in increments. Again, readings were taken once the temperature reached a steady value for each step. The water thermocouple calibration curve is shown in figure 5.3, while figure 5.4 shows the curve for the thermocouple embedded in the copper block under the hot film sensor used for simultaneous heat transfer and flow visualisation testing.

Equations 5.1 through 5.4 show the linear fits applied to the calibration data for the jet air, Micro-Foil® , water reservoir and copper block thermocouples respectively.

$$T_{RTD} = 0.9973 T_{Jet} - 0.0963 \tag{5.1}$$

$$T_{RTD} = 0.9891 T_{MicroFoil} + 0.025569 \tag{5.2}$$

$$T_{RTD} = 1.0014 T_{Water} - 0.2007 \tag{5.3}$$

$$T_{RTD} = 1.0031 T_{Hot,film} - 0.1902 \tag{5.4}$$

Analogous to the standard deviation of a data sample, the standard error for a linear regression curve fit is defined by Bendat and Piersol [139], who denoted it $s_{y|x}$, as

$$s_{y|x} = \left[\frac{1}{N-2} \sum (y_i - \hat{y}) \right]^{1/2} \tag{5.5}$$

where N is the number of samples, y_i is an arbitrary data point and $\hat{y}$ is the linear curve fit equation

$$\hat{y} = mx + c \tag{5.6}$$

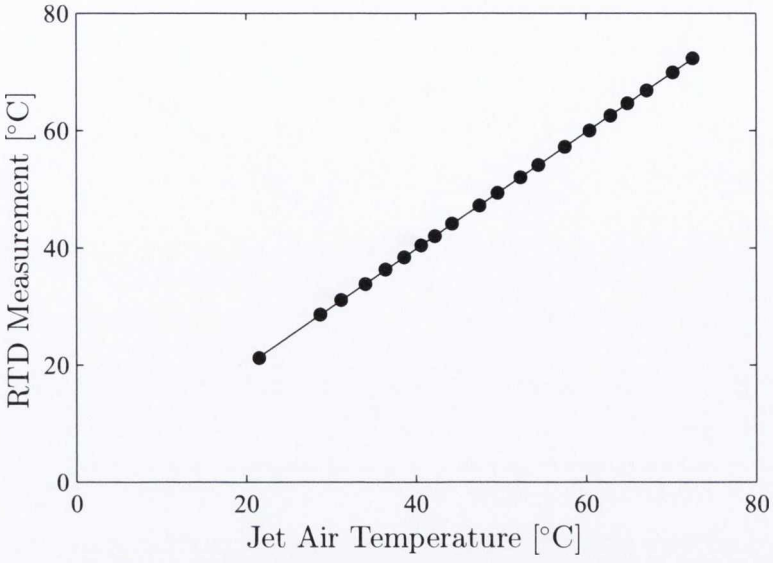

Figure 5.1: Jet air thermocouple calibration data

Table 5.1: Thermocouple uncertainties at typical operating temperatures

Thermocouple	Typical operating temperature, °C	Regression standard error, %	Uncertainty of curve fit, %
Jet air	25	0.85	0.84
Micro-Foil®	40	0.52	0.51
Water reservoir	25	1	0.93
Copper block	40	0.52	0.5

The standard error is the deviation of the measured data points, (x_i, y_i), about the predicted linear regression curve fit. The linear regression itself is also subject to an uncertainty of curve fit for a given data point x_0, denoted $U_{\hat{y}}$, given by Bendat and Piersol [139] as

$$U_{\hat{y}} = s_{y|x} t \left[\frac{1}{N} + \frac{(x_0 - \bar{x})^2}{\sum (x_i - \bar{x})^2} \right]^{1/2} \tag{5.7}$$

where t is a Student's t-distribution factor for a 95% confidence interval. Table 5.1 show the standard errors and linear regression uncertainty for typical operating temperatures of the thermocouples. The uncertainty associated with the RTD probe is added to the error for each thermocouple reading, and the total uncertainty is what is presented in each case in table 5.1.

5.1.2 RdF Micro-Foil® Heat Flux Sensor Calibration

The operating principle of the Micro-Foil® heat flux sensor is detailed in chapter 4. Briefly, the heat flux measurement is proportional to the voltage signal produced by the sensor. This

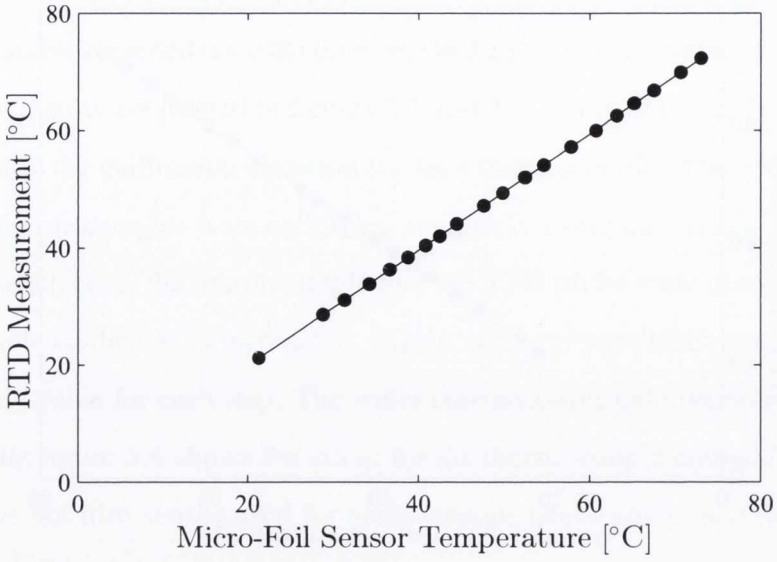

Figure 5.2: Micro-Foil® sensor thermocouple calibration data

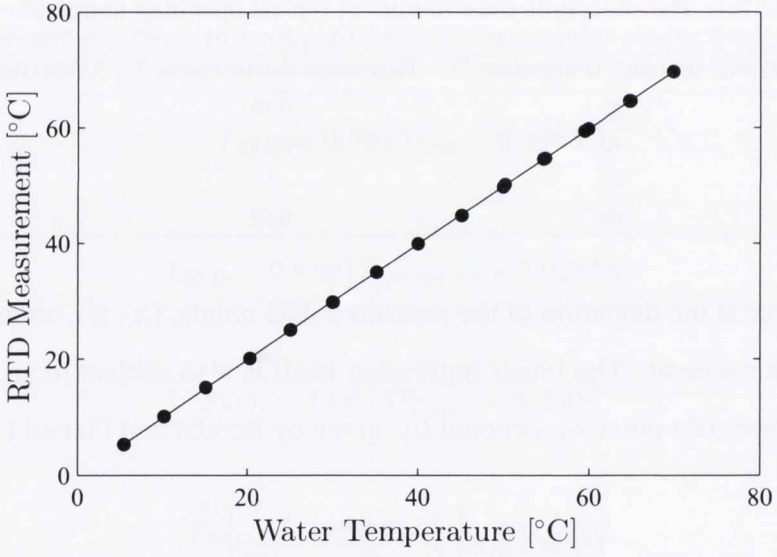

Figure 5.3: Water reservoir thermocouple calibration data

voltage is amplified by a factor of 1000 to improve the signal-to-noise ratio. Owing to the sensor's large physical geometry, it has a relatively poor response time and as such it is used for time-averaged convective heat flux from the surface only.

Previous work that has used the Micro-Foil® heat flux sensor to measure convective heat flux, for example work on the convective heat flux from a conventional round air jet by O'Donovan and Murray [4], calibrated the Micro-Foil® sensor output voltage against a stagnation Nusselt number correlation for an impinging jet; an example of such a correlation

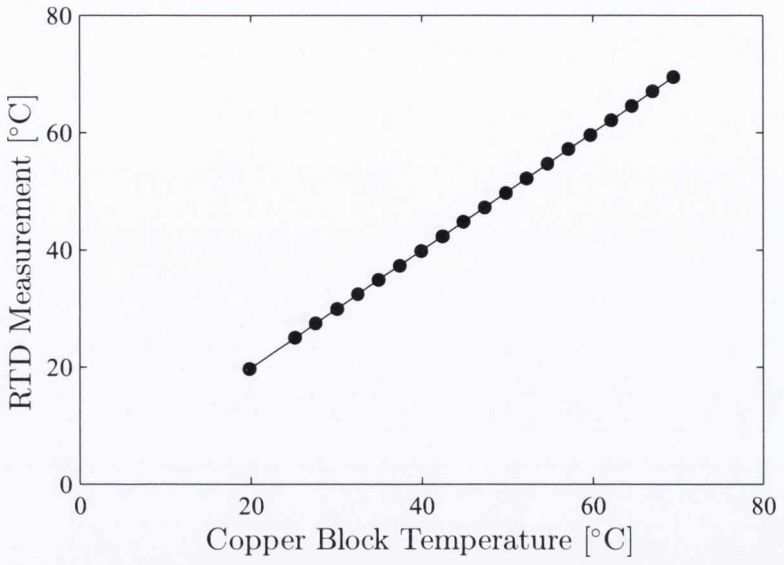

Figure 5.4: Copper block hot film sensor thermocouple calibration data

can be found in Lytle and Webb [3] for a long straight pipe nozzle with $0.25 < H/D < 1$ and a Reynolds number range of 3600 – 27600:

$$\mathrm{Nu}_{stag} = 0.835\mathrm{Re}^{0.53}\mathrm{Pr}^{0.4}(H/D)^{-0.19} \tag{5.8}$$

The jet nozzle was positioned at a H/D within the range for the correlation such that the Micro-Foil® sensor was under the stagnation point of the jet. The voltage produced by the sensor for a range of known Reynolds numbers was recorded and correlated to the heat flux, q'', calculated using the correlation in equation 5.8 for each Reynolds number, since

$$\mathrm{Nu} = \frac{hD}{k_f} \tag{5.9}$$

where k_f is the thermal conductivity of air, and

$$q'' = h(T_s - T_j) \tag{5.10}$$

where T_s and T_j are the surface and jet temperatures respectively.

Using this method, it was possible to calibrate the sensor voltage against heat fluxes approximately between 4000 and 7000 W/m^2, which was sufficient for air jets as the heat fluxes expected lay within this range. However, for a mist jet, the heat flux is significantly

higher, with q'' in this study typically an order of magnitude higher than for an air only jet. As a result of this, it was concluded that using the manufacturer's calibration would be more appropriate as it is rated to a maximum heat flux of $\sim 5.7 \times 10^5$ W/m^2.

Holmberg and Womeldorf [141] performed a comparison study on the performance of different heat flux sensors. In their investigation they considered three sensors: a cylindrical plug sensor, typically used for radiative heat flux measurements; a disc shaped button sensor, often selected for low heat flux scenarios; and a flat polymide sensor, which was in fact an RdF Micro-Foil® heat flux sensor. The authors compared calibration results obtained from a purpose-built forced convection rig versus calibration data presented by the sensor manufacturers. It was concluded that the heat flux measured by the Micro-Foil® sensor matched closely to the reference heat flux, performing better than the other sensors investigated, and that the measured responsiveness of the sensor was in good agreement with the manufacturer's calibration.

According to the manufacturer's calibration certificate, included in appendix B, the Micro-Foil® sensor voltage, V, and heat flux for the sensor used in this investigation is

$$q'' = 1.76 \times 10^7 V \tag{5.11}$$

The calibration certificate notes that the responsivity is a function of temperature, and includes a graph of the multiplication factor versus temperature. The range of temperatures considered in this study are all below the saturation temperature of water. For this range, the multiplication factor is ~1. The calibration certificate did not include an uncertainty on the heat flux, however Holmberg and Womeldorf [141] reported that the uncertainty on the heat flux for their sensor was 5%. This will be used in the calculation of the total uncertainty in this investigation. The sensor manufacturer's website quotes a similar calibration accuracy of 3–5 %, and reports a reproducibility of 1%.

5.1.3 Senflex® Hot Film Sensor Calibration

As discussed in chapter 4, a Dantec Dynamics 90C10 CTA Module CTA constant temperature anemometer (CTA) system is used in conjunction with a Senflex® hot film sensor to obtain a heat flux measurement. As was the case for the Micro-Foil® sensor, the high heat fluxes

achieved by the mist jet meant that established calibration techniques for the hot film sensor, used in the work of Beasley and Figliola [142], O'Donovan and Murray [4] or O'Donovan et al. [143], were not appropriate since they rely in part on the use of a reference convective heat flux from an air jet. In these studies, the hot film sensor was used to characterise the spatial variation in heat transfer fluctuations, whereas in this study it is used to examine the temporal distribution of the heat transfer signal. Thus, the sensor has not been used to obtain exact magnitudes of temporal variations in the heat flux, rather, the hot film sensor output voltage is used to characterise the effect of the impinging water droplets on the mist jet heat transfer. This section presents the methodology and calibration required to use the sensor in this configuration.

The basic principle, as described in section 4.4.3, is that the CTA is used to set and maintain the temperature of the nickel film element in the hot film sensor to an overheat above the surface temperature, typically ~7 °C, and the power required to maintain this overheat temperature under the action of, for example, an impinging mist jet is equal to the heat dissipated from the nickel film, q''. The sensor outputs a voltage signal, the square of which is proportional to the heat flux from the sensor as per

$$q'' \propto \frac{E^2}{R_s} \tag{5.12}$$

where R_s is the hot film sensor resistance.

Therefore in order to operate the sensor, a means of setting the overheat temperature is required. This is done by controlling the sensor film resistance using the CTA, since a linear relationship exists between the nickel film's electrical resistance and its temperature, and as such a specific film overheat can be achieved if the film resistance can be set. This process is outlined here.

The CTA and hot film sensor effectively form a Wheatstone bridge, with the hot film probe forming one arm of the bridge, as shown in figure 5.5 where it is denoted as R_{probe}. The resistance of the hot film sensor probe is the sum of the resistance of the hot film sensor element, R_s, and the resistance of the cable, connectors and leads connecting the hot film element to the CTA, R_c. The CTA module contains three other resistors: the top resistance in the same arm as the probe, $R_{t,1}$, is set at 20 Ω. The Wheatstone bridge ratio is 20:1, therefore

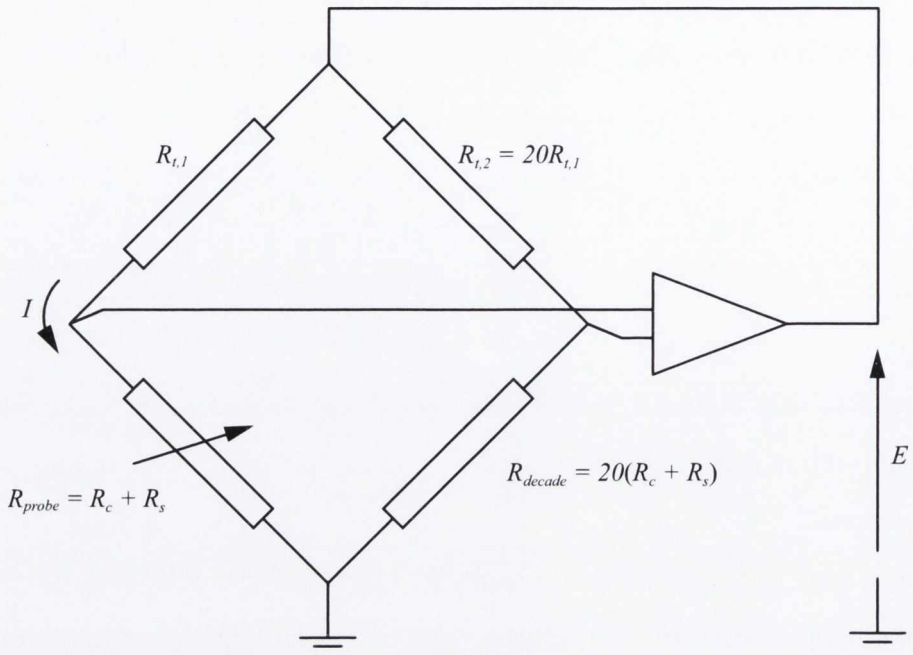

Figure 5.5: Wheatstone bridge in constant temperature anemometry circuit with bridge ratio 20:1. The top resistor, $R_{t,1}$ is set to 20 Ω

when the bridge is balanced the resistors in the other arm of the bridge, $R_{t,2}$ and R_{decade}, are 20 times the corresponding resistances in the sensor arm. Throughout the operation of the CTA, $R_{t,1}$ and $R_{t,2}$ remain constant.

The CTA sets the hot film element temperature by balancing the bridge, i.e. set R_{probe} to $R_{decade}/20$ since $R_{t,1}$ and $R_{t,2}$ are unchanging and are already balanced. This is done by applying a voltage, E, across the hot film sensor, which drives a current through the film element. This current causes the film element to heat, due to Joule heating, which in turn increases the film resistance. By varying the voltage, the film resistance can be set such that the bridge is in balance, i.e. $20 \times R_{probe} = R_{decade}$. Thus, the decade resistance is the controlling resistance, and if the relationship between the film element resistance and temperature is known, R_{decade} can be set such that a specific film temperature can be obtained when the bridge is balanced. As the sensor film experiences a change in temperature, the CTA adjusts the sensor voltage to keep the sensor resistance constant. The voltage signal, E, is output from the CTA, and is indicative of the film heat flux, as per equation 5.12.

The relationship between the film resistance and temperature is typically given in the

following form

$$R_s = R_{s,ref}[1 + \alpha(T_s - T_{s,ref})] \tag{5.13}$$

where T_s is the film temperature corresponding to the resistance R_s, $R_{s,ref}$ is the film resistance at a reference film temperature $T_{s,ref}$, and α is the temperature coefficient of resistance (TCR), with units of K^{-1}, which represents the change in resistance of the film per unit Kelvin change. This relationship must be calibrated in order to use the hot film sensor. This is done after the hot film sensor is embedded on the impingement surface, as deforming the film element can affect its resistance. The hot film sensor is covered in insulation and the impingement surface is heated incrementally. The temperature at each step is measured using the same RTD probe as in the thermocouple calibrations, positioned directly beside the film element, and for each temperature increment the resistance of the probe, R_{probe}, is measured using an ohmmeter. The linear relationship between the film and the temperature determined using this procedure is

$$R_{probe} = 0.0337T_s + 9.433 \tag{5.14}$$

The corresponding calibration data are shown in figure 5.6. The resistance of the cables that connects the hot film sensor to the CTA was measured using an ohmmeter to be 0.43 Ω. The resistance of the copper leads on the hot film sensor itself is also required. According to the manufacturers, the copper leads have a resistance of 0.05 Ω/inch, resulting in a resistance of 0.073 Ω. Thus, the total resistance of the leads and cables, R_c, is 0.503 Ω. The relationship between the hot film resistance, R_s, and temperature can now be found by taking R_c into account.

$$R_s = 0.0337T_s + 9.433 - R_c = 0.0337T_s + 8.93 \tag{5.15}$$

For this calibration, the standard error, calculated as per equation 5.5 is 0.011 Ω, or 0.63% at a typical operating resistance of 10.257 Ω, including the uncertainty associated with the RTD reference probe. The uncertainty of curve fit for a confidence interval of 95% at the same operating resistance, as per equation 5.7, is 0.016 Ω, or 0.63%, at a typical operating temperature of 40 °C and again including the RTD probe uncertainty.

As per the CTA manual [144], α is calculated by determining the fractional change of the

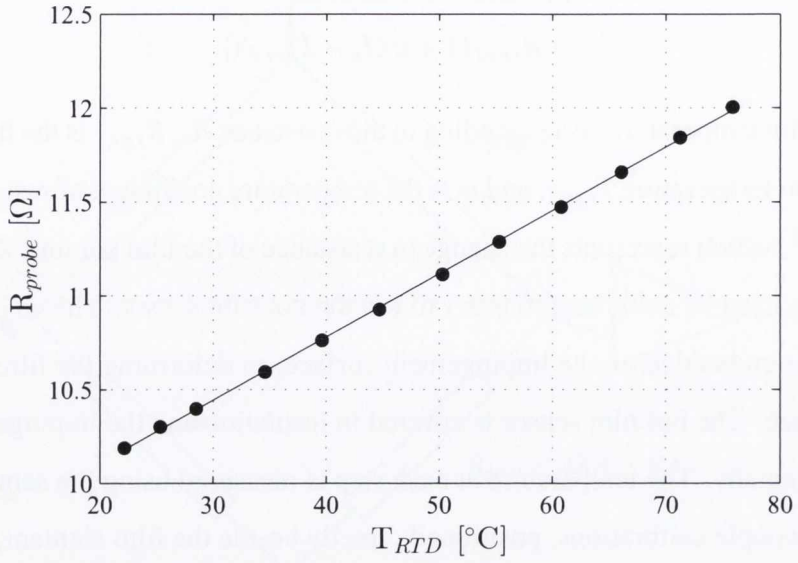

Figure 5.6: Hot film wire resistance versus temperature calibration data

hot film resistance, R_s, due to a 1 °C temperature change. Thus

$$\alpha_{21} = \frac{R_{s,21} - R_{s,20}}{R_{s,20}} \tag{5.16}$$

Using the relationship in equation 5.15, the temperature coefficient of resistance is found to be 0.004225 K^{-1}; this is referred to as α_{21}. It should be noted that as α can vary slightly with increasing temperature, the final TCR at the overheat, α, should be calculated, as recommended by the manufacturers [144], using the following expression.

$$\alpha = \frac{\alpha_{21}}{[1 + \alpha_{21}(T_s - 21)]} \tag{5.17}$$

Thus, the CTA can now be used to set the hot film sensor overheat temperature, with the output bridge voltage, E, being monitored and recorded by the data acquisition system.

In order to use the hot film sensor to calculate heat flux, and hence heat transfer coefficient, the sensor area must be known. However, Beasley and Figliola [142], among others [145], have reported that the effective sensor area varies with sensor overheat due to lateral conduction from the film to the surrounding sensor coating. Thus, in order to accurately determine heat flux using the hot film sensor, the effective area must be determined. This can be done by comparing measured heat transfer coefficient data with correlated data, using a Nusselt

number correlation such as that of Liu and Sullivan [48] for an impinging air jet, to determine the effective sensor area [143, 145]. However, this method is not appropriate for the case of a mist jet, as the heat flux range of the mist flow is well beyond that encompassed by single phase jet correlations. Further work on the calibration of hot film sensors for high heat flux situations is required before the hot film sensor can be used for precise quantification of the high-speed fluctuations in the mist jet heat flux. For the current study, the hot film voltage squared is used as an indicator of the variations in heat flux due to droplet impingement in the simultaneous shadowgraph flow visualisation and hot film sensor testing.

5.2 Water Pump Calibration

The Watson-Marlow 120 U/DV Auto/Manual Control peristaltic pump used to control the water flow rate in this investigation was rated by the manufacturers for flow rates of 0.004 to 8 ml/min for the 0.8 mm bore tubing used, with the flow rate adjustable by setting the revolutions per minute, rpm, of the peristaltic roller. Owing to the very small flow rates being considered, it was deemed prudent to calibrate the flow rate in situ. This was done by placing the water reservoir on an Avery Berkel TSA 3001 mass balance and measuring the change in mass over a measured period of time, no shorter than 40 minutes, for a set pump rpm, and hence calculating the water flow rate in ml/min, Q_w; more measurements were performed at the lower end of the flow rates as this is the parameter range under investigation. Increasing the pump rpm and repeating the measurement of the water reservoir mass resulted in the linear relationship given by

$$Q_w = 0.0224 \times \text{rpm} + 0.0014 \tag{5.18}$$

The calibration data is shown in figure 5.7. The maximum standard error for the calibration data was 5 % with a corresponding maximum calibration uncertainty of 3.59 %, both found at the lowest liquid flow rate examined in this study of 0.035 ml/min.

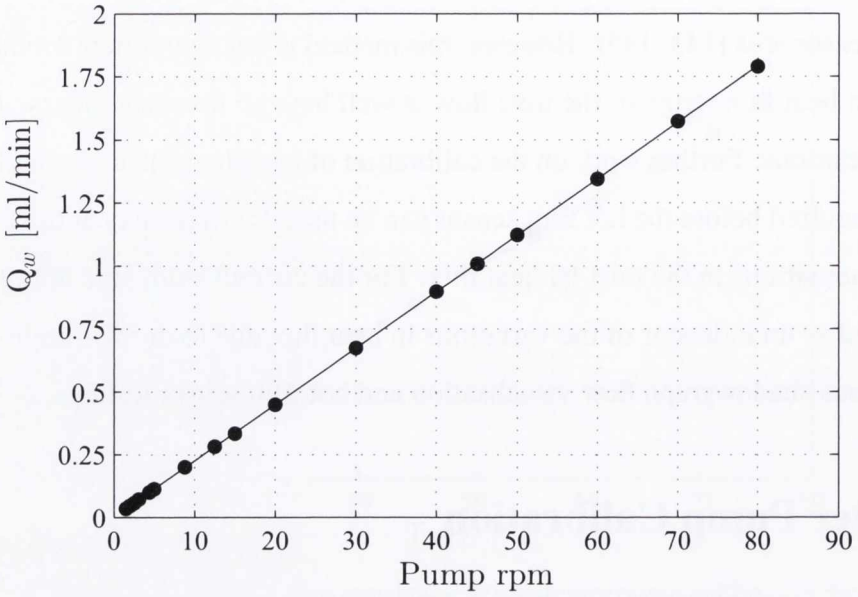

Figure 5.7: Pump flow rate calibration data

5.3 Uncertainty in Heat Transfer Coefficient

This section examines the uncertainty in the heat transfer coefficient, Δh, associated with the two different heat transfer measurements: the time-averaged heat transfer coefficient measured using the Micro-Foil® sensor and the temporal fluctuating heat transfer coefficient measured using the hot film sensor. The uncertainty in the heat transfer coefficient consists of its measurement uncertainties, U_h, and also the uncertainties associated with the mist jet air and water flow rates, U_{mist}. The total uncertainty in the heat transfer coefficient, Δh is given by

$$\Delta h = \sqrt{U_h^2 + U_{mist}^2} \tag{5.19}$$

Time-averaged heat transfer coefficient uncertainty

As a result of the nature of the mist jet flow and impingement, the transient heat flux of the mist jet exhibits significant deviation from the mean. To illustrate this, figure 5.8 shows the temporal distributions of the hot film sensor voltage squared, E^2, which is indicative of the heat flux, for a sample mist loading fraction of $f = 0.003$ for a jet Reynolds number of Re = 4500 and also for an air-only jet at the same Reynolds number. Significantly larger fluctuations in the signal can be seen for the mist jet than the air; these do not indicate error

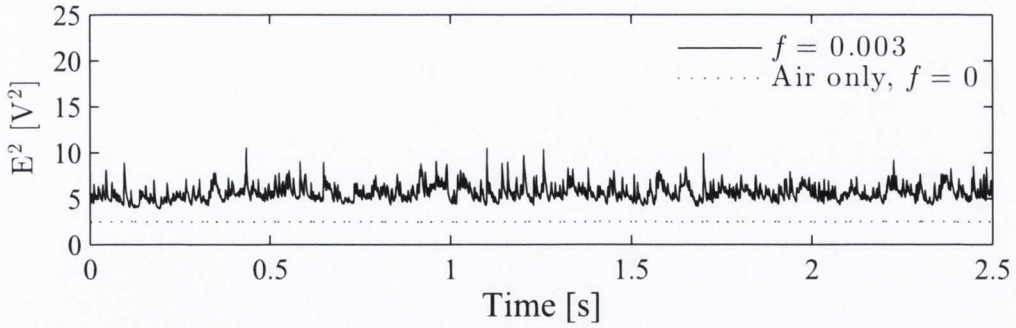

Figure 5.8: Comparison of time traces of the hot film sensor voltage squared, E^2, for the mist jet with mist loading fraction of $f = 0.003$ and Re = 4500 and an air jet at Re = 4500

in the measurement, but rather flow aspects of the jet, as examined in chapter 7. As such, if the standard deviation of the transient signal were to be used to quantify the uncertainty in the time-averaged h it would significantly over-estimate this uncertainty. Therefore, the uncertainty in the time-averaged heat transfer coefficient is based on the standard deviation of the mean of the temporal distribution in E^2, as well as the calibration uncertainties for the thermocouples and Micro-Foil® sensor uncertainty, as outlined here.

To calculate the standard deviation of the mean of a data population, $\sigma_{\bar{x}}$, the following expression is used

$$\sigma_{\bar{x}} = \frac{\sigma_x}{\sqrt{n}} \tag{5.20}$$

where σ_x is the standard deviation of the population and n is the number of measurements. However, n is the number of discrete measurements, whereas in the time-trace in figure 5.8 the data points are likely to be inter-dependent. Thus it is necessary to estimate this inter-dependence to obtain a value for n. This can be done by considering the autocorrelation of the signal, which is the cross-correlation of the signal with itself and is used to determine similarities between samples. The autocorrelation for the mist jet time-trace voltage in figure 5.8 is shown in figure 5.9. This figure shows that the signal exhibits self-similarity for, on average, a lag of 20 samples. Thus, for a sampling rate of 1000 Hz and measurements over 2.5 seconds, the number of discrete samples in figure 5.8, n, can be estimated to be

$$n = \frac{2500}{20} = 125 \tag{5.21}$$

The standard deviation of the mean, $\sigma_{\bar{x}}$, can now be calculated, with the uncertainty of $\sigma_{\bar{x}}$,

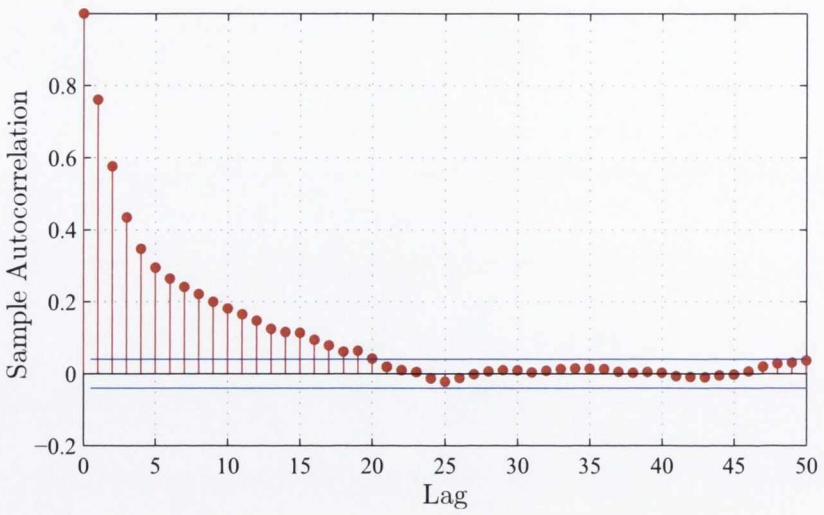

Figure 5.9: Autocorrelation of time-trace of the mist jet hot film sensor voltage squared signal in figure 5.8; mist loading fraction f = 0.003 and Re = 4500

$U_{\sigma_{\bar{x}}}$, given by

$$U_{\sigma_{\bar{x}}} = 2 \times \sigma_{\bar{x}} \tag{5.22}$$

In order to then calculate the total uncertainty in the measurement of the time-averaged heat transfer coefficient, U_h, the calibration uncertainties are required for typical operating values of the jet and Micro-Foil® embedded plate thermocouples, U_{Jet} and U_{Plate} respectively, as well as the Micro-Foil® sensor voltage uncertainty, U_{Micro}. Thus, the total uncertainty for the time-averaged heat transfer coefficient is given by:

$$U_h = \sqrt{U_{\sigma_{\bar{x}}}^2 + U_{Jet}^2 + U_{Plate}^2 + U_{Micro}^2} \tag{5.23}$$

As will be discussed in chapter 7, the temporal heat flux, as indicated by E^2, varies significantly depending on the flow parameters and nozzle-to-plate spacing, and as such, the autocorrelation will also vary, causing $U_{\sigma_{\bar{x}}}$ and hence U_h to change as well. Thus, the maximum uncertainty in the time-averaged heat transfer coefficient was calculated to be U_h = 11.5 %, while the mean uncertainty across the full range of flow parameters was U_h = 8.5 %.

As per section 5.2, the maximum uncertainty in the water flow rate was 3.59 %, while the air Reynolds number uncertainty was 3.9 %. Therefore, the maximum total uncertainty in the

time-averaged heat transfer coefficient is calculated to be

$$\Delta h = \sqrt{10.8^2 + 3.59^2 + 3.9^2} = 12.7\% \tag{5.24}$$

The average across the flow parameter range is 10 %.

Uncertainty in the temporal hot film sensor voltage

Because of the highly chaotic and random nature of the mist jet and its impingement, it is difficult to quantify the uncertainty in the fluctuating hot film sensor voltage signal. Using the standard deviation of the fluctuating signal is likely to overestimate the uncertainty, as these fluctuations are not error but rather are inherent in the flow. The main influence on its uncertainty is likely to be due to uncertainty in the mist jet flow parameters, although error in the sensor resistance calibration against temperature will also contribute. As was the case for the time-averaged heat transfer coefficient, the standard deviation of the mean of the temporal signal could also be used as a means to estimate the voltage uncertainty. Although this provides a conservative estimate, this is the approach that has been taken here, with the standard deviation of the mean being combined with the resistance calibration and pump calibration uncertainties to give a maximum uncertainty of 11.6 % and a mean uncertainty of 8.6 %.

5.4 Uncertainty in Shadowgraph Imaging

As shadowgraph imaging is a direct imaging technique, attempts to quantify the uncertainty associated with data obtained using this technique tend to focus on comparing images of objects of a known size with physical measurements of the object's size [41, 136]. Thus, in this study the uncertainty associated with shadowgraphy measurements depends on the sizing of the water jet nozzle outer diameter, as this was the object of known size used to calibrate the pixel to μm scale, and also on the uncertainty associated with setting this scale itself.

To measure the nozzle diameter, an optical microscope was used, with 10 discrete diameter measurements being taken; the uncertainty associated with this measurement was calculated to be 0.62 %. In terms of setting the pixel to μm scale, errors associated with choosing the correct pixel as the edge of the reference object arose; as a result the scale was set 10 separate

Table 5.2: Experimental uncertainties associated with this investigation

Measurement	Uncertainty %
Re	3.9
R_f	0.63
Q_w	3.59
Δh_{max}	12.7
Δh_{mean}	10
ΔE_{max}	11.6
ΔE_{mean}	8.6

times, with the mean of the 10 being used. The uncertainty associated with this technique was calculated to be 2.06 %. Thus, again using the square root of the sum of the squares of these two measurement uncertainties, the total uncertainty for the shadowgraph data is determined to be 2.16 %. This value is comparable to that of Zhang et al. [41], who used standard particles, GBW(E)120007 produced by the Beijing Research Institute of Chemical Engineering and Metallurgy, to calibrate their system; an uncertainty of approximately 2 % was reported using this method.

In this investigation, custom code developed for the Matlab software package was used to perform droplet detection, rather than the proprietary DaVis software that is used to perform the shadowgraph acquisition. As discussed previously, this was done in order to facilitate improved noise removal, and also to allow more controllability over the output results from the droplet detection. An example of the improvement that was achieved using the custom code can be seen by considering figures 5.10 (a), 5.10 (b), 5.10 (c) and 5.10 (d). A sample raw shadowgraph image is shown in figure 5.10 (a). This image has been processed using the DaVis software for two different sets of options for the particle tracking and filtering: in figure 5.10 (b) the case is shown when the settings are such that almost all of the droplets are detected, but significant surface noise is also included as droplets; some out-of-focal-plane droplets are also detected; in figure 5.10 (c), the filtration settings are such that no surface noise has been included as a droplet, but several actual droplets in the flow have been missed. Figure 5.10 (d) shows the results of using the custom code; it can be seen that the code performs well in terms of detecting droplets while rejecting surface noise. Another advantage of the developed code is that it is able to detect non-spherical droplets, and to calculate their actual size, whereas DaVis assumes a sphere for all calculations of diameter. As well as this,

(a) Raw shadowgraph image

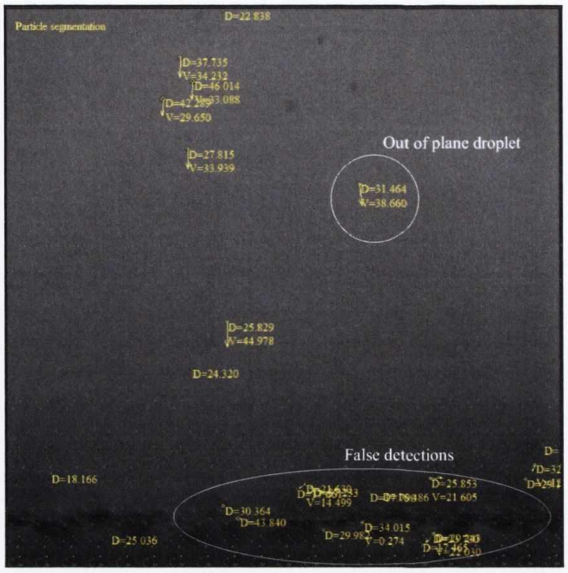

(b) High level of droplet detection using DaVis software

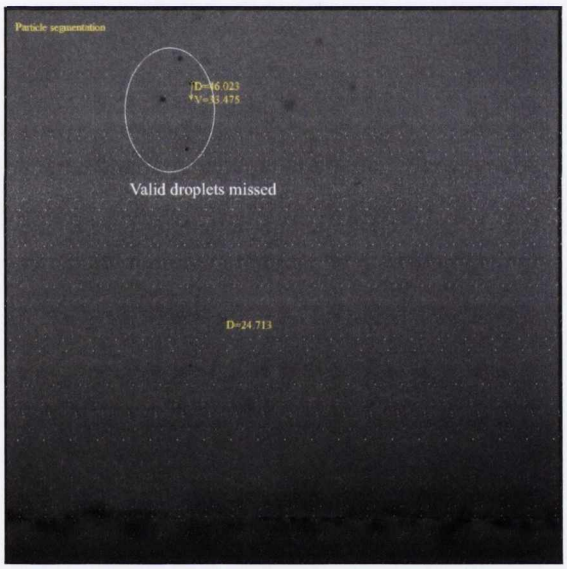

(c) Low level of droplet detection using DaVis software

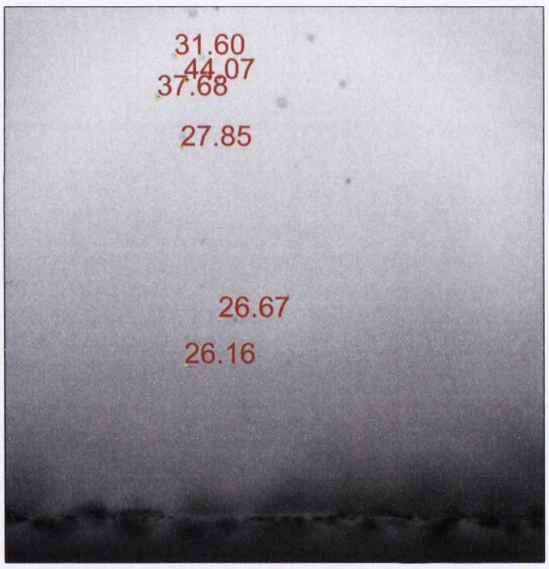

(d) Droplet detection using custom code

Figure 5.10: Different methods for the processing of shadowgraph images

the data output from the DaVis software was in a format not amenable to easy manipulation and data extraction, further strengthening the case to develop the Matlab code.

Chapter 6

Results: Mist Jet Structure

6.1 Introduction

In this chapter, results for the atomisation process and structure of the mist jet, in terms of its droplet properties, are presented and discussed. As well as this, results for the liquid film that forms on the surface due to the impinging mist jet are also analysed. The flow structure results consist of high-speed imagery and droplet properties obtained using shadowgraph imaging.

Several parameters exist that affect the structure of a mist jet and its resulting liquid film. Among these parameters are some which are common to both mist jets and standard air jets such as nozzle-to-plate spacing, H/D, and air jet Reynolds number, Re. For mist jets, the liquid mass fraction, or mist loading fraction, f, is another important parameter, and the Weber number, We, is also pertinent. In this chapter, the effect of these parameters on the mist jet structure is examined in terms of droplet size and velocity

Results are presented for a mist jet at three nozzle-to-plate spacings, $H/D = 2.5, 5, 10$, two different Reynolds numbers, Re = 4500, 7800, for each H/D, and 15 liquid flow rates, Q_w, resulting in 15 different mist loading fractions, f, for each air Reynolds number; the parameters are presented in table 6.1.

This chapter first examines the atomisation behaviour of the mist jet for the parameter range under investigation. Next, the structure of the mist jet in the far-field is considered for the downstream regions associated with the two nozzle-to-plate spacings under investigation. The far-field behaviour is linked to the atomisation region mist jet structure where possible. Finally, local analysis of the behaviour of the liquid that gathers on the impingement surface under the mist jet is performed. The effect of the mist jet structure on the surface liquid and the different morphologies that arise are examined. These analyses are performed with a view

Table 6.1: Flow parameters in this study: water flow rate, Q_w, and corresponding mist loading fractions, f, and momentum flux ratios, M with air Reynolds numbers Re = 4500 and Re = 7800

Q_w [ml/min]	$f_{Re=4500}$	$f_{Re=7800}$	$M_{Re=4500}$	$M_{Re=7800}$
0.035	0.003	0.0017	1.05×10^6	2.54×10^6
0.042	0.0035	0.002	7.39×10^5	1.79×10^6
0.046	0.0039	0.0022	6.02×10^5	1.46×10^6
0.051	0.0043	0.0025	5.01×10^5	1.21×10^6
0.057	0.0049	0.0028	3.9×10^5	9.44×10^5
0.064	0.0054	0.0031	3.13×10^5	7.58×10^5
0.071	0.006	0.0034	2.56×10^5	6.2×10^5
0.087	0.0073	0.0042	1.72×10^5	4.16×10^5
0.1	0.0085	0.0048	1.29×10^5	3.11×10^5
0.107	0.009	0.0052	1.13×10^5	2.73×10^5
0.113	0.0096	0.0055	1×10^5	2.42×10^5
0.158	0.013	0.0077	5.14×10^4	1.24×10^5
0.203	0.017	0.0098	3.12×10^4	7.55×10^4
0.248	0.021	0.012	2.09×10^4	5.07×10^4
0.281	0.024	0.0136	1.62×10^4	3.93×10^4

to obtaining a better understanding of the heat transfer mechanisms of a dilute mist jet, as discussed in chapter 7.

6.2 Atomisation of the Mist Jet

As discussed in section 2.1.2, a coaxial annular air jet provides the energy necessary to atomise the liquid jet. Several authors [22, 23, 30, 31, 33, 35] have presented results on the nature of this atomisation process. However, there is a lack of information for the parameter range considered in this work, i.e. the dilute mist jet, characterised by very low mist loading fractions, f, and very high momentum flux ratios, M (subsequently referred to as the dynamic pressure ratio by Lasheras and Hopfinger [30]). For convenience, their definitions are reshown here.

$$M = \frac{\rho_a U_a^2}{\rho_L U_w^2} \tag{6.1}$$

and

$$f = \frac{\dot{m}_w}{\dot{m}_a} \tag{6.2}$$

where ρ_a and ρ_w are the air and water densities, U_a and U_w the respective velocities and $\dot{m}_a$ and $\dot{m}_w$ the mass flow rates of air and water.

While the annular air jet velocities, Reynolds numbers and mist jet Weber numbers examined in this study are within the range studied previously, the significantly lower liquid flow rates here give rise to lower mass flow ratios (mist loading fractions) and higher momentum flux ratios than those within the literature. In the current study, the mist loading fraction, f, is between 0.0017–0.024 while the momentum flux ratio varies between 1.62×10^4–2.54×10^6, as shown in table 6.1. The studies reported in the literature have not considered the case of the dilute mist jet; typically the mist loading fraction is considerably higher than those under investigation here, and hence the momentum flux ratios are lower than those in this study. For example, in a recent study on the influence of the liquid jet diameter on airblast atomisation, Liu et al. [35] considered mist loading fractions that varied from 0.137 to 15.6, with momentum flux ratios of 0.03 to 36550. Ebgelbert et al. [22] examined a range of flow rates such that $0.37 < f < 2.7$. The very low liquid flow rates that result in the dilute mist jet give rise to correspondingly low liquid jet Reynolds numbers; in this study they range from 3 to 20, with the liquid jet diameter used as the characteristic length. In contrast to this, Lasheras et al. [23] examined liquid Reynolds numbers of the order of 1000, while Varga et al. [31] used values that were between 1700 and 15000; both of these studies also used the liquid jet as the characteristic length.

6.2.1 High-Speed Imagery of Mist Jet Atomisation

Instantaneous high-speed imagery of the atomisation of the mist jet for a range of mist loading fractions is presented in this section. Due to the chaotic nature of airblast atomisation, as reported in section 2.3, somewhat different structures may appear for similar flow conditions. Thus, two examples are included for each representative parameter set to aid understanding. In each figure, (a) and (b) denote the two individual cases. Figures 6.1 to 6.6 show the results for the air jet Reynolds number of 4500, while figures 6.1 to 6.6 relate to the higher Reynolds number of 7800. The same range of liquid flow rates, Q_w, was used for the two Reynolds

numbers, resulting in the different mist loading fractions and momentum flux ratios. In each of these figures, the distance downstream from the nozzle, y, is normalised by the outer air jet diameter, D, as is the radial displacement, r.

The Weber number is defined as per Engelbert et al. [22], Marmottant and Villermaux [33] and Liu et al. [35] as

$$\mathrm{We} = \frac{\rho_a (U_a - U_w)^2 D_w}{\sigma} \tag{6.3}$$

Here D_w refers to the diameter of the water jet, ρ_a the density of the destabilising jet, i.e. the air jet, and σ the surface tension of the water. The Weber number of the mist jet is essentially constant for each air Reynolds number. This is because the air velocity is many orders of magnitude greater than the water velocity. Thus, for Re = 4000 the Weber number is 146 and for Re = 7800 the Weber number is 353.

Considering figures 6.1 to 6.6 for the case of Re = 4500, the atomisation behaviour is clearly different from that reported within the literature, for example by Lasheras and Hopfinger [30]; figure 2.6 in chapter 2 shows a sample of the high-speed imagery reported in that study. Firstly, for the momentum flux ratios considered in this study, there is no initial liquid core; M is sufficiently high that the water jet is atomised as soon as it emerges from the nozzle. Indeed, using the approximate expression of Lasheras et al. [23] for determining the liquid core length, equation 2.10 in section 2.1.2, for the lowest M considered in this study of 16237 for Re = 4500, the liquid core length would be approximately 9×10^{-8} mm. Thus the current parameter range is beyond that for which near-field, or primary atomisation, of a liquid core takes place.

Instead of a liquid core that has an initial diameter that is the same as the liquid jet nozzle, for the current high momentum fluxes and low mist loading fractions it appears that the liquid jet is stretched and deformed by the annular air jet as it emerges from the nozzle. A ligament-like structure is observed extending from the liquid nozzle. As the ligament grows it is exposed to more of the coaxial air jet and it begins to disintegrate, leading to the dispersal of droplets into the mist jet. Potentially, near-field atomisation is taking place on the ligament, with instabilities growing and being drawn out into membranes which are then atomised by the co-flowing air. A formation of this sort of membrane can be seen in figure 6.1 (b). As the ligament moves downstream from the mist jet nozzle it is visibly thinned as droplets are shed.

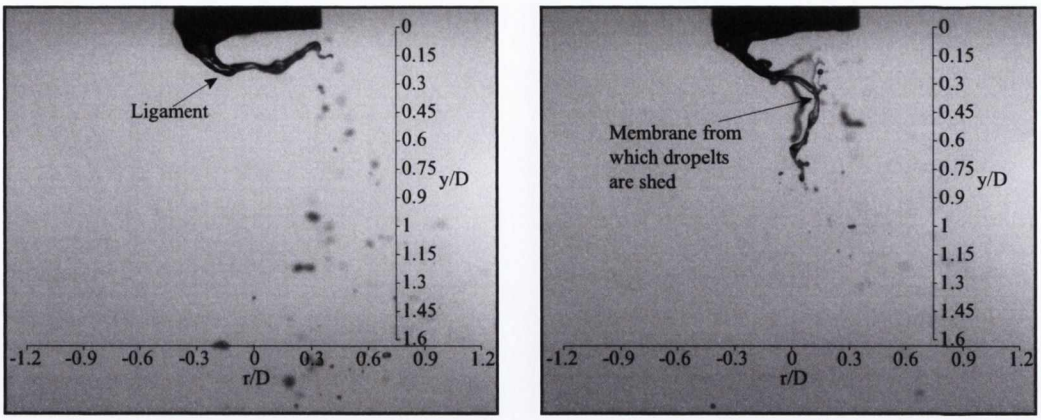

(a) (b)

Figure 6.1: Two cases of mist jet atomisation for Re = 4500, Q_w = 0.035 ml/min, f = 0.003, $M = 1.05 \times 10^6$

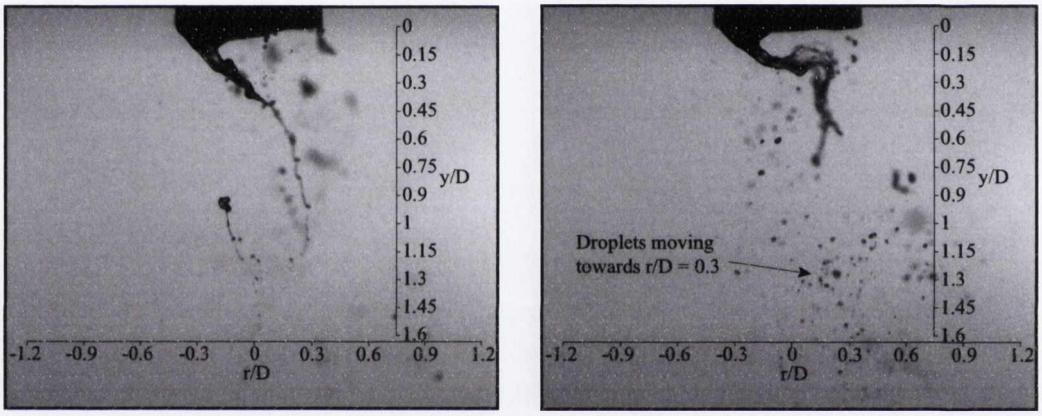

(a) (b)

Figure 6.2: Two cases of mist jet atomisation for Re = 4500, Q_w = 0.051 ml/min, f = 0.0043, $M = 5.01 \times 10^5$.

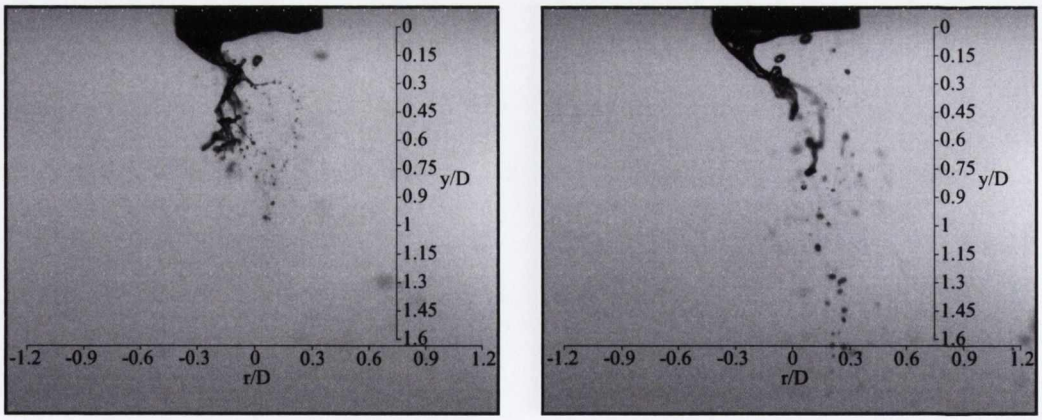

(a) (b)

Figure 6.3: Two cases of mist jet atomisation for Re = 4500, Q_w = 0.071 ml/min, f = 0.006, $M = 2.56 \times 10^5$.

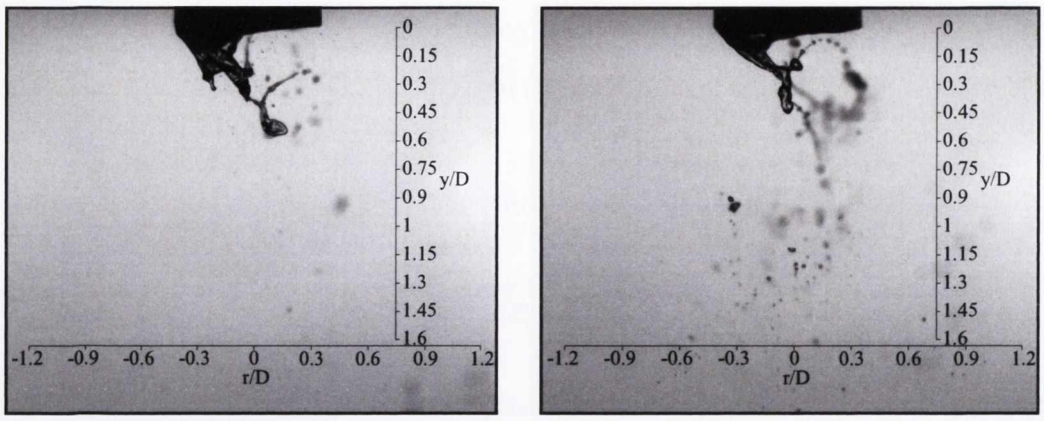

(a) (b)

Figure 6.4: Two cases of mist jet atomisation for Re = 4500, Q_w = 0.107 ml/min, f = 0.009, $M = 1.13 \times 10^5$.

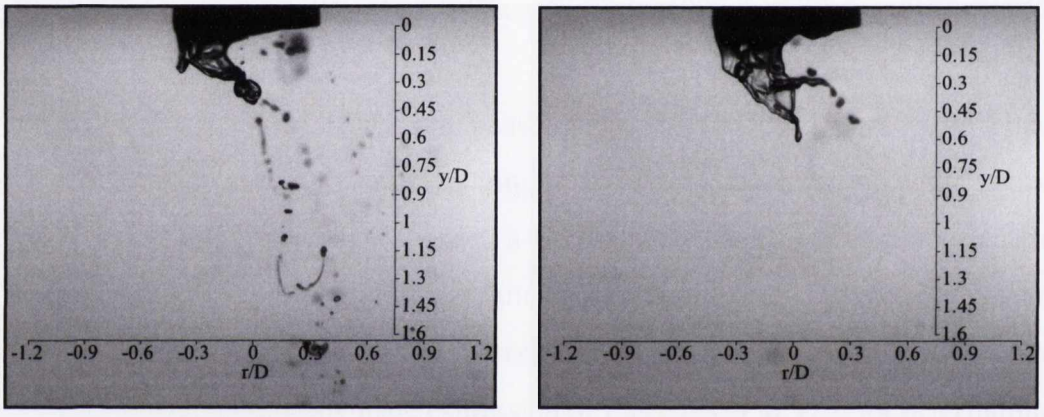

(a) (b)

Figure 6.5: Two cases of mist jet atomisation for Re = 4500, Q_w = 0.203 ml/min, f = 0.017, $M = 3.12 \times 10^4$.

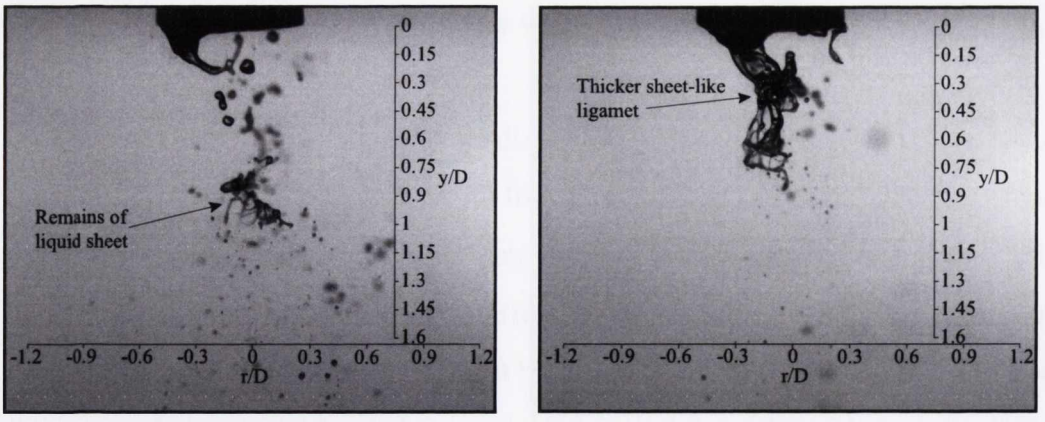

(a) (b)

Figure 6.6: Two cases of mist jet atomisation for Re = 4500, Q_w = 0.281 ml/min, f = 0.024, $M = 1.62 \times 10^4$.

The motion of this extended ligament tends to follow the typical structure for an annular air jet close to the nozzle exit, as described in section 2.3.1. Recirculation zones close to the nozzle exit cause the liquid to turn towards the centreline of the nozzle. Indeed, for the lower values of f, the ligament structure turns back towards the nozzle exit, with some droplets being shed in the opposite direction to the bulk mist jet motion. Section 6.2.4 considers the velocity vectors for this region in more detail. As the ligament extends beyond the recirculation zone, which was observed to end at $y/D \approx 0.5$ by Patte-Rouland et al. [52], of the annular jet, it tends to straighten, though typically away from the nozzle centreline and towards $r/D \approx 0.3$. This can be seen in figures 6.2 and 6.3.

At this Reynolds number of Re = 4500, it is evident that the atomisation of the ligament changes with increasing mist loading fraction, or decreasing momentum flux ratio. As f increases, the ligament tends to become thicker. There is a noted increase in the ligament size from figure 6.1 through to figure 6.5; in the latter case the ligament is now approximately half the width of the liquid jet diameter. As M decreases further, the ligament comes to resemble a sheet of liquid which breaks apart as it moves downstream; this can be seen in figure 6.6 (a), where the remains of the sheet can be seen at $y/D \approx 0.9$. This figure also shows that once the sheet has broken up, the remaining fluid resembles the ligaments for higher M until more fluid feeds the ligament and it once more becomes a sheet. As the mist loading fraction increases and the momentum flux ratio decreases, the transfer of momentum from the air to the liquid will also decrease, allowing the ligament to spread and grow. Eventually, the ligament would reach the size of the liquid jet with the usual liquid jet core forming. It is interesting to note that increasing the mist loading fraction does not appear to lead to an increase in the length of the ligament. The liquid jet core length has been shown to be dependent on the momentum flux ratio, as illustrated by the expression of Lasheras et al. [23], given again here for convenience.

$$\frac{L}{D_L} \approx \frac{6}{\sqrt{M}} \left(\left| 1 - \frac{U_L}{U_a} \right| \right)^{-1} \tag{6.4}$$

That this ligament does not lengthen with decreasing M indicates that it is a flow structure distinct from the liquid core observed for lower momentum flux ratios. It appears that instead the ligament thickness must first increase until it reaches the liquid jet diameter; it is assumed that further increases in mist loading fraction, and hence decreases in M, would be expected

to give rise to the liquid core behaviour reported by Lasheras et al. [30], although this was beyond the parameter range of this investigation

Beyond the ligament, droplets are seen to spread away from the nozzle centreline, although there is a tendency to the opposite side from the ligament, as identified in figure 6.2 (b). The droplets are thrown from the liquid structure as the surface tension of the water in the ligament is overcome by the disturbing action of the air jet. This is less evident as the mist loading fraction increases, corresponding to a decrease in the momentum flux ratio. When this is the case, chunks of the ligament tend to break off, with secondary atomisation, or far-field atomisation, occurring as these chunks are sheared by the action of the air jet. The spread of droplets is more uniform as a result.

Considering now the case when Re = 7800, presented in figures 6.7 to 6.12, the first thing of note is that the ligament structure is less coherent in general due to the increased air velocity and hence higher momentum flux ratio. Thus, instead of droplets being shed from the end of the ligament, or stripped from it as membranes formed, as occurred at a Reynolds number of Re = 4500, here the ligament undergoes violent disintegration in all cases. As well as this, the ligament does not extend as far from the nozzle exit before being completely atomised, reaching $y/D \approx 0.45$ at its longest. The increased energy of the air jet due to its increase in velocity results in the earlier atomisation of the ligament. The rate of instability growth and generation in the liquid increases with increasing M [30] due to the higher air jet kinetic energy. However, as in the results for Re = 4500, the length of the ligament does not change appreciably as the momentum flux ratio decreases with increasing f.

While the length of the water ligament decreases for the higher Reynolds number case, it can still be seen that as the mist loading fraction increases, the ligament spreads in width until at the highest liquid flow rate considered in this study it is approximately half the diameter of the liquid jet nozzle. It is also worth noting that similar mist loading fractions and momentum flux ratios for the two different Reynolds numbers do not result in the same atomisation behaviour, as might have been expected.

Figure 6.13 shows the atomisation of the liquid jet for the two different Reynolds numbers with liquid flow rates that give rise to similar mist loading fractions; despite the similarity in f, the atomisation behaviour is quite different. For the lower Reynolds number case the liquid ligament remains intact at a greater distance downstream from the nozzle exit,

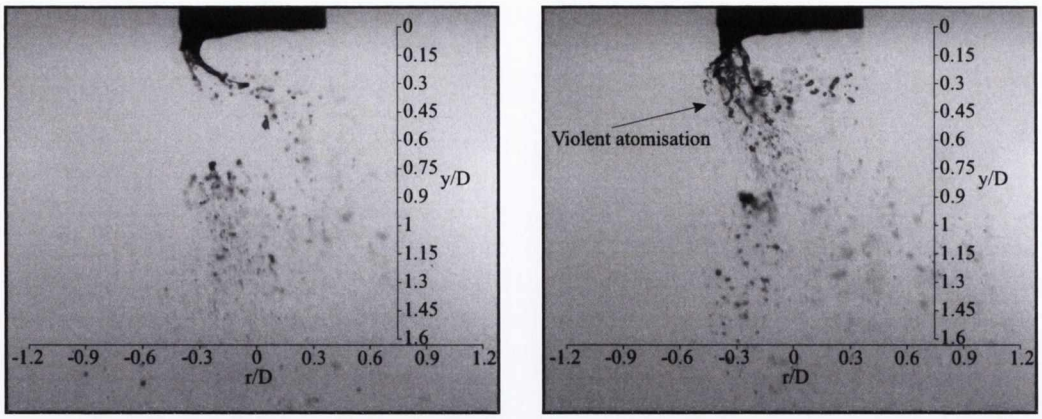

(a) (b)

Figure 6.7: Two cases of mist jet atomisation for Re = 7800, Q_w = 0.035 ml/min, f = 0.0017, $M = 2.54 \times 10^6$.

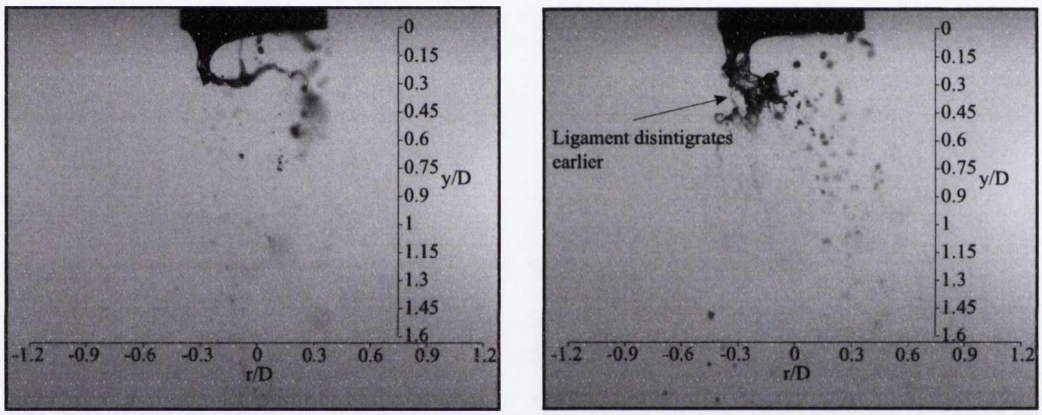

(a) (b)

Figure 6.8: Two cases of mist jet atomisation for Re = 7800, Q_w = 0.051 ml/min, f = 0.0025, $M = 1.21 \times 10^6$.

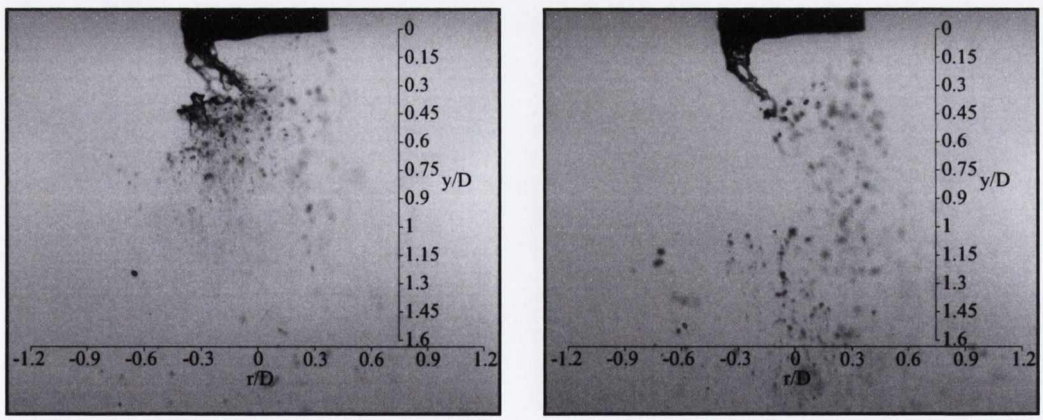

(a) (b)

Figure 6.9: Two cases of mist jet atomisation for Re = 7800, Q_w = 0.071 ml/min, f = 0.0034, $M = 6.2 \times 10^5$.

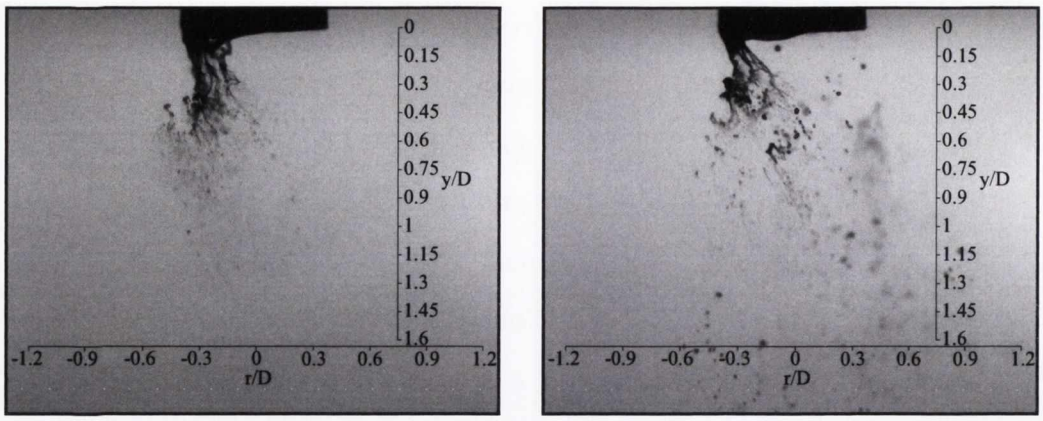

(a) (b)

Figure 6.10: Two cases of mist jet atomisation for Re = 7800, Q_w = 0.107 ml/min, f = 0.0052, $M = 273. \times 10^5$.

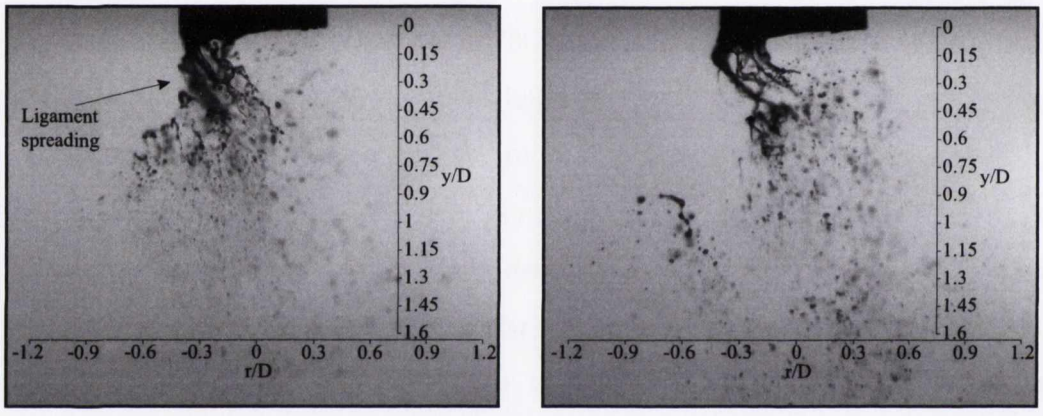

(a) (b)

Figure 6.11: Two cases of mist jet atomisation for Re = 7800, Q_w = 0.203 ml/min, f = 0.0098, $M = 7.55 \times 10^4$.

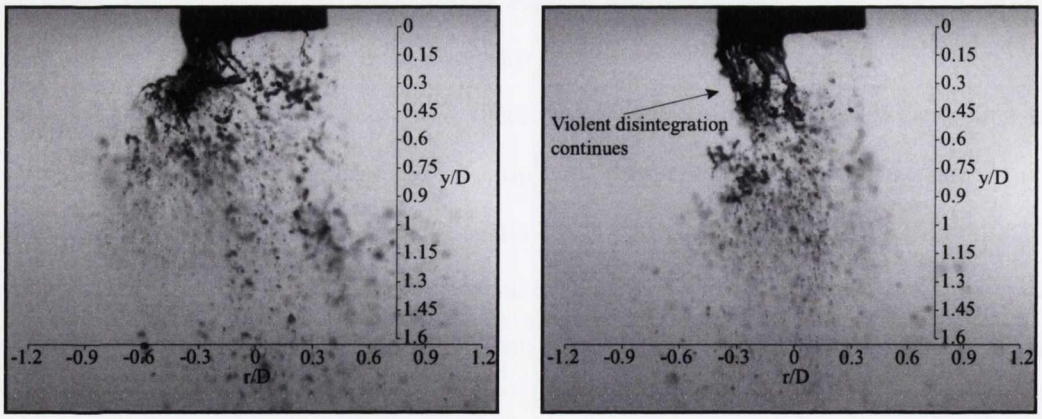

(a) (b)

Figure 6.12: Two cases of mist jet atomisation for Re = 7800, Q_w = 0.281 ml/min, f = 0.0136, $M = 3.93 \times 10^4$.

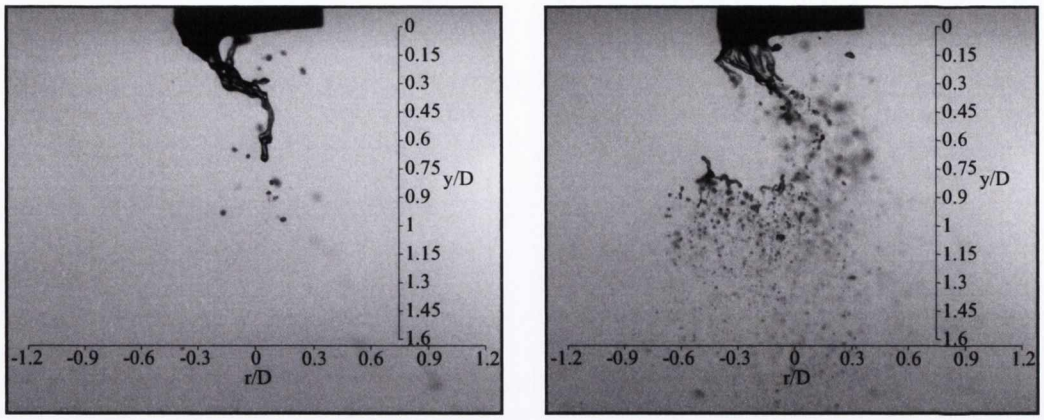

(a) (b)

Figure 6.13: Comparison of mist jet atomisation at similar f for different Re; (a) Re = 4500, Q_w = 0.064 ml/min, f = 0.0054 and $M = 3.13 \times 10^5$ (b) Re = 7800, Q_w = 0.113 ml/min, f = 0.0055 and $M = 2.42 \times 10^5$

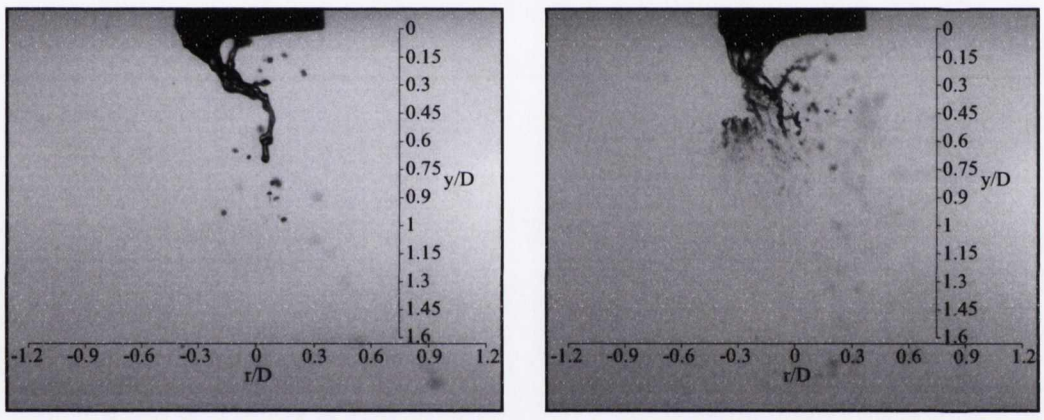

(a) (b)

Figure 6.14: Comparison of mist jet atomisation at similar M for different Re; (a) Re = 4500, Q_w = 0.064 ml/min, f = 0.0054 and $M = 3.13 \times 10^5$ and (b) Re = 7800, Q_w = 0.1 ml/min, f = 0.0048 and $M = 3.11 \times 10^5$

$y/D \approx 0.75$, than for the higher Reynolds number mist jet, $y/D \approx 0.45$. However, the droplets in figure 6.13 (b) do appear to follow a similar path to the intact ligament in figure 6.13 (a). Thus, despite the two similar mist loading fractions, with different momentum flux ratios the ligament is found to be shorter when M is lower. This is contrary to the relationship between the liquid jet core length and momentum flux ratio defined in equation 6.4, where the core length, L, decreases as the momentum flux ratio increases. It appears that when the mist loading fraction is such that a liquid core does not form, the momentum flux ratio is not necessarily the dominant parameter in the length of the liquid ligament-like structure.

If figures 6.13 (a) and (b) are considered in terms of the Weber numbers, as defined in

equation 6.3, for the case when Re = 4500, the Weber number is 146, while for Re = 7800, We = 353. Thus an increase in Weber number coincides with a decrease in the ligament length. Considering the change in liquid jet velocity is very small in comparison to the increase in air jet velocity between figures 6.13 (a) and (b), the increase in Weber number is essentially due entirely to this air jet velocity increase from 153 m/s to 238 m/s, resulting in the slip velocity between the air and liquid streams also increasing. This change in behaviour with Weber number would indicate that for very low f, the atomisation mechanism is mainly secondary, or far-field, atomisation; as discussed in section 2.1.2, such Weber number dependence has been observed for this atomisation regime [23, 30]. Thus, the atomisation of the liquid jet in this low mist loading fraction range appears to be caused by far-field shear break-up, as described in section 2.1.2. This is in contrast to results for higher mist loading fractions where a liquid core is subjected to near-field atomisation in the form of a build-up in surface instabilities leading to droplet shedding, as discussed in section 2.1.2.

Figures 6.14 (a) and (b) show two different Reynolds numbers and liquid flow rates that result in similar momentum flux ratios of $M = 3.13 \times 10^5$ and $M = 3.11 \times 10^5$. Despite the similar momentum fluxes, the ligament structures are quite different, with the higher Reynolds number leading to a shorter, more chaotic and violently atomised ligament structure than the lower Reynolds number. However, the structures bear more of a resemblance when the momentum flux is similar than when the mist loading fraction is, as shown in figure 6.13. This suggests that the momentum flux is a more important parameter than the mist loading fraction in terms of the atomisation behaviour in this parameter space. Again, these images suggest that the increase in the slip velocity, and hence the Weber number, is the dominant parameter in determining the atomisation behaviour for these low f values. This Weber number dependence under similar momentum flux ratios serves to support the hypothesis that the atomisation that the liquid jet is undergoing is what has been termed far-field atomisation within the literature [23, 30]. High-speed flow visualisation across the range of parameters in figure 6.1 were consistent with the sample data presented here and support this conclusion.

6.2.2 Droplet Size in Mist Jet Atomisation Region

Using the shadowgraph imaging method described in chapter 4, data on the droplet size in the atomisation region of the mist jet have been obtained. The droplet sizes are presented here in terms of both the Sauter mean diameter, $D_{3,2}$, and the arithmetic mean diameter, $D_{1,0}$, the definitions of which are shown here again.

$$D_{3,2} = \frac{\sum n_i d_i^3}{\sum n_i d_i^2} \tag{6.5}$$

$$D_{1,0} = \frac{\sum n_i d_i}{\sum n_i} \tag{6.6}$$

As discussed in section 2.2, the Sauter mean diameter is the droplet diameter that has the same ratio of volume to surface area as that of the whole mist jet In other words, it is a measure of the fineness of the mist; a lower SMD indicates a finer mist. Thus it is pertinent in this discussion on the atomisation of the mist jet as it shows the level to which the liquid jet has been atomised. The arithmetic mean diameter is also used as it allows for comparisons based purely on the number of droplets detected without weighting the mean towards larger droplets, as is the case for $D_{3,2}$.

Figure 6.15 shows the average droplet diameters for varying mist loading fraction and momentum flux rations at Re = 4500 for the same area as in the high speed images in figures 6.1 through 6.12, i.e. $-1.2 < r/D < 1.2$ and $0 < y/D < 1.6$; this is referred to here as the full atomisation region. In figure 6.16, however, the mean droplet diameters are for $y/D < 0.4$, which is within the initial liquid jet break-up zone and is referred to as the nozzle exit region. In general, both the Sauter mean and the arithmetic mean diameters are seen to decrease as the mist loading fraction increases whereas the droplet sizes increase as the momentum flux ratio increases, although asymptotically. This behaviour is contrary to the findings of Lasheras et al. [23], who reported that $D_{3,2}$ increased with liquid velocity. However, Lasheras et al. [23] did not measure $D_{3,2}$ in the region at the nozzle exit; the data reported were for y/D greater than 7. Also, as described above the atomisation regime in the current study is very different from the work of Lasheras et al. [23], with lower mist loading fractions and momentum flux ratios being investigated here. This may affect the droplet size

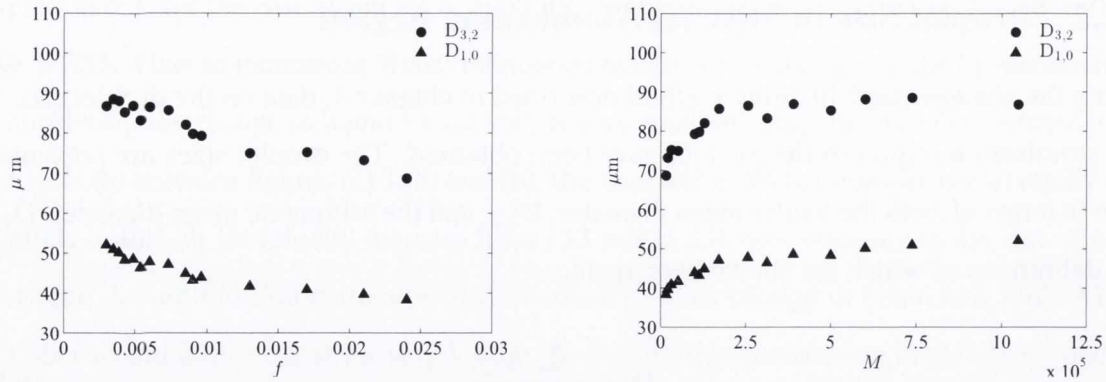

Figure 6.15: Sauter mean and arithmetic droplet diameters across the same area as high-speed imagery for Re = 4500; (a) increasing f and (b) increasing M

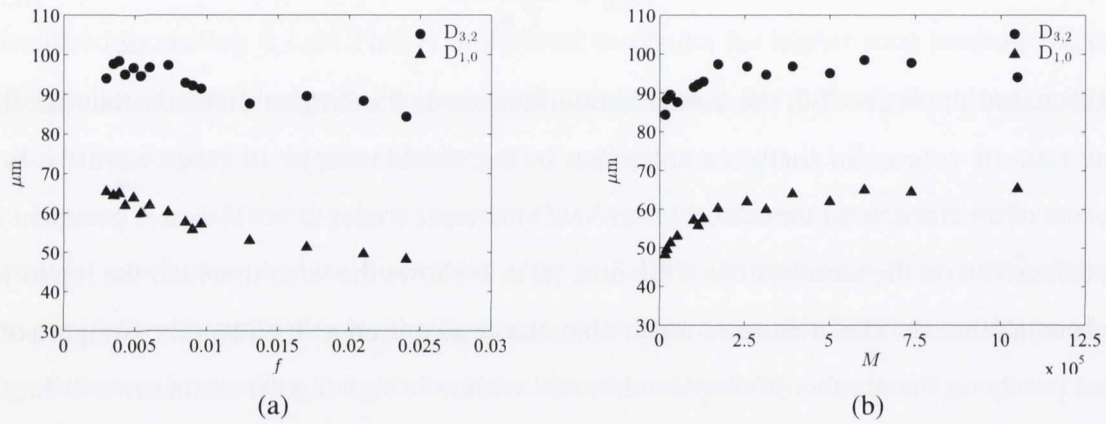

Figure 6.16: Sauter mean and arithmetic droplet diameters at nozzle exit, $0 < y/D < 0.4$ for Re = 4500; (a) increasing f and (b) increasing M

variations appreciably, as the atomisation process is different.

Examining the droplet size number distributions that correspond to the flow rates in figures 6.15 and 6.16 provides an insight into the behaviour of the mean droplet diameters. These distributions are presented in figures 6.17 and 6.18 for a representative sample of the mist loading fractions tested; the same mist loading fractions are considered here as in the high-speed imagery shown in figures 6.1 to 6.12. Figure 6.17 represents the distributions across the full atomisation region, corresponding to figure 6.15; figure 6.16 corresponds to the smaller nozzle exit region as in figure 6.16. For clarity, the locations of the Sauter mean and arithmetic mean diameters are marked on each distribution.

From figures 6.17 and 6.18, it can be seen that as the mist loading fraction increases the number of droplets detected also rises, as the volume of liquid available for atomisation has

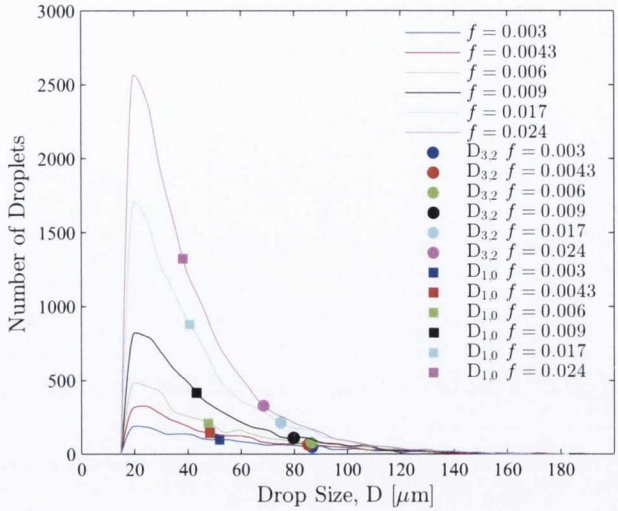

Figure 6.17: Number distributions of droplet diameter in the region $y/D < 1.6$, corresponding to figure 6.15, Re = 4500

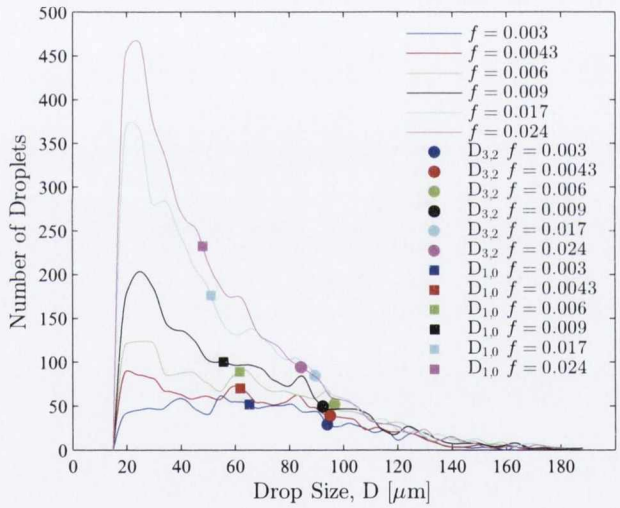

Figure 6.18: Number distributions of droplet diameter in the region $y/D < 0.4$ corresponding to figure 6.16, Re = 4500

increased. However, this increase in the number of droplets is not uniform across all droplet sizes. It is clear that there is a stronger increase in the number of smaller droplets being detected at higher mist loading fractions. For the lower mist loading fractions of $f = 0.003$ and $f = 0.0043$, the number of droplets detected varies little across the size range from 20 to 100 µm, especially close to the nozzle exit (figure 6.18). As f increases, the number of droplets in the range of 20 to 40 µm rises significantly. The droplet size with the peak in droplet number varies little with increasing mist loading fraction. Thus, as the liquid flow rate, and hence the mist loading fraction, increases, the presence of greater numbers of

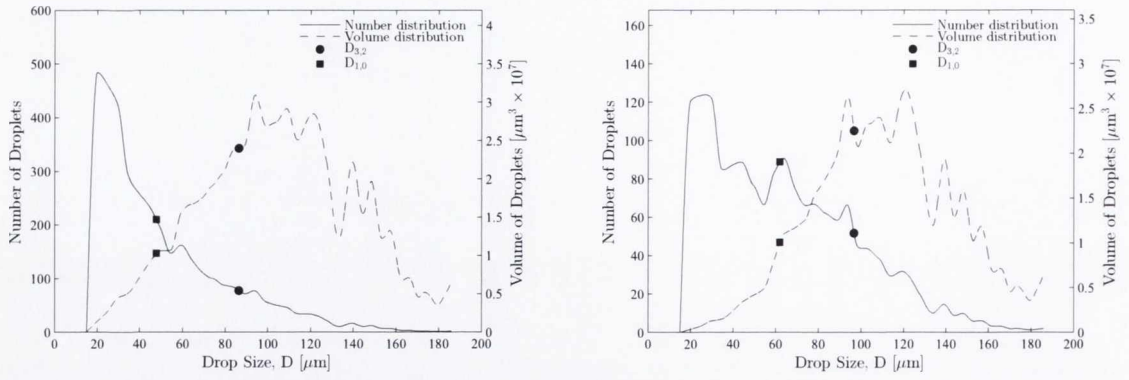

(a) (b)

Figure 6.19: Number and volume distributions of droplet diameter for Re = 4500 and f = 0.006 in (a) the full atomisation region and (b) the nozzle exit region

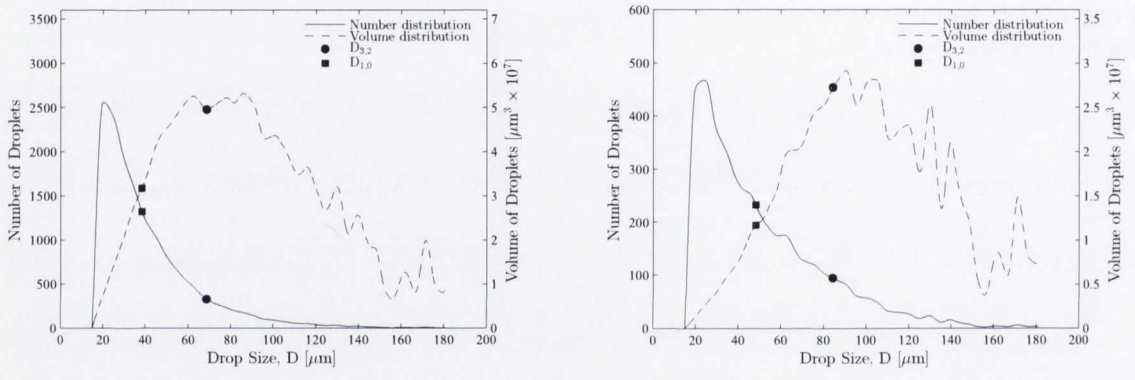

(a) (b)

Figure 6.20: Number and volume distributions of droplet diameter for Re = 4500 and f = 0.024 in (a) the full atomisation region and (b) the nozzle exit region

smaller droplets leads to a finer mist, with a greater fraction of the liquid volume comprising of these smaller droplets. This in turn gives rise to the decreasing Sauter mean diameter with increasing mist loading fraction.

To illustrate this further, in figures 6.19 and 6.20 the volume distributions are shown simultaneously with the diameter distributions for mist loading fractions of f = 0.006 and f = 0.024. Comparing the two cases, when the mist loading fraction is higher (figure 6.20) the volume distribution is across a broader range of droplet sizes, with a higher fraction of the mist volume being comprised of the smaller droplets; this is true for both the nozzle exit and the full atomisation regions.

The decrease in mean droplet size observed here may be explained by considering the Weber number of the mist jet. As identified in section 6.2.1, in this investigation, the range

of liquid flow rates are significantly smaller than the air flow rates, such that although the mist loading fraction and momentum flux ratios change by appreciable amounts, the Weber number, as defined in equation 6.3, changes negligibly for a given Reynolds number. Since the Weber number is essentially constant with increasing mist loading fraction, the resistive surface tension force does not increase, as the Weber number is the ratio of the destabilising air inertial forces to the restorative liquid surface tension. As discussed in section 6.2.1, in the parameter range under investigation the atomisation behaviour predominantly resembles far-field atomisation, which is driven by shear between the air flow and liquid droplets and dependent on the Weber number. The constant Weber number implies that the atomisation behaviour is not changing with increasing f. Rather, there is more liquid available to atomise, leading to an increase in the number of similarly sized small droplets being stripped from the liquid jet, thus lowering the mean droplet size. This is reflected in figures 6.17 and 6.18, where a clear increase in the number of droplets detected is observed for increasing mist loading fraction, with the peak not occurring at different droplet sizes. For the peak to change location, the Weber number, and hence the atomisation behaviour, would have to change.

The Sauter and arithmetic mean diameters for the higher Reynolds number of 7800 are shown in figures 6.21 and 6.22, again for both the full atomisation region and the nozzle exit region respectively. Here again $D_{3,2}$ and $D_{1,0}$ decrease with increasing f and increase with increasing M, with larger average droplet sizes at the nozzle exit than in the full atomisation region. The droplet size distributions shown in figures 6.23 and 6.24 for this higher Reynolds number case display the same behaviour as at the Reynolds number of 4500, with increasing mist loading fractions resulting in an increase in the amount of smaller droplets, but without the peak number in droplet size varying. This points to the same explanation for the decrease in mean droplet size with increased mist loading fraction as before; the atomisation behaviour does not change, but instead a larger number of small droplets are stripped from the emerging liquid jet. Simultaneous size and volume distributions in figure 6.25 and 6.26 for $f = 0.0034$ and $f = 0.0136$ respectively at Re = 7800 again show that for the higher mist loading fraction the volume distribution is broader with a larger portion of it made up of smaller droplets.

Comparing the two Reynolds number cases, the average droplet size is smaller for Re = 7800 than Re = 4500, even for similar mist loading fractions. For clarity, the Sauter and arithmetic mean diameters, respectively for the two different Reynolds numbers, are shown

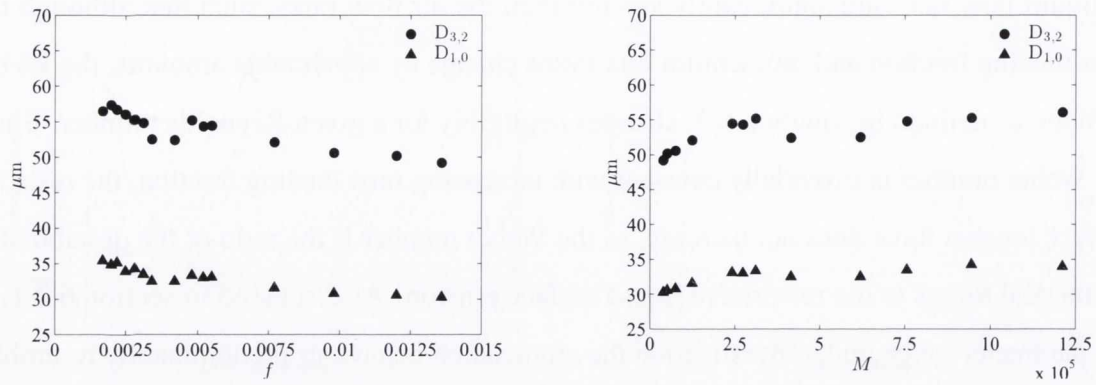

(a) (b)

Figure 6.21: Sauter mean and arithmetic droplet diameters across the same area as high-speed imagery for Re = 7800; (a) increasing f and (b) increasing M

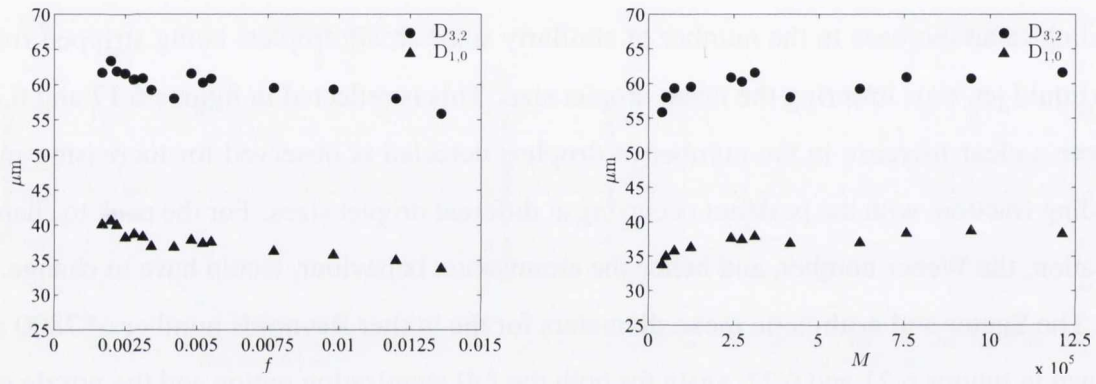

(a) (b)

Figure 6.22: Sauter mean and arithmetic droplet diameters at nozzle exit, $0 < y/D < 0.4$ for Re = 7800; (a) increasing f and (b) increasing M

in the same plots in figures 6.27 and 6.28. This serves to show once more that the Weber number is the controlling parameter for the range of mist loading fractions considered in this study and that the break-up mechanism is most similar to that of far-field atomisation. In the range of $80 < We < 2 \times 10^4$, Lasheras and Hopfinger [30] describe the atomisation as occurring due to ligaments being stripped from the surface of the liquid and disintegrating into small droplets, decreasing in size with We. This is reflected in the behaviour of the mean droplet diameters observed in this investigation.

6.2.3 Local Droplet Distributions in the Mist Jet Break-Up Region

While the mean droplet diameters in the atomisation region vary with mist loading fraction and Reynolds number, droplet sizes and the number of droplets detected will also vary for different

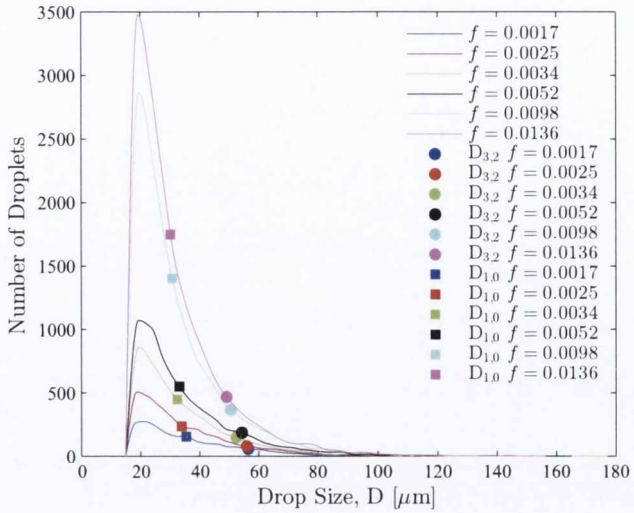

Figure 6.23: Number distributions of droplet diameter in the full atomisation region, Re = 7800

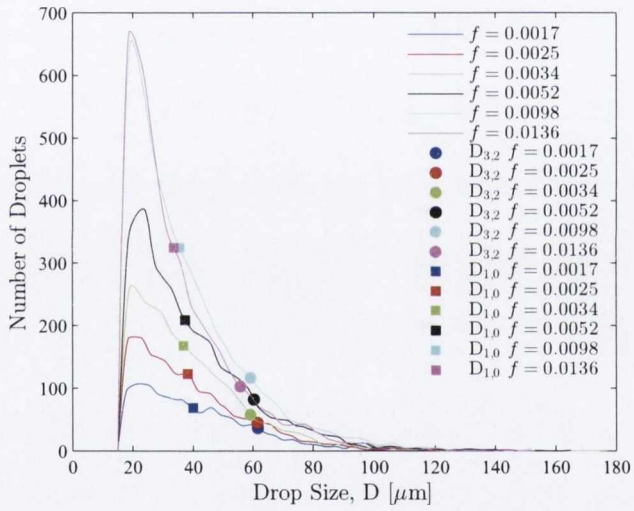

Figure 6.24: Number distributions of droplet diameter in the nozzle exit region, Re = 7800

locations downstream from the nozzle exit within the mist jet atomisation region. These distributions are examined in this section. Here, and in subsequent sections, a specific y/D refers to the mean of the droplet size measurements up to that y/D location, i.e. $y/D = 0.2$ takes into account the droplets in the range $0 < y/D \leq 0.2$, $y/D = 1.2$ represents the region $1.0 < y/D \leq 1.2$ and so on.

The variation in Sauter and arithmetic mean diameters with increasing downstream distance from the nozzle exit for Re = 4500 are shown in figures 6.29 and 6.30 respectively. There is more variability in the Sauter mean diameter data with f, which is most likely due to the fact that $D_{3,2}$ is weighted towards larger droplets, so the presence of a small number of

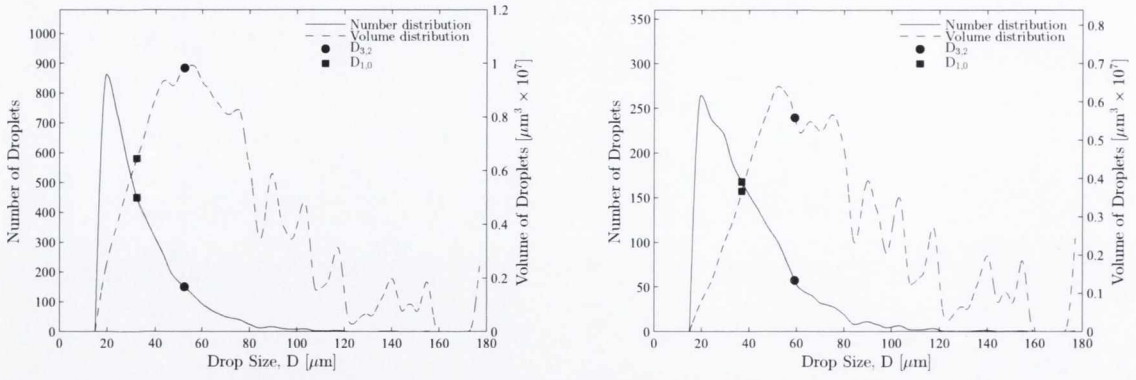

(a) (b)

Figure 6.25: Number and volume distributions of droplet diameter for Re = 7800 and f = 0.0034 in (a) the full atomisation region and (b) the nozzle exit region

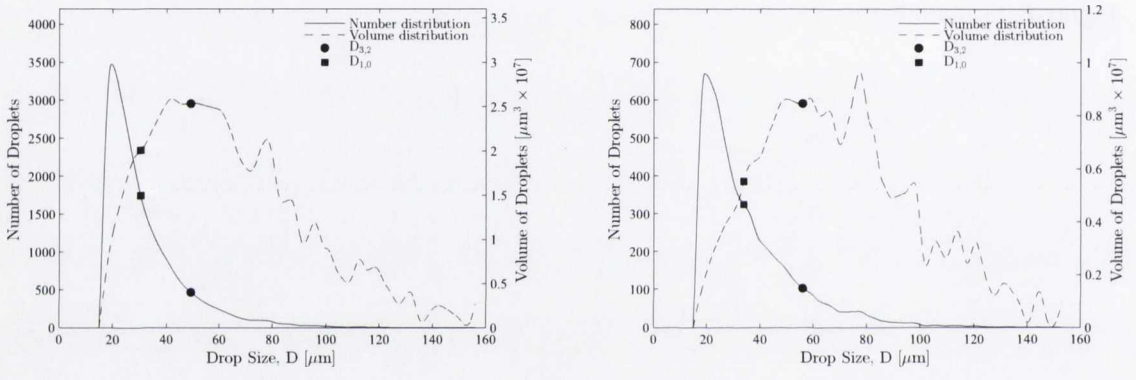

(a) (b)

Figure 6.26: Number and volume distributions of droplet diameter for Re = 7800 and f = 0.0136 in (a) the full atomisation region and (b) the nozzle exit region

much larger droplets, which still exist this close to the nozzle exit, can disturb the results. Thus while $D_{3,2}$ is a good means of examining the "fineness" across the whole mist jet or across large regions within the mist, it does not capture well the mean size of the droplets within smaller regions; for this the arithmetic mean can be used.

As the mist jet moves downstream from the nozzle exit, the mean droplet size, $D_{1,0}$, decreases across all liquid flow rates, rapidly at first when $y/D < 1$ before tending towards a minimum value between 30 and 35 μm. As the liquid droplets move downstream, resulting in increased exposure to the air jet, larger droplets are subject to shear action from the air jet and tend to atomise further into smaller droplets, decreasing the average droplet size. As the mist jet moves downstream, it also becomes more uniform, as evidenced by the decrease in the standard deviation in droplet diameters, D_σ, downstream distance,a shown in figure 6.31. In

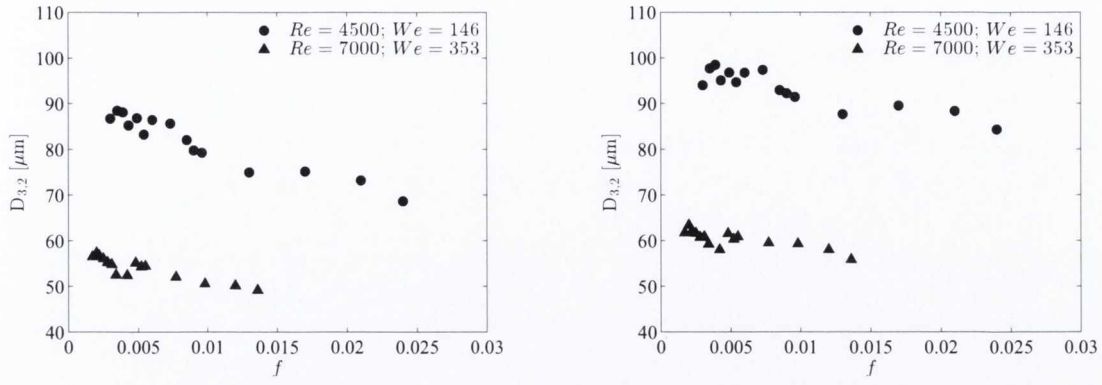

Figure 6.27: Comparison of $D_{3,2}$ behaviour as a function of mist loading fraction for Re = 4500 and We = 146, and Re = 7800 and We = 353; (a) full atomisation region and (b) nozzle exit region

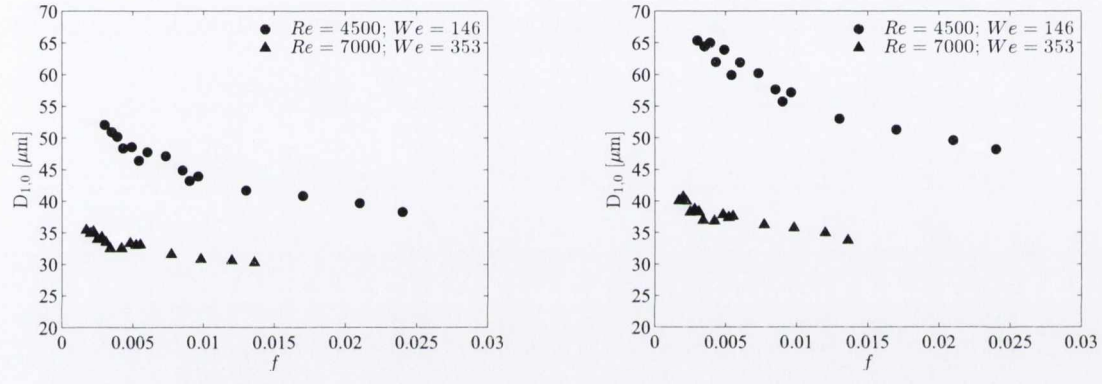

Figure 6.28: Comparison of $D_{1,0}$ behaviour as a function of mist loading fraction for Re = 4500 and Re = 7800; (a) full atomisation region and (b) nozzle exit region

terms of the mean diameter variation with f as the mist jet moves downstream, as the distance from the nozzle increases the arithmetic means for the different mist loading fractions tends towards each other. This can be seen in figure 6.30. This implies that, despite the different initial atomisation, as seen in section 6.2.1, the mist jet becomes more uniform as it moves downstream when Re = 4500.

The number of droplets detected for increasing y/D is shown in figure 6.32. The number of droplets detected decreases initially with increasing y/D across all bar the highest mist loading fractions examined here. This is likely due to the droplets moving out of the narrow focal plane of the image detection system, either towards or away from the camera, as the mist jet spreads with movement downstream from the nozzle exit. For the three higher mist loading fractions, $f = 0.009, 0.017$ and 0.024, the number of droplet detected reaches a

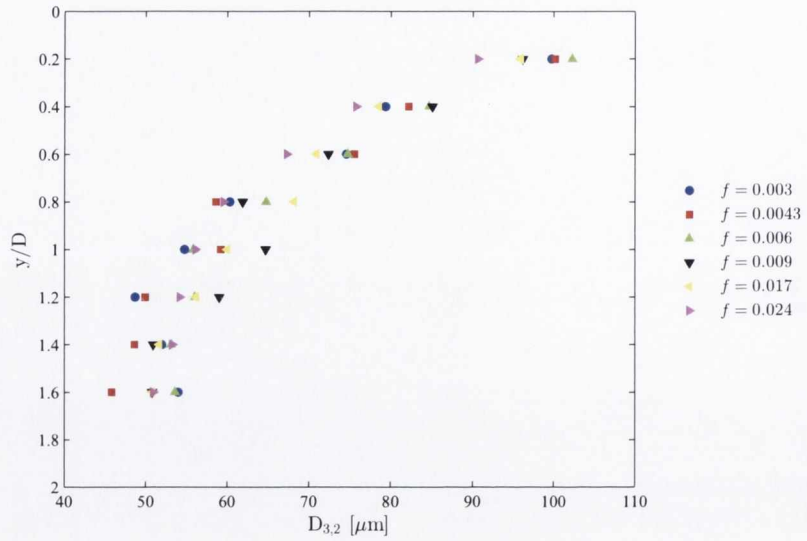

Figure 6.29: Sauter mean diameter, $D_{3,2}$, as a function of y/D for different mist loading fractions and Re = 4500

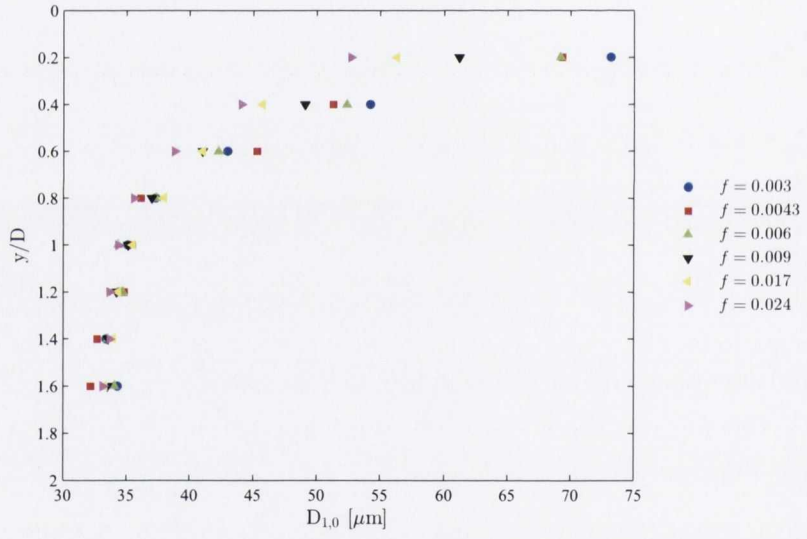

Figure 6.30: Arithmetic mean diameter, $D_{1,0}$, as a function of y/D for different mist loading fractions and Re = 4500

minimum at $y/D \approx 1.2$ before increasing again. This is most likely as a result of larger droplets undergoing secondary atomisation and breaking up into smaller droplets, which resulted in the decrease in the mean droplet size with y/D as seen in figure 6.30. For the highest mist fraction, $f = 0.024$, the number of droplets detected does not decrease initially but rather undergoes a slight increase; as there is more liquid available to atomise, more droplets are being generated, countering the decrease due to outward spreading that is seen in the lower mist loading fractions.

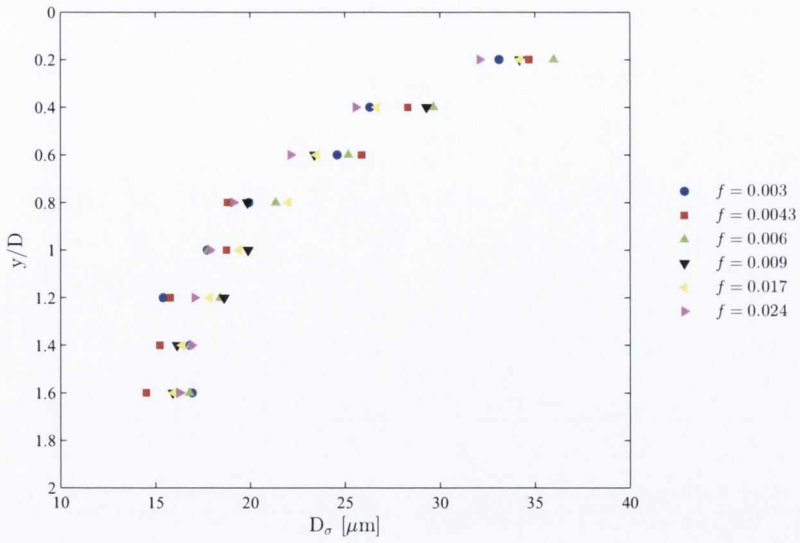

Figure 6.31: Standard deviation in droplet size, D_σ, as a function of y/D for different mist loading fractions and Re = 4500

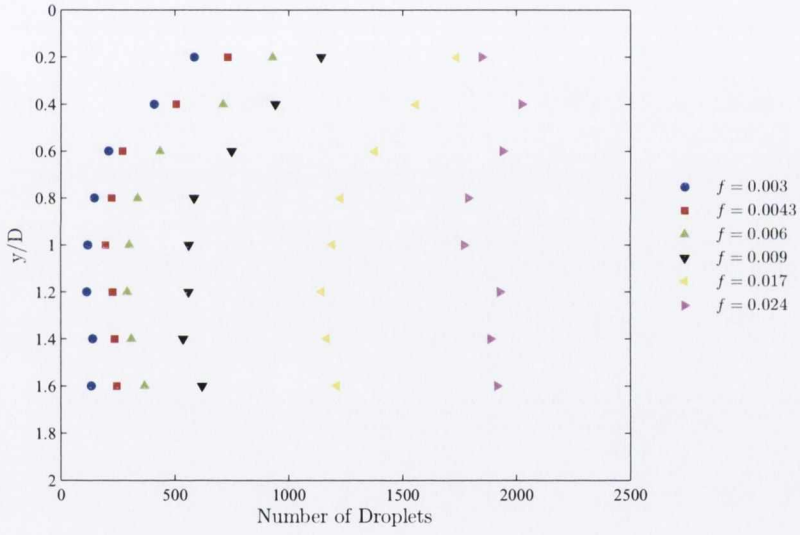

Figure 6.32: Number of droplets detected as a function of y/D for different mist loading fractions and Re = 4500

The droplet size behaviour as the mist jet moves downstream for the higher Reynolds number of Re = 7800 is similar. Figures 6.33 and 6.34 show the behaviour of the Sauter and arithmetic mean droplet diameters respectively. Again, as the mist jet moves downstream, the droplet sizes decrease, and to a greater degree than for Re = 4500 due to the higher Weber number from the higher air velocity, as discussed above. This can be seen in the trends plotted for both $D_{3,2}$ and $D_{1,0}$. Lasheras and Hopfinger [30] reported that for higher Reynolds numbers, of the order of 10^4 or 10^5, velocity fluctuations in the air jet on the scale of the droplet diameters due to turbulent stresses can cause dynamic pressure forces in the droplet

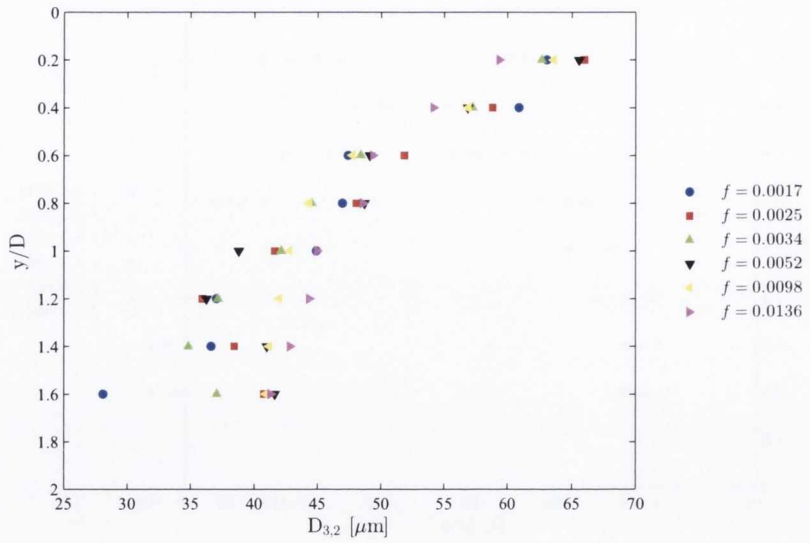

Figure 6.33: Sauter mean diameter, $D_{3,2}$, as a function of y/D for different mist loading fractions and Re = 7800

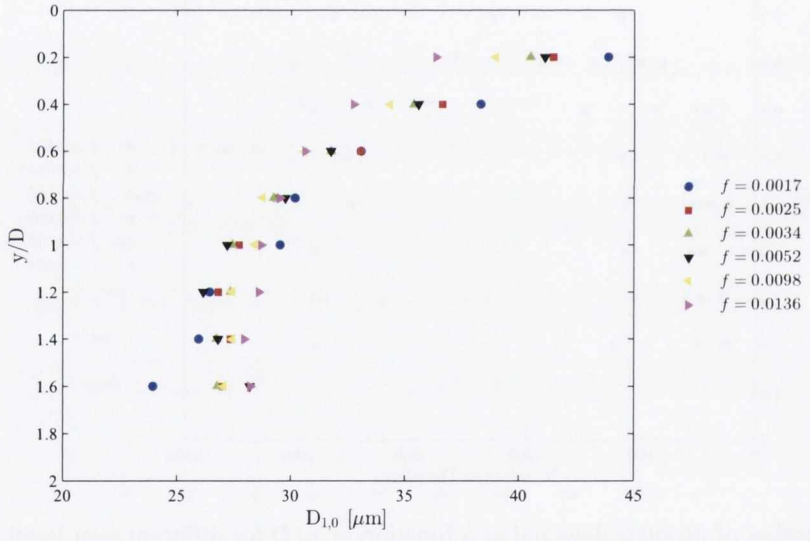

Figure 6.34: Arithmetic mean diameter, $D_{1,0}$, as a function of y/D for different mist loading fractions and Re = 7800

sufficient to overcome its viscosity. Though the Reynolds number here is lower than the range investigated by Lasheras and Hopfinger [30], this turbulent break-up mechanism may be contributing to the atomisation of the droplets as they move downstream. A variation in this mechanism with mist loading fraction, may contribute to the increased spread in droplet sizes for the same y/D that is observed for Re = 7800.

The droplet size standard deviation, D_σ, at different downstream locations in the mist jet is shown in figure 6.35 for the Reynolds number of Re = 7800. As for Re = 4500, D_σ decreases

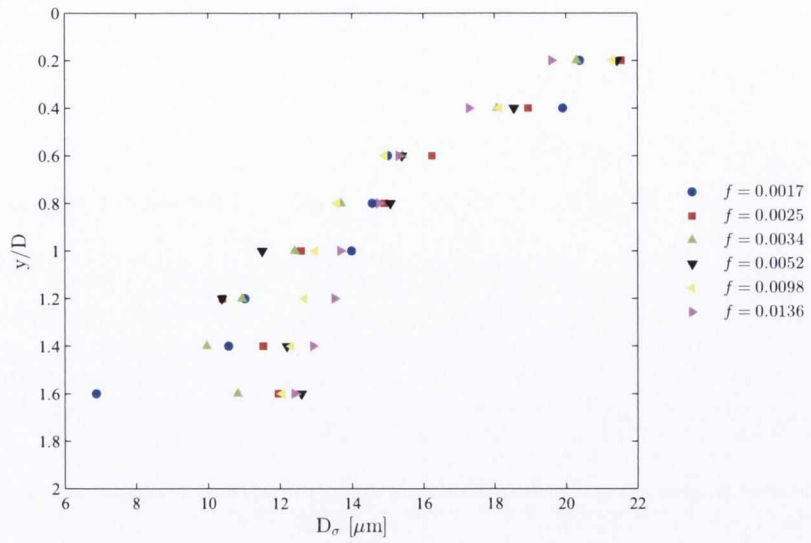

Figure 6.35: Standard deviation in droplet size, D_σ, as a function of y/D for different mist loading fractions and Re = 7800

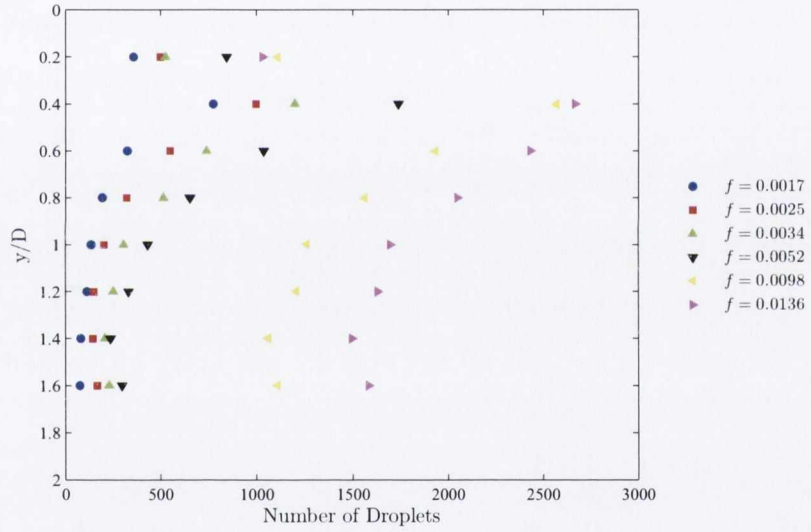

Figure 6.36: Number of droplets detected as a function of y/D for different mist loading fractions and Re = 7800

as the mist moves downstream, indicating that the mist jet is becoming more uniform in terms of droplet size. Indeed, the standard deviation is less here than when Re = 4500, although as the droplet sizes are also lower this does not necessarily point to more uniformity in droplet size for this Reynolds number.

The number of droplets detected in different downstream regions of the mist jet for Re = 7800 is presented in figure 6.36. For all mist loading fractions, as y/D initially increases from 0.2 to 0.4, the number of detected droplets increases to a maximum before decreasing again as the jet moves downstream, with this increase becoming more significant

with increasing f. This contrasts with the Re = 4500 case, where the maximum number of droplets detected was at $y/D = 0.2$ for all but the highest mist loading fraction. This difference in behaviour can be explained by considering the high speed images of the mist jet atomisation that were shown in section 6.2.1; for all f in the higher Reynolds and Weber number case, some level of violent disintegration of the liquid jet is observed to occur at $y/D \approx 0.45$, with little atomisation occurring before this. In contrast, no such disintegration of the water jet is seen for the lower Reynolds number mist jet, with the ligament tending to be stretched and then broken apart, rather than undergoing disintegration. As the mist jet moves downstream the droplets spread outwards; this jet spreading is more significant for the higher Reynolds number, giving rise to the lower number of droplets detected downstream from the nozzle exit than when Re = 4500.

With regards to the radial behaviour of the mist jet droplets in the atomisation region, the highly random and chaotic nature of the atomisation process means that it is difficult to determine any radial trends in droplet size in the atomisation region with a good degree of certainty. Within the literature, measurements of the radial behaviour of the droplets have not been produced for downstream locations less than 6 diameters for this reason [22, 23]. Further investigation, potentially at a higher camera frame rate than was possible under the current experimental set-up may shed further light on this aspect of the atomisation of the dilute mist jet.

6.2.4 Droplet Velocity in the Mist Jet Break-Up Region

The same shadowgraphy data that were used to determine droplet sizes in section 6.2.2 can be used to calculate the velocity vectors of droplets in the atomisation region of the mist jet used in this study. The velocity vectors for both the full atomisation and nozzle exit regions are presented in this section. Radial and axial distributions corresponding to the vector plots are also given.

Velocity vectors in the full atomisation region

Figures 6.37 and 6.38 show the velocity vectors for the full atomisation region for Re = 4500 and Re = 7800 respectively, across the same representative sample of mist loading fractions as the high speed images in figures 6.1 to 6.12.

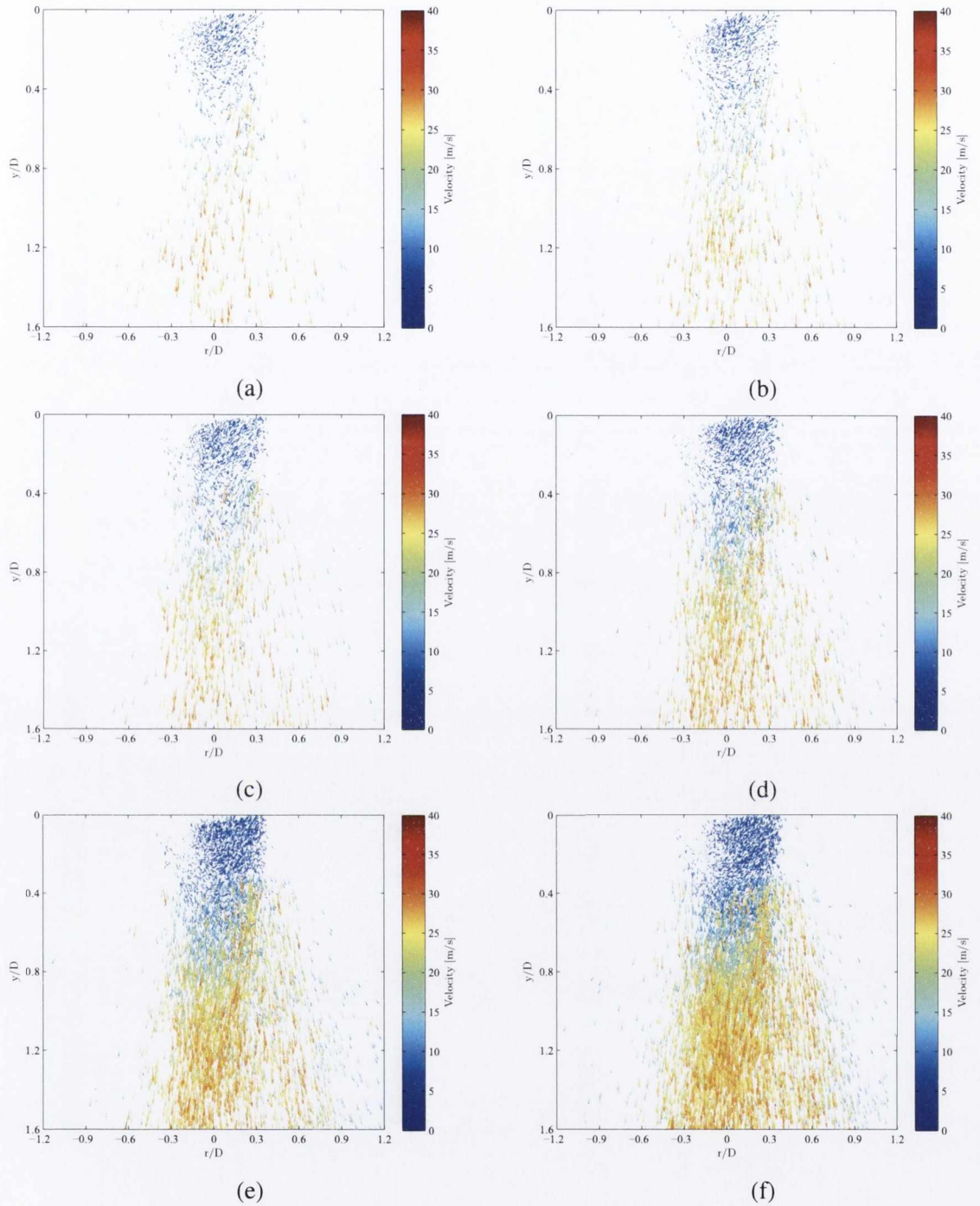

Figure 6.37: Velocity vectors in the full atomisation region for Re = 4500 and (a) f = 0.003, (b) f = 0.0043, (c) f = 0.006, (d) f = 0.009, (e) f = 0.017 and (f) f = 0.024

In figure 6.37, the fact that higher mist loading fractions result in more droplets is reflected in the higher number of vectors visible as f increases. For all mist loading fractions, the droplets accelerate as they move downstream from the nozzle exit and undergo more of a transfer of momentum from the air to the water. Within the nozzle exit region there is a core

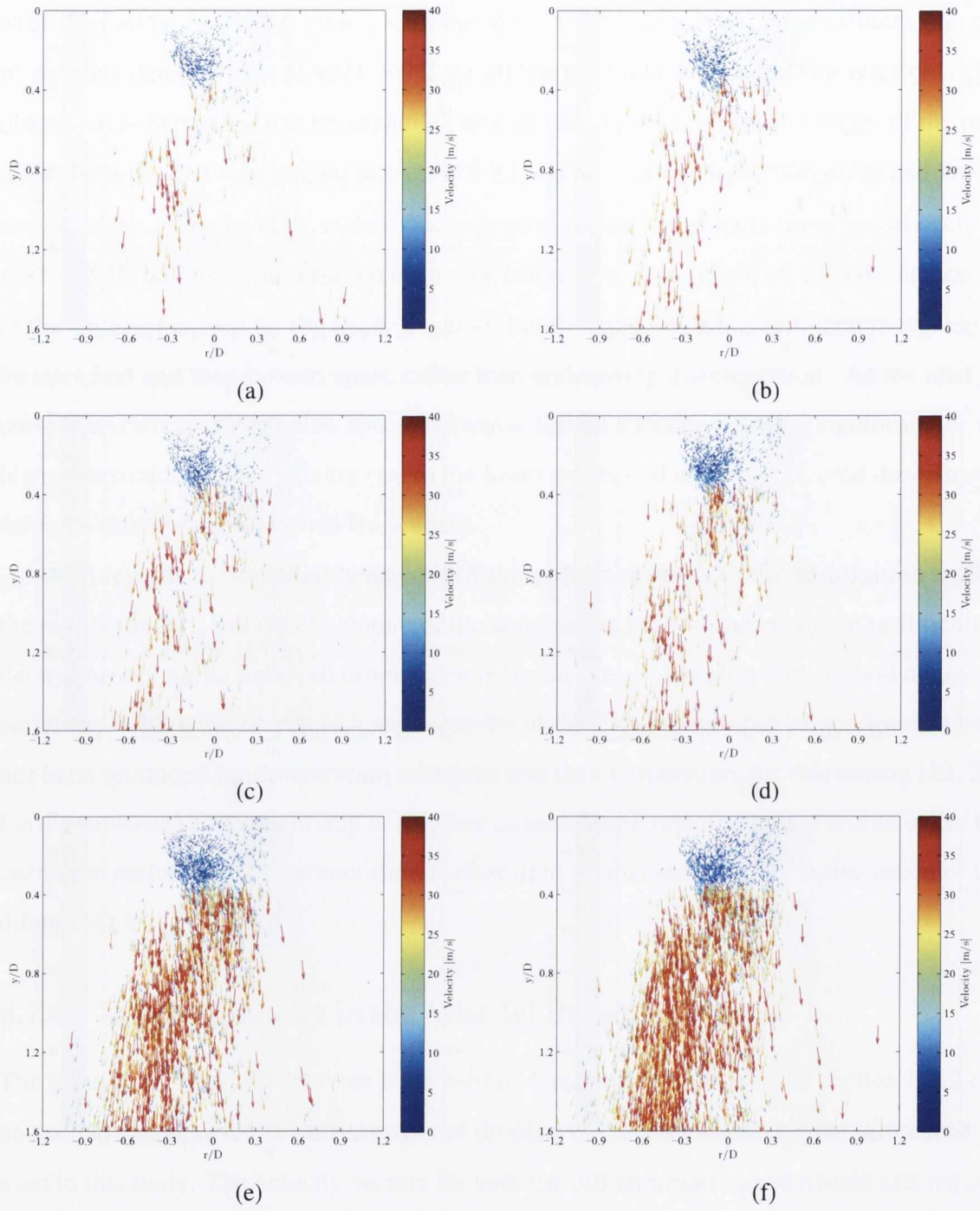

Figure 6.38: Velocity vectors in the full atomisation region for Re = 7800 and (a) f = 0.0017, (b) f = 0.0025, (c) f = 0.0034, (d) f = 0.0052, (e) f = 0.0098 and (f) f = 0.0136

of low velocity droplets that initially do not move downstream with the air jet as discussed in more detail below in the section on the nozzle exit velocity vectors. Further downstream, the droplets now follow the direction of the air jet, moving away from the nozzle exit and spreading outwards as y/D increases. As the mist loading increases, the mist jet spreads

radially, with more lower velocity droplets being ejected outwards from the main body of the mist. These outlying droplets most likely experience a lower velocity as they have moved beyond the core of the air jet and are decelerating.

For the case of Re = 7800 as shown in figure 6.38 the droplets again accelerate downstream from the nozzle exit region as the liquid droplets gain momentum from the air jet. For the increased air velocity, the droplet velocities are also higher, as is acceleration, than when Re = 4500. The path of the velocity vectors is also quite different, with a definite tendency towards $r/D > 0$, which becomes more pronounced as f increases. This reflects the high-speed images of the atomisation of the liquid jet at this Reynolds number, where the water undergoes violent disintegration as it moves downstream; in the high-speed imagery there was also a distinct tendency towards $r/D < 0$. Thus, the asymmetry in velocity vectors may be a result of the atomised droplets retaining their initial trajectory due to their high inertia. As well as this limitations in the shadowgraphy technique may have an influence; if the droplet is moving out of the focal plane of the camera, its velocity cannot be calculated. Thus, the asymmetry potentially points to significant movement of the liquid droplets towards and away from the camera, and is an indicator of the increased spreading of the jet for Re = 7800 as discussed above.

Nozzle exit region vectors

For both Reynolds numbers, in the nozzle exit region the droplet paths and velocities are markedly different from the flow further downstream. As such, the velocity vectors in the nozzle exit region, $0 < y/D < 0.3$, are considered in isolation here for a sample of the mist loading fractions examined. Figure 6.39 shows the nozzle exit velocity vectors for Re = 4500 and mist loading fractions of (a) $f = 0.003$, (b) $f = 0.009$ and (c) $f = 0.024$. The vector plots for the higher Reynolds number case of Re = 7800 are shown in figure 6.41 for (a) $f = 0.0017$, (b) $f = 0.0052$ and (c) $f = 0.0136$.

The bulk motion of the mist jet droplets in the nozzle exit region is not in the downstream direction at the Reynolds number of 4500; in figure 6.39 the majority of the droplets move radially and up towards the nozzle exit at a low velocity. This is most likely as a result of the recirculation zone, identified in figure 6.39, in the annular air jet turning the droplets away from the bulk jet motion. Thus, figure 2.9, from the work of Patte-Rouland et al. [52],

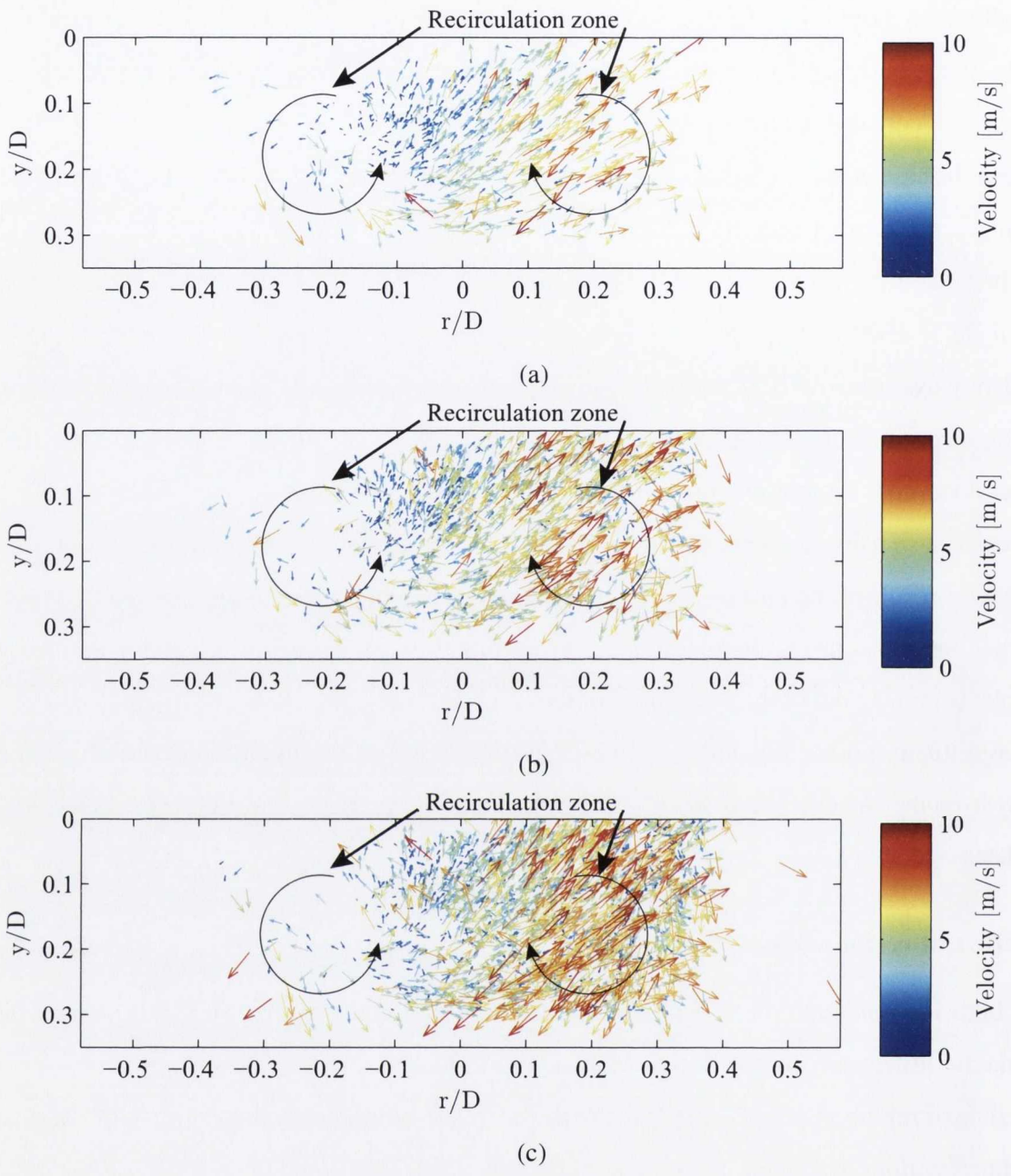

Figure 6.39: Velocity vectors in the nozzle exit region for Re = 4500 for (a) $f = 0.003$, (b) $f = 0.009$ and (c) $f = 0.024$

shows clearly this recirculation for an upward facing annular air jet. With increasing mist loading fraction, the number of droplets in the recirculation zone increases, although there is no noticeable increase in their speed as the air jet velocity remains constant. The dominant direction of the droplets' motion also remains the same as f increases, as again the structure of the air jet should be unchanged.

Considering the region $-0.3 < r/D < -0.2$, for Re = 4500 very few droplets are detected

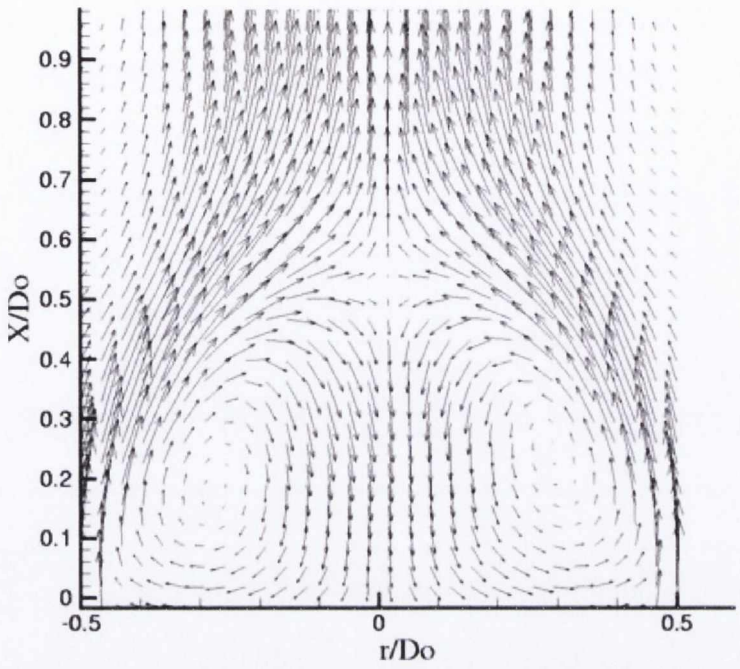

Figure 6.40: Average velocity field for an upward facing annular free jet, with Re = 7680, [52]

for the all three mist loading fractions cases presented in figure 6.39, and those that are detected have very low velocities; this region corresponds to where the water ligament structure emerges from the liquid nozzle, as seen in the high-speed images in section 6.2.1. The mist jet droplets shed from this ligament are captured by the recirculation zone of the annular jet, accounting for the low vector count in the ligament region. The vector plots show the droplets accelerating in the positive r/D direction as they are exposed to more of this recirculation zone for all mist loading fractions. At the downstream edge of this region at $y/D \approx 0.3$, some higher speed droplets are observed moving in the direction of the jet centreline, $r/D = 0$, from both sides of the distribution, though the majority are found on the positive r/D side. These are the droplets that have been ejected from the recirculation zone and are now being accelerated downstream. Comparing these paths with the annular air jet structure displayed in figure 6.40, it can be seen that the droplets are following the bulk motion of the annular jet, which tends towards the centreline beyond the recirculation zone, beginning approximately between $X/D_o = 0.3$ and $X/D_o = 0.4$. The droplets on the left side of the vector plots in figure 6.39, at the edge of the atomisation region, are those that were stripped from the edge of the ligament when it extends far enough such that they are not captured by the recirculation zone of the annular jet.

For the higher Reynolds number case of Re = 7800, as plotted in figure 6.41, the droplets do not appear to follow the recirculation zone of the annular jet to the same extent as at the lower Reynolds number. While some of the vectors do move back towards the nozzle, the majority of the droplets are found on the negative side of the r/D distribution and tend to head downstream and towards the jet centreline. This is most likely due to the atomisation behaviour at the higher Reynolds and Weber numbers. Thus, in the high-speed images in section 6.2.1 corresponding to this situation, the liquid ligament underwent more violent disintegration closer to the nozzle exit than for Re = 4500. As the ligament bursts apart the droplets are immediately captured by the stronger jet, and although the recirculation of the jet does cause some of them to move upstream, most of the droplets are instead turned towards the centreline by the action of the edge of the recirculation zone and accelerate downstream. Again, the behaviour is similar for the three mist loading fractions considered, although as more liquid is available for atomisation, a higher number of droplets are detected moving downstream at the end of the nozzle region at an increased velocity.

The vector maps shown in figure 6.41 reveal the more chaotic nature of the nozzle exit region at the higher Reynolds number. With the increase in Re and consequent change in the atomisation behaviour, more high speed droplets can be seen moving downstream within the nozzle exit region. The droplets are accelerated more quickly in this case, causing them to move counter to the recirculation zone. Overall, the droplets seem less likely to follow the annular jet structure here than at the lower Reynolds number. The violent atomisation of the liquid jet may be the reason for this, as droplets may be ejected from the ligament at velocities sufficient to overcome the influence of the recirculation zone. The chaotic behaviour in the nozzle exit zone is continued throughout the full atomisation region of the mist jet for this higher Re case, as was seen in figure 6.38, which exhibits a non-uniform pattern of vectors about $r/D = 0$. This indicates that the velocity asymmetry in the velocity vectors about $r/D = 0$ in figure 6.38 is due to the droplets following their initial trajectory, as suggested above.

Axial distributions of droplet velocity

The axial distributions of the droplet velocities provide further information on the mist jet development. Figure 6.42 (a) shows the mean magnitude of the velocity of the water droplets

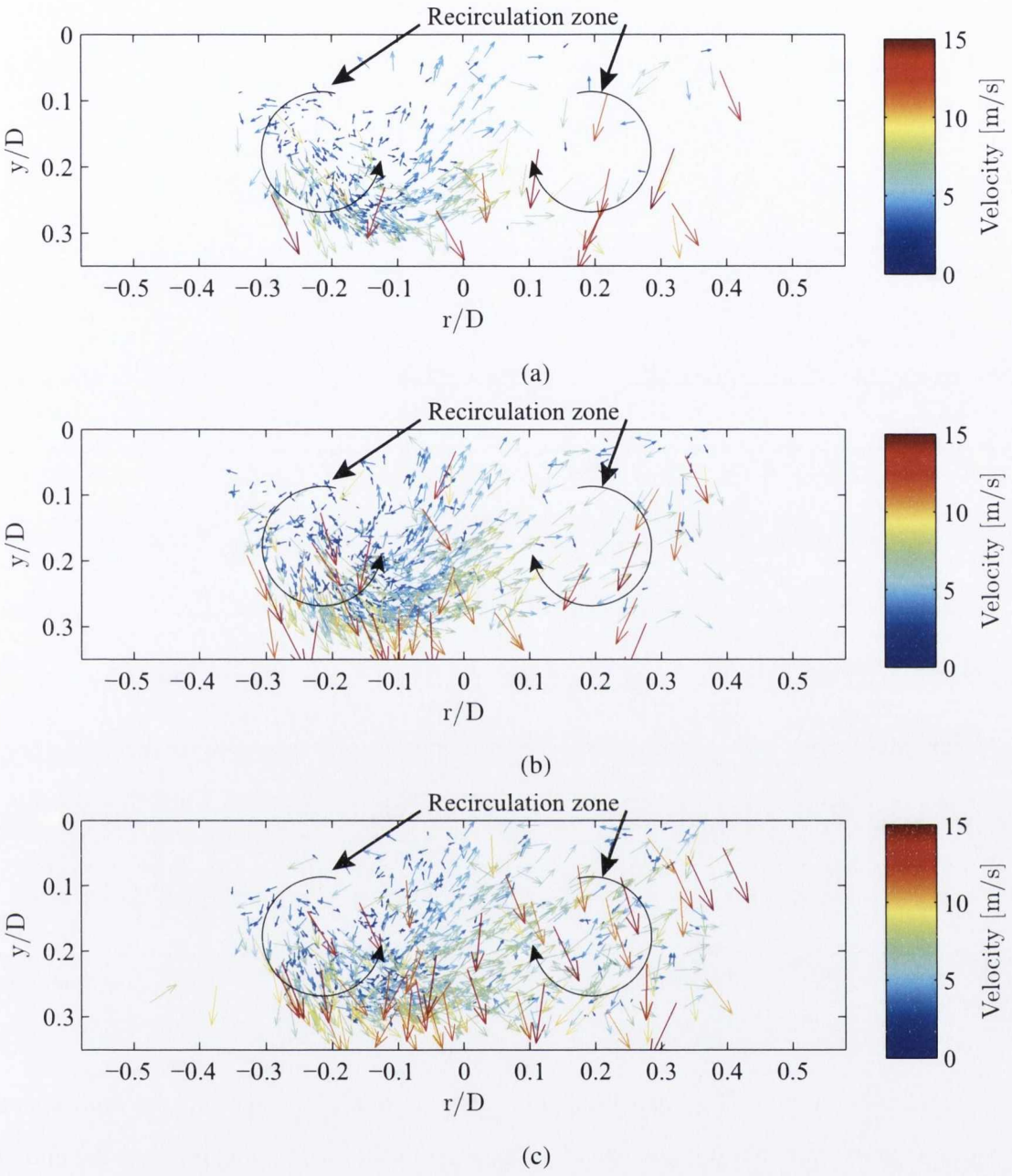

Figure 6.41: Velocity vectors in the nozzle exit region for Re = 7800 (a) f = 0.0017, (b) f = 0.0052 and (c) f = 0.0136

for different mist loading fractions as a function of axial distance from the nozzle exit. The acceleration of the droplets as they move further away from the nozzle is clearly apparent for all loading fractions. The annular jet flow causes the droplets to initially accelerate rapidly between $y/D = 0.4$ and $y/D = 1$. Beyond this point, the acceleration slows considerably as the forces acting on the droplets approach equilibrium. In this region, the velocity magnitudes decrease slightly with increasing mist loading fraction whereas during the acceleration phase

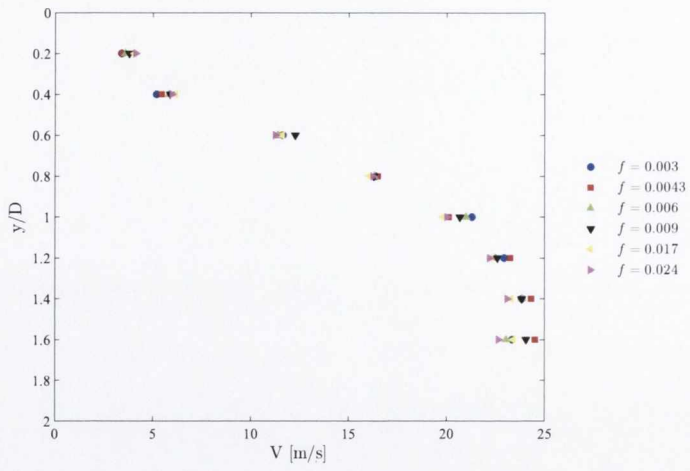

(a)

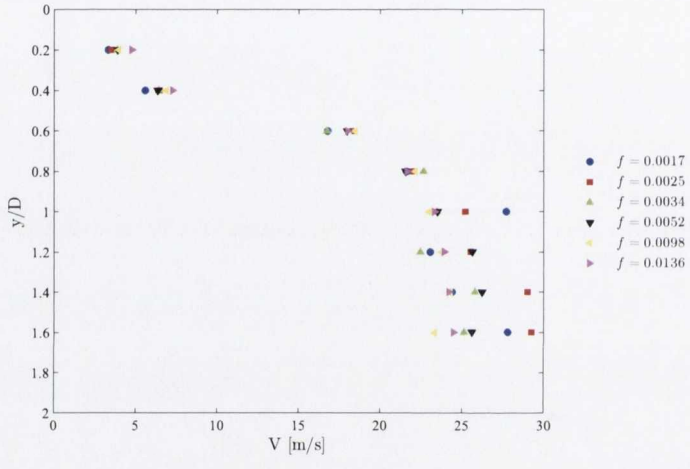

(b)

Figure 6.42: Droplet velocity magnitude V as a function of y/D, for different mist loading fractions; (a) Re = 4500 and (b) Re = 7800

there was no clear trend. The higher concentration of water was seen in the high-speed imagery of section 6.2.1 to result in some larger clusters of liquid breaking off from the end of the water jet which would accelerate slower than the smaller droplets, potentially decreasing the average velocity for the higher mist loading fractions.

Figure 6.42 (b) shows the mean velocity magnitude at increasing y/D for Re = 7800. As in figure 6.42 (a) for the lower Reynolds number, the acceleration of the droplets as they move away from the nozzle is clearly evident. The mean velocities in the nozzle exit region, around $y/D = 0.2$ and $y/D = 0.4$, are similar in magnitude to those of figure 6.42 (a). However, for $y/D = 0.6$ and above, the acceleration of the droplets is noticeably greater at Re = 7800, due to the higher air velocity. Again, the rate of acceleration decreases as the droplets move

downstream, although there is a greater spread in the mean velocities with mist loading fractions in this case, with no clear trend emerging.

Figure 6.43 shows the evolution of the axial velocity component, $V_{y/D}$, with increasing y/D at Re = 4500 and mist loading fractions of (a) $f = 0.003$, (b) $f = 0.009$ and (c) $f = 0.024$. For all three mist loading fractions, initially, when $y/D = 0.4$ the droplets are concentrated in the low velocity nozzle exit region, with those close to the centreline moving back upstream, as seen also in the nozzle exit vector plots of figure 6.39. As y/D increases, the acceleration of the droplets is evident, with the droplets spreading outwards and with lower axial velocities for greater distances from the jet centreline. Of note is when $y/D = 0.8$, where a local velocity minimum in on the jet centreline is found. Considering the annular jet structure in figure 6.40, the corresponding region of $y/D = 0.4$ to $y/D = 0.8$ in the annular jet is the location of the end of the recirculation zone, with a local stagnation point occurring at $y/D \approx 0.5$. This reduction in jet velocity may cause any droplets that have left the recirculation zone in this region to experience less of an acceleration than those that are released into the higher velocity annular jet flow around the recirculation zone away from the jet centreline. As the droplets move further downstream, the centreline acceleration continues, with the maximum in axial velocity now located on the mist jet centreline, before decaying radially outwards as the droplets leave the core of the annular jet flow. Increasing the mist loading fraction tends to widen the region about the centreline over which the axial velocity is uniform.

At the higher Reynolds number of 7800 it is harder to determine clear trends in the droplet axial velocity as the mist jet moves downstream. Figure 6.44 shows the r/D distributions of the axial velocity at Re = 7800 and mist loading fractions of (a) $f = 0.0017$, (b) $f = 0.0052$ and (c) $f = 0.0136$. Across the three mist loading fractions, the velocity increases with y/D, as expected, due to the acceleration of the droplets by the annular jet. In this instance there is no evidence of a delayed acceleration of the droplets as was seen at $y/D = 0.8$ when Re = 4500. There is evidence of a local maximum in the droplet velocity between $r/D = 0$ and $r/D = -0.5$; this corresponds well with the vector plots in figure 6.38, which show a definite trend towards the negative r/D side of the distribution. The axial velocity evolution with downstream distance highlights the chaotic nature of the mist jet for the higher Reynolds number, most likely arising from the violent atomisation behaviour of the liquid

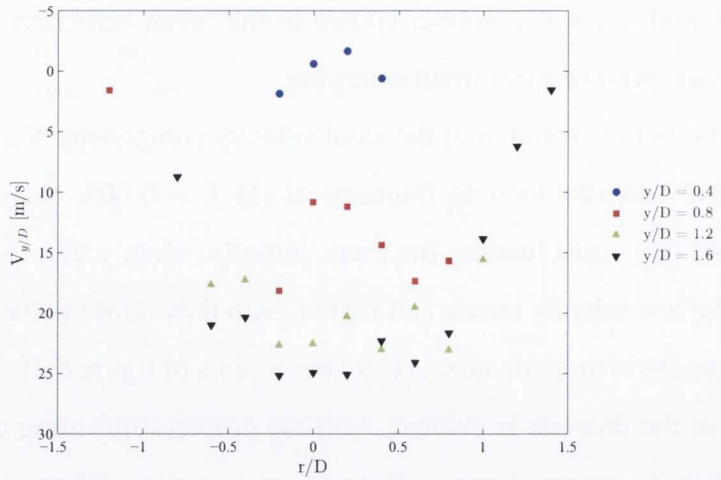

(a)

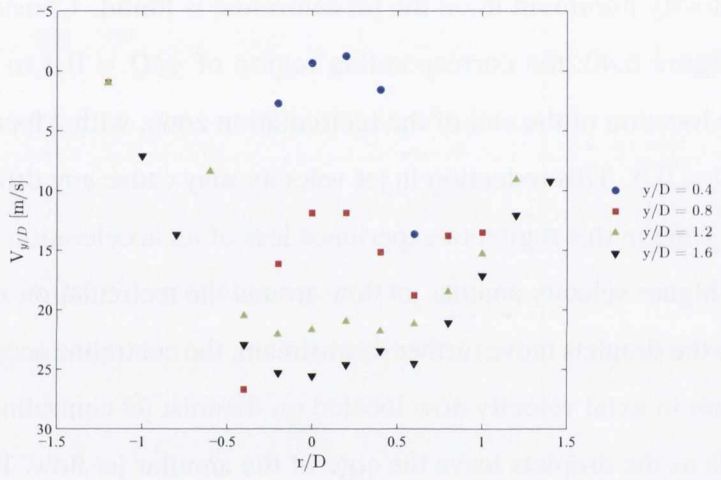

(b)

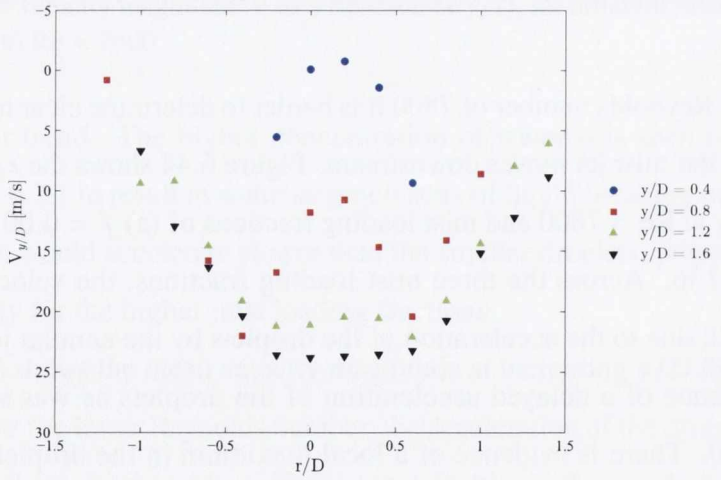

(c)

Figure 6.43: Radial distributions of droplet axial velocity $V_{y/D}$ as a function of y/D and Re = 4500; (a) f = 0.003, (b) f = 0.009 and (c) f = 0.024

jet preventing the droplets from establishing a uniform radial distribution as the droplets are carried downstream before they can spread radially.

Relationship between droplet velocity and size

The relationship between the size of the water droplets and their velocities within the atomisation region, $y/D \leq 1.6$, is shown in figures 6.45 (a) and (b) for representative mist loading fractions at Re = 4500 and Re = 7800 respectively. For both Reynolds numbers and all mist loading fractions, it is clear that, within the atomisation region, as the droplet diameter increases, the velocity tends to decrease. This occurs as close to the nozzle exit, the greater mass, and hence inertia, of the larger droplets results in a slower acceleration than the smaller lighter droplets. As is to be expected, the higher Reynolds number air jet gives rise to greater average velocities in general. As the mist loading fraction increases, the mean droplet velocity for a given size is seen to also undergo an increase for both Reynolds numbers. This may be because the number of droplets increases with mist loading fraction, resulting in a greater number of droplets being accelerated to high velocities and hence increasing the mean value for a given droplet size. In other words when the mist loading fraction is lower and there are fewer droplets detected, the presence of low velocity outlier droplets may have more of an influence on the mean velocity for a distinct droplet size.

6.2.5 Summary of Mist Jet Atomisation

The atomisation behaviour for the different flow conditions considered within this investigation has been examined. The atomisation of a mist jet at low mist loading fractions, and correspondingly high momentum flux ratios, has been seen to be markedly different from that reported in the literature for cases of higher liquid flow rates. This difference in behaviour is attributed to the lack of a liquid core at the mist jet nozzle, with the Weber number being identified as a parameter of importance. The structure of the mist jet in the atomisation region has been presented in terms of the droplet properties, together with vector maps of the droplet velocities being examined. Axial distributions of droplet diameters and velocities have also been examined. The following section deals with the mist jet structure outside the atomisation region, and attempts to link it to the atomisation behaviour considered in this section.

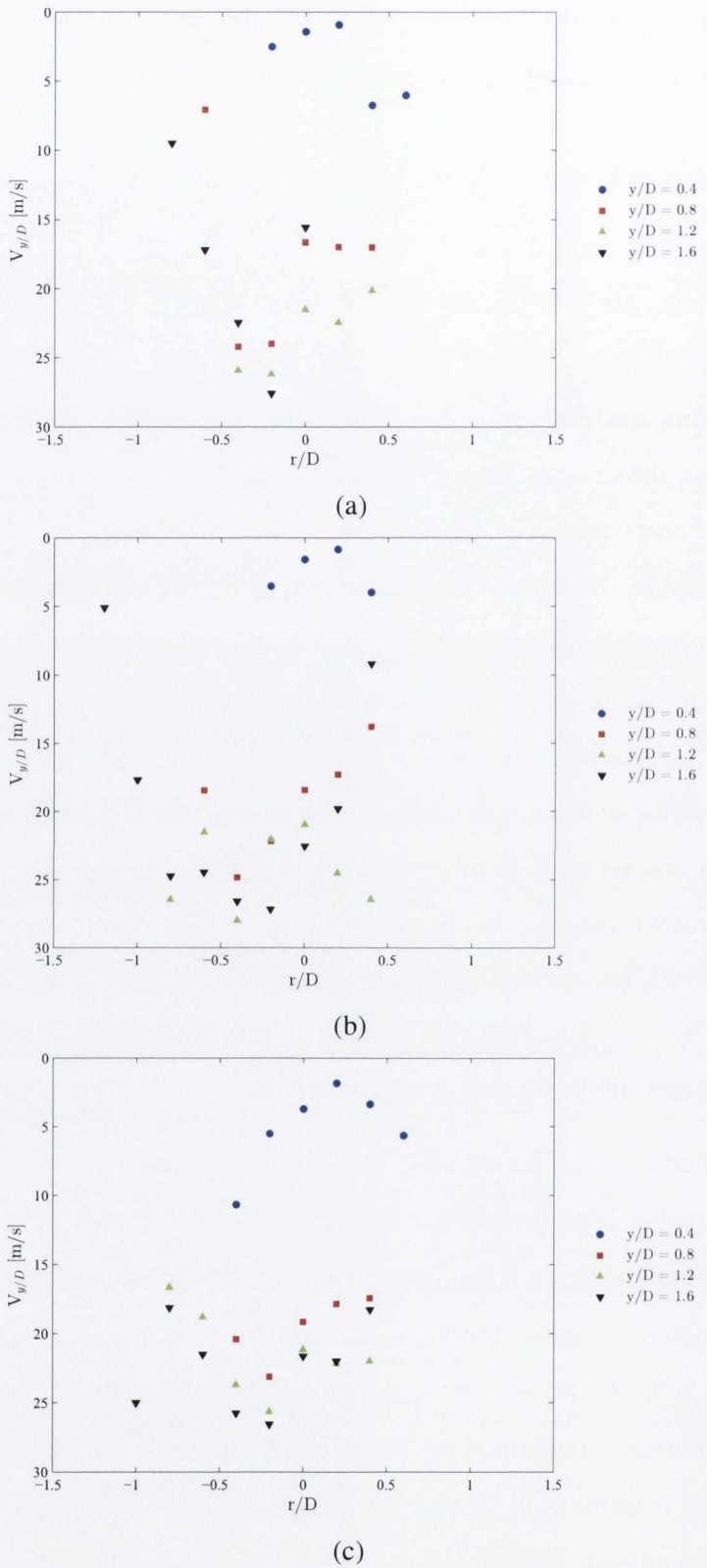

(a)

(b)

(c)

Figure 6.44: Radial distributions of droplet axial velocity $V_{y/D}$ as a function of y/D and Re = 7800; (a) f = 0.0017, (b) f = 0.0052 and (c) f = 0.0136

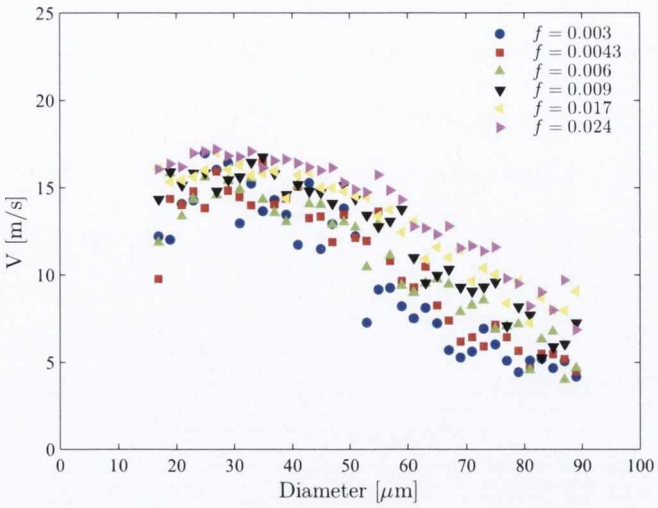

(a)

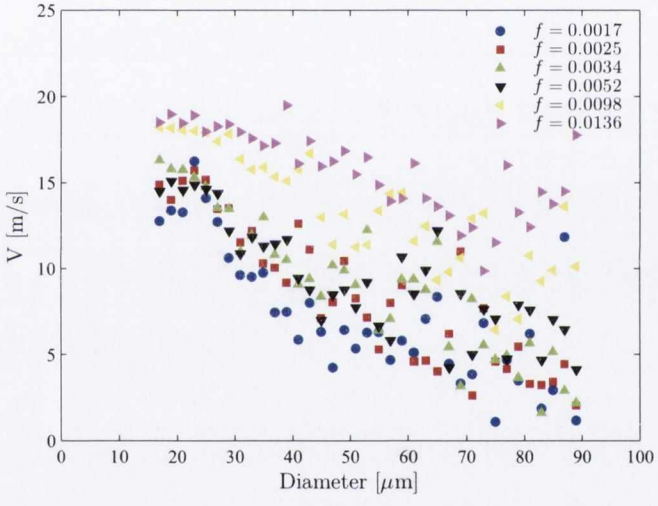

(b)

Figure 6.45: Relationship between droplet diameters and velocities for representative samples of f within the atomisation region; (a) Re = 4500 and (b) Re = 7800

6.3 Droplet Properties in the Mist Jet Far-Field

In this section, the properties of the droplets in the far-field region of the mist jet , i.e. outside of the atomisation zone, are presented. Results here are given in terms of the mist loading fraction, f, for the range of parameters in table 6.1; results in terms of the momentum flux are not included in this section, but are rather presented in appendix A.

As described in section 4.3, shadowgraph imaging in the region of an impingement surface was performed simultaneously with heat transfer measurements from the surface.

Therefore, results are presented for droplet properties in two regions, corresponding to the two H/D cases considered in the heat transfer experiments: $H/D = 5$ and $H/D = 10$. As per section 4.5, it was not possible to perform shadowgraphy within one nozzle diameter of the impingement surface, due to the noise generated by shadows cast by the surface. Therefore, the droplet size and velocity data presented here are for the regions of $2.6 < y/D < 4$ and $7.6 < y/D < 9$ for $H/D = 5$ and $H/D = 10$ respectively. The radial distance considered is the same, $-1.2 < r/D < 1.2$. Figure 6.46 shows schematically the regions examined associated with $H/D = 5$ and $H/D = 10$ respectively. The atomisation region is also shown in this.

This section first considers the mean droplet sizes in the above two regions for varying mist jet flow rates. Then, the axial and radial distributions of the droplet sizes within the two far-field regions are presented. Next the velocity of the droplets is examined in terms of vector plots and radial and axial distributions, and the relationship between droplet size and velocity is also demonstrated.

6.3.1 Droplet Sizes in the Far-Field

Droplet sizes are presented here in terms of the Sauter mean diameter, $D_{3,2}$, and the arithmetic mean diameter, $D_{1,0}$, for the two far-field regions shown schematically in figure 6.46. Figures 6.47 (a) and 6.47 (b) show the average droplet diameters for varying f at Re = 4500, corresponding to We = 146, for $H/D = 5$ and $H/D = 10$ respectively.

Considering figure 6.47 (a) first, it is immediately noticeable that both the Sauter and the arithmetic mean diameters are almost constant across the range of mist loading fractions, although there is some scatter in $D_{3,2}$ at the lower mist loading fractions. This is in contrast with the data for the atomisation region, presented in figure 6.15, where a decrease in the mean diameters with increasing f was observed. This trend was attributed to an increase in the number of smaller droplets as the mist loading fraction increased and it was hypothesised that the nature of the atomisation process of the mist jet was not changing for this range of parameters as the jet Weber number remained constant across the range of f. The fact that the mean droplet diameter is constant outside the atomisation region serves to affirm this hypothesis.

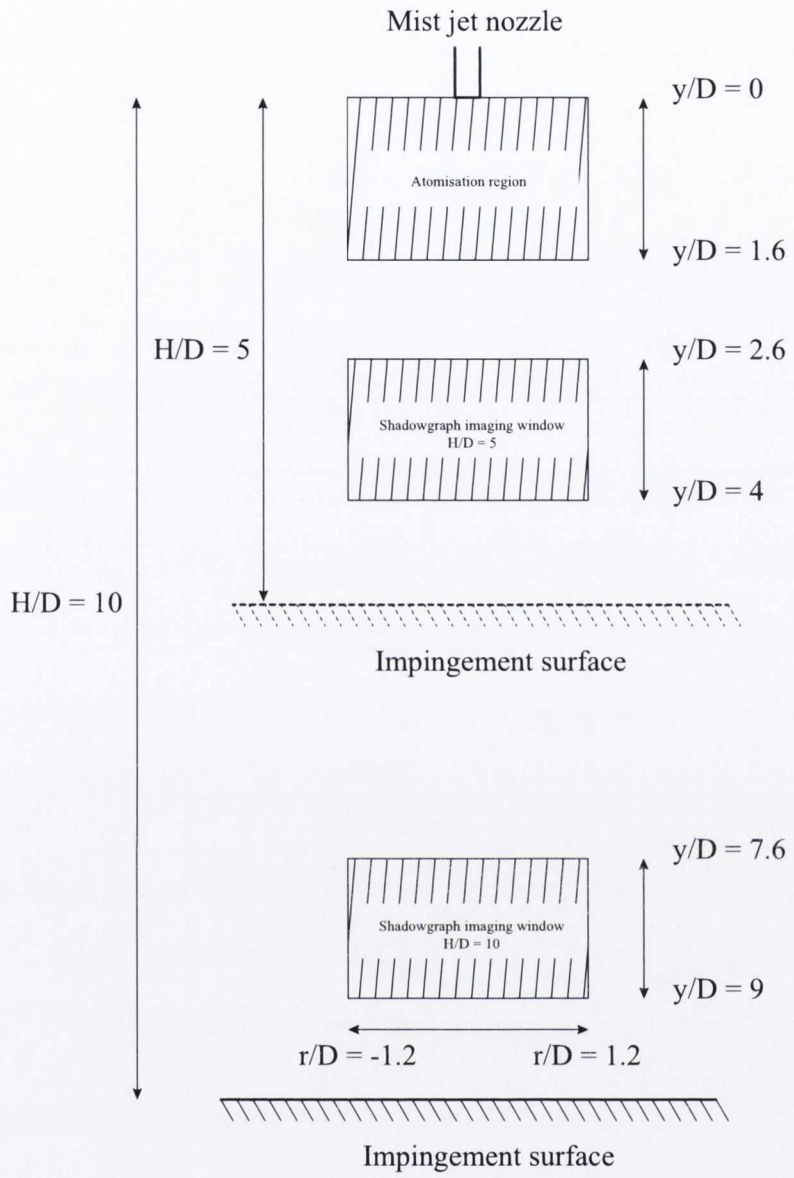

Figure 6.46: Far-field shadowgraph imaging regions associated with nozzle-to-plate spacings $H/D = 5$ (dashed line) and $H/D = 10$

The data for even further downstream at $H/D = 10$ show similar behaviour across the range of f examined, again with scatter in the Sauter mean diameter for the lower mist loading fractions. There does, however, appear to be a slight initial increase in $D_{1,0}$ with f. This could be related to the increasing number of droplets generated as f increases and not to a change in the atomisation behaviour. Thus, as the droplets move downstream they are subjected to the air jet for a longer period and hence undergo more secondary atomisation. When f is larger and there is a higher concentration of droplets, there is a greater chance of

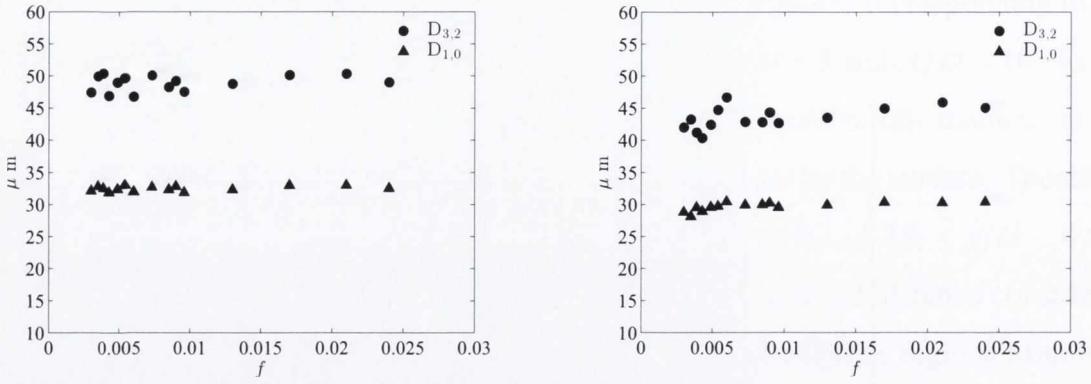

Figure 6.47: Sauter mean and arithmetic droplet diameters as a function of mist loading fraction at Re = 4500 and We = 146; (a) $H/D = 5$ and (b) $H/D = 10$

bigger droplets surviving downstream, thereby resulting in slightly smaller droplet sizes at the lowest f considered here.

Comparing figure 6.47 (a) with the mean diameter data for the atomisation region in figure 6.15, it is clear that both $D_{3,2}$ and $D_{1,0}$ have decreased as the mist jet moves downstream from the atomisation region; this applies across the range of f. This is consistent with the trend seen in figures 6.29 and 6.30, which showed the mean droplet diameters decreasing as the mist jet moved downstream from the nozzle exit towards $y/D = 1.6$. Indeed, the arithmetic mean diameter in figure 6.30 is converging towards a value of between 30 and 35 μm, which matches well with $D_{1,0}$ for this range of $2.6 < y/D < 4$. Similar behaviour was seen for the Sauter mean diameter, which converges towards ~50 μm in figure 6.29, approximately equal to $D_{3,2}$ across the range of f in figure 6.47 (a). If the mean diameters for $H/D = 10$, i.e. the region where y/D increases from 7.6 to 9, are considered, the droplet sizes have decreased again, although not significantly. This decrease in droplet size as the mist jet moves downstream is consistent with that reported by Lasheras et al. [23] for similar H/D and is due to the secondary atomisation of the droplets under the continued shearing action of the air jet.

The fact that the mean droplet sizes beyond the atomisation region do not vary significantly as the mist jet moves downstream for this Reynolds number indicates that the mist jet structure stabilises in terms of the droplet size very early after the atomisation region; the mean diameters have not changed substantially between $y/D = 1.6$ and $y/D = 9$. It is possible

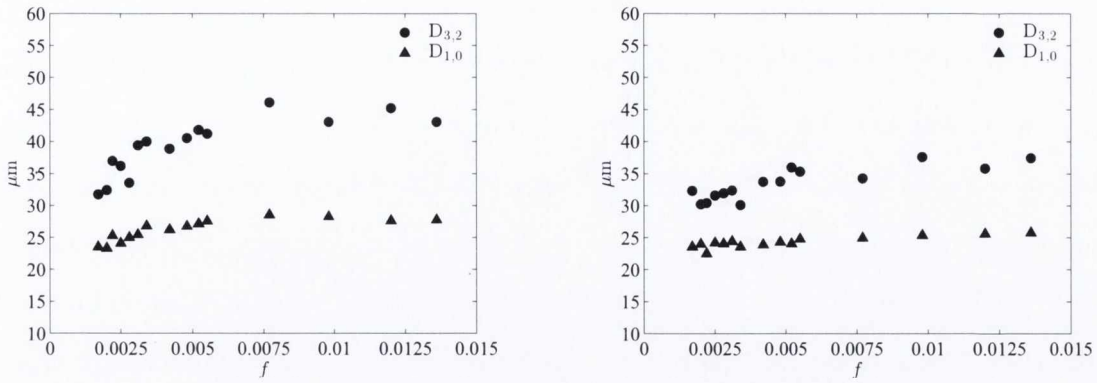

Figure 6.48: Sauter mean and arithmetic droplet diameters as a function of mist loading fraction at Re = 7800 and We = 353; (a) $H/D = 5$ and (b) $H/D = 10$

that with further increases in y/D, coalescence of droplets might occur within the mist jet resulting in an increase in the mean diameter; this was reported by Lasheras et al. [23], for the region beyond $y/D = 20$. However, for this Reynolds and Weber number case, the mean droplet diameters at impingement for the two H/D cases considered are similar, with little variation in f.

The mean diameter data for the higher Reynolds number of Re = 7800, corresponding to We = 353, are presented in figure 6.48 (a) for the nozzle at $H/D = 5$ and figure 6.48 (b) for $H/D = 10$. As expected from figure 6.21, the mean diameters are smaller for the higher air jet Reynolds number. The trends in mean diameters with f are, however, different here from the lower Reynolds number, particularly for the region associated with $H/D = 5$. At Re = 7800, both the arithmetic and the Sauter mean diameters are seen to increase initially with mist loading fraction, before becoming constant. This behaviour may again be due to fewer large droplets remaining intact this far downstream for lower f, due to a lower droplet concentration in the mist jet. The fact that the increase is more significant than for Re = 4500 in figure 6.47 (b) is most likely due to the increased kinetic energy at the higher Reynolds number causing more secondary atomisation of the few large droplets found at the lower mist loading fractions. This trend can be seen emerging in the downstream evolution of the droplet size for the same Reynolds number, in the atomisation region shown in figures 6.33 and 6.34; in these figures, the decrease in droplet size with y/D for the larger f has slowed considerably, while the droplet sizes for the smallest f are still decreasing at $y/D = 1.6$.

The increase in droplet size with mist loading fraction is not as strong in the region corresponding to $H/D = 10$. In this case, the droplet sizes associated with the lower mist loading fractions have changed little from when $H/D = 5$; the mean diameters when $H/D = 10$ for the higher mist loading fractions, $f > 0.0075$, are seen to decrease towards the same values as the lower f. This indicates that as the mist jet moves downstream at the higher Reynolds number, the droplet diameters tend towards a constant value, but not at the same rate across the range of mist loading fractions. This may be due to more large droplets being carried downstream in the mist jet for the higher mist loading fractions.

The droplet size distributions for the far-field regions provide further information on the mist jet development. Figures 6.49 and 6.50 show the number distributions at Re = 4500 for a representative sample of the mist loading flow rates in the regions associated with $H/D = 5$ and $H/D = 10$ respectively. Comparing these distributions with the equivalent information for the atomisation region in figure 6.17, it can be seen that the range of droplet sizes is not as broad in these downstream regions. Thus the mist jet is finer in these regions, containing a higher concentration of smaller droplets. This is because the larger droplets have undergone secondary atomisation as the air jet continues to shear the droplets, resulting in lower mean droplet diameters in the mist jet. The size distributions for $H/D = 10$ provide evidence for the assertion that the increase in mean droplet diameter with f in this region is due to an increase in the number of larger droplets in the mist jet; the distributions for the higher mist loading fractions are clearly broader than those for lower f values, encompassing larger numbers of bigger droplets.

Comparing the downstream regions for $H/D = 5$ in figure 6.49 and $H/D = 10$ in figure 6.50, the droplet size distributions become slightly narrower again as the mist moves downstream from $2.6 < y/D < 4$ ($H/D = 5$) to $7.6 < y/D < 9$ ($H/D = 10$), again giving rise to the small decrease in $D_{1,0}$ and $D_{3,2}$.

It can also be seen that the number of droplets detected in the mist jet decreases as the region of interest changes from $H/D = 5$ to $H/D = 10$. As the droplet sizes have not increased, this does not indicate that coalescence has taken place; rather, it is indicative of the spreading of the mist jet as it moves downstream, since as the droplets travel away from the mist jet nozzle exit, they tend to spread outwards, both radially out of the detection region and also out of the focal plane of the camera.

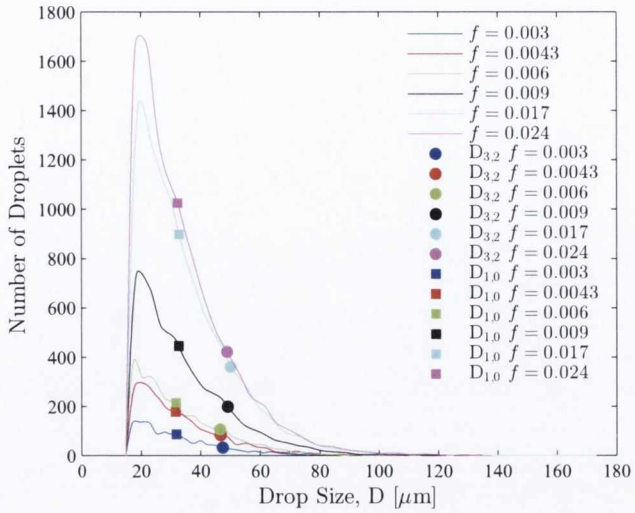

Figure 6.49: Number distributions of droplet diameter for H/D = 5, Re = 4500, We = 146 and a representative sample of f

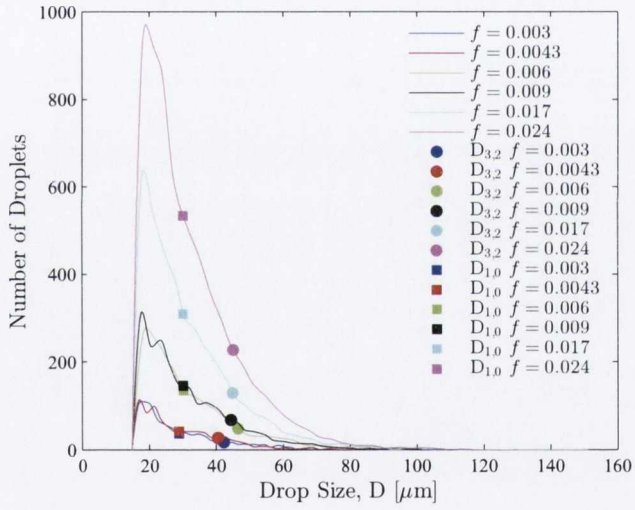

Figure 6.50: Number distributions of droplet diameter for H/D = 10, Re = 4500, We = 146 and a representative sample of f

The droplet size distributions for the higher Reynolds number case of Re = 7800 and We = 353 are presented in figures 6.51 and 6.52 for the same downstream regions associated with H/D = 5 and H/D = 10. Again, the droplet size distributions in the downstream regions are narrower than the distribution for the atomisation region, shown in figure 6.23, indicating a finer mist jet; indeed this is more noticeable here than when Re = 4500. The distributions are also narrower than those for the lower Reynolds number in figures 6.49 and 6.50. This is to be expected as the higher air jet Reynolds number leads to more secondary atomisation resulting in smaller droplets in the mist jet. One feature that was not anticipated is the fact

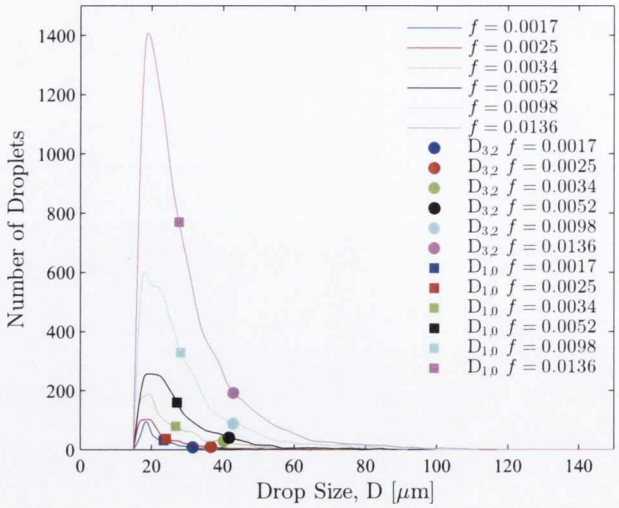

Figure 6.51: Number distributions of droplet diameter for H/D = 5, Re = 7800, We = 353 and a representative sample of f

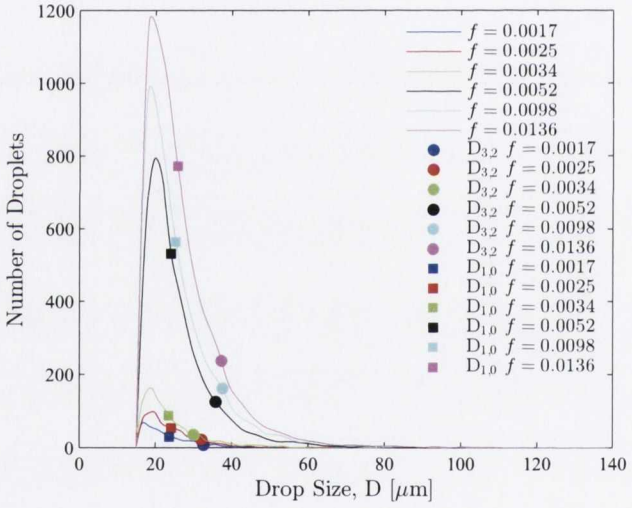

Figure 6.52: Number distributions of droplet diameter for H/D = 10, Re = 7800, We = 353 and a representative sample of f

that the number of droplets detected for some of the mist loading fractions in the Re = 7800 case is higher for the more advanced axial location corresponding to H/D = 10; this can be seen for f = 0.0098 and f = 0.0052 in particular. This behaviour was not observed for the lower Reynolds number case and may result from larger droplets undergoing secondary atomisation, resulting in more smaller droplets being detected downstream at H/D = 10. However, this trend was not replicated in the majority of cases and the possibility exists that it is an artefact of the lighting conditions during testing. Further investigation of this effect is warranted before a firm conclusions can be drawn. The size distributions of the lower mist

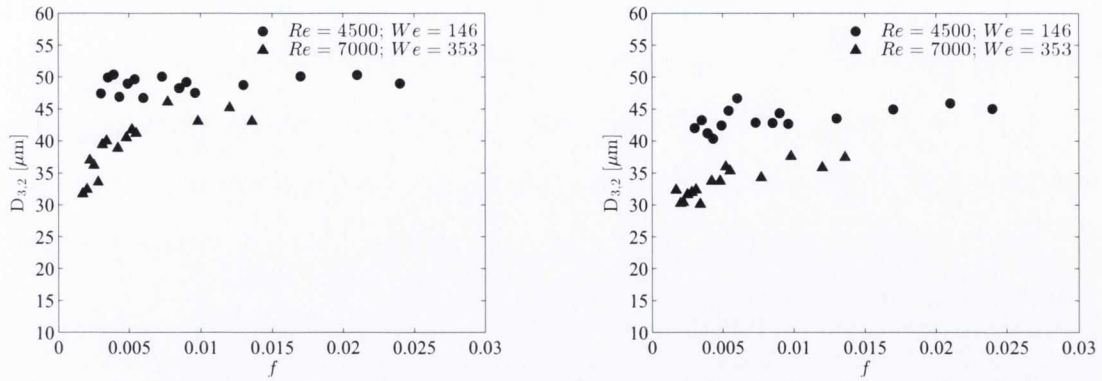

Figure 6.53: $D_{3,2}$ with varying f for Re = 4500 and Re = 7800; (a) H/D = 5 and (b) H/D = 10

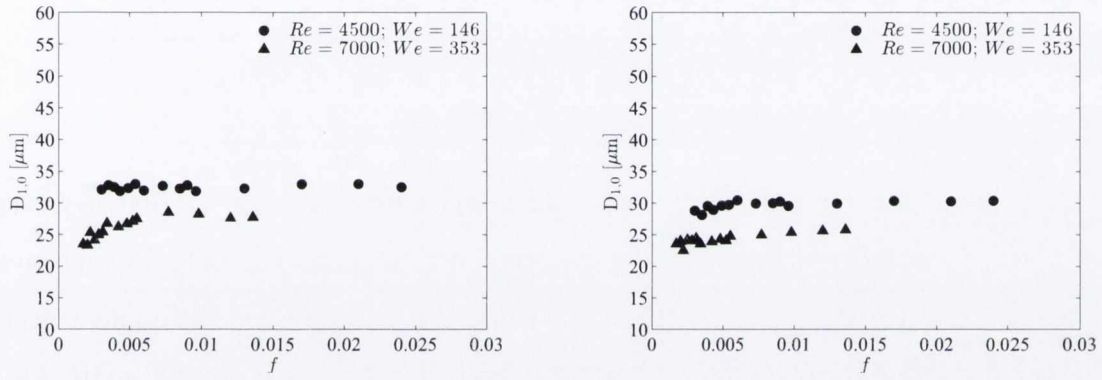

Figure 6.54: $D_{1,0}$ with varying f for Re = 4500 and Re = 7800; (a) H/D = 5 and (b) H/D = 10

loading fractions do not change appreciably between the two locations, possibly as a result of the few large droplets in the mist jet at these f having already disintegrated into smaller droplets before the H/D = 5 region.

For Re = 7800 in figures 6.51 and 6.52, the increase in the mean droplet size with increasing mist loading fraction can be linked to an increase in the number of larger droplets detected with increasing f. The higher kinetic energy of the air jet when Re = 7800 is more effective at atomising the existing larger droplets, in particular when the mist loading fraction is lower, potentially as there is a lower concentration of larger droplets to begin with for low f. Thus, as f increases and more large droplets are generated, it is more likely that large droplets will survive downstream and hence increase the mean diameter.

When the Sauter and arithmetic mean diameters in the downstream regions associated with H/D = 5 and H/D = 10 are plotted together for the two different Reynolds numbers,

as in figures 6.53 and 6.53, it is seen that trends are consistent with those observed in the atomisation region, shown in figures 6.27 and 6.28. For similar mist loading fractions, the droplet sizes are consistently larger for the lower Reynolds number, and hence for the lower Weber number. Therefore, downstream from the nozzle exit, the Weber number is still the controlling parameter in terms of the droplet size, with the initial atomisation behaviour defining the downstream structure of the mist jet.

6.3.2 Droplet Distributions in the Mist Jet Far-Field

The droplet sizes and number counts are examined in this section for different axial and radial locations within the two main far-field regions considered, as marked on figure 6.46.

Axial Distributions

The axial distributions for the arithmetic mean diameters in the downstream regions associated with $H/D = 5$ and $H/D = 10$ for Re = 4500 are presented in figures 6.55 and 6.56 respectively. The consistency in droplet size at these locations is clearly seen; $D_{1,0}$ is essentially constant in both regions, and there is only a slight decrease as H/D changes from 5 to 10, due to ongoing atomisation. The same uniformity in droplet size is seen when Re = 7800, as evident from figures 6.57 and 6.58 for $H/D = 5$ and $H/D = 10$ respectively. The smaller diameters recorded in this case are due to the higher kinetic energy of the air jet resulting in a finer mist as discussed previously. This uniformity of droplet size contrasts with the axial distributions in the atomisation region, where a clear decrease in the mean diameters was found as the mist jet moved downstream and the droplets were exposed to the air jet. Although not shown here, the Sauter mean diameter displays similar behaviour, but with more scatter in the data than the arithmetic mean, as was the case in the atomisation region. This indicates that in terms of the droplet size, the mist jet structure is changing little with y/D, beyond the atomisation region, across the range of mist loading fractions and nozzle-to-plate spacings considered in this investigation.

Radial Distributions

Figure 6.59 shows the radial distributions of $D_{1,0}$ at different axial locations for the $H/D = 5$ case, with two sample mist loading fractions and Re = 4500. Here, as in section 6.2.3, the

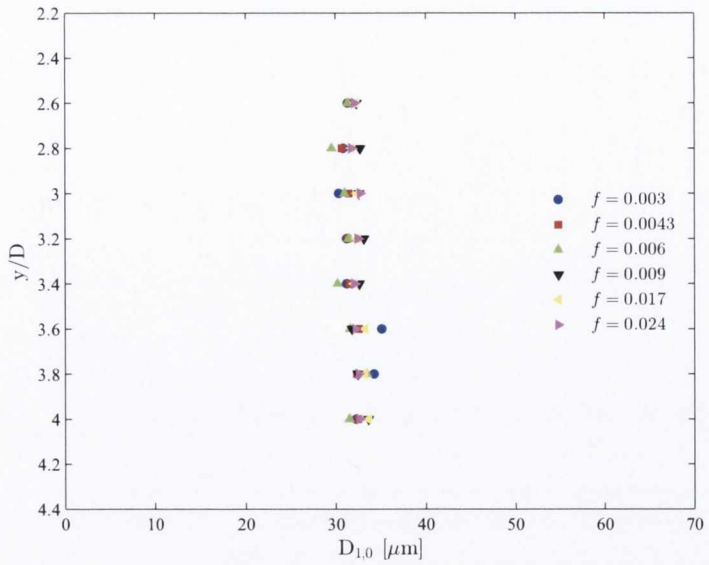

Figure 6.55: Axial variation in arithmetic mean diameter as a function of f, H/D = 5 and Re = 4500

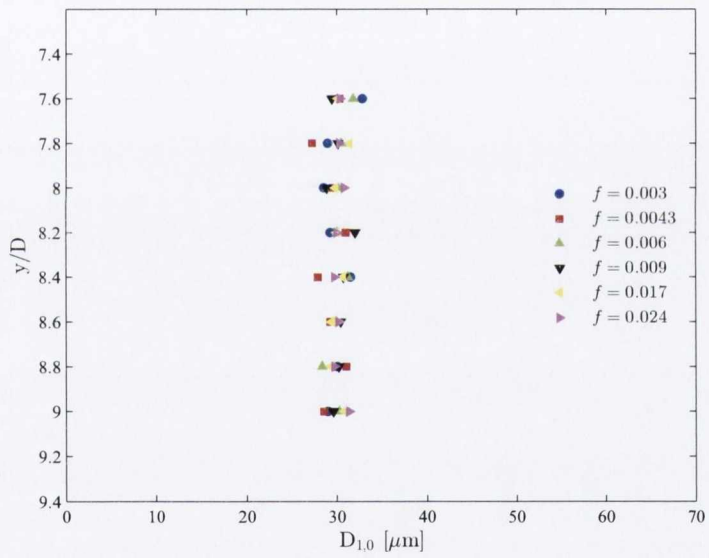

Figure 6.56: Axial variation in arithmetic mean diameter as a function of f, H/D = 10 and Re = 4500

results presented for y/D = 2.8 refer to the mean across all the droplets found between y/D = 2.4 and y/D = 2.8, and so on. These radial distributions reflect the uniformity of the mist jet in terms of droplet size discussed above; there is little variation across either r/D or y/D in the ranges considered, although there are some outliers at r/D = 1 in figure 6.59 (a). These are potentially due a smaller sample size in these locations. The distributions for the lower mist loading fraction vary slightly more with y/D than the higher case, although the effect is small. At the greater axial distances associated with H/D = 10, not displayed here,

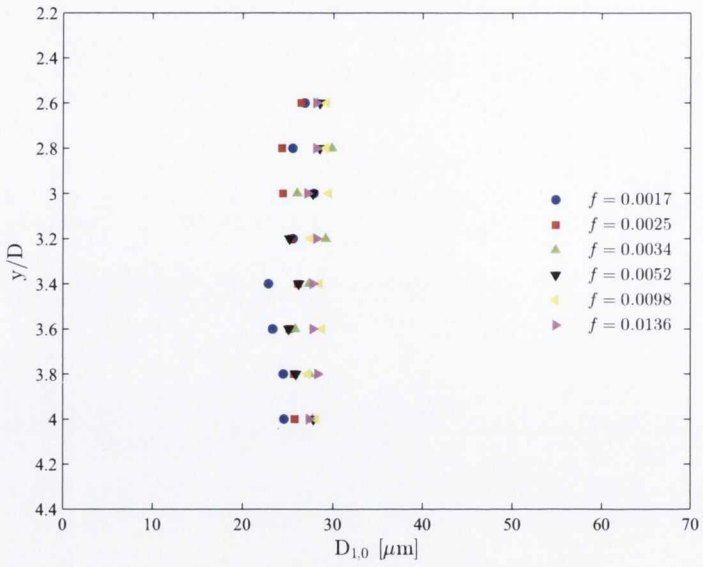

Figure 6.57: Axial variation in arithmetic mean diameter as a function of f, H/D = 5 and Re = 7800

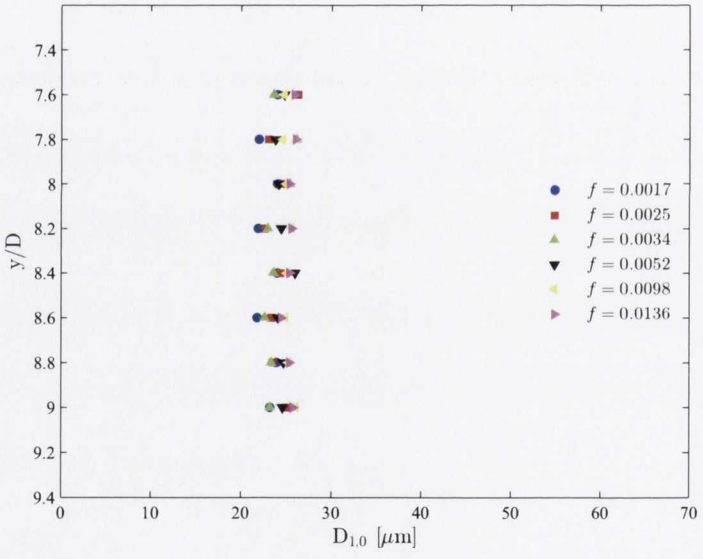

Figure 6.58: Axial variation in arithmetic mean diameter as a function of f, H/D = 10 and Re = 7800

the behaviour is broadly similar to the trends shown here.

The case when Re = 7500 and H/D = 5 is presented in figure 6.60. There is more variability in the droplet distributions of figure 6.60 (a) for the higher Reynolds number case than when Re = 4500, although the distributions become more uniform as the mist loading fraction increases, as seen in figure 6.60 (b). In particular, the droplet sizes are more uniform on the positive r/D side. This radial asymmetry may be a result of the more violent nature of the atomisation process at the higher Reynolds number, as discussed in section 6.2.1. The

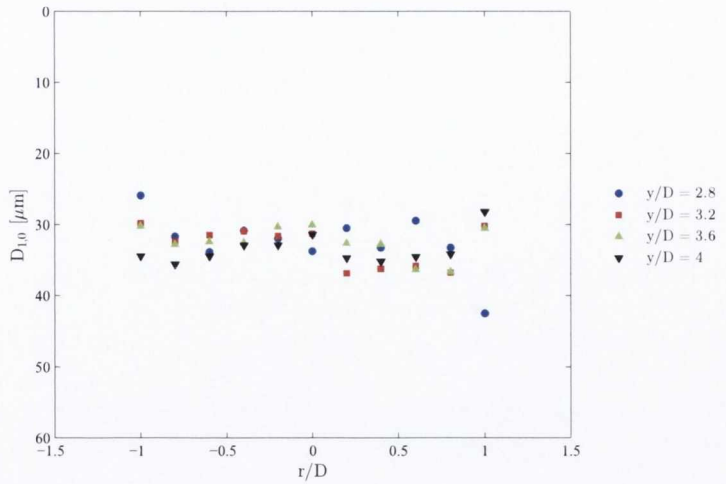

(a)

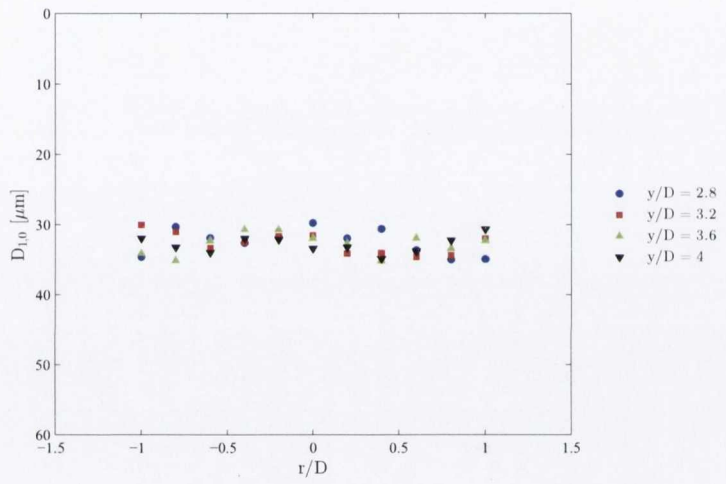

(b)

Figure 6.59: Radial distributions of $D_{1,0}$ for $H/D = 5$ as a function of y/D and Re = 4500; (a) $f = 0.009$ and (b) $f = 0.024$

high-speed images and droplet velocity vectors and distributions in the atomisation region shown in figures 6.38 and 6.44 respectively, displayed a definite trend in the droplets towards the negative r/D direction. However, the number of droplets detected when $H/D = 5$ for Re = 7800 shows a clear maximum towards the opposite, positive r/D across all f, as evident from figure 6.61 (a).

This apparent anomaly can potentially be explained by consideration of the work of Varga et al. [31], who observed what was referred to as a "helical wave" structure in the water jet in the atomisation region; this then disintegrated into droplets following roughly the same paths. Though Varga et al. [31] described the paths as helical, in the imagery presented in

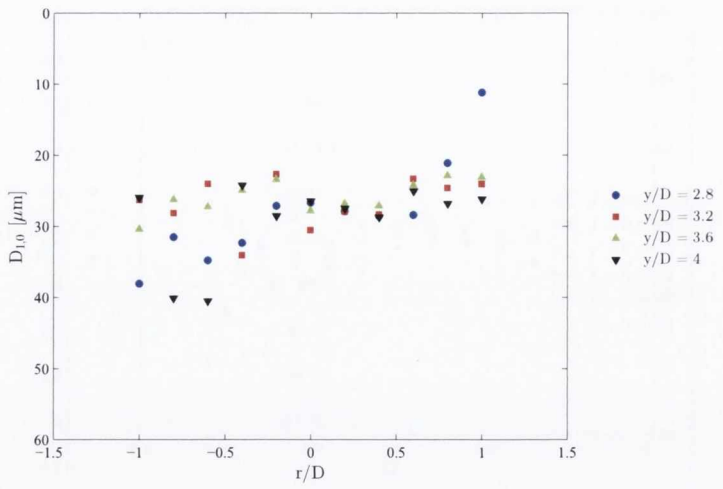

(a)

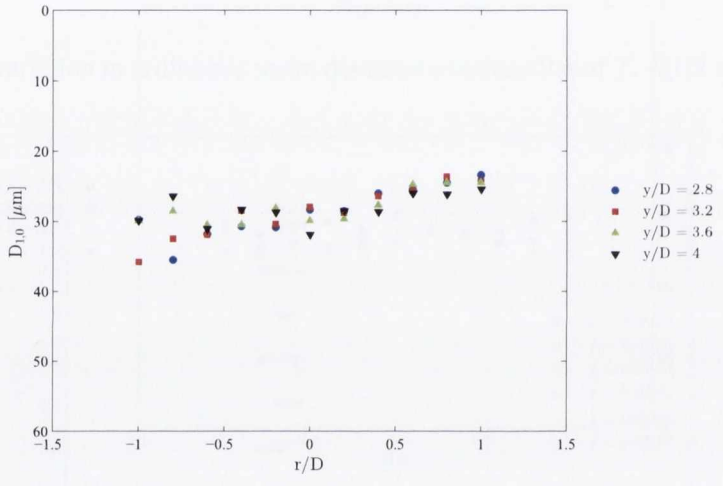

(b)

Figure 6.60: Radial distributions of $D_{1,0}$ when $H/D = 5$ as a function of y/D and Re = 7800; (a) $f = 0.0052$ and (b) $f = 0.0136$

that study the pattern appears to suggest a side-to-side, whip-like motion, rather than a helix. However, for consistency with that study, the phrase helical is used here. These helical paths were determined to be due to shear instabilities between the liquid and gas streams arising from the Rayleigh-Taylor waves generated in the liquid jet by the air jet. Varga et al. [31] presented high-speed imagery which showed these helical paths becoming more prevalent as the momentum flux ratio, M, increased, although M in their work was much lower than in the present investigation as both the air and liquid jet velocities were significantly higher than here but closer in magnitude. Nevertheless, this helical behaviour offers the best explanation for why the peak number of droplets detected has shifted from the left to the right as the mist

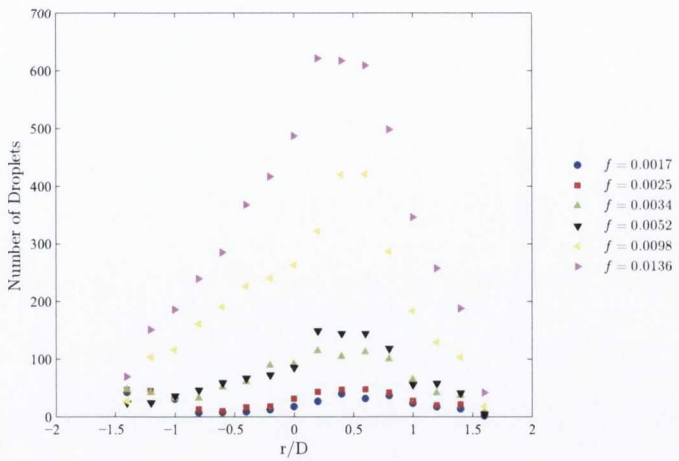

(a)

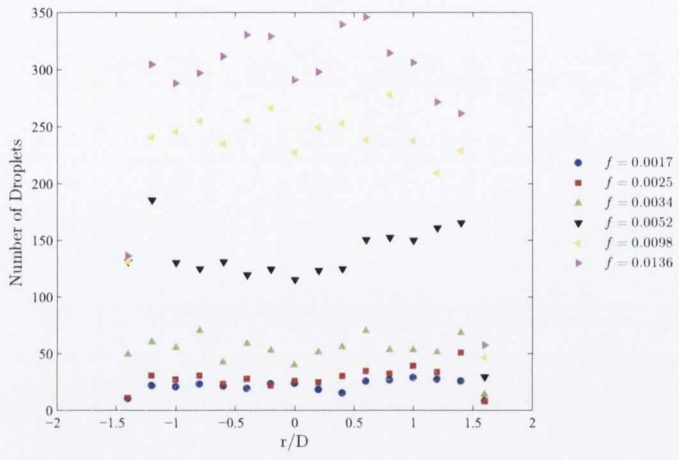

(b)

Figure 6.61: Number of detected droplets for r/D when Re = 7800 as a function of f; (a) $H/D = 5$ and (b) $H/D = 10$

jet moves downstream from the nozzle exit. The increased uniformity in the mean droplet diameter where there is a higher concentration of droplets may be because the bulk flow of the water droplets follow the helical flow pattern, leaving a sub-optimal sample of droplets on the opposite side of the distribution. For the same Reynolds number with $H/D = 10$, shown in figure 6.61 (b), the radial distribution of droplet number has become more symmetric about $r/D = 0$, suggesting that the droplets in the mist jet may no longer be following the initial helical path.

This type of behaviour is more significant for the higher air jet velocity than for the lower Reynolds number case, as the growth rate of the Rayleigh-Taylor instabilities that cause the helical path is linked to the acceleration of the liquid jet by the air jet, which clearly increases with increasing air jet Reynolds number. Thus, for Re = 4500, the air jet velocity may not be

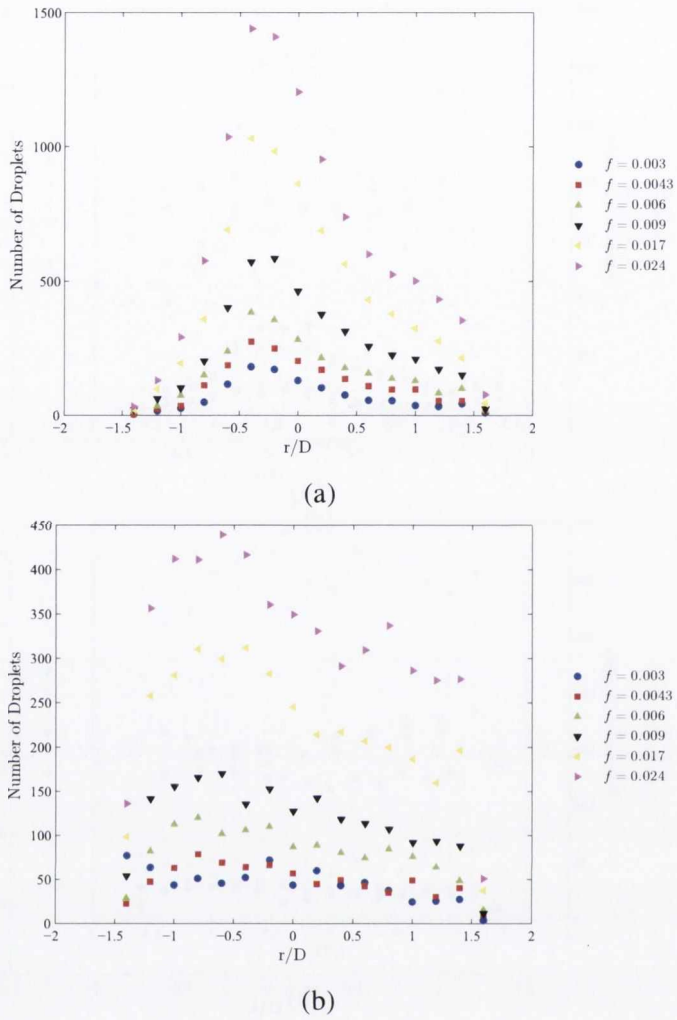

Figure 6.62: Number of detected droplets for r/D when Re = 4500 as a function of f; (a) $H/D = 5$ and (b) $H/D = 10$

sufficient for clear examples of this type of path to emerge. Interestingly, however, the droplet number radial distributions for Re = 4500, for both $H/D = 5$ and $H/D = 10$, show a distinct trend towards a maximum in the region of $r/D = -0.25$, rather than the jet centreline; these data are shown in figure 6.62. While this may be due to the same helical path of the liquid induced by the Rayleigh-Taylor, the velocity vectors for the atomisation region in figure 6.37 offer another potential explanation. As the mist jet moves downstream from the nozzle exit region, a definite tendency for the droplets to move towards the negative r/D can be seen, particularly beyond $y/D = 1.4$. These are most likely droplets that initially travelled to the right hand side of the nozzle exit due to the action of the recirculation zone of the annular air jet; as discussed in section 6.2.4, these droplets are then accelerated by the bulk motion of the

air jet, which can be seen in figure 6.40 to be towards the jet centreline. Thus, these droplets have a strong initial acceleration in the negative radial direction, and once they cross the jet centreline, the inertia of the droplets is such that the air jet bulk motion cannot reverse the direction of the droplets. Thus, the situation arises where there is a larger number of droplets slightly towards $r/D < 0$. The fact that the distribution of the droplets continues to exhibit a maximum at negative r/D as the mist jet moves downstream towards the region associated with $H/D = 10$ serves to reaffirm this. Indeed, the location of the peak number of droplets has moved even further from the centreline for $H/D = 10$ as the droplets continue along their initial paths. While this is a hypothesis only, the observed data appears to support this assertion.

6.3.3 Droplet Velocity in the Mist Jet Far-Field

As in the atomisation region, the droplet velocities at the two downstream axial locations for $H/D = 5$ and $H/D = 10$ are calculated using the same shadowgraph data as for the droplet sizes. Velocity vector maps for the two far-field regions are presented, as are radial and axial distributions, and the relationship between droplet sizes and velocities is examined.

Velocity vectors

The velocity vectors associated with the droplets in the mist jet for Re = 4500 in the downstream zone examined for the $H/D = 5$ case are shown in figure 6.63 for a representative sample of the mist loading fractions considered in this study. As was the case in the atomisation region, seen in figure 6.37, the increase in the number of droplets detected with increasing f is reflected in the velocity vectors, which become more dense as the mist loading fraction increases. As is expected, the vectors have a higher magnitude here than in the atomisation region, as they have been exposed to more of the air jet, experiencing continued acceleration by the co-flowing air jet to the higher velocities seen here. The increased spread in the jet is also evident, particularly at the higher mist loading fractions. Whereas in the atomisation region, the majority of the droplets were within the approximate region of $-0.6 < r/D < 0.6$ for the largest mist loading fraction of $f = 0.024$, here large numbers of droplets can be seen over the full radial extent of $-1.2 < r/D < 1.2$ as the mist spreads as it moves downstream.

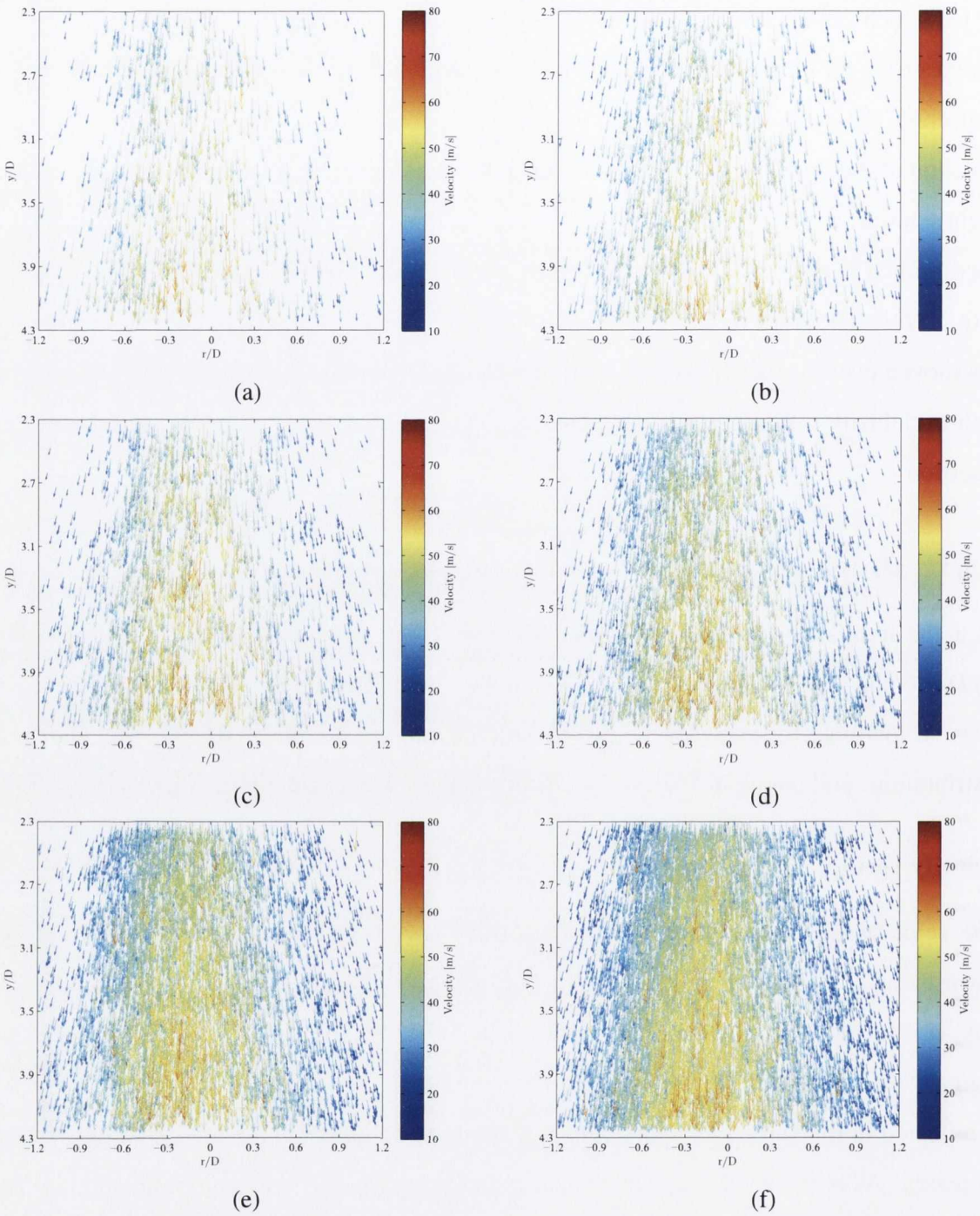

Figure 6.63: Velocity vectors in the $2.6 < y/D < 4$ zone for the $H/D = 5$ case at Re = 4500 and (a) $f = 0.003$, (b) $f = 0.0043$, (c) $f = 0.006$, (d) $f = 0.009$, (e) $f = 0.017$ and (f) $f = 0.024$

A central core of higher velocity droplets is clearly visible in the vector maps for each mist loading fraction, becoming more pronounced as f increases. The droplets in this high-speed core also appear to have a lower radial component, tending to move straight downstream, whereas the droplets at the edge of the mist jet can be seen to have a higher radial velocity,

contributing to the continued spread of the jet. The lower velocities at the edge of the jet can be attributed to the decay of the air jet velocity radially from its central core. As the mist loading fraction increases, there are a larger number of droplets seen at the higher velocity, although the maximum velocities observed do not appear to vary appreciably with f.

The high-speed core of the droplets is not symmetric about the jet centreline of $r/D = 0$, but rather is slightly towards the negative side of the radial distribution, as seen before in the number distribution of figure 6.62 (a). This follows on from the velocity vectors in the atomisation region in figure 6.37, which showed a similar tendency towards the negative r/D direction.

For $H/D = 10$ when Re = 4500, shown in figure 6.64, the core of higher velocity droplets appears to have spread further radially than for the shorter axial distances involved when $H/D = 5$, with higher velocity vectors being detected here across the range of mist loading fractions. This indicates that as far away as 9 diameters from the nozzle exit, the droplets are still accelerating, with larger velocities being detected in the region of $y/D \approx 9$ than towards the top of the vector plot. The jet has continued to spread radially as it moved downstream towards $H/D = 10$, with the edge of the jet now completely beyond the shadowgraphy camera window. The radial shift towards the negative r/D side is not as apparent at this downstream distance; the vector map for the region associated with $H/D = 10$ appears to be characterised by a more uniform, higher velocity distribution of velocity vectors across the range of f, than when $H/D = 5$. Fewer vectors have been detected also for this case, indicative of the continued spreading of the mist jet as it moves downstream.

The velocity vector maps for the higher Reynolds number of Re = 7800 are presented in figure 6.65 for the $H/D = 5$ case. Significantly fewer droplet vectors have been detected at the higher Reynolds number; this is likely due to limitations within the experimental set-up, specifically the camera frame rate. This was limited to 1000 Hz to improve lighting conditions, making it more difficult to detect large numbers of the higher velocity droplets associated with the Re = 7800 case. A refinement of the experimental set-up may provide more information, although it would require investment in a different light source than that used here.

A striking aspect of these maps is the asymmetry of the distributions; as indicated by the number distribution in figure 6.61 (a), the positive r/D side clearly has a larger proportion of

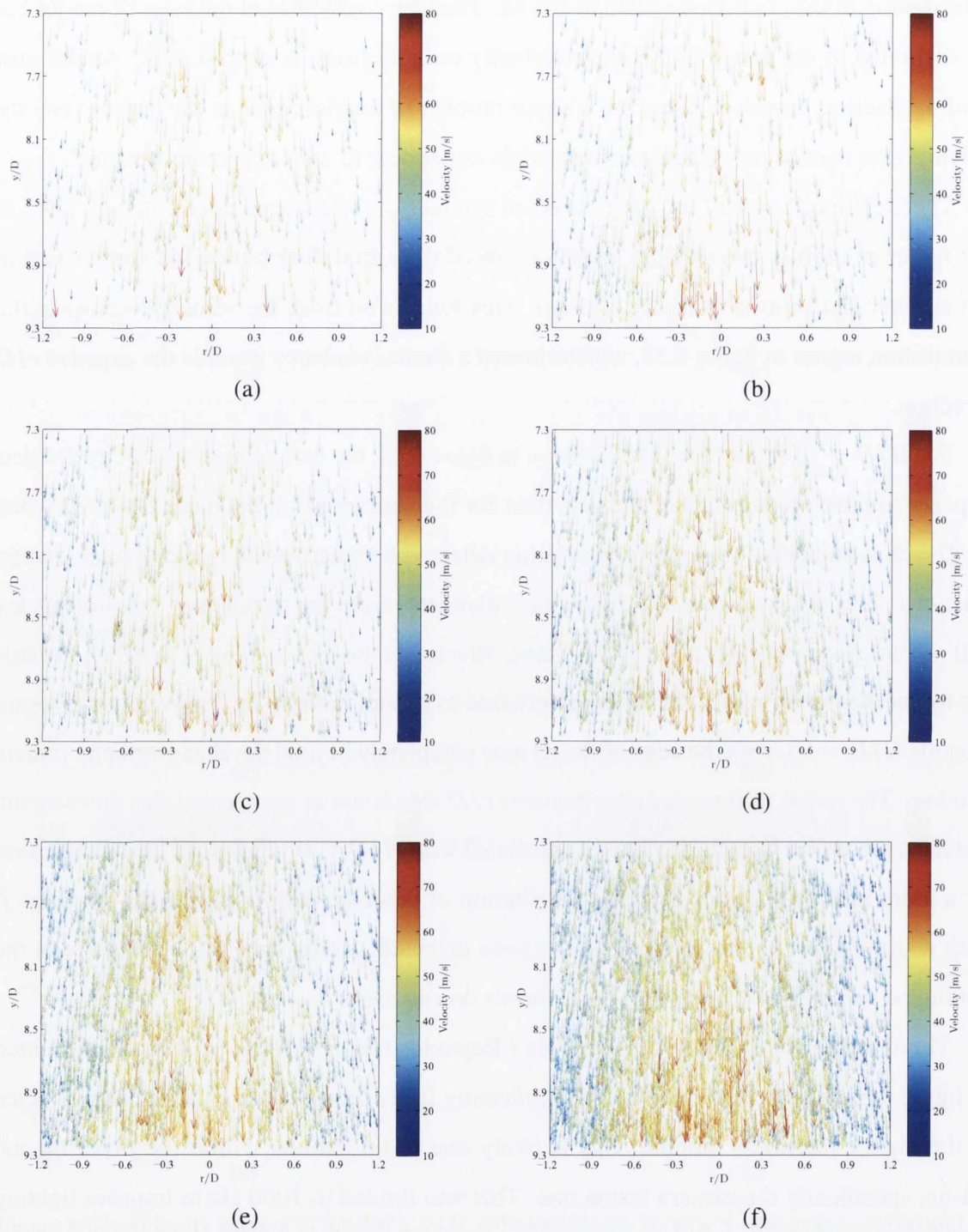

Figure 6.64: Velocity vectors in the $7.6 < y/D < 9$ zone for the $H/D = 10$ case at Re = 4500 and (a) $f = 0.003$, (b) $f = 0.0043$, (c) $f = 0.006$, (d) $f = 0.009$, (e) $f = 0.017$ and (f) $f = 0.024$

the droplet vectors detected. As well as this, the vector plots show that these droplets on the right hand side tend to have a higher velocity. If the droplets are indeed following the helical path described above, and as shown by Varga et al. [31], this offers an explanation as to why

the velocity magnitudes are greater on the side where more droplets are located. If the bulk flow is helical, the droplets that have been ejected form the bulk path, i.e. the droplets on the left side of the vector maps will begin to decelerate as they move away from the driving flow. Because of the asymmetry of the droplet velocities, there does not appear to be a central core of high-speed droplets, rather droplets that are following the helical path and droplets that have been ejected from this path. As is to be expected, the droplet velocities in general are higher than for Re = 4500, due to the higher air velocity.

When $H/D = 10$ for the same Reynolds number of Re = 7800, the velocity vector maps shown in figure 6.66 are different again as the mist jet has moved downstream. As was the case for Re = 4500, the droplets have continued to accelerate downstream, with higher velocities being detected in the $H/D = 10$ case. However, where there was a clear tendency of the vectors towards the positive r/D when $H/D = 5$, further downstream this behaviour is no longer visible. Indeed, there appears to be a slight bias towards the negative r/D for $H/D = 10$, indicating that the helical path might still have some influence, although the vectors are more uniform about $r/D = 0$ here. The fact that the droplets may be still following the helical path, which Varga et al. [31] attributed to interfacial Rayleigh-Taylor instabilities, at a distance of almost 10 diameters downstream from the nozzle exit shows the influence that the atomisation behaviour of the mist jet has on the droplet velocities downstream.

The mist jet droplets have also continued to spread radially as they move downstream, although again to a lesser extent than when Re = 4500. This behaviour has previously been reported by Engelbert et al. [22], and may be as a result of the droplets' tendency to follow their initial trajectories due to their relatively high inertia; when the Reynolds number is higher, the axial acceleration component is greater and causes the droplets to accelerate downstream before a significant radial velocity component can develop.

Droplet velocity distributions

The radial and axial distributions of the droplet velocities provide more detail on the droplet behaviour in the far-field and are considered here. The mean droplet velocity magnitude, V, with Re = 4500 for the same representative sampling of f as in the vector maps is shown in figures 6.67 (a) and 6.67 (b) for the cases of $H/D = 5$ and $H/D = 10$ respectively. The continued acceleration of the droplets as they move downstream is clearly evident in each

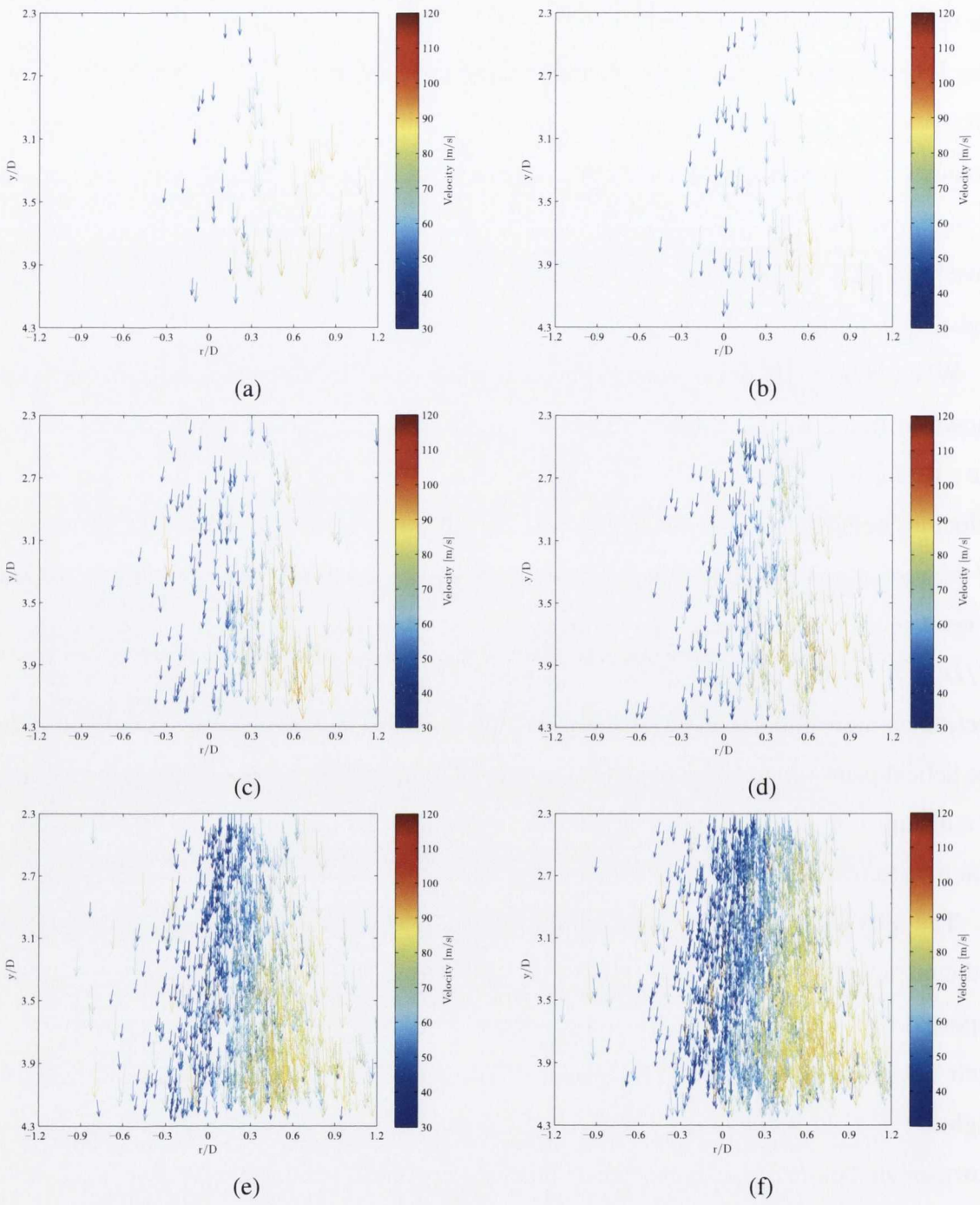

Figure 6.65: Velocity vectors in the $2.6 < y/D < 4$ zone for the $H/D = 5$ case at Re = 7800 and (a) $f = 0.0017$, (b) $f = 0.0025$, (c) $f = 0.0034$, (d) $f = 0.0052$, (e) $f = 0.0098$ and (f) $f = 0.0136$

zone, and between the two regions, with little change in the mean velocity across the range of f considered here; there is a little more variability with f when $H/D = 10$. The variation in the mean velocity magnitude for the higher Reynolds number case shows broadly similar behaviour, with continued acceleration as the mist jet moves downstream in the far-field

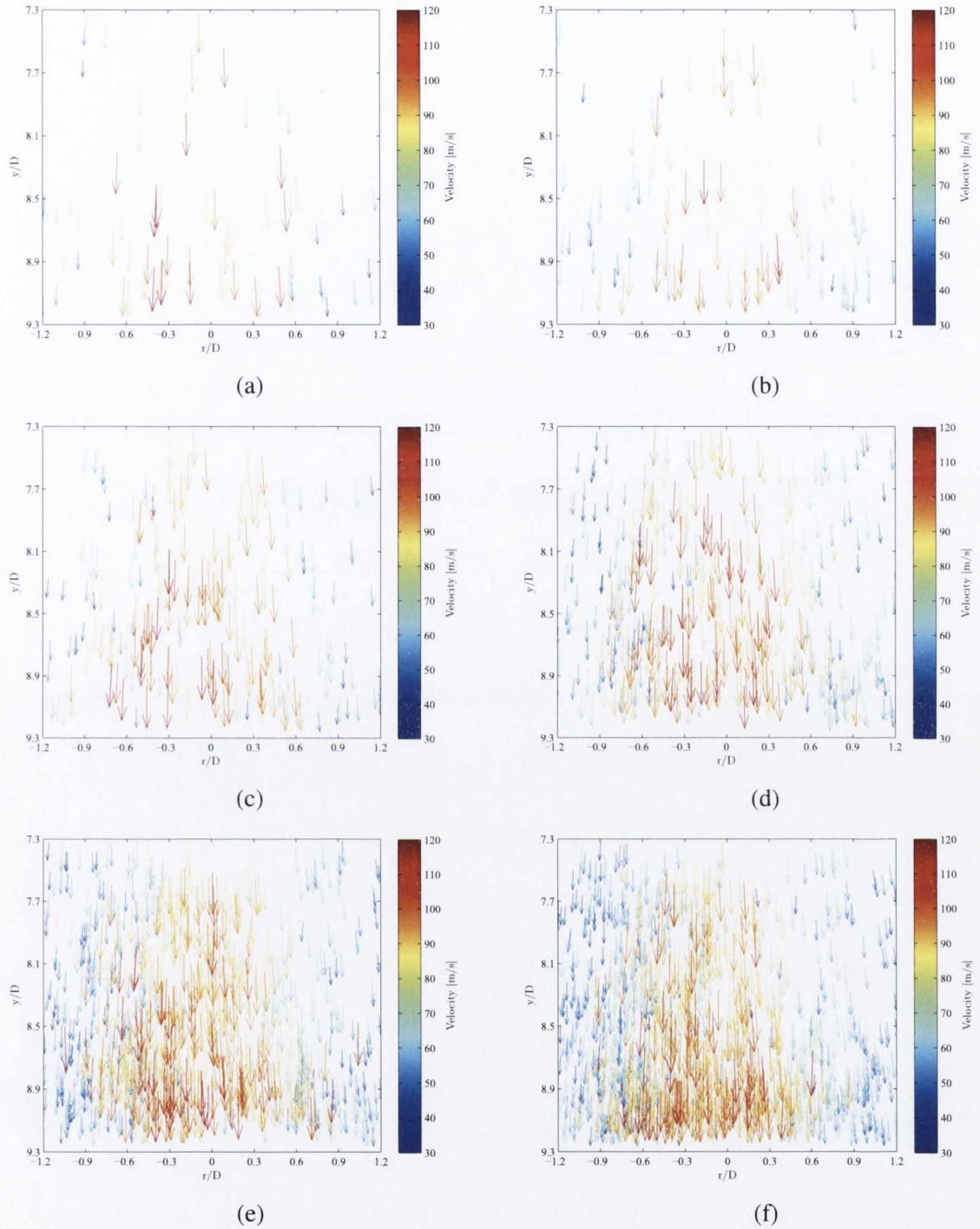

Figure 6.66: Velocity vectors in the $7.6 < y/D < 9$ zone for the $H/D = 10$ case at Re = 7800 and (a) $f = 0.0017$, (b) $f = 0.0025$, (c) $f = 0.0034$, (d) $f = 0.0052$, (e) $f = 0.0098$ and (f) $f = 0.0136$

evident for both H/D; these data are shown in figure 6.68. There is more scatter in velocity with f for both H/D at Re = 7800, possibly caused by the violent atomisation behaviour resulting in droplets moving in a more chaotic fashion. The smaller sample-size, due to frame

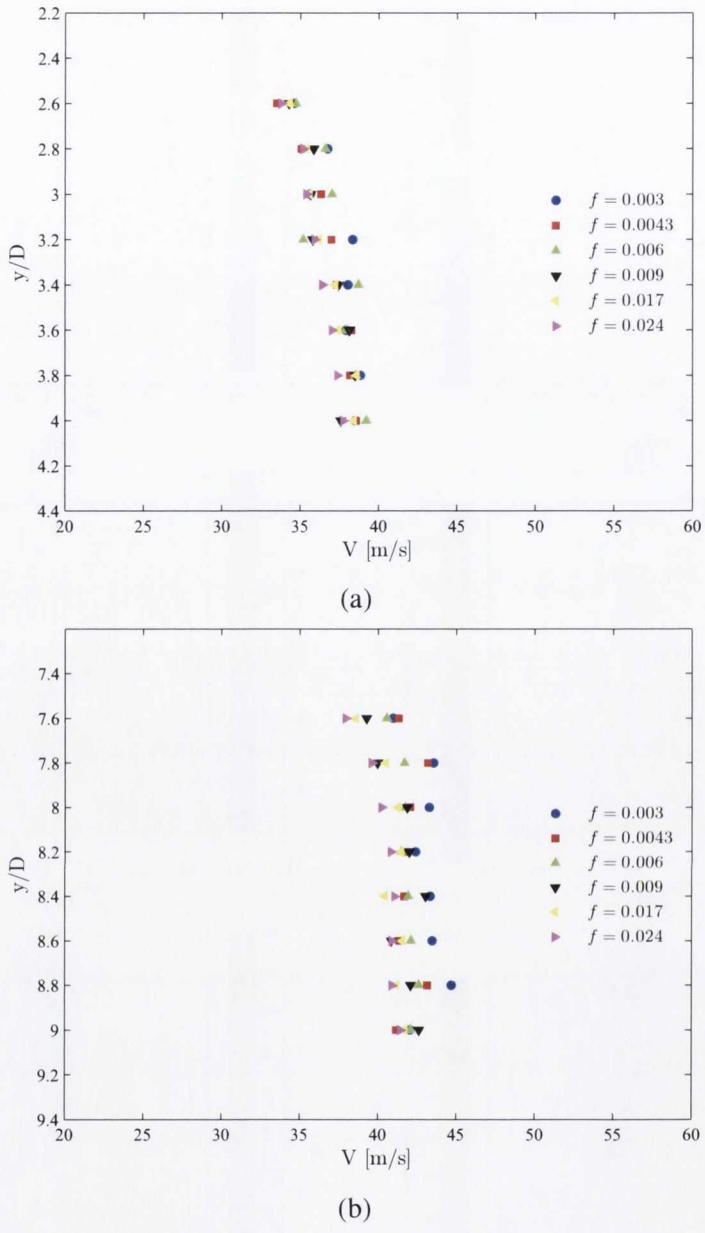

Figure 6.67: Mean droplet velocity magnitudes V as a function of axial location for a range of mist loading fractions, f, when Re = 4500; (a) $H/D = 5$ and (b) $H/D = 10$

rate limitations as discussed previously, may also be a factor.

The mean droplet radial velocity distributions in the far-field provide some further support for the hypothesis that the mist jet is moving in a helical path when Re = 7800. Figure 6.69 shows the radial distributions of the radial velocity component, $V_{r/D}$, for varying axial locations, y/D, in the two far-field regions; the mist loading fraction of $f = 0.0136$ is used as an example. For the $H/D = 5$ case in figure 6.69 (a), the radial location at which $V_{r/D}$ is zero is not on the jet centreline, but has shifted to $r/D \approx 0.4$; when $H/D = 10$ in figure 6.69 (b),

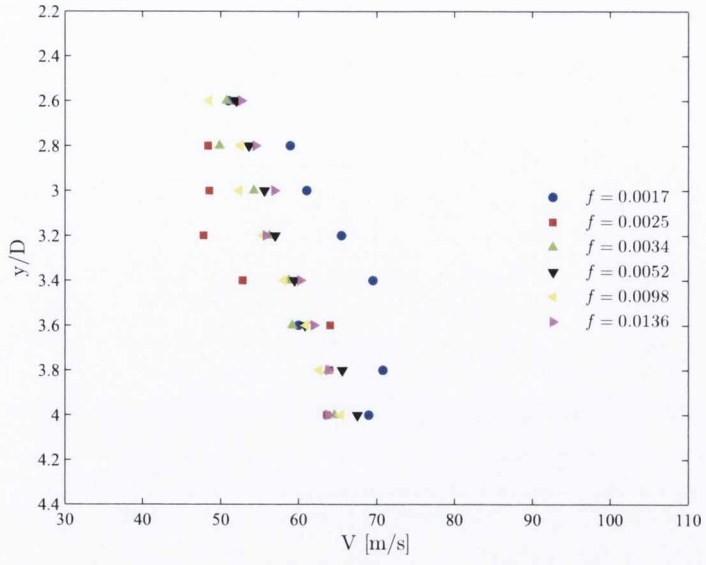

(a)

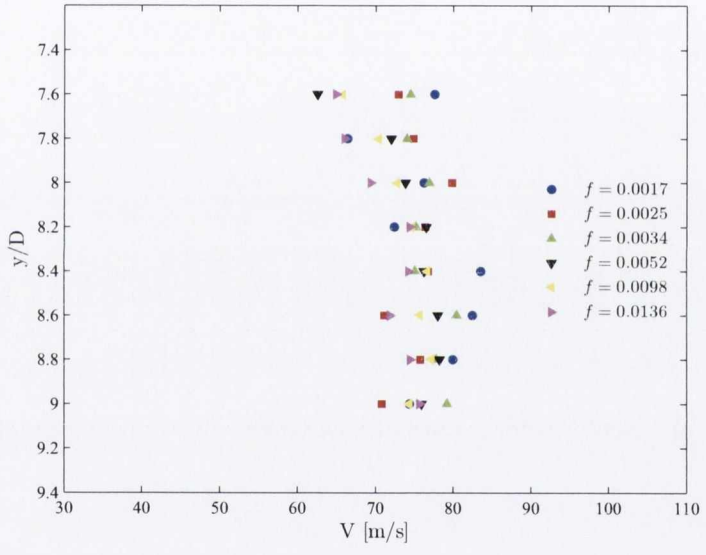

(b)

Figure 6.68: Droplet velocity magnitudes V for y/D and as a function of f when Re = 7800; (a) H/D = 5 and (b) H/D = 10

the point for $V_{r/D} = 0$ has now moved across the jet centreline to $r/D \approx -0.4$. This shifting radial symmetry is consistent with a helical path in the droplet flow, as discussed above. This behaviour occurs across the full range of mist loading fractions investigated, although it can be difficult to discern for the lower values of f as insufficient numbers of droplets are to be found at the edge of the jet. This may also be the cause of the outliers seen in figure 6.69 (a) between $r/D = -0.5$ and $r/D = -1$.

In the atomisation region, there was a clear trend in the evolution of the axial velocity as

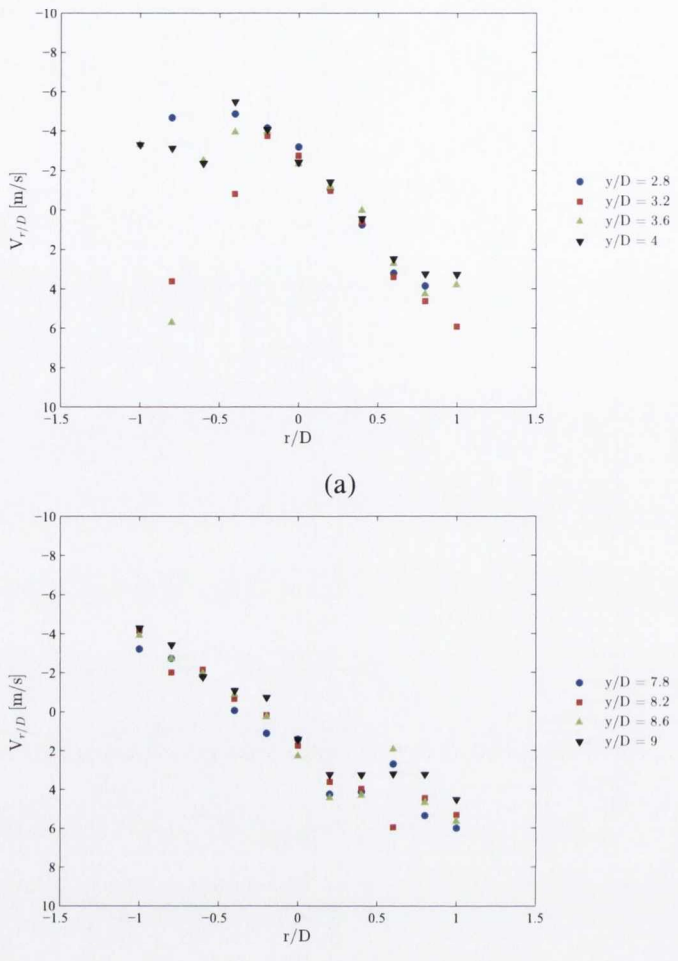

Figure 6.69: Radial distribution of mean droplet radial velocity $V_{r/D}$over a range of axial zones for f = 0.0136 and Re = 7800; (a) H/D = 5 and (b) H/D = 10

y/D increased from 0.4 to 1.6 for both Reynolds numbers across a representative sampling of f; this was shown in figures 6.43 and 6.44. The acceleration of the droplets as they begin to move downstream from the nozzle exit was evident in these figures, as was the emergence of a central core of higher velocity droplets. For Re = 4500 with H/D = 5 and H/D = 10, shown in figure 6.70 for f = 0.024, it is clear that the central core discussed above is well established. A definite maximum in the droplet velocity along the jet centreline can be seen, with the axial velocity decreasing with radial distance from the centreline. The continued acceleration as the droplets move downstream is visible, although with a lower rate of acceleration across y/D when H/D = 10; this is a consequence of the decay in air jet velocity, reducing the rate of droplet acceleration. These data show that for Re = 4500, the mist jet has established a characteristic profile in terms of the velocity by H/D = 5. This behaviour is seen across the

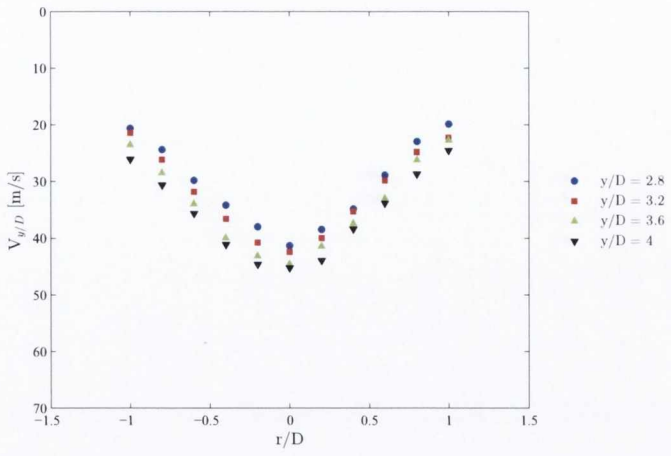

(a)

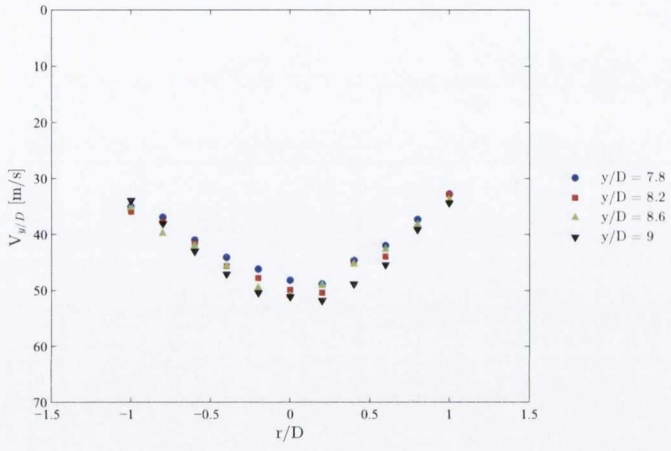

(b)

Figure 6.70: Radial distribution in droplet axial velocity $V_{y/D}$ at a range of axial locations for $f = 0.0246$ and Re = 4500; (a) $H/D = 5$ and (b) $H/D = 10$

range of mist loading fractions considered in this study, although only the case of $f = 0.024$ is presented here.

For Re = 7800, the chaotic nature of the mist jet due to its more violent atomisation under the higher Weber number is evident in the axial velocity distributions for the $H/D = 5$ case, as seen in figure 6.71 (a) for $f = 0.0136$. Here, the axial velocity is at a maximum away from the jet centreline at $r/D \approx 0.75$. Again, if the jet is following a helical path, as per Varga et al. [31], due to the Rayleigh-Taylor instabilities that arise during atomisation under the higher Weber number, then an offset in maximum velocity from the jet centreline is to be expected. The lower velocity droplets at the jet centreline and to the left of the distribution may be droplets that have been ejected from the bulk flow of the droplets. At $H/D = 10$ for the same Reynolds number and mist loading fraction, as shown in figure 6.71

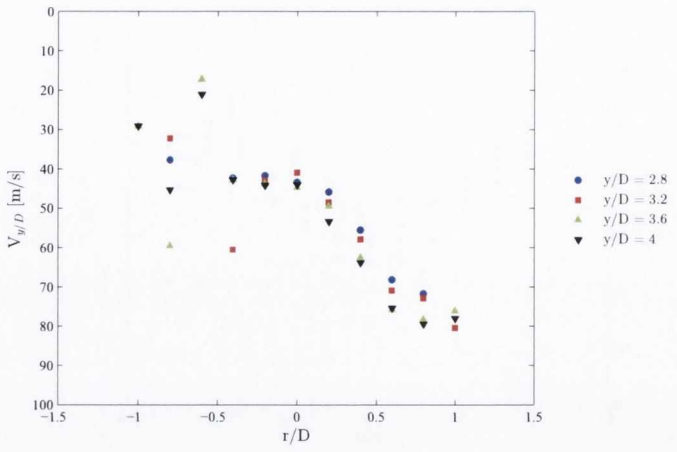

(a)

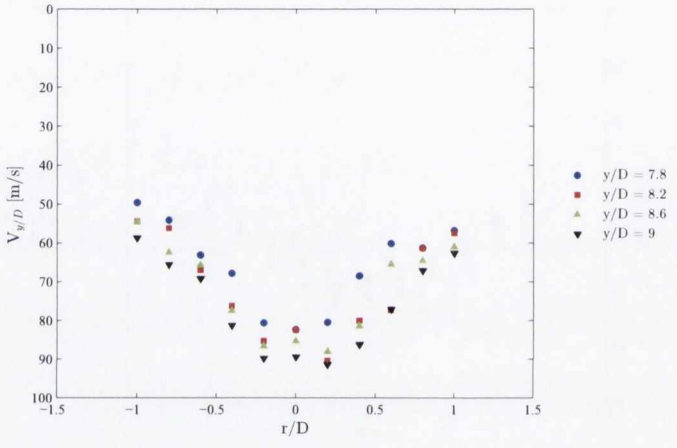

(b)

Figure 6.71: Radial variation in droplet axial velocity $V_{y/D}$ at a range of axial locations for $f = 0.0136$ and Re = 7800; (a) $H/D = 5$ and (b) $H/D = 10$

(b), the behaviour is very similar to the lower Reynolds number case, with a maximum in $V_{y/D}$ found on the jet centreline, along with a gradual decay in the axial velocity with increasing radius. This indicates that the mist jet droplets have been delayed in establishing a uniform axial velocity profile under the higher Reynolds number of 7800, potentially due to the more chaotic nature of the atomisation. The vector plots for Re = 7800 in the zone associated with $H/D = 5$, shown in figure 6.65, indicate that while the vectors have a strong trend towards the positive radial direction, vectors can also be seen moving back towards the jet centreline, $r/D = 0$. Thus, as the axial distance increases to the zone for $H/D = 10$, these droplets may be responsible for the development of the more uniform droplet velocity profile seen in figure 6.71 (b).

Relationship between droplet velocity and size

As was the case for the atomisation region in section 6.2.4, figures 6.72 (a) and 6.72 (b) show the relationship between the droplet size and velocity for Re = 4500 when H/D = 5 and H/D = 10 respectively, and figures 6.73 (a) and 6.73 (b) show the same for the Re = 7800 case. Considering figure 6.72 with Re = 4500, the same general decrease in droplet velocity as the droplet diameter increases is seen here as was observed in the atomisation region, shown in figure 6.45; this trend is particularly clear for H/D = 5. At the downstream locations, however, the range of droplet sizes detected is smaller, as larger droplets have undergone further atomisation. The variation with f is also reduced, with the mist jet becoming more uniform with mist loading fraction as it moves away from the atomisation region. When H/D = 10, the decrease in velocity with diameter is less defined than for H/D = 5. Indeed, the smaller droplets have not accelerated from the H/D = 5 location, resulting in the maximum droplet velocity being seen for a diameter of ~30 μm. This observation of smaller droplets having lower velocity may arise due to the smaller droplets being ejected from the main body of the mist jet and decelerating; Engelbert et al. [22] reported observations of smaller droplets at the edge of their mist jet. For droplets larger than 30 μm, the velocities are seen to decrease as was the case for H/D = 5, as the larger inertia of the bigger diameter droplets continues to inhibit their acceleration.

For Re = 7800, shown in figure 6.73, there is considerably more scatter in the data, with several outliers being detected, particularly for the larger droplet sizes. Nevertheless, there is still more uniformity with mist loading fraction here than in the atomisation zone, and the general trend of a decrease in velocity with increasing diameter can just be seen. For the H/D = 10 case, there may be a slight local maximum in velocity for a diameter of approximately 30 μm, as was seen for Re = 4500, although the level of scatter makes it difficult to identify trends. As is to be expected, across the range of droplet sizes the velocity has increased due to the increased kinetic energy of the air jet at the higher Reynolds number; the rate of acceleration between the two axial locations is greater here than when Re = 4500, as seen previously in the discussions on droplet velocities.

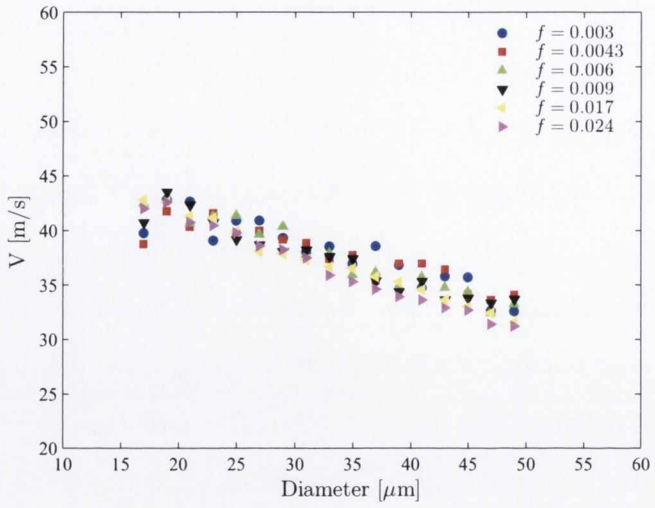

(a)

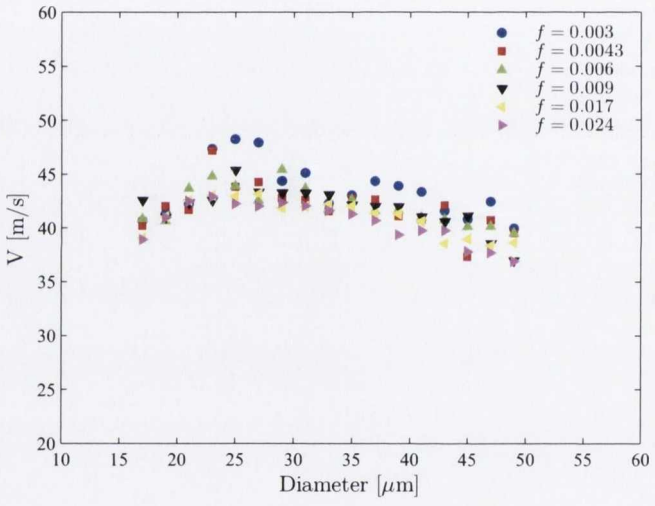

(b)

Figure 6.72: Relationship between droplet diameters and velocities for representative samples of mist loading fraction and Re = 4500; (a) $H/D = 5$ ($2.6 < y/D < 4$) and (b) $H/D = 10$ ($7.6 < y/D < 9$)

6.3.4 Summary of Far-Field Mist Jet Structure

The far-field behaviour of the mist jet structure in terms of droplet velocities and diameters has been examined in this section for the different flow parameters under investigation. The behaviour of the mist jet structure is seen to be markedly different for the two Reynolds number cases, as was also seen in the atomisation region. Thus, the atomisation of the mist jet can be seen to have a continued influence on the mist jet structure in the far-field regions considered here. While the mist jet at the lower Reynolds number exhibited a consistent

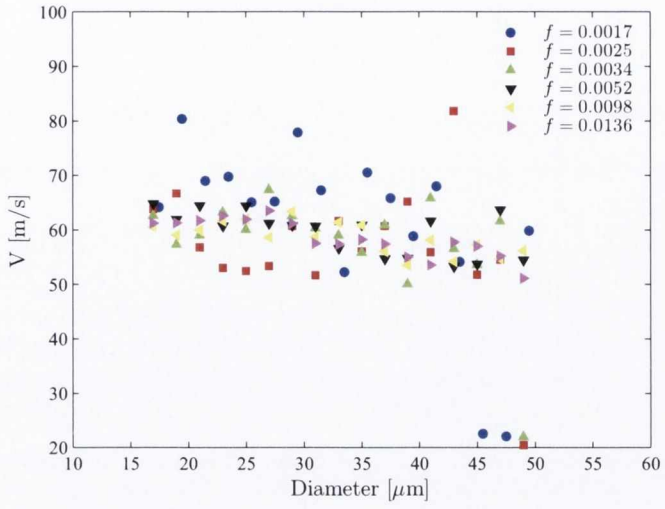

(a)

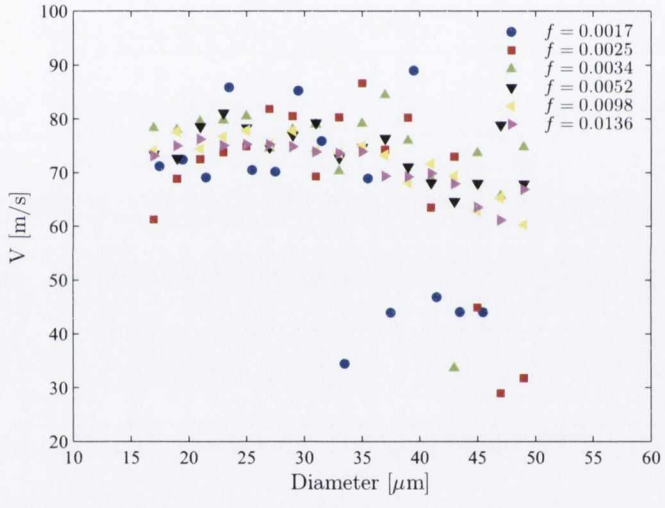

(b)

Figure 6.73: Relationship between droplet diameters and velocities for representative samples of f and Re = 7800; (a) $H/D = 5$ and (b) $H/D = 10$

profile in terms of the radial and axial distributions of droplet properties, for the higher Reynolds number the behaviour was somewhat more chaotic. It is hypothesised, based on the observations of Varga et al. [31], that the droplets follow a helical path, arising from the nature of the atomisation of the liquid jet. The following section presents an examination of the surface liquid film that forms under the mist jet at the different flow parameters of this investigation, and attempts to determine the link between the droplet flow structures identified in the above section and the behaviour of the liquid film on the impingement surface.

6.4 Surface Liquid Film

When the temperature of the impingement surface is lower than the saturation temperature of the mist jet droplets, as in this investigation, liquid will gather on the surface. The form this liquid takes has typically been referred to as a thin film [19, 20], the behaviour of which plays an important part in impinging mist jet heat transfer. As discussed in section 3.6.1, both Graham and Ramadhyani [20] and Chang and Su [19] identified convective heat transfer from the liquid film to the air flow, and sensible heating of the film on the surface. In addition, "laminar-like" [19] convective flow of the film away from the impingement zone, removing heat as it flows outwards, was considered to be significant. Oliphant et al. [21] also suggested that droplet impacts on the film create an unsteady boundary layer, further enhancing heat transfer.

The liquid flow rates considered in those studies were such that the authors assumed a continuous liquid film to form on the surface. However, this may not be the case for the lower flow rates examined in the current investigation. Indeed, Graham and Ramadhyani [20] noted that if the liquid flow rate is very small, the film may evaporate; this is significant as it implies a different mist heat transfer mechanism at very low liquid flow rates as there will be no laminar film flow. Despite this, no local analysis of the liquid film has been performed to date. To address this deficiency, this section uses the high-speed imagery from the shadowgraph imaging data to examine qualitatively the behaviour of the surface liquid film for the range of flow rates and nozzle-to-plate spacings reported in this investigation. For clarity, the surface liquid behaviour is analysed individually for the two Reynolds numbers. For all surface images in this section, $r/D = 0$ corresponds to the jet centreline, as was the case above, and the dimensionless distance from the surface, H/D, is shown on the vertical axis. To aid in identifying the surface in these greyscale images, it is marked with a yellow line.

It should be noted that the nature of the shadowgraph set-up is such that interpreting individual images can be difficult on first viewing. However, repeated testing and extensive examination of the images has led to the identification of the characteristic features discussed in this section with a good degree of confidence. Thus the images here serve to attempt to convey these trends in a concise manner.

6.4.1 Liquid Film for Re = 4500

The behaviour of the liquid film for Re = 4500 displays similar traits for both nozzle-to-plate spacings in this study and can be separated into three regimes for low, intermediate and high mist loading fraction ranges considered in this study.

Surface liquid regime for low mist loading fraction ($0.003 < f < 0.006$)

Figures 6.74, 6.75 and 6.76 show the behaviour at the surface the mist loading fractions of 0.003, 0.0043 and 0.006 respectively. It can be seen from these images that for these relatively low mist loading fractions the liquid on the surface does not form a continuous film. Instead, the low f regime is characterised by the gathering of the surface water into discrete liquid slugs, leaving areas of the surface dry. This behaviour is seen for both H/D, although the slugs are larger when $H/D = 5$ than when $H/D = 10$. In this regime, the high-speed imagery shows that close to the jet centreline, these discrete liquid slugs develop and grow as droplets impinge on the surface. The slugs grow either due to direct impact from an impinging droplet, or else by coming in contact with another nearby liquid slug. In general, if slug coalescence occurs the discrete slug will jump outwards towards the other slug. In this manner, the surface liquid flows outwards from $r/D = 0$. Within this regime, the number of slugs increases with f, and the portion of the surface that remains dry decreases.

Moving radially away from the centre, the slugs are larger because they are the result of the discrete liquid drops that have developed in the centre of the impingement zone coalescing as they move away from $r/D = 0$. These drops are seen to experience a jump not only when they come in contact with another slug, but also when an impinging droplet hits the slug. This impact imparts momentum to the discrete liquid drop, which is transferred to a sudden movement away from the centre. The radially outwards motion of the air wall jet may be promoting motion in this direction; indeed when a slug is hit by an incoming droplet, the resultant splash is generally biased away from the centreline. This is consistent with the findings of Samenfink et al. [73], who examined droplets impinging on a shear driven film and reported that the resultant splash and secondary droplets moved in the direction of the shear flow.

The impingement behaviour of individual droplets, obtained using the high-speed images,

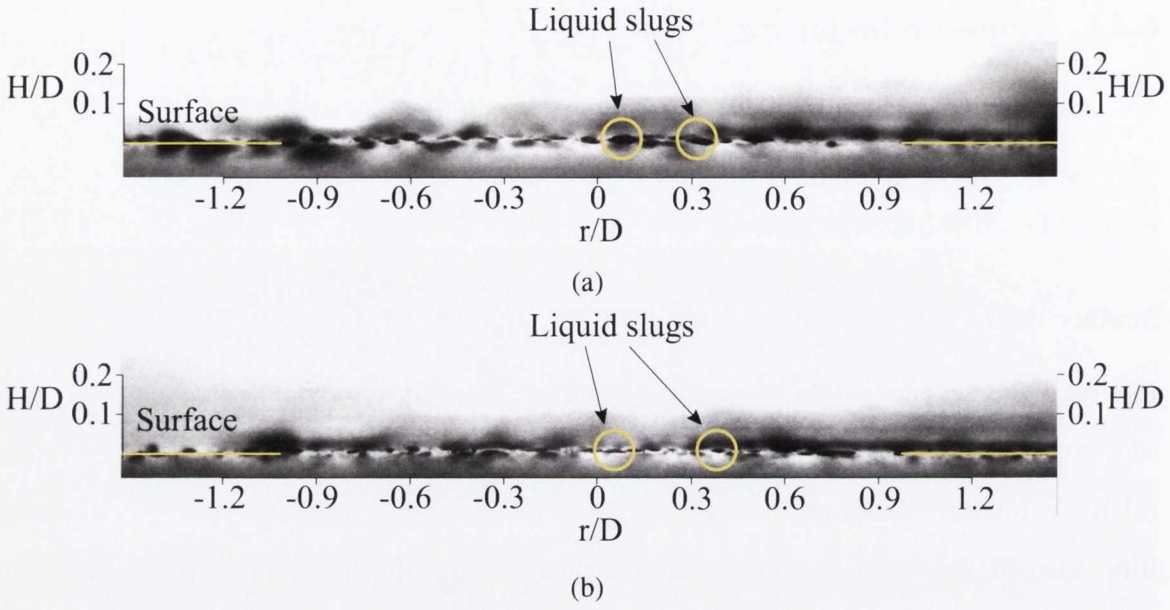

Figure 6.74: Liquid film in the low f regime for Re = 4500 and f = 0.003; (a) H/D = 5 and (b) H/D = 10

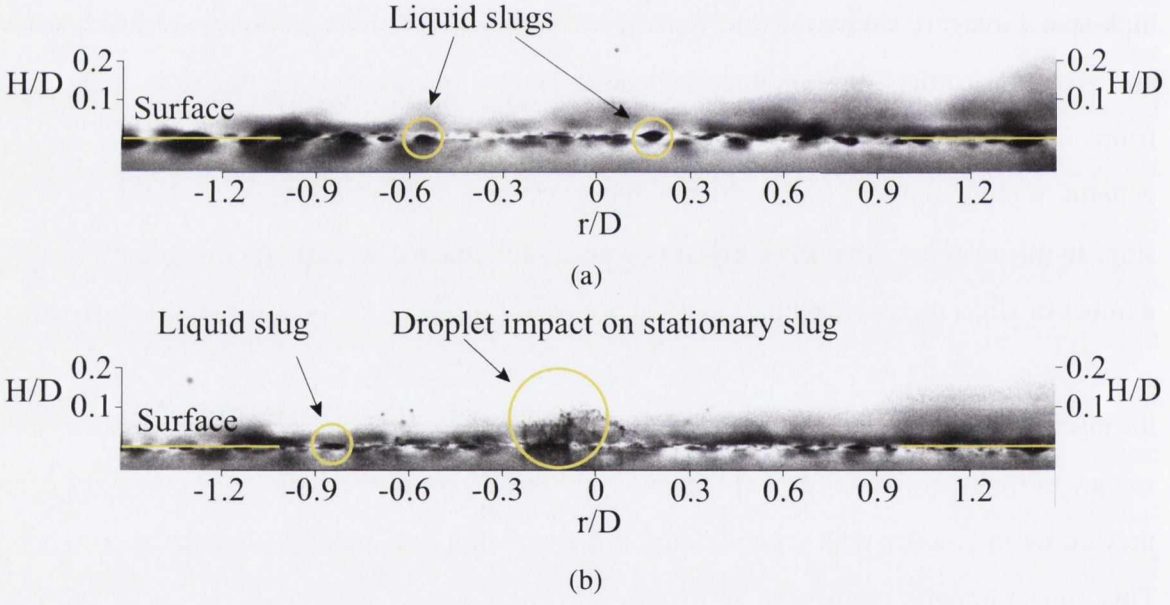

Figure 6.75: Liquid film in the low f regime for Re = 4500 and f = 0.0043; (a) H/D = 5 and (b) H/D = 10

is seen to differ depending on whether the droplet strikes a liquid slug or not. The double-pulse high-speed imagery, as described in section 4.5, results in the capture of frames 5 μs apart, sufficiently fast to allow this type of analysis to be performed. A pair of the double-pulse high-speed images are shown in figure 6.77 for the impingement of a mist jet droplet; figure 6.77 (a) shows the droplet just before impingement, whereas figure 6.77 (b), separated

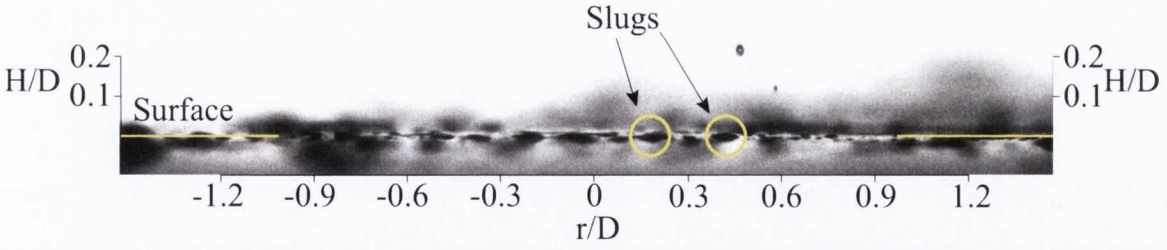

(a)

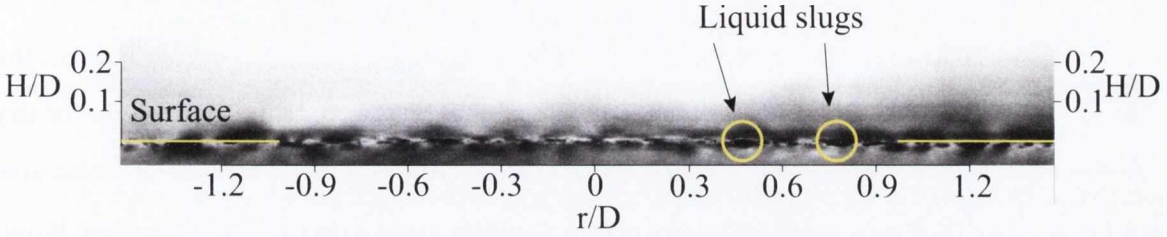

(b)

Figure 6.76: Liquid film in the low f regime for Re = 4500 and f = 0.006; (a) H/D = 5 and (b) H/D = 10

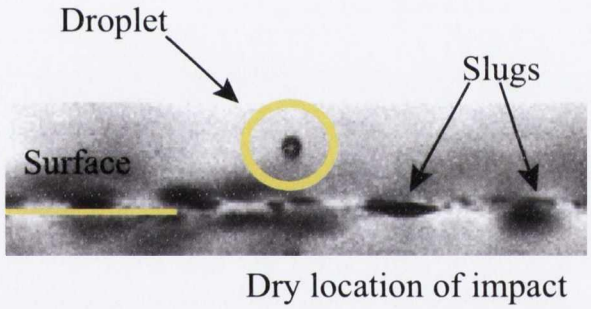

(a)

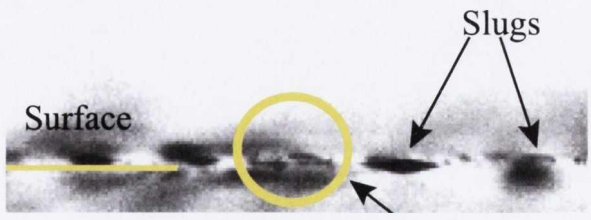

(b)

Figure 6.77: Impact of a liquid droplet on a dry portion of the surface in the low f surface liquid regime. Re = 4500, f = 0.003 and H/D = 5. (a) Before impact and (b) after impact

from the first image by 5 μs, shows the droplet just after impingement. It can be seen that when the droplet strikes the surface between the liquid slugs, as in this case, it tends to

spread without any splashing occurring. As discussed in section 2.5.1, correlations have been produced for determining the splashing threshold for a droplet hitting a dry surface, although significant discrepancies between these exist. Thus, the correlation of Mundo et al. [71], which is based on the Weber number and Reynolds number, gives a threshold which is orders of magnitude larger than that of Walzel [69]. As well as this, the correlations produced have been for droplets falling under gravity, whereas the present study involves a co-flowing air jet. Thus, the process of droplet impact and splashing may be quite different. Indeed, the high-speed imagery in this low f regime shows that the impingement of droplets on the dry surface is characterised by a lack of splashing, as seen in figure 6.77. This is a representative example of behaviour that was repeatedly observed across the images in the surface liquid regime for low mist loading fractions.

Comparing this with images of a droplet impinging on a liquid slug, as shown in figure 6.78 a clear difference in behaviour can be seen. An undisturbed liquid slug can be seen in figure 6.78 (a), while figure 6.78 (b) shows the same slug 1 ms later, just after a droplet impact. Already a crater can be seen developing in the slug, with the beginning of a splash emerging. In the next image, figure 6.78 (c), 5 μs later, a clear splash has been established by the impact of the impinging droplet. This sequence is characteristic of the behaviour when a droplet hits a liquid slug in the low f surface liquid regime. The different impact morphologies that have been observed provide support for the assertion that the surface is not completely covered in liquid in this regime, but rather that discrete liquid slugs exist with dry surface between them. In the work of Roisman and Tropea [63], an image is presented of a droplet impinging on the edge of a liquid film, so half of it hits the film and half the dry surface; this image is reproduced here as figure 6.79. The impact behaviour is very similar to what is seen in this investigation in the low f surface liquid regime. Where the droplet strikes the liquid film, a clear splash is seen to emerge, whereas on the dry surface no such behaviour is seen, with the liquid in the droplet spreading from the impact zone. This is similar to the findings in the work of Yarin and Weiss [72], who reported results for a train of droplets of the same size and velocity striking an initially dry surface that becomes wetted under the repeated impacts of the droplet train. The authors [72] observed that for a given droplet train, droplet parameters that resulted in a splash on the wetted surface did not necessarily give rise to splashing when the surface was initially dry. As discussed in section 2.5.1, Yarin and

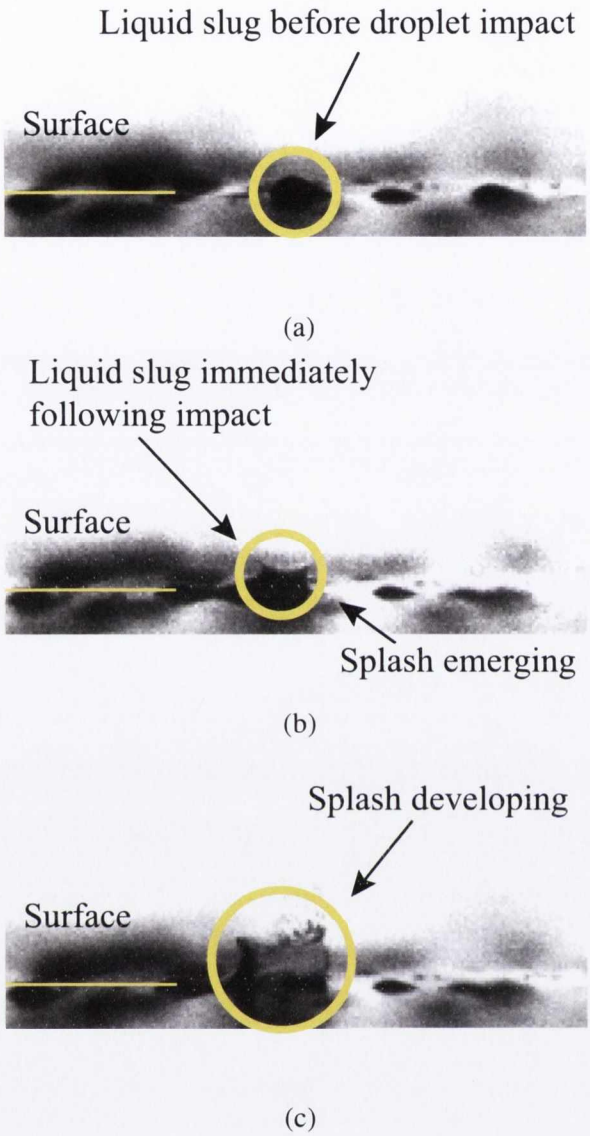

Figure 6.78: Impact of a liquid droplet on a liquid slug in the low f surface liquid regime. Re = 4500, f = 0.003 and H/D = 5. (a) Before impact and (b) and (c) after impact

Weiss [72] identified the splashing resulting from a liquid droplet impinging on a liquid film as being due to a kinematic discontinuity in the film, resulting in a splash occurring more readily for a droplet striking a liquid film than a dry surface. This provides further support for the hypothesis that the surface is likely dry in part in the low f regime.

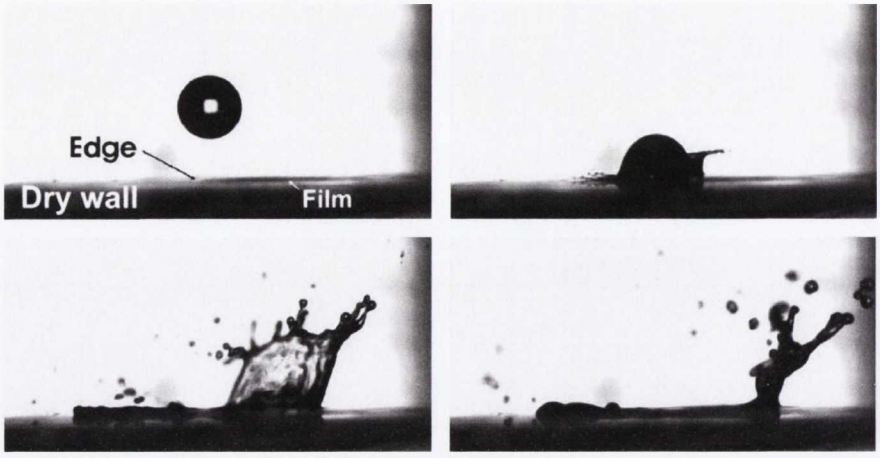

Figure 6.79: Sequence of images from Roisman and Tropea [63] showing the impact of a liquid droplet on the edge of a liquid film. The left side is dry initially and the right side is wetted

Surface liquid regime for intermediate mist loading fractions ($0.006 < f < 0.013$)

As the mist loading fraction increases in the low f regime, the liquid slugs become more numerous and closely spaced, in particular at the centre of the impingement zone. With further increases in f, the behaviour of the liquid on the surface enters what is identified here as the intermediate f regime. Figures 6.80 and 6.81 show sample mist loading fractions that exhibit this intermediate regime behaviour: $f = 0.009$ in figure 6.80 and $f = 0.013$ in figure 6.81. This regime is characterised by the development of a continuous liquid film in the region of $r/D = 0$, with the continued presence of liquid slugs away from the centre.

As f increases and more slugs gather on the surface in the central impingement region, the tendency of the liquid to coalesce increases as the likelihood of contact increases, and the liquid slugs become thinner and elongated, essentially forming localised films. As this happens, the liquid flows outwards in more continuous fashion than when in slug form under the action of the impinging droplets. Thicker slugs remain evident on the periphery of these films; these slugs continue to exhibit the outwards jumps that were seen in the low f regime under the impacts of droplets and coalescence with nearby slugs. Graham and Ramadhyani [20] asserted in their analysis that when a liquid film forms it is thickest in the region where the droplet concentration is highest. However, this investigation shows that when the mist loading fraction is sufficiently low, such that a continuous liquid film is not established, the surface liquid is thicker in regions with less droplet impingement as it takes the form of the liquid slugs described above. This behaviour is seen for both H/D regions at

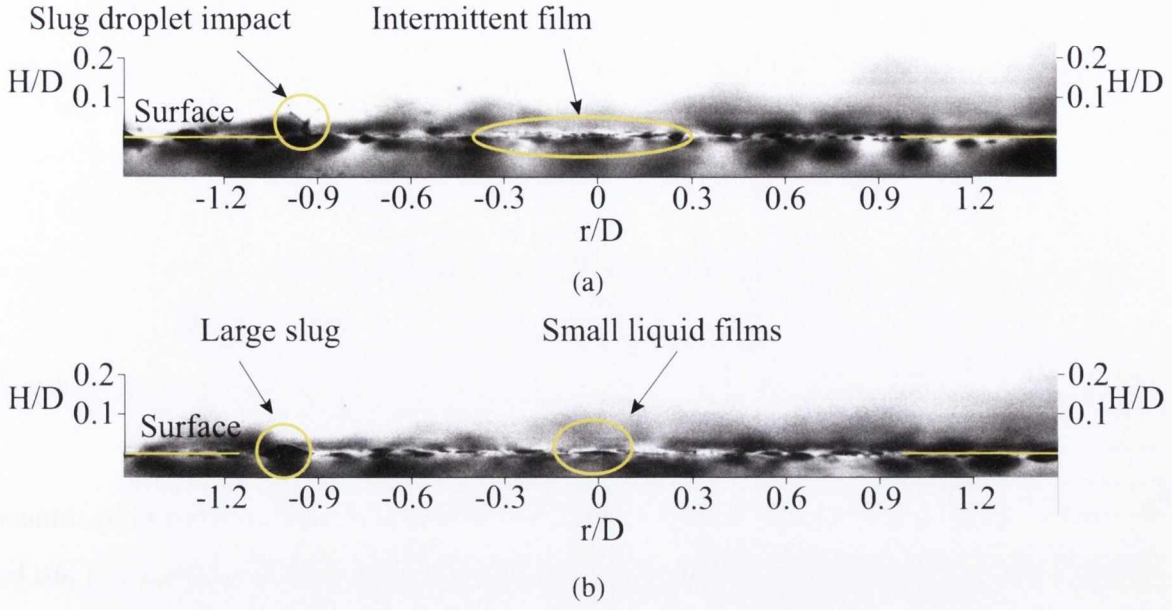

Figure 6.80: Liquid film in the intermediate f regime for Re = 4500 and f = 0.009; (a) H/D = 5 and (b) H/D = 10

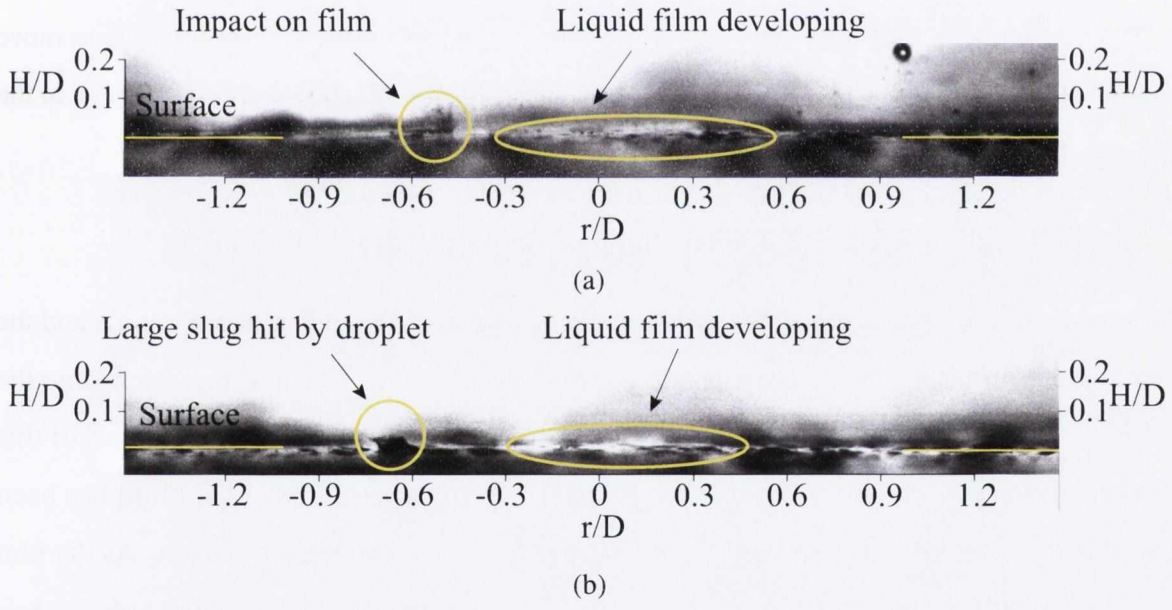

Figure 6.81: Liquid film in the intermediate f regime for Re = 4500 and f = 0.013; (a) H/D = 5 and (b) H/D = 10

the same mist loading fractions. As the mist loading fraction increases, these localised films tend to flow together and merge, leading to the development of a continuous liquid film in the centre of the impingement region and the onset of the high f regime.

In this intermediate f regime, when the droplet strikes one of the peripheral slugs, as seen in figure 6.80 (a), the same splashing behaviour can be seen as when impingement on a

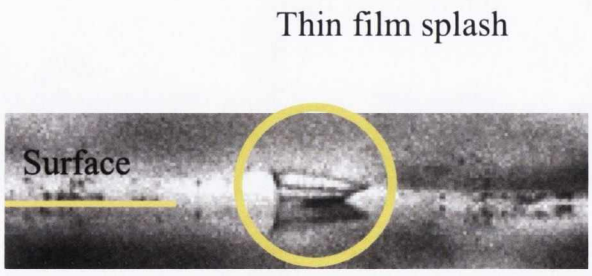

Figure 6.82: Example of the splashing behaviour on the developing liquid film in the intermediate f regime. Re = 4500, $H/D = 5$ and $f = 0.009$

slug occurs in the low f regime. Impacts on the developing film are characterised by thinner splashes forming more uniform crowns. An example of this, although not distinct can just be seen in figure 6.82. This impingement morphology is similar to the thin film droplet impacts studied by Wang and Chen [79] and shown in figure 2.18 in section 2.5.1. The splash tends to form a wider crown that disintegrates into smaller secondary droplets; these are seen to move away from $r/D = 0$, most likely under the influence of the wall jet, in a similar fashion to the shear driven flow of Samenfink et al. [73].

Surface liquid regime for high mist loading fractions ($0.013 < f < 0.024$)

As the mist loading fraction increases within the intermediate f surface liquid regime and the small liquid films begin to coalesce into a continuous film, the behaviour transitions into the regime where a continuous liquid film exists. Figures 6.83 and 6.84 show examples of this regime for $f = 0.017$ and $f = 0.024$ respectively. Here, a continuous liquid film has been established, and towards the edge of the film, some slugs can be seen to remain. As the film flows outwards under the action of the incoming droplets, the momentum imparted from their impacts is eventually dissipated and the film decelerates due to the area increase from radial spreading and friction of the impingement surface. As this happens, the film tends to revert to liquid slugs, again due to the water surface tension. These peripheral slugs are found at the edge for all cases in which a continuous liquid film is established. Evident in these images are the thin liquid crowns that arise from splashing of droplets upon impingement on a thin liquid film. The difference between the liquid crowns formed by droplet impact on a thin film and on a liquid slug is likely due to the fact that the thickness of the slug is significantly

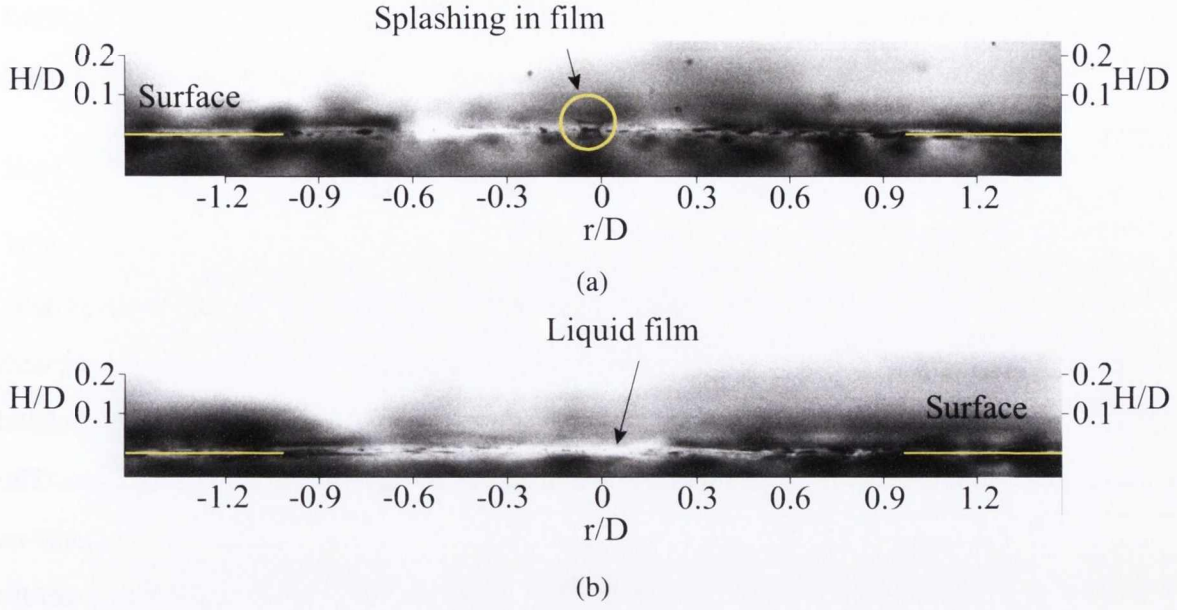

Figure 6.83: Liquid film in the high f regime for Re = 4500 and f = 0.017; (a) H/D = 5 and (b) H/D = 10

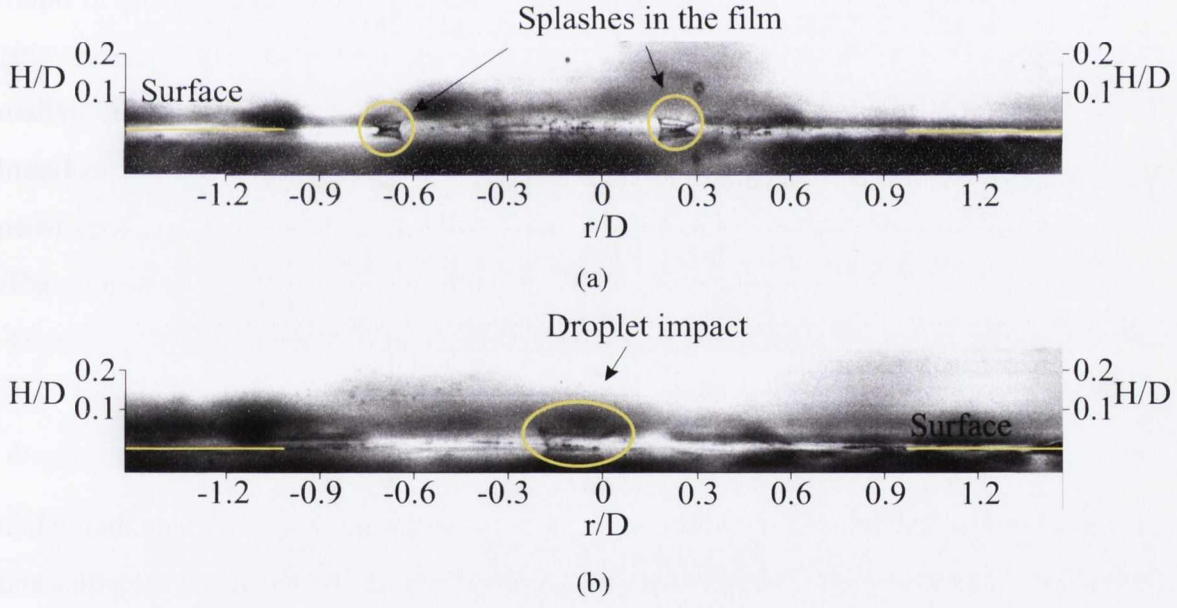

Figure 6.84: Liquid film in the high f regime for Re = 4500 and f = 0.024; (a) H/D = 5 and (b) H/D = 10

larger than that of the thin film, and thus a larger volume of liquid is contained within the local slug than the film. Hillen et al. [82] presented high-speed images of the impact of a droplet on films of different thickness for the same Reynolds and Weber numbers, with larger splashes emerging from thicker films; Wang and Chen [79] reported similar findings. Again, similar behaviour is seen for the two H/D regions considered in this investigation. As the

mist loading fraction is increased further, the continuous liquid film spreads over a greater area of the surface, but is otherwise unchanged. However, it must be noted that no quantitative examination of the film thickness was possible with this experimental set-up.

Summary of liquid film behaviour for Re = 4500

When Re = 4500, the presence of the liquid on the impingement surface evolves with increasing mist loading fraction from the case where discrete liquid slugs are interspersed with dry surface patches, to a transitional regime with thinner, elongated slugs forming localised films, and finally to a continuous liquid film as these localised films coalesce together. The increase in the number of droplets with f is clearly the driving mechanism, because as reported in section 6.3, the droplet sizes and velocities do not vary significantly with f across this range of parameters. The splashing behaviour of the impinging droplets varies from spreading without splash on the dry surface in the low f regime, to large splashes as liquid slugs are struck and to thin crowns similar to those previously reported in the literature [79]. Studies to date on mist jet heat transfer in the non-boiling regime, such as that of Graham and Ramadhyani [20], have considered high liquid flow rates for which a continuous liquid film is assumed to exist. However, for the lower mist loading fractions considered here when Re = 4500, different surface liquid behaviour exists with a consequent effect on heat transfer mechanisms to be expected. This will be considered in the next chapter.

6.4.2 Liquid Film for Re = 7800

The behaviour of the liquid film when Re = 7800 is somewhat more complex than when Re = 4500. This was also the case for the droplet properties, in particular the velocities and the distributions of the number of droplets detected. As a result of the (hypothesised) helical path of the droplets, differences in the impact behaviour of the droplets on the surface exist between the two cases of $H/D = 5$ and $H/D = 10$, particularly in terms of the location of the impacts. However, similarities exist in the behaviour of the surface liquid morphologies for the two H/D regions as the mist loading fraction changes. Indeed, the change in surface liquid behaviour with increasing mist loading fraction bears a resemblance to the lower Reynolds number case. Thus, as was the case for the lower Reynolds number, the surface liquid behaviour is considered here in terms of three f regimes. It should be noted that

because of the higher air mass flow rate when Re = 7800, the mist loading fractions for the same liquid mass flow rates are lower than at the lower Reynolds number.

Surface liquid regime for low mist loading fractions ($0.0017 < f < 0.0034$)

When the mist loading fraction is relatively low, the liquid on the impingement surface is seen to gather in discrete slugs, as was the case when Re = 4500; this is seen for both H/D regions. Examples of this are seen in figures 6.85, 6.86 and 6.87 for $f = 0.0017$, $f = 0.0025$ and $f = 0.0034$ respectively. For both H/D, the liquid slugs are smaller when Re = 7800 than at the lower Reynolds number case. Considering the droplet properties presented in section 6.3, when the Reynolds number is higher, the droplet size decreases; it is likely that the surface liquid slugs are smaller due to this decrease in the droplet size.

While these discrete liquid slugs are seen for both H/D, how they behave differs for the two regions when Re = 7800. As was seen in figure 6.61, when Re = 7800 and $H/D = 5$ there is a distinct tendency for more droplets to be detected on the positive r/D side of the radial distribution; this was also seen in the velocity vectors in section 6.3.3. This observation was attributed to the potential existence of a helical flow path. When $H/D = 10$, this bias to one radial side was not seen to be as strong, and a more uniform distribution was found. This is reflected in the behaviour of the liquid slugs when Re = 7800, which are spread more evenly on the impingement surface for the higher nozzle-to-plate spacing.

When $H/D = 5$, shown in figures 6.85 (a), 6.86 (a) and 6.87 (a), the majority of the droplet impacts occur on the positive r/D side in a small region extending from $r/D = 0.3$ to $r/D = 0.9$. As a result of this, there is a higher concentration of liquid slugs in this area. The slugs present in this region tend to move away from the impingement zone initially at a higher velocity than when Re = 4500. This may be due to greater droplet velocities in the higher Reynolds number case. However, for the region associated with $H/D = 10$, as shown in figures 6.85 (b), 6.86 (b) and 6.87 (b), the liquid slugs do not move away from the impingement zone at high velocity, but rather remain almost stationary in the low f regime. Thus, the initial rapid movement of the slugs when $H/D = 5$ is more likely due to the high concentration of droplet impacts. The surface liquid must spread out upon impact, and as asserted by Pais et al. [125], forces the liquid to move rapidly away from the impingement zone. These slugs tend to have decelerated by $r/D = 0.6$, and have increased in size due to

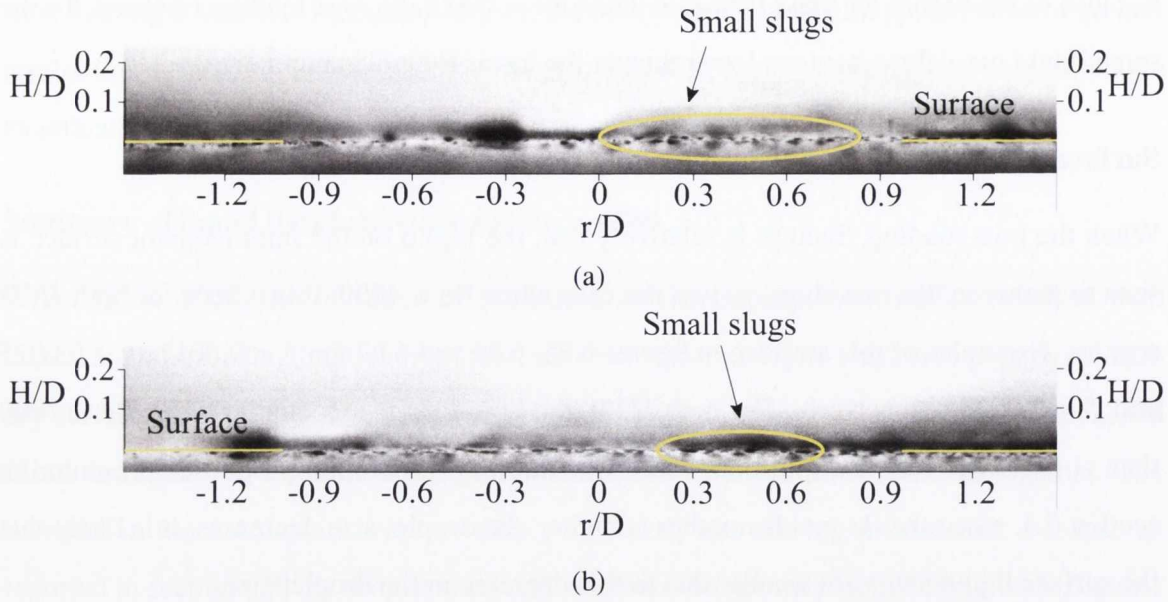

Figure 6.85: Liquid film in the low f regime for Re = 7800 and f = 0.0017; (a) H/D = 5 and (b) H/D = 10

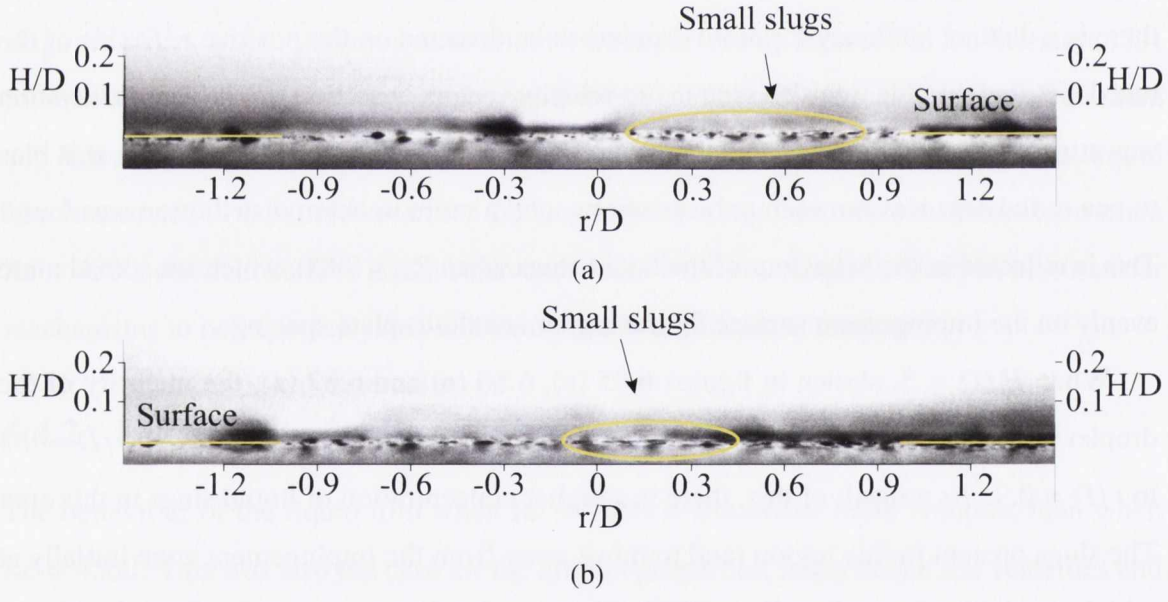

Figure 6.86: Liquid film in the low f regime for Re = 7800 and f = 0.0025; (a) H/D = 5 and (b) H/D = 10

coalescence. If another liquid slug does not come into contact with a stationary slug, it is seen to decrease in size while remaining in the same place as evaporation takes place.

The more uniform radial distribution of the detected droplets for the region associated with H/D = 10 means that the discrete liquid slugs in this case are more evenly spread across the impingement surface. In this case, as mentioned above, the discrete liquid slugs tend to

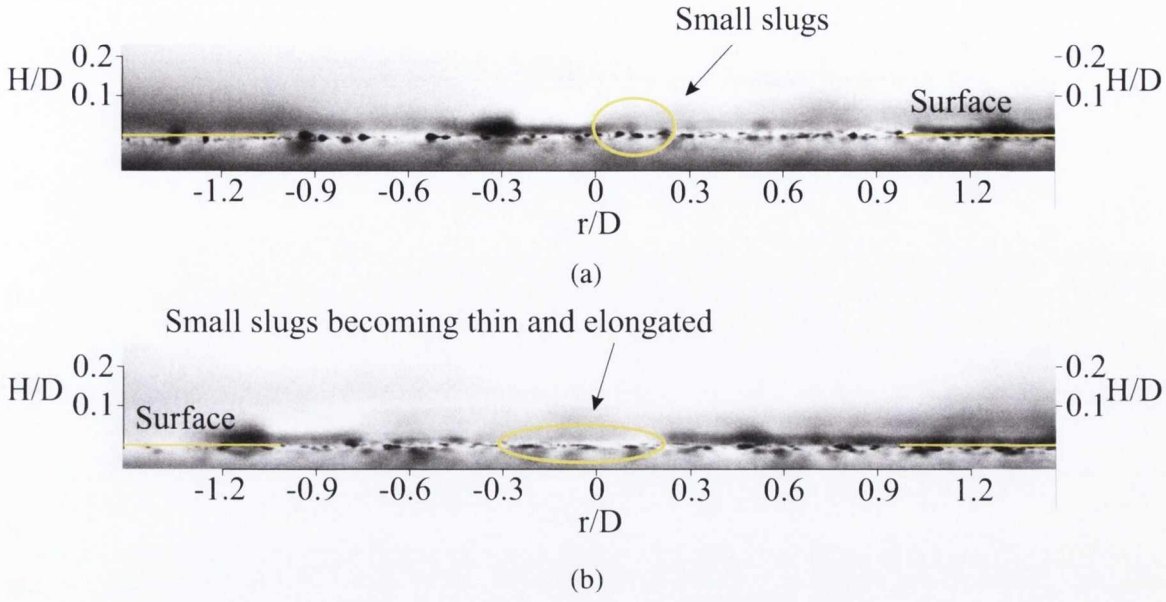

Figure 6.87: Liquid film in the low f regime for Re = 7800 and f = 0.0034; (a) H/D = 5 and (b) H/D = 10

remain mostly stationary while oscillating slightly under the action of the air wall jet, only moving outwards if directly struck by a droplet or coming in contact with a neighbouring slug; this is less common than when Re = 4500. As the liquid remains mostly stationary, the slugs are seen to decrease in size over time as they evaporate, unless they are refreshed by coalescence with a neighbouring slug or a droplet impact.

Increasing the mist loading fraction within this regime results in an increase in the number of slugs for both H/D cases. This means that for the H/D = 5 surface region, the liquid slugs spread further before coming to a stop, and can be seen to increase in size. The impingement zone also expands with f for H/D = 5, since the number of detected droplets was shown in section 6.3 to increase radially with f. For the case of H/D = 10, the behaviour is similar to the lower Reynolds number case. Increased mist loading fraction results in a larger number of discrete slugs, and hence more interaction and coalescence between the slugs, resulting in more movement of the slugs radially outwards. At the upper end of the mist loading fraction within this regime, f = 0.0034, the liquid slugs near the centre become more elongated and thin for the H/D = 10 case, and begin to take on the appearance of localised films, previously seen to be present in the intermediate f regime for Re = 4500 in section 6.4.1.

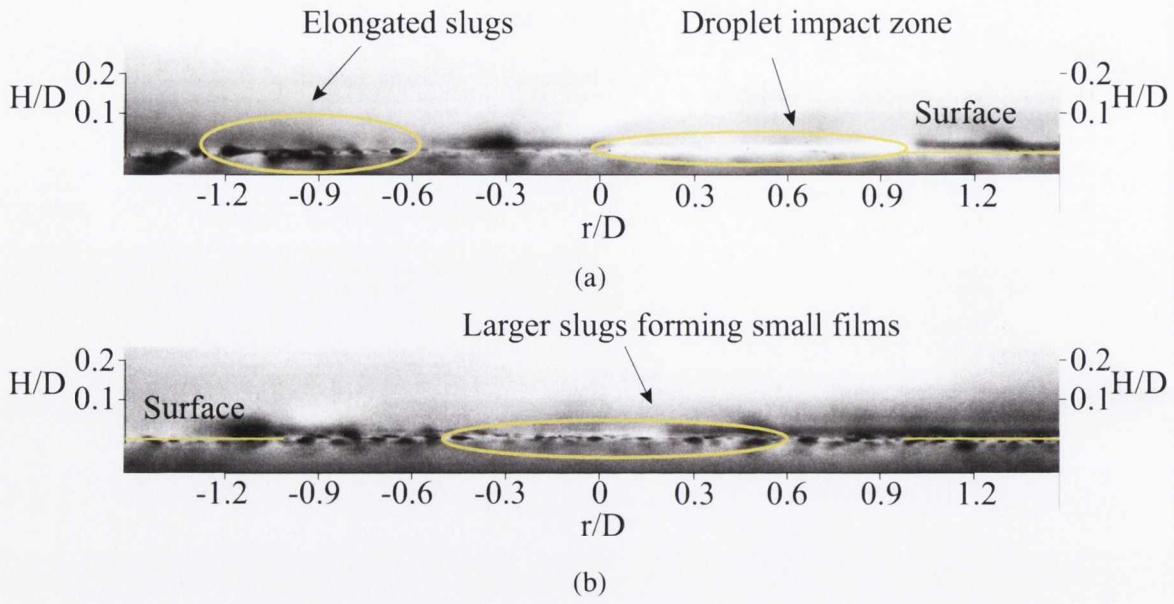

Figure 6.88: Liquid film in the intermediate f regime for Re = 7800 and f = 0.0052; (a) H/D = 5 and (b) H/D = 10

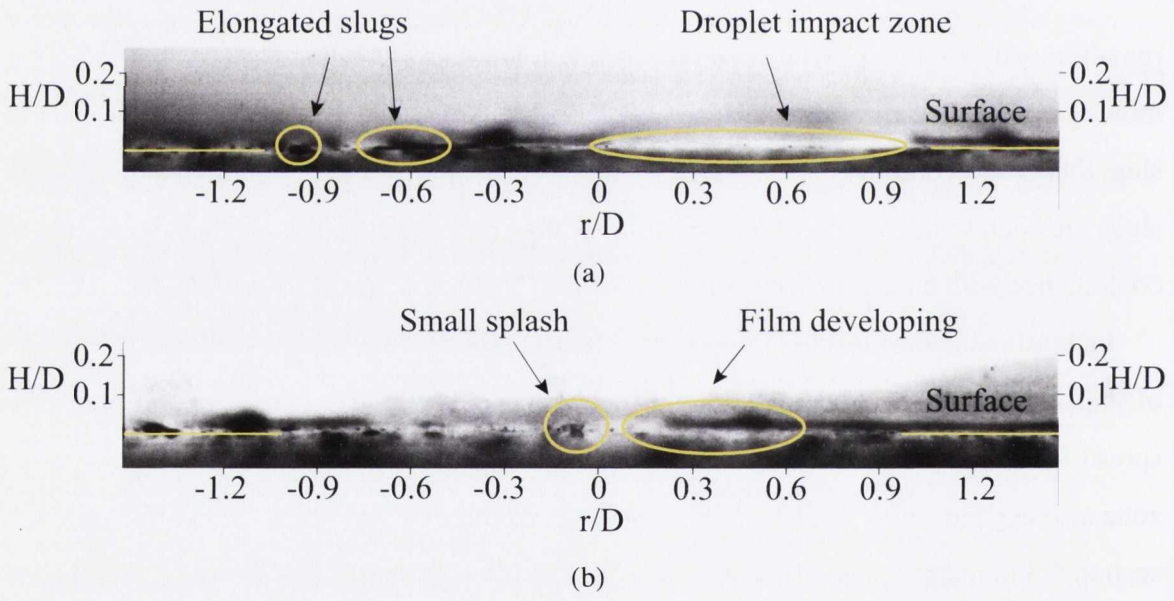

Figure 6.89: Liquid film in the intermediate f regime for Re = 7800 and f = 0.0077; (a) H/D = 5 and (b) H/D = 10

Surface liquid regime for intermediate mist loading fractions ($0.034 < f < 0.0077$)

At Re = 4500, the intermediate f surface liquid regime was characterised by the emergence of a continuous film as the concentration of slugs, and hence coalescence, increased, and localised films began to merge. For the region associated with H/D = 10 the same behaviour is seen at Re = 7800 for intermediate mist loading fractions; this can be seen in figures 6.88

(b) and 6.89 (b) for $f = 0.0052$ and $f = 0.0077$ respectively. As more liquid arrives on the surface with increasing f, the discrete liquid slugs become more elongated and thin as they begin to flow together and coalesce, forming the same sort of localised films as seen for Re = 4500 in the intermediate f range. Further increases in f lead to these films coming into contact and merging, beginning the formation of a continuous liquid film that flows outwards from the impingement zone. Again, slugs remain on the periphery of these localised films, as was also the case when Re = 4500. Small splashes in the developing films also begin to appear, as identified in figure 6.89 (b).

When $H/D = 5$ in this intermediate range, the droplets continue to strike the impingement surface primarily on the positive r/D side, as expected from the distributions in section 6.3, with the impact zone spreading further with increasing mist loading fraction. Figures 6.88 (a) and 6.89 (a) show the impingement behaviour for $H/D = 5$ with the droplet impingement zones marked in both images. From the high-speed images, it appears that as the concentration of droplets impinging on the surface in the impact zone increases with f in the intermediate regime, intermittent liquid films develop and are flushed rapidly away from the impingement zone; this is followed by the re-establishment of a film from the high droplet concentration at impact. This results in larger liquid slugs forming at the edge of the impact zone that become elongated, as identified in figure 6.88 (a), and start to resemble the localised films found when $H/D = 10$. As f increases in this region, the generation of these intermittent films increases in frequency and they spread radially, until the high f surface liquid regime is established and an essentially continuous film in the impingement zone exists. The slugs at the edge move faster and become more elongated as mist loading fraction increases, resulting in small localised films that move outwards more rapidly than when $H/D = 10$. As the mist loading fraction continues to increase, these localised films form more frequently as the frequency of concentrated droplet impacts increases.

Surface liquid regime for high mist loading fractions ($0.0077 < f < 0.0136$)

As was the case for Re = 4500, in the high mist loading regime for Re = 7800 a continuous liquid film has been established on the impingement surface. However, the means by which this has been formed differs for the two H/D regions, and follows on from the behaviour of the intermediate f regime for each case. Figures 6.90 and 6.91 show the surface liquid behaviour

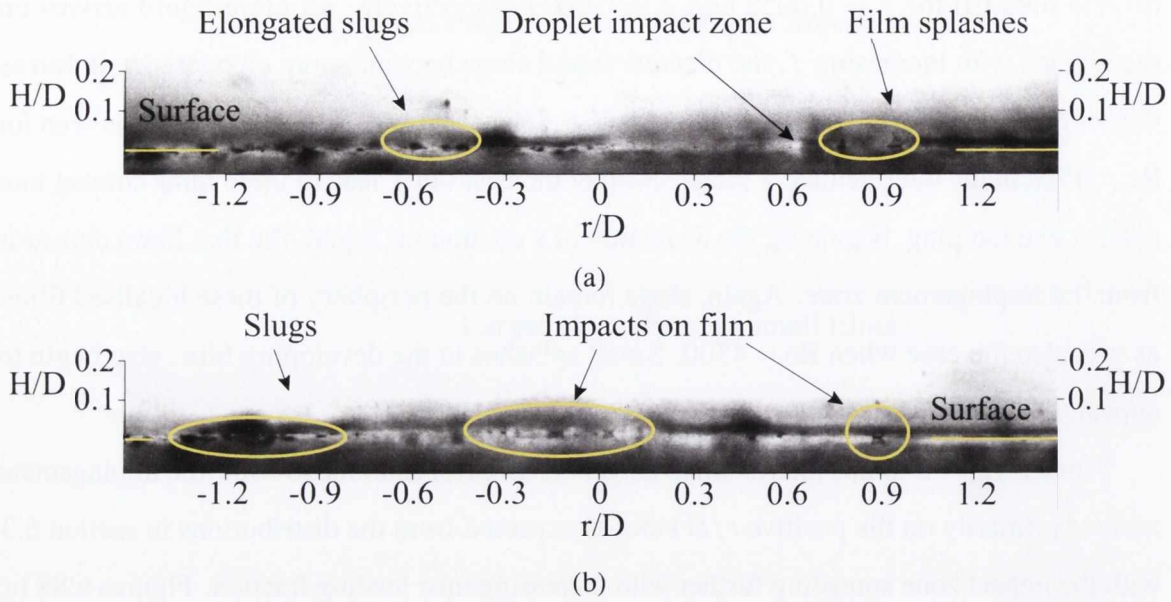

Figure 6.90: Liquid film in the high f regime for Re = 7800 and f = 0.0098; (a) H/D = 5 and (b) H/D = 10

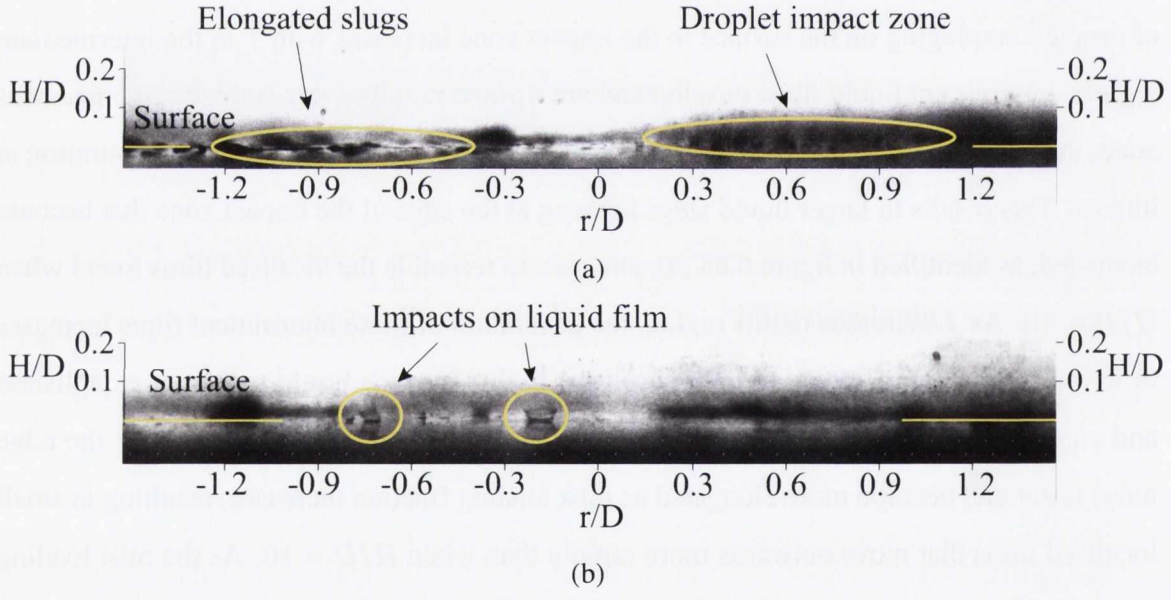

Figure 6.91: Liquid film in the high f regime for Re = 7800 and f = 0.0136; (a) H/D = 5 and (b) H/D = 10

for f = 0.0098 and f = 0.0136 respectively with the region associated with H/D = 5 shown in part (a) of each figure, and the region associated with H/D = 10 in part (b).

When H/D = 5, the frequency of concentrated droplet impacts is such that a continuous liquid film has developed. This film is rapidly flushed away and refreshed by the droplet impacts. Splashes in the film can be seen in both examples shown here. As the mist loading

fraction increases in this region, the continuous film spreads further outwards from the impingement zone, again primarily on the positive side of the radial distribution between $0 < r/D < 0.9$. The elongated slugs are more frequent here, leading to more of the localised films occurring at the periphery of the continuous film. These are now more likely to encounter another film and coalesce, increasing the size of these localised films. For $H/D = 10$, the localised films have merged into a continuous film, the same as in the lower Reynolds number case. This continuous film spreads outwards under the action of impinging droplets. Similar splashes from droplet impacts on the film can be seen as were identified for the lower Reynolds number.

Summary of liquid film for Re = 7800

For the higher Reynolds number, the behaviour of the liquid on the impingement surface changes with mist loading fraction. Although the behaviour differs somewhat from that at the lower Reynolds number, the surface liquid morphology undergoes broadly similar changes with increasing mist loading fractions as was seen for the lower Reynolds number. Initially discrete liquid slugs are seen for both H/D. In the intermediate f regime, the behaviour differs for the two cases; when $H/D = 5$ intermittent films that are rapidly flushed away are observed whereas when $H/D = 10$, the liquid slugs become thinner and more elongated, coalescing with their neighbours into small localised films. Further increases in f lead to the establishment of continuous liquid films for both H/D, although the formation process differs for the two cases; this follows from the surface liquid behaviour observed.

6.4.3 Synopsis of Liquid Film Behaviour

The high-speed images of the impingement surface examined in this section show that, despite some differences in surface liquid characteristics with jet Reynolds number and nozzle-to-plate spacing, the mist loading fraction regime primarily determines the overall surface liquid behaviour. In all cases, with increasing mist loading fraction the surface liquid evolves from discrete liquid slugs, to localised films, followed by the formation of the continuous liquid film assumed by previous authors [19–21] to exist under mist jet impingement. For the mist loading regime considered in this investigation, a map of changing surface liquid morphologies can be produced, similar to the maps shown in chapter 2 for the atomisation of

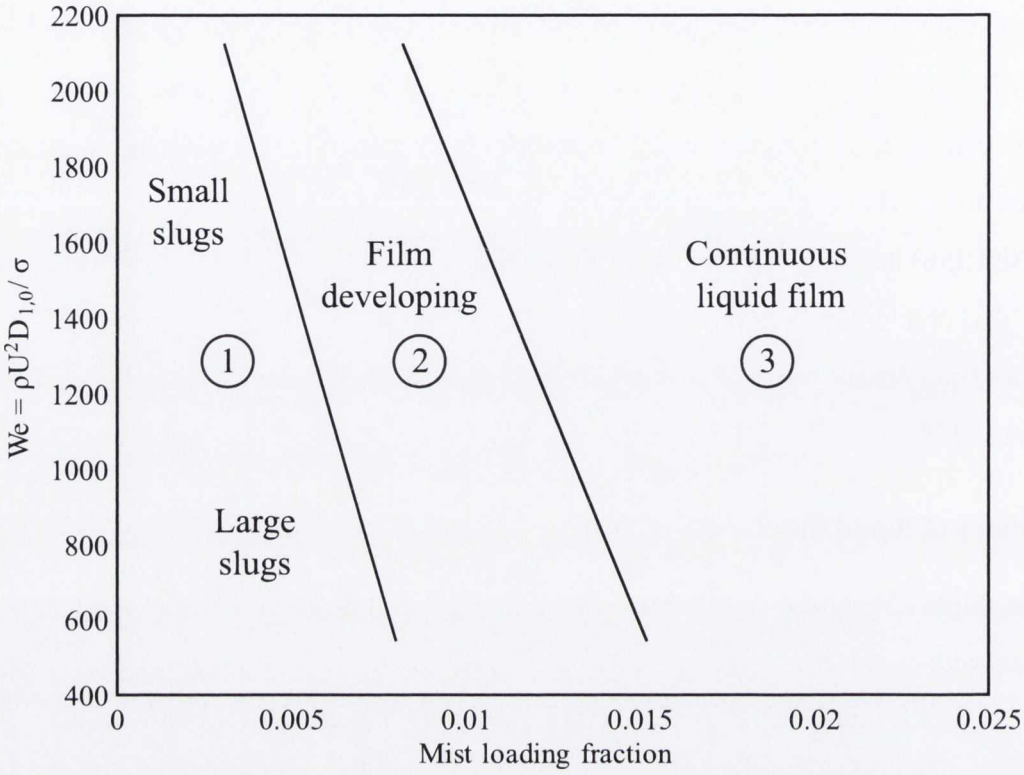

Figure 6.92: Classification of surface liquid behaviour for low mist loading fractions.

a liquid jet into a spray or a mist jet. This map is shown in figure 6.92. Here, the mean droplet Weber number, defined as $We = \rho U^2 D_{1,0}/\sigma$ and based on the droplet properties, is plotted versus the mist loading fraction f. The mean droplet velocity and diameter used is that for the two regions associated with the different H/D, found using the shadowgraph imaging data of section 6.3. The Weber number is chosen as it encapsulates both droplet velocity and size; the arithmetic mean diameter is used as the characteristic length rather than the Sauter mean diameter because $D_{3,2}$ can be biased towards larger droplets, as discussed in section 6.2.

The three regimes in this map can be described as:

1. Low f regime. Discrete liquid slugs form on the surface that move outwards from the impingement zone due to coalescence with neighbouring slugs or under direct droplet impact.

2. Intermediate f regime. This is characterised by the merging of the discrete liquid slugs into thinner, elongated localised films, with some slugs remaining at the edge.

3. High f regime. A continuous liquid film that flows outwards from the impingement zone is seen. Liquid slugs remain at the edge, due to surface tension, as the film momentum dissipates.

In studies to date on the heat transfer without boiling of an impinging mist jet it has been assumed that a continuous liquid film exists on the surface. For the mist loading fractions in this investigation this has been found not to be the case. As such, the following chapter examines the heat transfer behaviour of the impinging mist jet in the light of the three surface liquid regimes identified here. A specific objective is to arrive at a clearer understanding of the heat transfer mechanisms when a continuous liquid film is not established on the impingement surface.

6.5 Summary of Mist Jet Structure Results

In this chapter, the structure of the mist jet has been examined, in terms of droplet size and velocity, as a function of Reynolds number, mist loading fraction and nozzle-to-plate spacing. The atomisation behaviour was first considered, with information on the evolution of the droplet properties provided. The Weber number was identified as an important parameter in determining the atomisation behaviour. Next, the behaviour of the mist jet in the far-field was examined, using the atomisation region data to explain the structures that were observed where possible. These far-field data showed that the mist jet developed a uniform structure in terms of droplet velocities and sizes, although this occured at different downstream distances, depending primarily on the jet Reynolds number. Finally, the behaviour of the liquid on the impingement surface was considered, as no such investigation has been reported to date of the local impingement surface for a mist jet in the current parameter. Again, the structure of the mist jet in both the atomisation region and the far-field was used to aid understanding of the surface liquid morphology. It was determined that for the dilute mist jet, at the very lowest mist fractions the impingement surface was not completely wetted. Three regimes dependent on the mist loading fraction were identified, with the surface liquid forming discrete slugs for the lowest mist fractions, which began to coalesce into localised thin films as f increased, before finally a continuous film emerged with further increases in mist fraction. The information presented in this chapter will be used in the next chapter to develop a clearer

understanding of dilute mist jet heat transfer without boiling.

Chapter 7

Mist Jet Heat Transfer Results

In this chapter, heat transfer results for the impinging non-boiling regime mist jet are presented and discussed, in light of the flow visualisation contained in chapter 6. The objective is to enhance current understanding of the heat transfer phenomena involved in dilute mist jet impingement without boiling.

To begin, single phase heat transfer results for the atomising nozzle, using air only, are presented. This serves to provide baseline results to facilitate examination of the mist jet heat transfer enhancement. Next, time-averaged heat transfer profiles are presented for the mist jet for varying mist loading fraction, Reynolds number and nozzle-to-plate spacing, H/D. For the same parameter range, simultaneous temporal heat transfer fluctuations and flow visualisation data, obtained using the shadowgraph imaging technique, are also examined in order to explain more fully the trends observed in the time-averaged profiles, and thus the underlying heat transfer phenomena.

7.1 Single Phase Heat Transfer Distributions

The motivation behind the addition of water droplets to an air jet is to improve the cooling performance of the air jet. Therefore, in order to illustrate this improvement, single phase air heat transfer results are presented in this section. As reported in section 2.3.1, the outer diameter of the annular nozzle, D, is used to normalise the radial and nozzle-to-plate distances, r/D and H/D respectively, while the hydraulic diameter, D_h is used to calculate the Reynolds number. Thus, the Reynolds number is defined as

$$\mathrm{Re} = \frac{U_a D_h}{\nu} \tag{7.1}$$

As discussed in section 2.3.1, Trávníček and Tesař [55] observed bistability and hysteresis

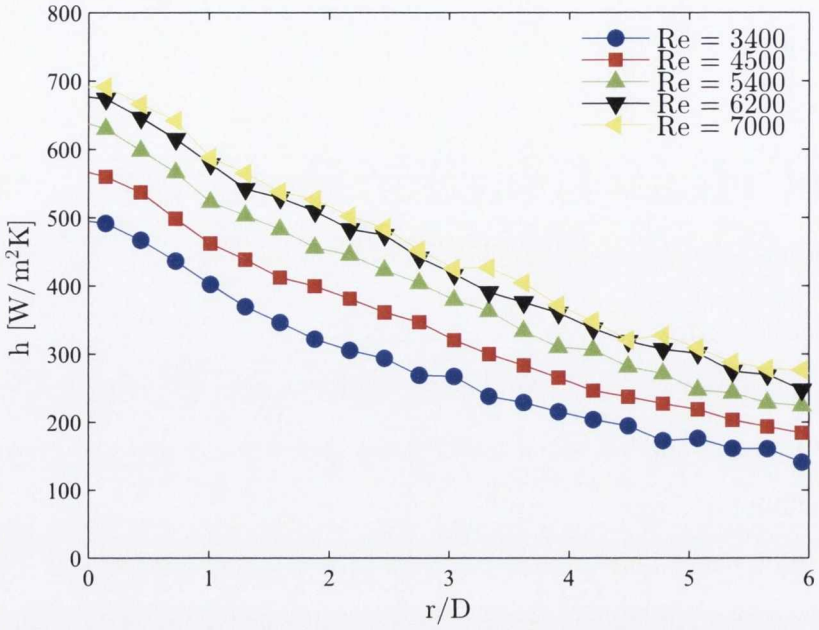

(a)

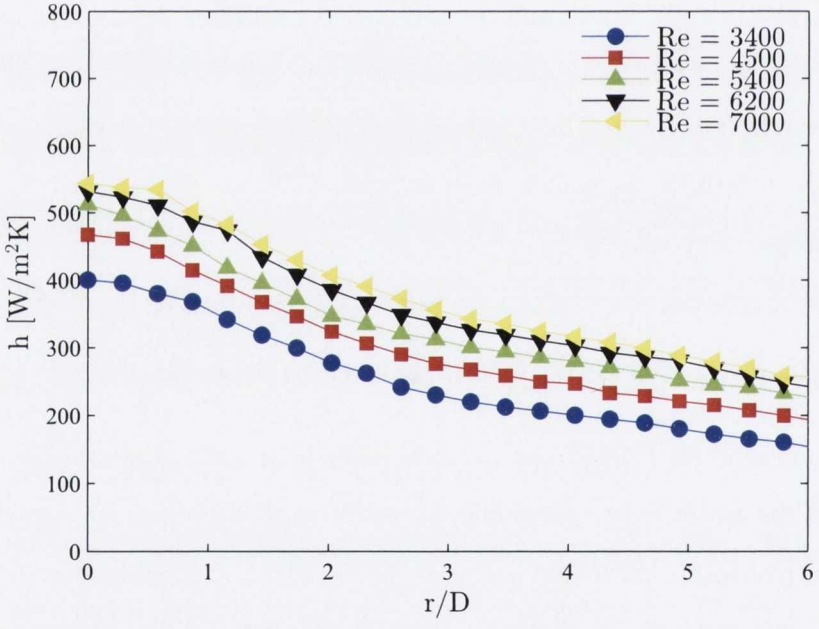

(b)

Figure 7.1: Annular air jet time-averaged heat transfer profiles as a function of Reynolds number for (a) $H/D = 5$ and (b) $H/D = 10$

in the structure of the annular air jet, which could have an influence on the jet heat transfer. However, the authors surmised that this bistability was linked to very small annular jet widths; hysteresis in jet structure was observed for a diameter ratio of $D_i/D_o = 0.947$, but

not for $D_i/D_o = 0.767$. In the current study, the diameter ratio is $D_i/D_o \approx 0.74$ and the nozzle-to-plate spacings considered are all higher than that for which hysteresis has been observed. As such it is concluded that this aspect of annular jet flow is not present here.

The time-averaged heat transfer coefficient profiles for the air only annular jet are presented in figures 7.1 (a) and 7.1 (b) for $H/D = 5$ and $H/D = 10$ respectively and a range of Reynolds number. Typically for single-phase jets, the Nusselt number is used to characterise heat transfer. Here, however, the heat transfer coefficient is used as this is what is used to quantify the mist jet heat transfer, as discussed in section 3.3.

As with a conventional round air jet, the annular air jet profiles show a bell-shaped distribution, with a peak in heat transfer in the stagnation region and a decrease as the radial distance increases from the stagnation zone [4]. For an air jet, the peak in stagnation heat transfer coefficient is attributed to higher instantaneous velocities on the jet axis and the continuous entrainment and mixing of cold fluid into the stagnation region, resulting in a high driving temperature difference in this location. Yang et al. [46] observed, using PIV, that for $H/D = 4.1$ the annular jet impinges on a surface in a similar manner to a circular air jet, with a peak in pressure and heat transfer on the jet axis. The smallest H/D reported here is 5, so the observation of a local maximum on the jet axis as seen in figures 7.1 (a) and 7.1 (b) is to be expected. As is the case for a circular air jet in the same H/D region, the Nusselt number increases with Reynolds number as a result of the increased air jet velocity leading to more turbulent mixing in the wall jet region; O'Donovan and Murray [4] reported a local maximum in heat transfer fluctuations in the stagnation region for similar H/D. As the radial distance increases, the wall jet velocity decays, resulting in less turbulent mixing of the boundary layer and lower heat transfer fluctuations, leading to a decrease in Nu [4]. Heat transfer distributions for large radial distances have not been reported for annular jets; however as the structure becomes more like that of a circular jet with increasing H/D it can be assumed that the annular jet in this study exhibits similar behaviour.

Small secondary inflections in the heat transfer distributions can just be seen for $H/D = 5$ and the higher Reynolds numbers at a radial location of approximately $r/D = 2.5$. For circular air jets, these have been attributed to a transition in the wall jet boundary layer to a turbulent flow [4]. The inflections are not visible for $H/D = 10$ as increasing the nozzle height results in the shear layer of the jet penetrating the jet centre, so the transition to a

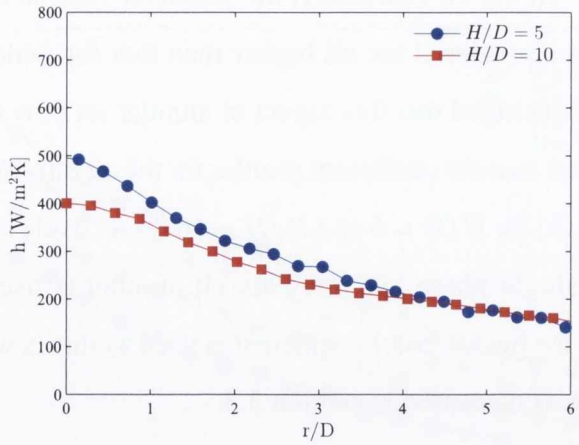

(a) Re = 3400

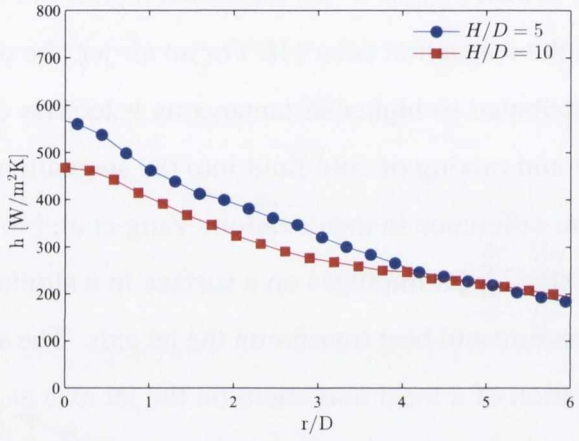

(b) Re = 4500

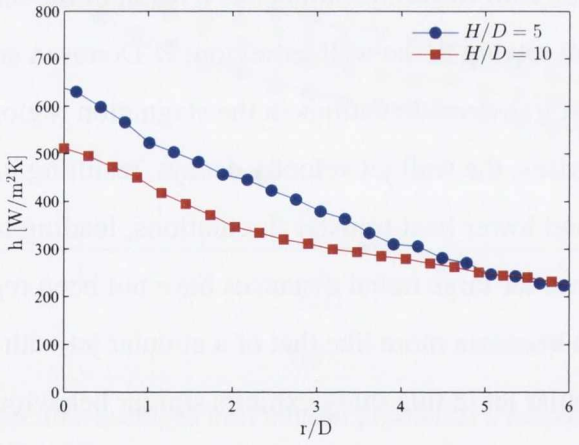

(c) Re = 5400

Figure 7.2: Annular air jet time-averaged heat transfer coefficient distributions: effect of nozzle-to-plate height

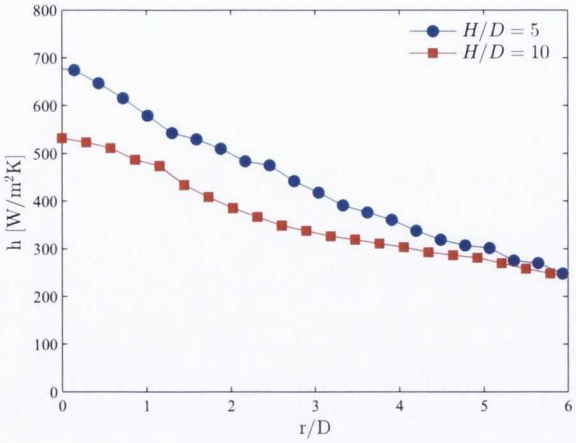

(a) Re = 6200

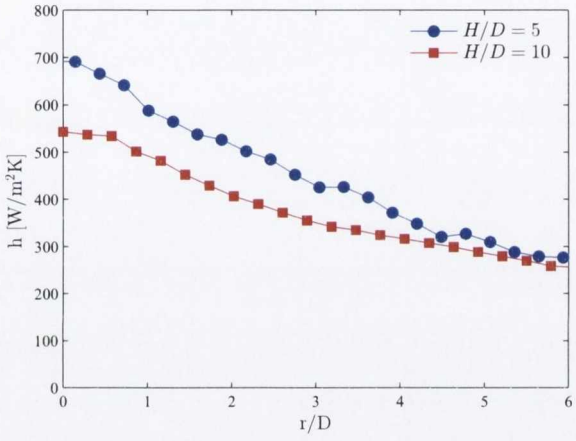

(b) Re = 7800

Figure 7.3: Annular air jet time-averaged heat transfer coefficient distributions: effect of nozzle-to-plate height at higher Reynolds numbers

turbulent flow has occurred before the jet reaches the impingement surface as the plate is beyond the jet potential core.

The effect of varying H/D can be inferred from a comparison of figures 7.1 (a) and 7.1 (b), but for clarity the heat transfer coefficient profiles for a range of fixed Reynolds numbers at the two nozzle heights of $H/D = 5$ and $H/D = 10$ are shown in figures 7.2 and 7.3. With increasing H/D the stagnation heat transfer coefficient decreases as the jet centreline velocity decays downstream from the nozzle exit. This becomes more pronounced with increasing Reynolds number. The increased jet energy for higher Re delays the deceleration of the jet as it moves away from the nozzle.

For each Reynolds number examined in figures 7.2 and 7.3, the radial decay in the heat

transfer coefficient differs between the two nozzle-to-plate spacings. This may be attributed to the increased energy of the wall jet when H/D is lower, as the centreline velocity has not decayed as much as when $H/D = 10$, thereby increasing the disturbance to the boundary layer and improving heat transfer. It is clear as well that increasing the Reynolds number delays the radial location for convergence of the heat transfer distributions. While this has been observed before for air jets [4], the literature on annular air jet heat transfer has not reported radial distances large enough to verify this against. However, the behaviour of pressure distributions in the work of Yang et al. [46] appear to suggest this is valid for annular jets.

The heat transfer results presented in this section provide a baseline with which the enhancement due to the introduction of water droplets to form the mist jet can be compared. There is a distinct lack of data reported in the literature for annular air jet heat transfer in general, and, as a consequence, for comparable nozzle parameters and test conditions to this investigation. Thus, a meaningful comparison with previous annular air jet studies cannot be made. While the single phase heat transfer results presented here are lower than previously reported results [45, 46], this is to be expected as a result of the very different parameter ranges, particularly in terms of the nozzle-to-plate spacing, which is significantly higher in this study than has previously been investigated.

Within the literature on the subject of mist jet heat transfer, only Chang and Su [19] have reported on the heat transfer distributions of the mist jet nozzle used in an air only configuration. However, the mist jet nozzle used by Chang and Su [19] is the inverse of that of the current study; a circular air jet is surrounded by an annular water jet. The familiar bell-shaped Nu distribution was reported [19], but for magnitudes closer to those of a conventional circular air jet [4], as would be expected.

7.2 Mist Jet Heat Transfer

Time-averaged heat transfer distributions are presented in this section. As per section 3.3, the data are presented in terms of the heat transfer coefficient, h, rather than the Nusselt number. As well as these data, the fluctuating voltage squared signal, E^2, from the hot film sensor is also presented. As discussed in section 5.1.3, the hot film sensor voltage, E, is indicative of

the heat flux from the sensor, q'', as per the relationship

$$q'' \propto \frac{E^2}{R} \tag{7.2}$$

where R is the electrical resistance of the sensor. While fluctuating heat transfer coefficients are not presented here due to the issues surrounding the hot film sensor calibration, detailed in section 5.1.3, the E^2 signal provides useful information on the temporal behaviour of the impinging mist jet heat transfer.

The heat transfer results here relate to the same parameter space as used for the mist jet characterisation study of chapter 6, given in table 6.1. Thus, the mist loading fractions, f, are at the low end of the spectrum, corresponding to a dilute mist jet. Results for a representative sample of mist loading fractions are reported in this section.

Time averaged heat transfer coefficient profiles are shown in figures 7.4 and 7.5 for varying mist loading fractions and Reynolds numbers of Re = 4500 and Re = 7800 respectively, with nozzle-to-plate spacings of $H/D = 5$ and $H/D = 10$ considered for both Reynolds numbers. Also included are the air only data at the same Reynolds numbers for comparative purposes. From figures 7.4 and 7.5 it can be seen that the heat transfer profile for the mist jet has the same bell-shaped distribution as observed for the annular air jet in figures 7.1 (a) and 7.1 (b). The heat transfer coefficient peaks at the jet centreline, $r/D = 0$, before decreasing as the radial distance increases. Profiles in the work of Chang and Su [19] also showed a similar bell-shaped heat transfer distribution, albeit for a much higher liquid flow rate. The heat transfer coefficients seen here are consistent with previous work on mist jet heat transfer without boiling reported by Graham and Ramadhyani [20] and Tay et al. [97]. Thus, for similar surface temperatures to this investigation and somewhat higher liquid flow rates, as detailed in table 3.1, Graham and Ramadhyani [20] reported heat transfer coefficients of approximately 5600 W/m^{2}K upwards. Tay et al. [97] found heat transfer coefficients in the region of 3000 W/m^{2}K and higher. The higher heat transfer coefficients in those studies are not unexpected, as the mist loading fractions under investigation here are lower, as outlined in table 3.1. This profile shape indicates the continued influence of the annular air jet on the heat transfer of the mist jet. It is immediately clear that the addition of even very small amounts of liquid to the annular air jet has significantly enhanced the heat transfer coefficient

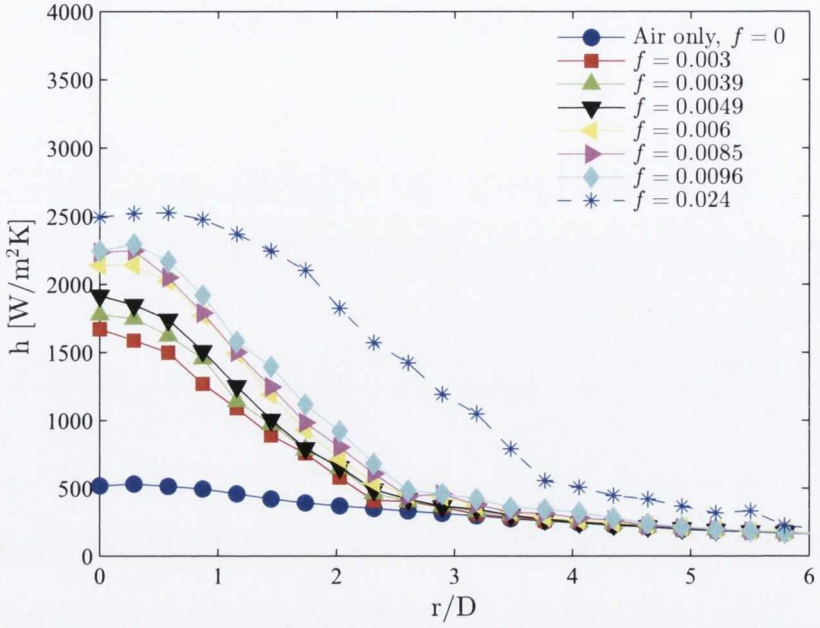

(a) H/D = 5

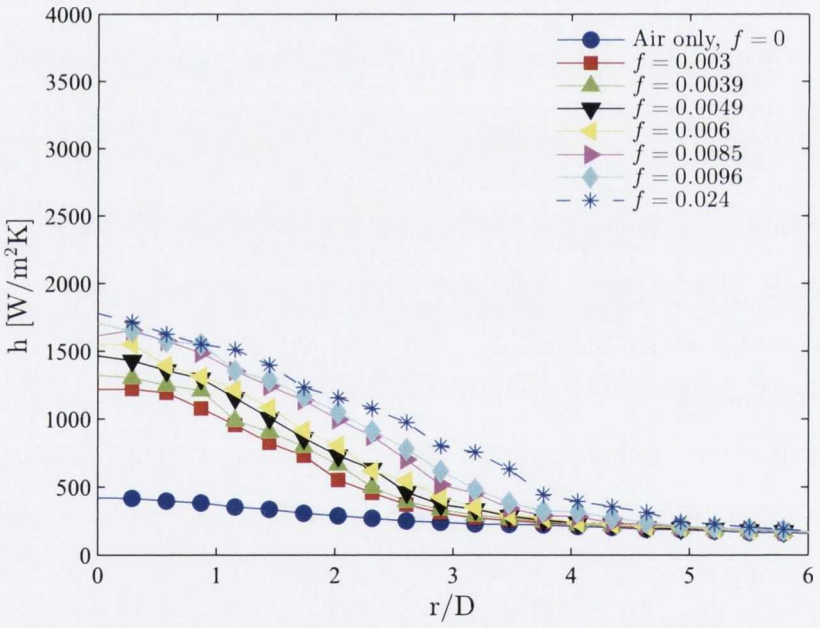

(b) H/D = 10

Figure 7.4: Time-averaged heat transfer coefficient profiles for Re = 4500 as a function of mist loading fraction, f

of the jet. These figures contain the effect of mist loading fraction, jet Reynolds number and nozzle-to-plate spacing, but for clarity these parameters are now addressed separately.

7.2.1 Effect of mist loading fraction

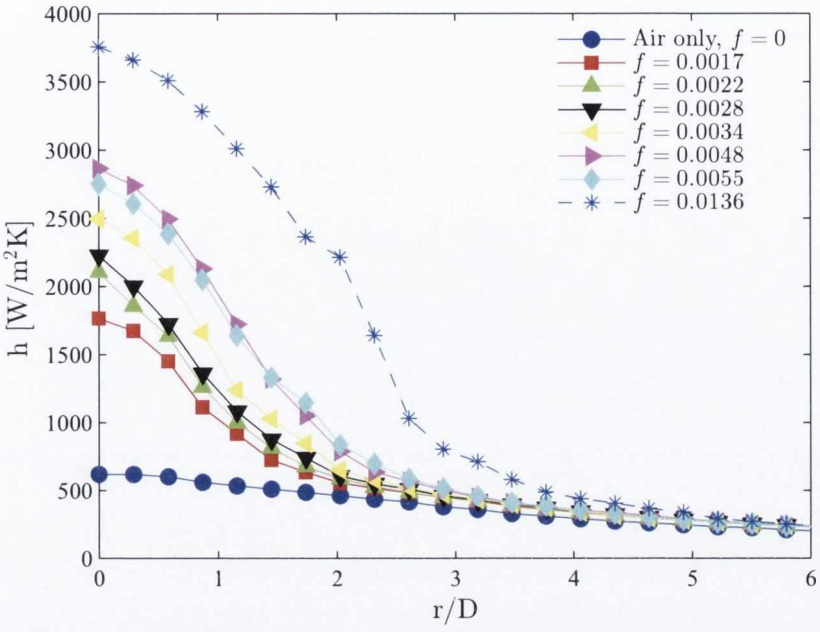

(a) $H/D = 5$

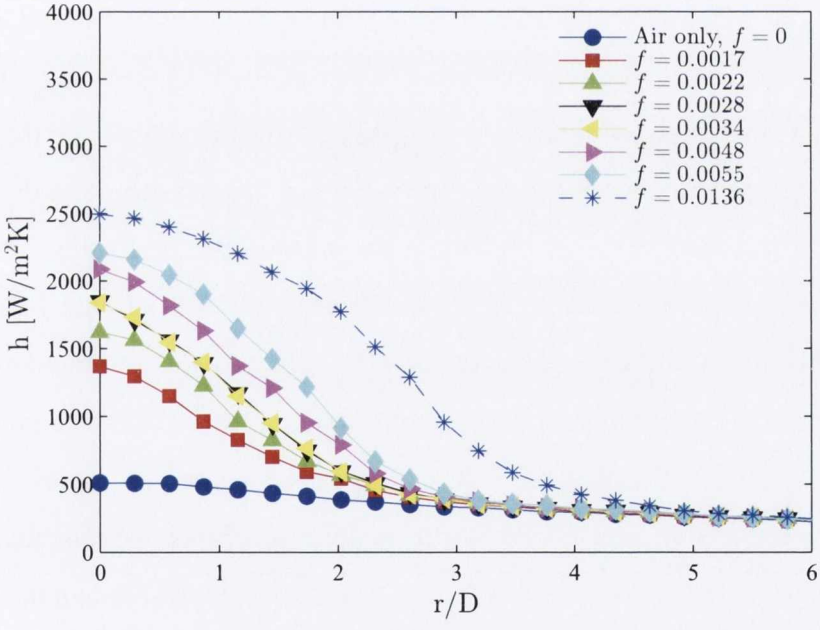

(b) $H/D = 10$

Figure 7.5: Time-averaged heat transfer coefficient profiles for Re = 7800 as a function of mist loading fraction, f

In general, the stagnation heat transfer coefficient is seen to increase with increasing mist loading fraction for the Reynolds numbers and H/D range examined here. However, the increase in h is not consistent across the range of f.

***Re* = 4500**

As can be seen from figure 7.4 (a) for $H/D = 5$, a significant increase in the heat transfer coefficient is achieved for the initial mist loading fraction of $f = 0.003$. The stagnation heat transfer coefficient continues to increase with mist loading fraction until $f = 0.0049$, with a larger increase in h between $f = 0.0049$ and $f = 0.006$. Subsequent to this, the heat transfer coefficient profiles are nearly identical for $f = 0.006$, $f = 0.0085$ and $f = 0.0096$, before rising somewhat and broadening significantly for $f = 0.024$. A similar mid-range plateau is seen for $H/D = 10$ (figure 7.4 (b)).

This behaviour is noteworthy when considered in terms of the surface liquid characterisation discussed in section 6.4.1. These plateau mist loading fractions correspond to the upper-end of the low f surface liquid regime and the transition to the intermediate regime. As identified in section 6.4.1, in the low mist loading fraction regime the liquid forms discrete liquid slugs on the surface; this was seen in figures 6.74 through 6.76. Increasing f results in more liquid slugs developing on the surface; these eventually start to coalesce into localised films as the intermediate surface liquid regime begins. Thus it appears that after the initial significant jump in heat transfer coefficient when water is added to the air jet, the mechanisms of which are discussed below, the increase in h slows as f moves through the low surface liquid regime, with little further enhancement for increasing mist loading fraction in the intermediate surface liquid regime. This implies that the presence of intermittent localised films is not sufficient to further enhance the mist jet heat transfer, and the development of the more continuous flowing films of the high mist loading fraction surface liquid regime is required to further increase heat transfer. This illustrates the complex nature of the surface liquid behaviour and its influence on the mist jet heat transfer when the mist loading fraction is very low, and provides an insight into the heat transfer mechanisms when the mist loading fraction is such that the impingement surface is not completely wetted.

The heat transfer mechanisms reported in the literature [19–21] rely on the establishment of a liquid film and describe sensible heating of the liquid film and convection to the flowing film as being of significance; Graham and Ramadhyani [20] reported that convection to the flowing film and its evaporation accounted for the vast majority of the mist jet heat transfer, with evaporation identified as having a significantly larger impact. However in the present case, high-speed imagery has shown that, for low f, the discrete liquid slugs that form on the

surface are either stationary or move outwards from the stagnation zone in a non-continuous fashion, while the localised films associated with intermediate f are intermittent and also not continuous. Thus it is postulated that, while the forced convection of the air jet together with sensible heating and evaporation from the discrete liquid slugs and partial films have an influence, the heat transfer enhancement can predominately be attributed to disturbance of the surface thermal boundary layer by droplet impacts when the surface is not completely wetted.

Increasing the mist loading fraction increases the number of discrete slugs in the low f regime, which should enhance the heat transfer through increased evaporation and sensible heating of the slugs. The time-averaged heat transfer coefficient profiles do increase from $f = 0.003$ to $f = 0.0049$, although the increase is small in comparison to the initial enhancement in heat transfer coefficient for $f = 0.003$ over the air only case, suggesting that these contributions to the mist jet heat transfer are small in comparison to the thermal boundary layer disturbances. The profiles for the mist loading fractions associated with the intermediate surface liquid regime are broadly similar with increasing f. The formation of a continuous liquid film, and the associated heat removal due to convective flow of the film and evaporation from it, is required to cause further enhancement in heat transfer coefficient. This suggests that the intermediate surface liquid regime may also correspond to an intermediate heat transfer regime, with a decrease in the influence of disturbances caused by droplet impacts, and an increase in the heat transfer mechanisms associated with the liquid film as described by Graham and Ramadhyani [20], i.e. evaporation and convective flow.

Further evidence for the influence of the droplet impacts can be found by considering the hot film voltage signal obtained simultaneously to the shadowgraph imaging, both recorded at a rate of 1000 Hz. These data are for the stagnation region of the mist jet, with the sensor extending over the range of approximately $-0.4 < r/D < 0.4$ on the surface. As discussed in section 5.1.3, the hardware used to perform the simultaneous tests introduced an internal delay between the two measurements. However, by performing a cross-correlation between the heat transfer signal and droplet detection in the recorded images, a strong dependence of the heat transfer on the impinging droplets is found. The variations in hot films sensor voltage squared, E^2, over a period of 2.5 s for the mist loading fractions of $f = 0.003$, $f = 0.0049$ and $f = 0.006$ at $H/D = 5$ are shown in figures 7.6 (a), 7.6 (b) and 7.6 (c) respectively. The first two mist loading fractions correspond to the low f surface liquid

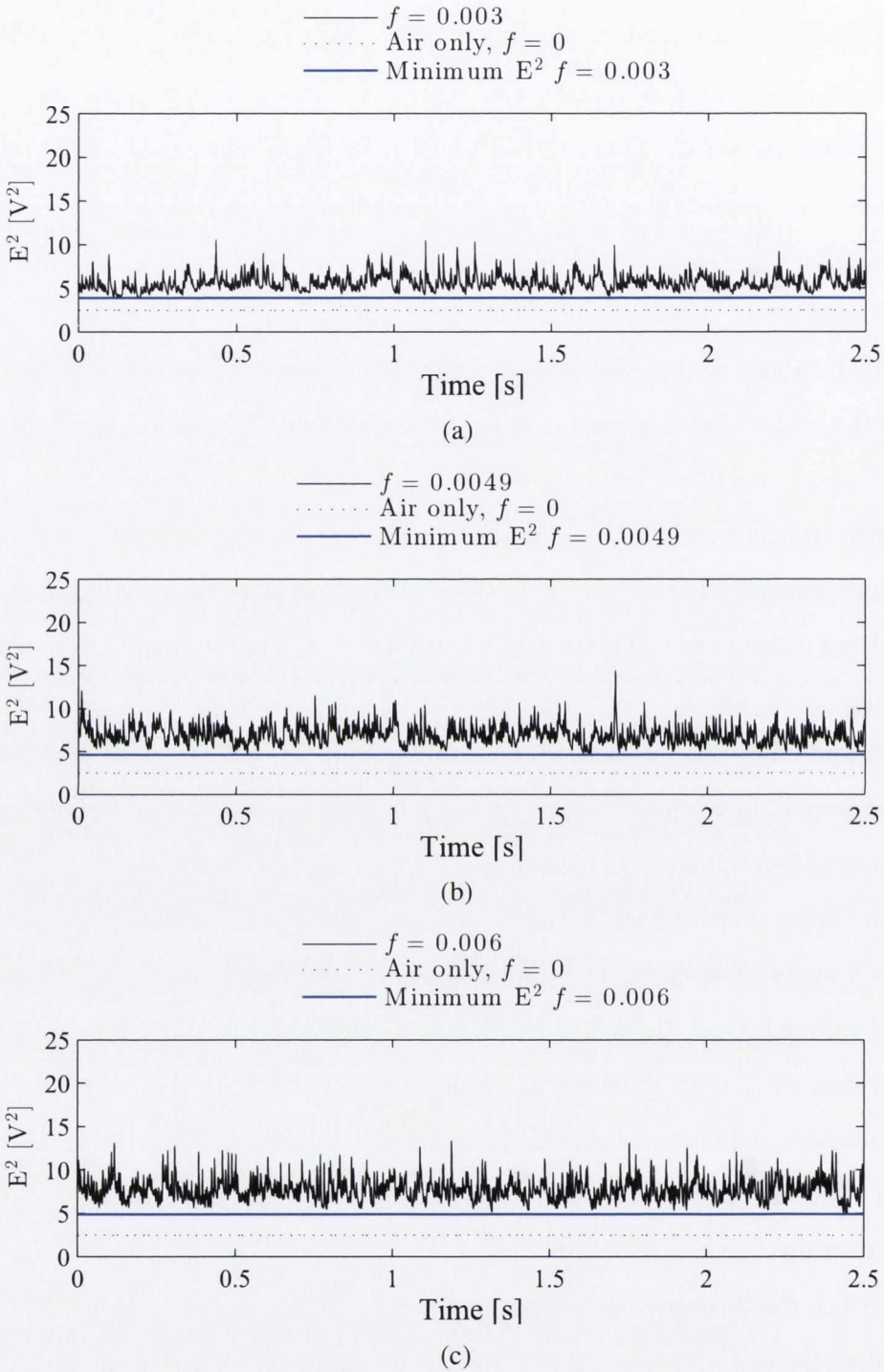

Figure 7.6: Temporal variations in hot film sensor voltage squared for H/D = 5 and Re = 4500 at low mist loading fractions of (a) f = 0.003, (b) f = 0.0049 and (c) f = 0.006

regime, characterised by discrete liquid slugs on the surface; the latter case represents the transition to the non-continuous localised liquid film behaviour, and the onset of the plateau in time-averaged heat transfer profiles of figure 7.4 (a) when H/D = 5 and Re = 4500. Also

shown in each figure is E^2 time trace for the air only tests, and the minimum of E^2 for each mist loading fraction across the measurement period.

Immediately apparent is how much more fluctuation there is in the mist jet hot film sensor voltage than for the corresponding air only case; clear spikes can be seen in the mist jet case. This variation alone may be indicative of the thermal disruption induced by the addition of the high heat capacity water droplets to the air jet. The trends in time-averaged stagnation heat transfer coefficients for the same mist loading fractions, seen in figure 7.4 (a), are reflected in these temporal distributions of the hot film sensor voltage. At the lowest mist loading fraction of $f = 0.003$, the initial increase in heat transfer coefficient with the addition of water to the air jet in figure 7.4 (a) is reflected by E^2 in figure 7.6 (a). Further significant increases in the voltage are not seen as the mist loading fraction increases. Rather, increasing the mist loading fraction results in more frequent spikes in the fluctuating voltage signal; these contribute to the time-averaged enhancement in heat transfer of the mist jet.

Considering the temporal variations in E^2 along with the simultaneous shadowgraph imagery, the observed spikes in voltage show a strong dependence on the impingement of droplets on the heated surface. This can be seen more clearly in figure 7.7, which shows the temporal variation in E^2 for 0.5 s, along with the corresponding number of droplets detected per frame. These results are for a mist loading fraction of 0.006, which corresponds to transition between the low and intermediate f surface liquid regimes, as seen in figure 7.8. These data are for the time period 2 s < t < 2.5 s in figure 7.6 (c). From figure 7.7, some peaks are evident in the voltage signal that do not correspond to spikes in the number of droplets detected. Although a different heat transfer phenomenon could be responsible, it is more likely that some droplets passing through the detection window in this high-speed flow have been missed due to hardware limitations of the camera. Thus, for a droplet travelling at 60 m/s, the time to pass through the detection window is approximately an order of magnitude shorter than that corresponding to the frame rate of 1000 Hz, which was the maximum frame rate that produced interpretable results.

The evolution of a sample spike in the hot film sensor voltage caused by the impinging mist jet, identified by an arrow in figure 7.7, provides further clarity to the observed behaviour. Figures 7.9, 7.10 and 7.11 show the change in E^2 at a higher temporal resolution along with the number of droplets detected and the corresponding high-speed shadowgraph image, again

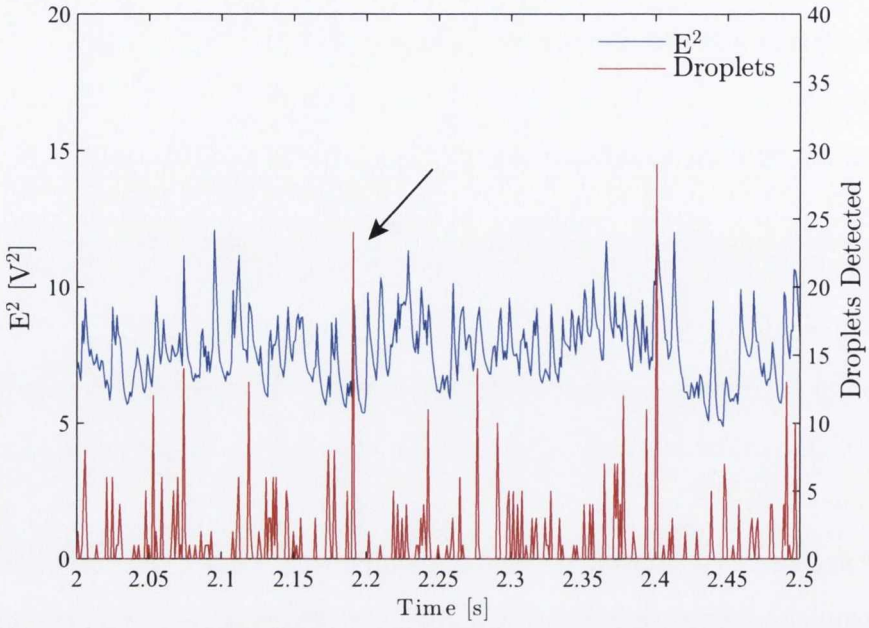

Figure 7.7: Combined simultaneous hot film sensor voltage squared and droplet detection for discrete 2 – 2.5 s period of figure 7.6 (c); H/D = 5, Re = 4500 and f = 0.006

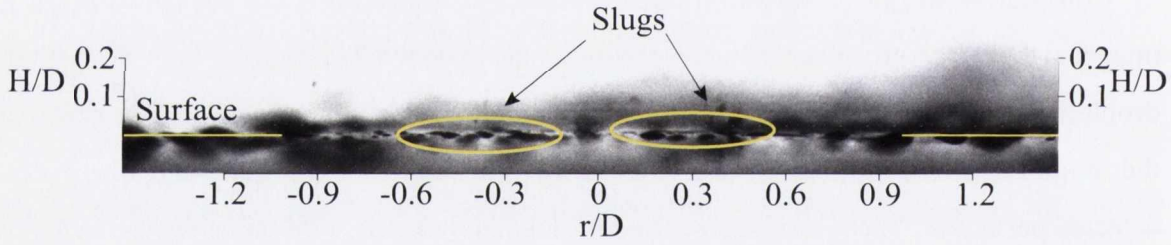

Figure 7.8: Surface liquid behaviour for peak identified in figure 7.7; H/D = 5, Re = 4500 and f = 0.006

for f = 0.006. Initially for a time t = 2.188 to t = 2.19 s, before the arrival of liquid droplets, the voltage is approximately 6 V^2; this is shown in figure 7.9. This voltage is higher than the air only case, with sensible heating and evaporation of the surface liquid slugs accounting for this enhancement. In figure 7.10, a large number of droplets are impinging on the heated surface. This can be seen in the high-speed image in figure 7.10 (b), with a corresponding peak in the detected droplets in figure 7.10 (a) and a near doubling of the voltage signal. Subsequent to this event, as shown in figure 7.11, E^2 begins to decay, approaching the level that existed before the impingement of the droplets.

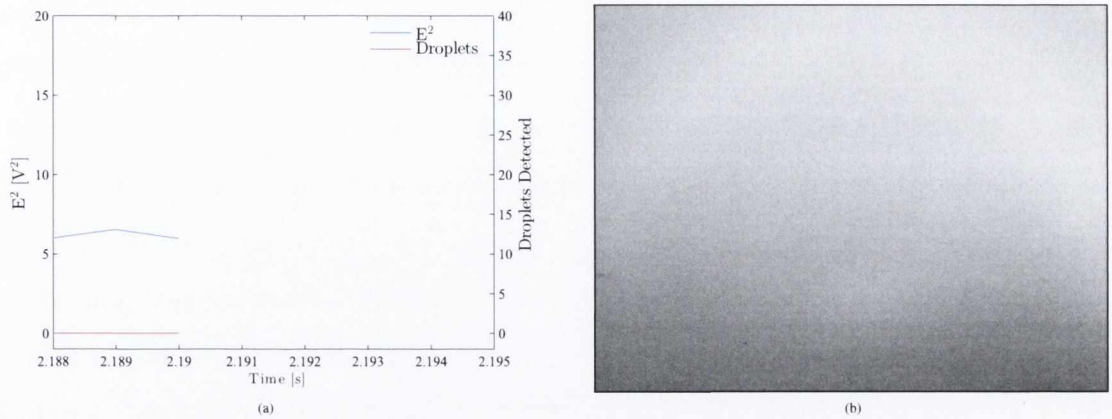

Figure 7.9: Before arrival of liquid droplets; (a) hot film sensor voltage squared and detected droplets and (b) shadowgraph image. Re = 4500, f = 0.006 and H/D = 5

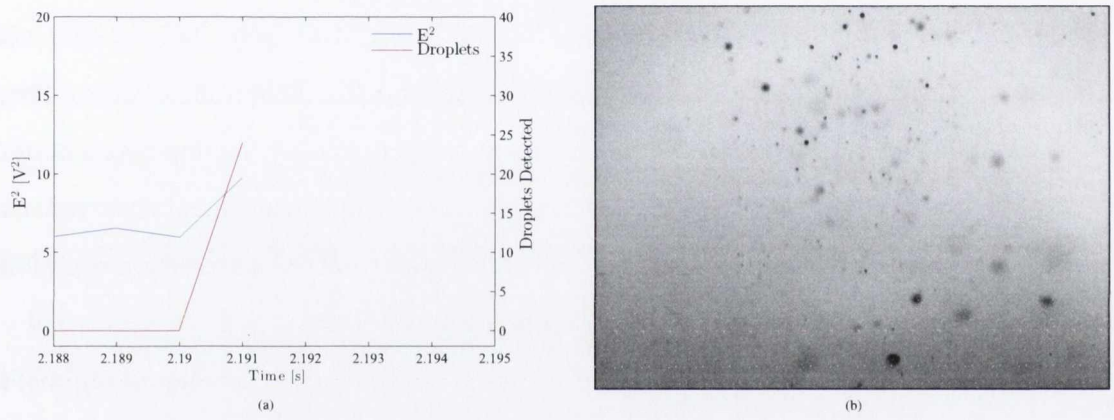

Figure 7.10: Arrival of liquid droplets; (a) hot film sensor voltage squared and detected droplets and (b) shadowgraph image. Re = 4500, f = 0.006 and H/D = 5

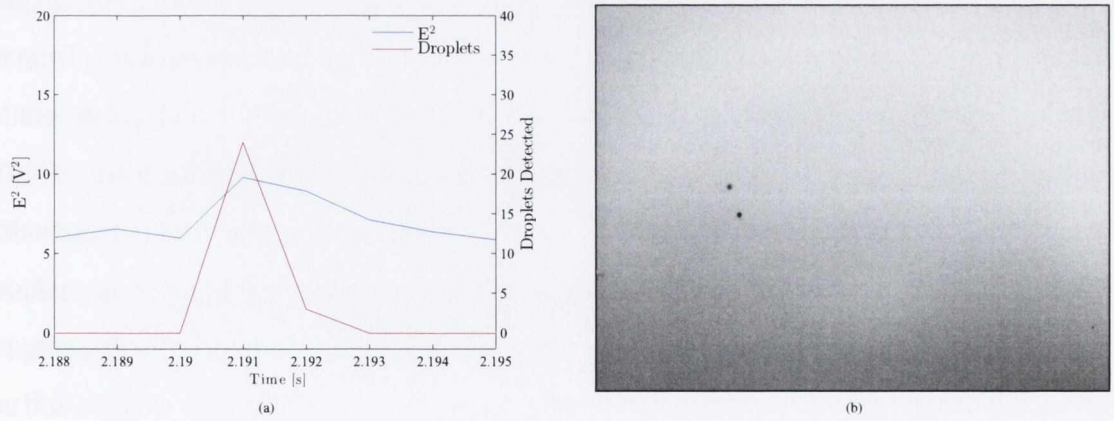

Figure 7.11: After arrival of liquid droplets; (a) hot film sensor voltage squared and detected droplets and (b) shadowgraph image. Re = 4500, f = 0.006 and H/D = 5

This sequence shows the influence of droplet impingement on mist jet heat transfer when the mist loading fraction is so low that a continuous liquid film is not established on the surface. An immediate response to the arrival of liquid droplets is seen. This serves to reaffirm the hypothesis that the disturbance of the surface thermal boundary layer is the most significant contributor to the heat transfer enhancement of the dilute mist jet. After the initial peak in the voltage, there is a more gradual reduction in E^2 with time; this indicates that the fresh liquid on the surface due to the droplet impingement is removing heat from the surface at a slower rate, likely through sensible heating of the liquid and also due to the outward movement of some liquid slugs. The voltage will continue to decrease towards a minimum level until a subsequent impingement event causes another spike in E^2, as seen in figure 7.7. The temporal variation in the sensor and droplet detections indicate that while the presence of liquid on the surface does serve to enhance the heat transfer above the air only level, in this low surface liquid regime the disturbance caused by the impingement of the liquid droplets is the main driver for the heat transfer coefficient enhancement observed in the time-averaged profiles in figure 7.4 (a). This behaviour was observed across the range of mist loading fractions that give rise to the discrete liquid slugs.

As the mist loading fraction moves through the intermediate surface liquid regime, the increase in heat transfer coefficient slows, with $f = 0.0085$ and $f = 0.0096$ exhibiting very similar profiles, seen in figure 7.4 (a). At the highest mist loading fraction of 0.024 a further increase is seen, as well as a significantly broader time-averaged profile. For this mist loading fraction, a continuous liquid film has been established which flows outwards from the stagnation zone, as seen in figure 7.12 (b), with convective flow of the film and its evaporation resulting in the observed enhancement at greater radial distances than for lower f. The plateau in the time-averaged heat transfer coefficient for mist loading fractions corresponding to the intermediate surface liquid regime may be due to competing heat transfer mechanisms. For the lower mist loading fractions, the surface is less wetted, and hence the droplets can more easily disturb the surface thermal boundary layer; when f is large, the evaporation and convective flow of the film has been identified as contributing significantly to the mist jet heat transfer. Potentially, for the intermediate range of f, the onset of intermittent localised films serves to dampen the influence of the droplet impacts as they are prevented from striking the surface but rather impinge on warmed liquid, while at the same time the rate at which

these films flow outwards is not sufficient to significantly enhance the heat transfer through convective action. However, further examination of the surface film beyond the scope of the current set-up is required for this regime to affirm this hypothesis.

Figure 7.12 (a) shows the temporal variation in the hot film sensor voltage squared for the mist loading fraction of 0.024. This corresponds to the high f surface liquid regime, which is characterised by the presence of a continuous liquid film, as illustrated in figure 7.12 (b). The presence of this film is reflected in the temporal E^2 distribution in figure 7.12 (a); the minimum instantaneous voltage for the mist jet is higher here when the continuous film is present than for lower mist loading fractions with intermittent films or discrete liquid slugs. This indicates that, while the droplet impingement still leads to temporary peaks in the voltage, the surface liquid film convective flow away from the impingement region and evaporation from the film both contribute significantly to heat transfer. Therefore the heat transfer mechanisms here when $f = 0.024$ are consistent with the findings of Graham and Ramadhyani [20] and others [19, 21], with convective action of the liquid film and its sensible heating providing significant heat transfer enhancement.

For the higher H/D, the increase in stagnation heat transfer coefficient once the liquid film begins to form is not as significant as for $H/D = 5$; this can be seen in figure 7.4 (b). This may be a consequence of the lower droplet flux at the higher H/D due to the spreading of the jet. The arrival of fresh liquid from the mist jet droplets is what causes the flow of the film, a key component of the mist jet heat transfer, and when there is a lower concentration of droplets the film will flow at a slower rate. Thus, convection from the surface to the film will be reduced and the heat transfer coefficient will not increase by the same degree as when the droplet flux is higher, as for the $H/D = 5$ case. Indeed, the temporal variations in hot film sensor voltage squared, indicative of heat flux, at the higher H/D as illustrated in figure 7.13 for $f = 0.024$, show spikes that are similar in magnitude to the much lower mist loading fraction of 0.006 when $H/D = 5$, seen in figure 7.7, as a result of the decreased droplet flux for the higher nozzle-to-plate spacing. Again, however, there is a strong correlation between the heat transfer spikes and peaks in the number of droplets detected, indicating the continued influence of the droplet impacts on the dilute mist jet heat transfer.

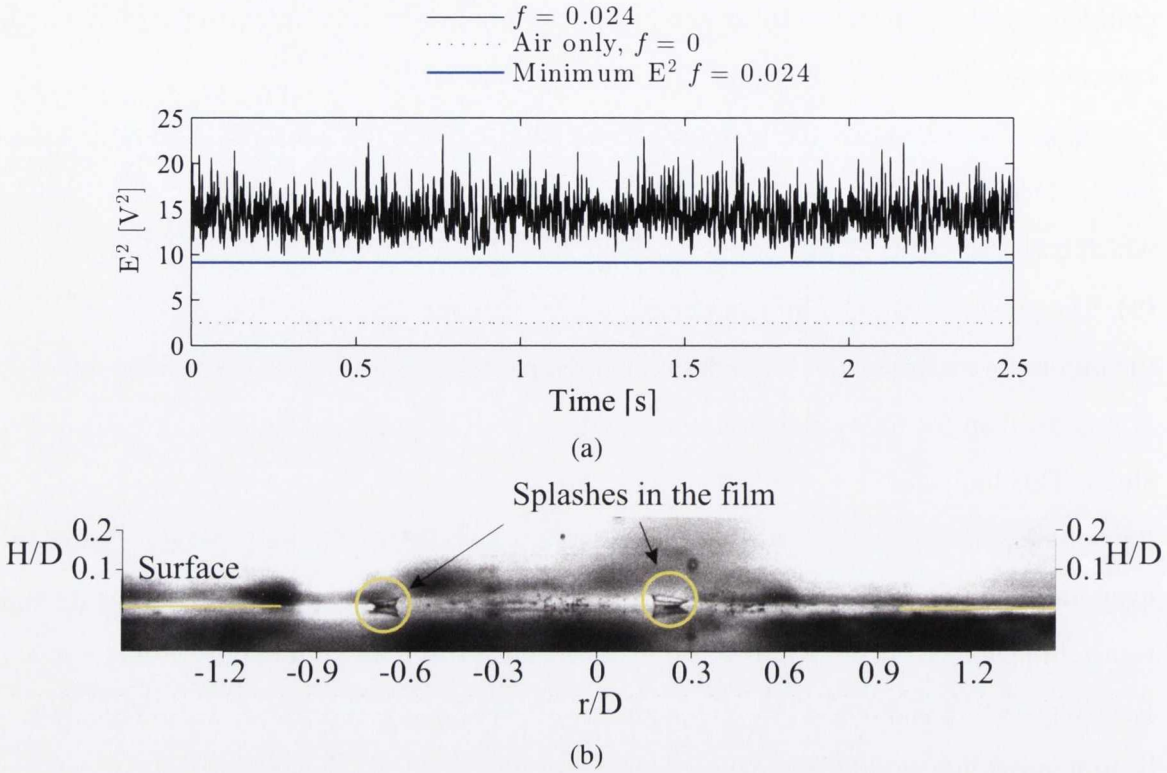

Figure 7.12: (a) Temporal variations in hot film sensor voltage squared and (b) continuous film surface liquid behaviour; both for a mist loading fraction of f = 0.024 when H/D = 5 and Re = 4500

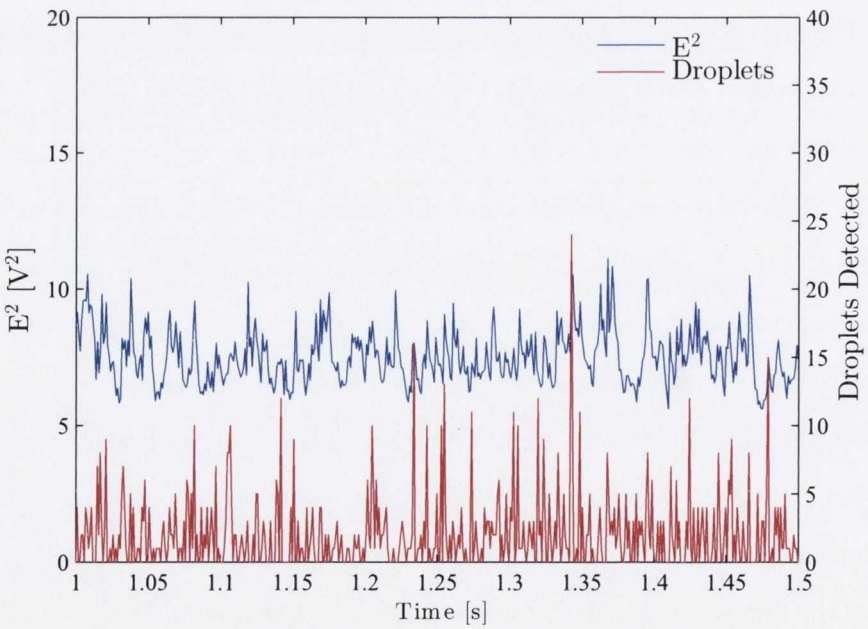

Figure 7.13: Combined simultaneous hot film sensor voltage squared and droplet detection; H/D = 10, Re = 4500 and f = 0.024

Re = 7800

The effect of the mist loading fraction in the higher Reynolds number case can be seen in figures 7.5 (a) and 7.5 (b) for $H/D = 5$ and $H/D = 10$ respectively. When Re = 7800, the heat transfer coefficient is seen to increase more uniformly with f than observed at the lower Reynolds number; this is particularly evident at $H/D = 5$. The impingement behaviour again offers potential explanations for these measured trends in heat transfer with mist loading fraction at the higher Reynolds number. As seen in section 6.4.2, the impingement behaviour of the mist jet droplets was somewhat different for the two nozzle heights. Considering first the $H/D = 5$ case, for the low mist loading fraction range ($f \leq 0.0034$) the impingement behaviour is characterised by concentrated, although intermittent, impacts of relatively large numbers of droplets that resulted in liquid slugs forming on the surface; these then move further radially across the surface than when Re = 4500. As the mist loading fraction increases, the droplet impacts become more frequent and concentrated, giving rise to intermittent liquid films that are rapidly flushed away; the loading fractions of $f = 0.0048$ and $f = 0.0055$ fall within this regime. With further increases in f the frequency of droplet impacts is such that a continuous film has developed; this is the case for the largest mist loading fraction of $f = 0.0136$. Examining the heat transfer trends in this context, it is apparent that the time-averaged heat transfer coefficient rises as the intermittent disturbances due to concentrated droplet impacts increase with mist loading fraction. There is then a levelling off of the heat transfer enhancement with an increase in mist loading fraction for $f = 0.0048$ and 0.0055 in the intermediate surface liquid range. This change in enhancement trend may be due again to the onset of the intermittent localised films and the competing heat transfer influences of the droplet disturbances and film flow and evaporation. A further increase in heat transfer coefficient is seen once a continuous liquid film is established when $f = 0.0136$, both in the stagnation region and radially as the film spreads outwards. The high heat transfer levels in this case are explained by frequent concentrated droplet impacts, which disturb the liquid film significantly while keeping it supplied with fresh cooler water.

The temporal distributions of the hot film sensor voltage for Re = 7800 again provide a more detailed insight into the heat transfer phenomena. Figures 7.14 (a), 7.14 (b) and 7.14 (c) show these distributions for $f = 0.0017$, $f = 0.0055$ and $f = 0.0136$ respectively. Again, the air only voltage signal is included for comparison purposes. It is clear that the temporal

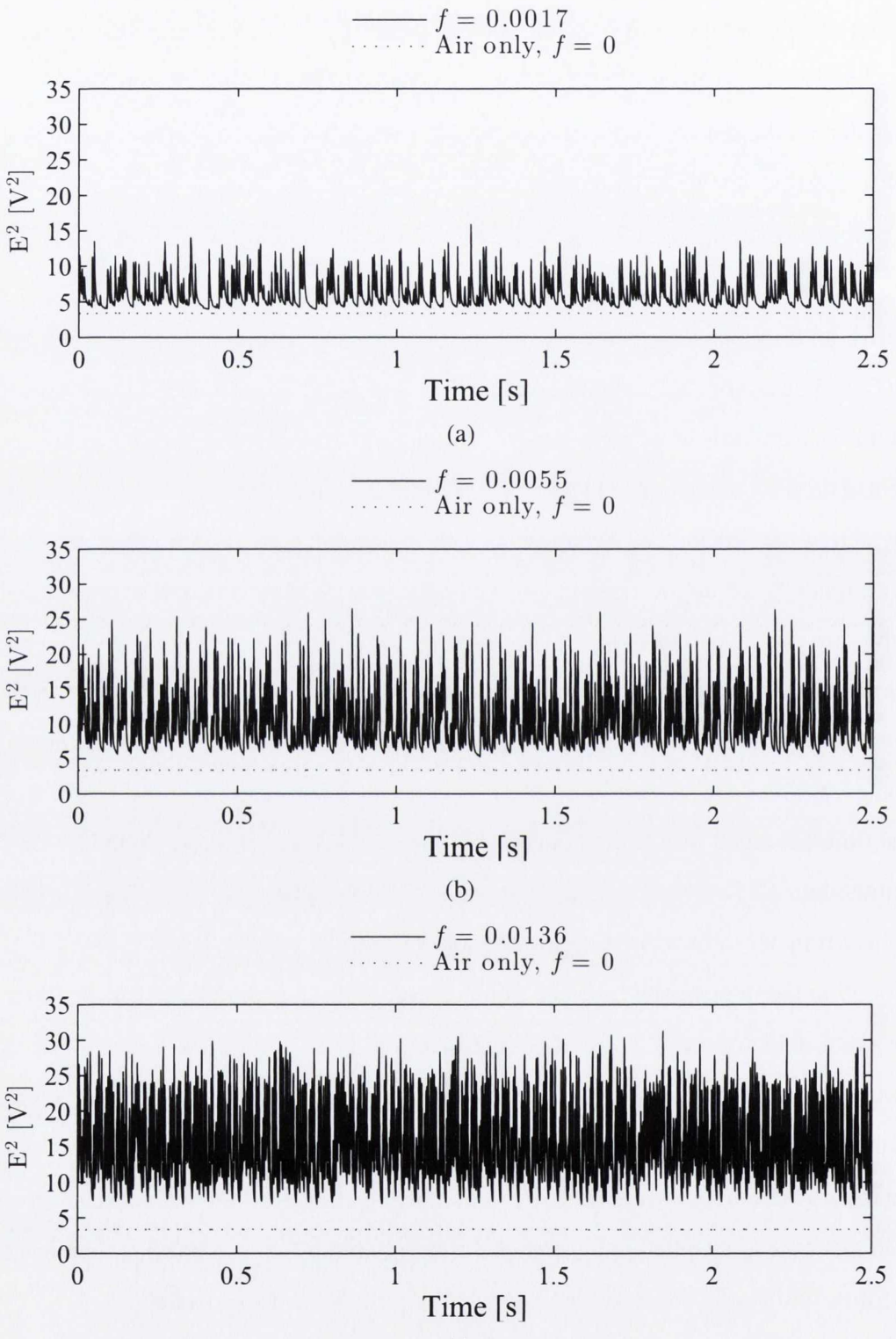

Figure 7.14: Temporal variations in hot film voltage squared when H/D = 5 and Re = 7800 for mist loading fractions of (a) f = 0.0017, (b) f = 0.0055 and (c) f = 0.0136

heat transfer behaviour, as indicated by the voltage signal, for the higher Reynolds number is characterised by peaks that are of a greater magnitude than when Re = 4500, and also more consistent in terms of both magnitude and frequency. This increase in the heat transfer fluctuations points to increased disturbance of the thermal boundary layer for the higher Reynolds number jet. As was the case for Re = 4500, the trends in time-averaged heat transfer profiles are reflected here in the temporal distributions of E^2. As the mist loading fraction increases from $f = 0.0017$ to $f = 0.0055$, the spikes in voltage increase in both magnitude and frequency, giving rise to an increase in the time-averaged heat transfer coefficient; this change in temporal behaviour with f comes about since the higher mist loading fraction provides more liquid for atomisation, and hence increasing the concentration of droplets in the mist jet. Further increases in mist loading fraction from $f = 0.0055$ towards $f = 0.0136$ do not lead to an appreciable change in the magnitude of the spikes in voltage. However, the frequency of the peaks increases, leading to an increase in time-averaged h. It can also be seen from figure 7.14 that at the lowest mist loading fraction the baseline voltage, after each peak, reduces almost to the level of the air only jet. This suggests that at times the surface is almost completely dry, likely due to the evaporation of the smaller discrete liquid slugs observed in section 6.4.2. In figure 7.14 (c) for the highest mist loading fraction considered here, the voltage does not reduce to as close to the air only value as it does for lower mist loading fractions. This is likely as a consequence of the more frequent droplet impingements continually refreshing the surface liquid and resulting in a continuous liquid film, as previously indicated by the high-speed surface imagery in section 6.4.2.

The use of the simultaneously obtained shadowgraph imaging provides further evidence for the influence of the droplet impingement on the time-averaged heat transfer coefficient for the parameter space considered here. Figure 7.15 shows the simultaneous temporal distributions of hot film sensor voltage and detected droplets for Re = 7800 and $f = 0.0055$ for the portion of figure 7.14 (b) corresponding to the period of 1.5 to 2 s. Again, a clear correlation between the peaks in heat flux, as indicated by the voltage, and peaks in droplet detection is seen, further supporting the hypothesis that the droplet impingement is the dominant heat transfer mechanism in this parameter space, i.e. for low mist loading fractions giving rise to a dilute mist jet. However, it should be noted that, to a greater extent than for the lower Reynolds number, heat transfer peaks are observed without corresponding peaks in

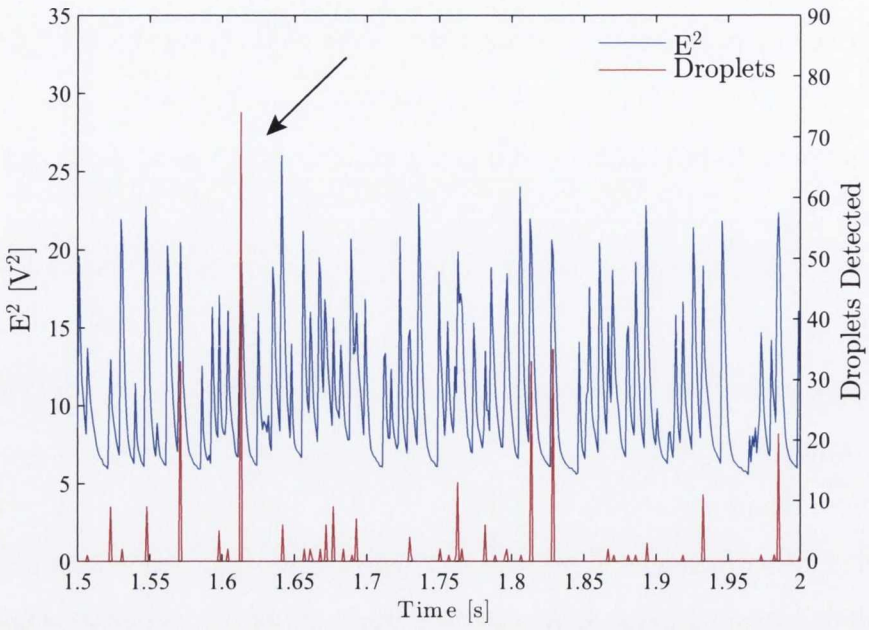

Figure 7.15: Combined simultaneous hot film sensor voltage squared and droplet detection for discrete 1.5 – 2 s period of figure 7.14 (b); H/D = 5, Re = 7800 and f = 0.0055

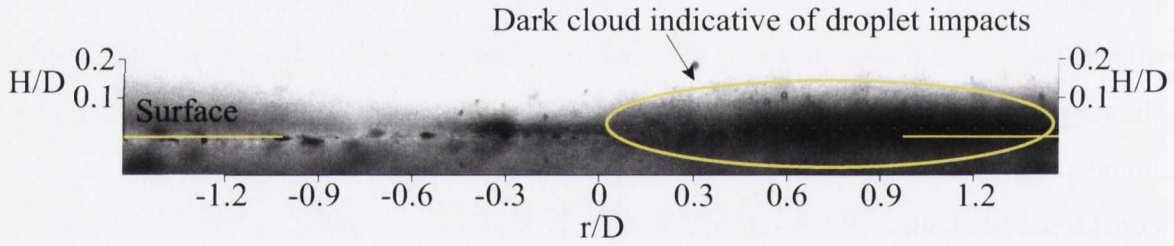

Figure 7.16: Surface liquid behaviour for peak identified in figure 7.15; H/D = 5, Re = 7800 and f = 0.0055

droplet detection. This is thought to be due to higher velocity droplets being more difficult to capture with the shadowgraph set-up as used in this investigation. Further simultaneous heat transfer and flow visualisation is likely necessary for this higher Reynolds number case, but the evidence available suggests a strong link between heat transfer and the intermittent droplet impingements.

Considering the spike in the voltage signal identified in figure 7.15, the same pattern in behaviour is observed as for the lower Reynolds number case in figures 7.9 to 7.11. These data are for a mist loading fraction of 0.0055, which corresponds to the intermediate surface liquid regime; figure 7.16 shows the surface liquid behaviour for the peak identified in figure 7.15; the dark cloud on the positive side of radial distribution is indicative of a large number of

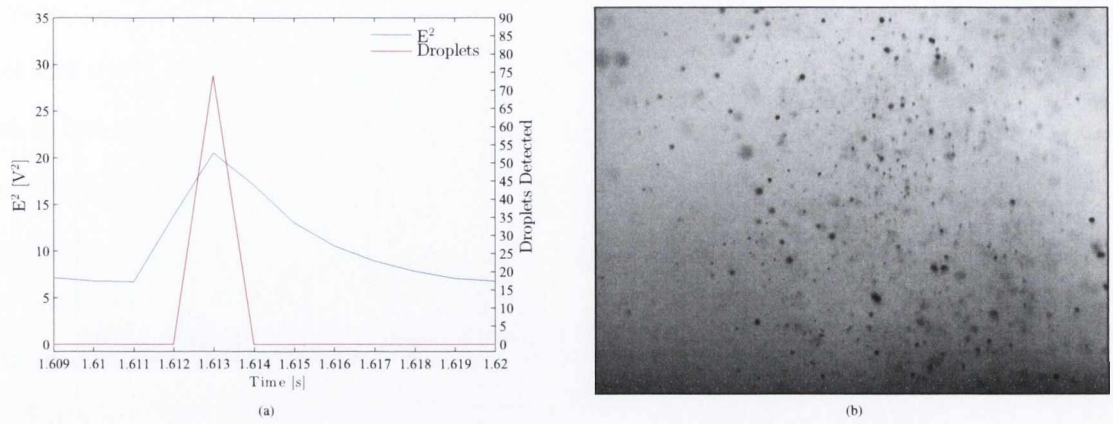

Figure 7.17: Re = 7800, f = 0.0055 and H/D = 5; (a) correlation between hot film sensor voltage squared and mist jet droplet detection and (b) high-speed shadowgraph image of event

droplets impinging on the surface. Figure 7.17 (a) shows the correspondence between the hot film sensor voltage and the number of droplets detected at this time at a higher temporal resolution, while figure 7.17 (b) shows the high-speed shadowgraph image of the mist jet for these conditions. The clear link between the detection of mist jet droplets and the spike in E^2 can be seen, with the voltage undergoing a sharp increase by a factor of approximately 3.5 due to the impingement of the mist jet droplets. The voltage spike then decays more gradually as the surface liquid moves away from the impingement zone, continuing to remove heat by evaporation and by the sensible heating and movement of the surface liquid. The voltage decays towards the level of the air only jet, until the subsequent impingement of further droplets causes another large spike in E^2. This illustrates the significant droplet induced disturbance that occurs, postulated here to be the driving heat transfer mechanism when the mist loading fraction is very low.

For the higher H/D of 10 when Re = 7800, the increase in heat transfer coefficient with mist loading fraction is more uniform than at the lower Reynolds number. However, the heat transfer profiles of figure 7.5 (b) for f = 0.0028 and f = 0.034 are near identical, while those of f = 0.0048 and f = 0.0055 are also quite similar. Recalling the high-speed imagery for Re = 7800 when H/D = 10, it was noted that the behaviour of the liquid on the surface resembled the lower Reynolds number, certainly more so than at H/D = 5, with localised films forming on the surface for mist loading fraction in this range. Thus, the similarities in the heat transfer behaviour are consistent with the similarity in impingement behaviour. Indeed, the temporal distributions for H/D = 10 show spikes in hot film sensor voltage of a

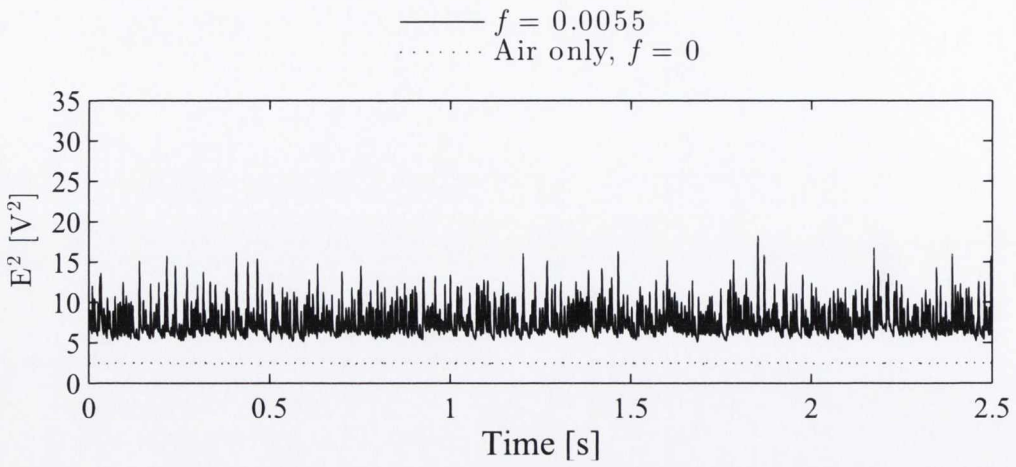

Figure 7.18: Temporal variations in hot film sensor voltage squared for $f = 0.0055$ when Re = 7800 and $H/D = 10$

lower magnitude than when $H/D = 5$, corresponding to the lower droplet flux; figure 7.18 illustrates this for $f = 0.0055$. The behaviour in figure 7.18 is broadly characteristic of the range of mist loading fraction for Re = 7800 at the higher H/D. The same radial broadening of the time-averaged heat transfer coefficient profiles with increasing mist loading fraction is seen for Re = 7800 as was the case for Re = 4500. Again, this is due to the increased spreading of the surface liquid with mist loading fraction.

7.2.2 Effect of jet Reynolds number

The increase in the jet Reynolds number has a clear influence on the mist jet heat transfer coefficient, with higher h observed for the higher Reynolds number with the same liquid flow rates; this corresponds to a lower mist loading fraction than when Re = 4500. This is consistent with the single phase results, where an increase in jet Reynolds number consistently gave rise to an increase in h due to increased turbulent mixing caused by the higher jet velocity in the stagnation region. Considering this observed increase in terms of the droplet properties, which were examined in detail in section 6.3, the droplet size decreases as the Reynolds number increases, while the droplet velocity increases. As before, it is difficult to attribute the increase in heat transfer coefficient with Reynolds number to changing droplet properties, as a parametric study on controllable droplet sizes and velocities would be required to accurately establish relationships; this is beyond the scope of the mist jet nozzle used in this study, (and

beyond that of most commercially available nozzles). The issue is further complicated by the fact that the droplet size decreases and the velocity increases with increasing H/D as well, but, as has been seen above, increasing H/D leads to a decrease in the heat transfer coefficient, a conflicting trend. It is probable that the increased air velocity leading to enhanced turbulent mixing in the boundary layer contributes to the increase in the heat transfer coefficient with Re, with the increased disturbance of the thermal boundary layer due to the more concentrated intermittent droplet impacts also enhancing heat transfer.

Sample temporal hot film sensor voltage distributions for the two Reynolds numbers at the same liquid flow rate (giving rise to $f = 0.006$ at Re = 4500 and $f = 0.0034$ at Re = 7800) are shown in figures 7.19 (a) and 7.19 (b) respectively; both are at $H/D = 5$. The enhancement in heat flux, indicated by the voltage squared, at the higher Reynolds number can clearly be seen, with the more intermittent but concentrated droplet impacts at Re = 7800 resulting in peaks in E^2 with a significantly higher magnitude than at the lower Reynolds number. These distributions are again indicative of the influence of the disturbance in the thermal boundary layer and mixing caused by the mist jet droplets.

Another Reynolds number influence that merits consideration is the issue of compressibility that arises due to the small hydraulic diameter ($D_h = 0.44$ mm) and the effect this may have on the fluid temperatures with increasing Reynolds number. Using compressible flow analysis, the local fluid temperature at the nozzle exit is predicted to be appreciably lower than the ambient temperature, particularly for the higher Reynolds number case; this will lead to a reduction in droplet temperature also. It is possible that the cooler air and droplet exit temperatures are partially responsible for the observed enhancement in heat transfer at the higher Reynolds number. Further investigation is needed to confirm the magnitude of this effect.

7.2.3 Effect of H/D

Comparison of figures 7.4 (a) and (b) for the mist jet at Re = 4500, and 7.5 (a) and (b), the case at Re = 7800, also reveals the effect of increasing H/D on the mist jet heat transfer coefficient. Across the range of mist loading fractions considered and for both Re, the stagnation heat transfer coefficient decreases with increasing nozzle-to-plate distance, H/D.

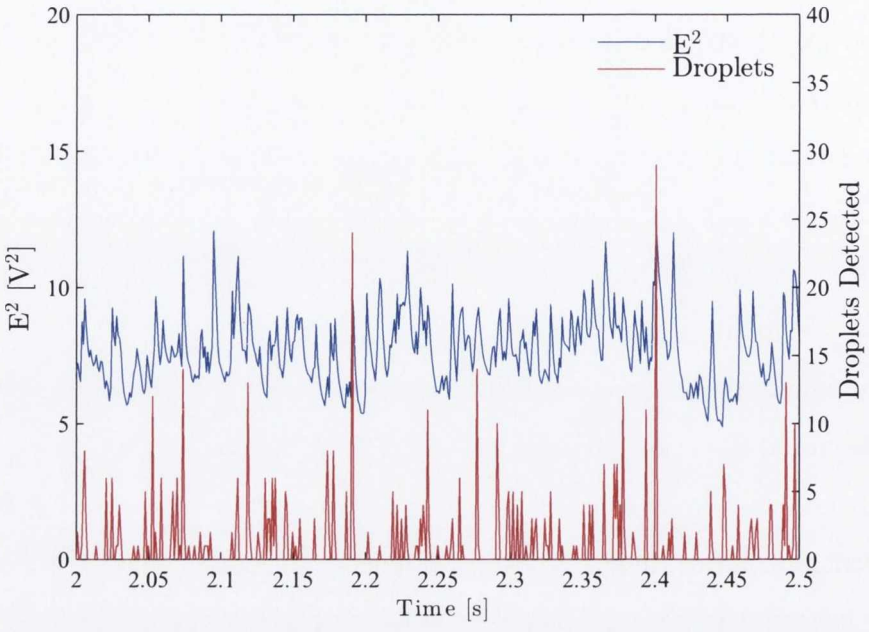

(a)

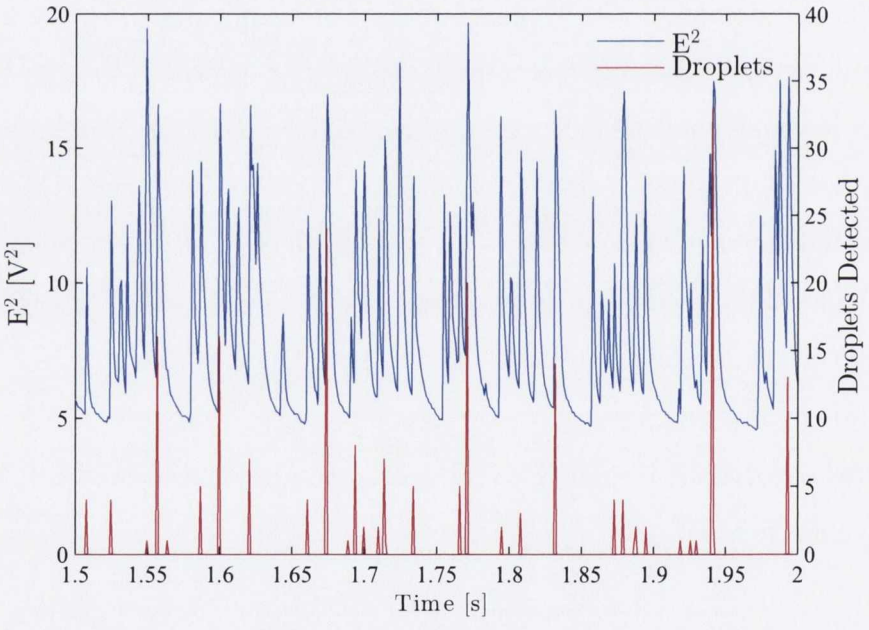

(b)

Figure 7.19: Combined simultaneous hot film sensor voltage and droplet detection when $H/D = 5$ for (a) Re = 4500 and $f = 0.006$ and (b) Re = 7800 and $f = 0.0034$

The radial profiles of h are broader, however, for the higher H/D of 10, as a consequence of the spreading of the mist jet as it moves downstream from the nozzle exit. Considering the change in droplet properties with H/D, it was seen in section 6.3 that when H/D increased

from 5 to 10 the mean droplet size decreased, while the mean axial droplet velocity increased. However, as discussed above, the same behaviour occurs for an increase in Reynolds number, and in that case the heat transfer coefficient increases. Therefore it is unlikely that the change in the droplet size or velocity is the primary cause for the decrease in the heat transfer coefficient with H/D.

The decrease in heat transfer coefficient with increasing H/D is therefore most likely due to the same spreading of the mist jet droplets that leads to the broader radial profiles. For low mist loading fractions, the concentration of droplets reaching the surface decreases with increasing H/D and the size of the liquid slugs decreases in both size and number; for higher mist loading fractions a decrease in the number of droplets impinging on the liquid film will result in a reduced flow rate of the liquid film. This spreading of the mist jet droplets is reflected in the temporal distributions of hot film sensor voltage, which show that with increasing H/D the peaks in E^2 caused by the impingement of the liquid droplets are of a lower magnitude; figures 7.20 (a) and 7.20 (b) show sample distributions for $H/D = 5$ and $H/D = 10$ respectively when $f = 0.006$. Thus, while increasing the nozzle-to-plate spacing is expected to result in a decrease in heat transfer as the mist jet velocity decays, it can also be seen from figure 7.20 that the decreased droplet flux with increasing H/D contributes to lower heat transfer. Both of these changes will contribute to a lower level of heat transfer enhancement.

7.3 Summary of Mist Jet Heat Transfer

The effects of the mist loading fraction, Reynolds number and nozzle-to-plate spacing on the time-averaged heat transfer coefficient for the dilute mist jet have been examined in this chapter. While the competing influences of the droplet sizes and velocities may have some influence on the heat transfer enhancement, the time-averaged data suggested a stronger link between the heat transfer coefficient and the impingement behaviour of the mist jet with corresponding surface liquid regimes. In previous studies it has been assumed that a continuous liquid film is established under the mist jet [19, 20], but in the high-speed imagery shown in section 6.4 a continuous film was not observed for the majority of the mist loading fractions examined, only forming for the highest f. Since the mist jet heat

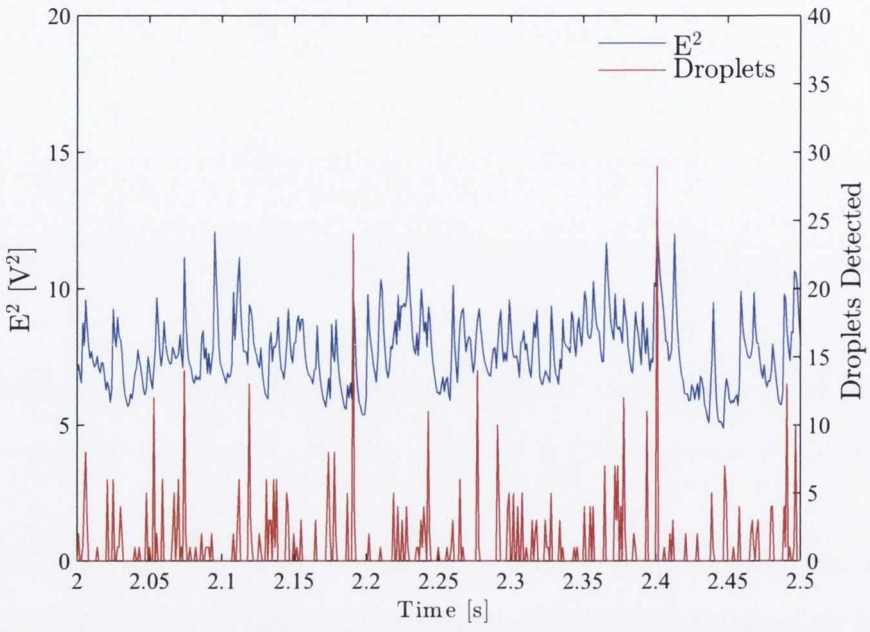

(a)

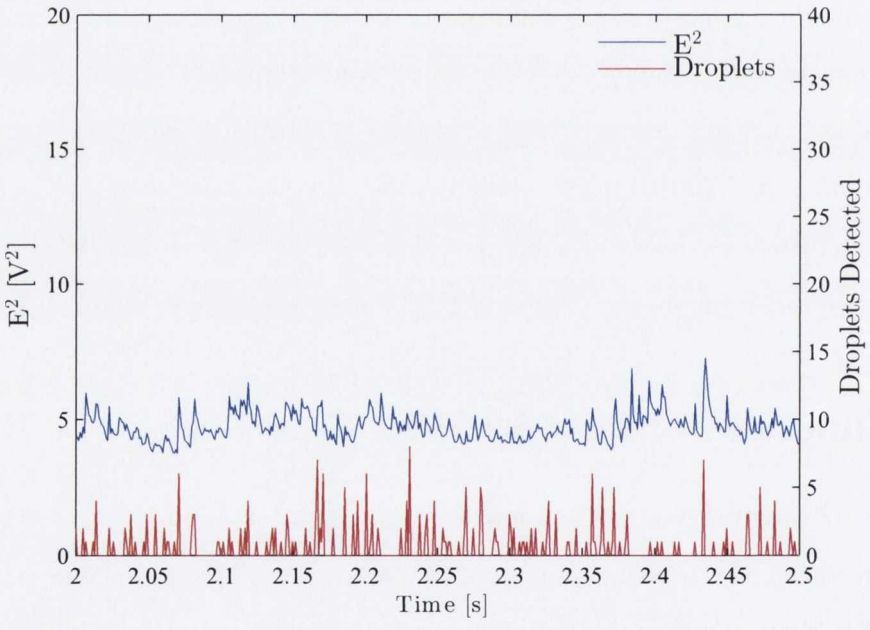

(b)

Figure 7.20: Combined simultaneous hot film sensor voltage squared and droplet detection when Re = 4500 and f = 0.006 for (a) H/D = 5 and (b) H/D = 10

transfer mechanisms identified in studies such as Graham and Ramadhyani [20] and Chang and Su [19] are predicated on the existence of this liquid film, further measurements were required to better understand the observed heat transfer behaviour. Thus, high-speed temporal

distributions of simultaneously obtained hot film sensor voltage, which is indicative of heat flux, and shadowgraph imaging data were examined in an attempt to identify the heat transfer mechanisms for the dilute impinging mist jet.

Considering the temporal data, the voltage was seen to exhibit significant and rapid fluctuations, with large peaks evident. This contrasted with the air only jet, which remained relatively constant across the measurement period. For the lower mist loading fractions which give rise to discrete liquid slugs on the surface, the voltage decayed towards the air only level in the intervals between the peaks, indicating that the voltage spikes, and thus spikes in heat flux, were responsible for much of the heat transfer enhancement. Thus, determining their cause was of importance in understanding the heat transfer mechanisms. Using the simultaneous shadowgraph imaging, a strong correlation was found to exist between the intermittent detection of impinging droplets and these peaks in the hot film sensor voltage. It was therefore postulated that the impingement of the high heat capacity liquid droplets on the heated surface was causing significant disturbance of the thermal boundary layer, resulting in the rapidly changing heat flux. Since the liquid on the surface was not sufficient at these low mist loading fractions to form a continuous film, and hence evaporation and sensible heating of the surface liquid was reduced, it was inferred that the dominant heat transfer mechanism was the intermittent disturbance caused by the liquid droplet impingement. This contrasts with previous studies, which describe evaporation of the liquid film and its convective flow across the surface as the dominant mechanisms [19, 20].

As the mist loading fraction increased, and the establishment of a continuous film was observed in the high-speed surface images of section 6.4, significant temporal variations in hot film sensor voltage continued to correlate with droplet impingements. However, the baseline voltage level was higher, indicating the increasing influence of evaporation and the convective action of the liquid film. Thus, as the mist loading fraction of the dilute mist jet increases from the regime where the surface liquid behaviour is characterised by discrete liquid slugs to that in which a continuous liquid film is established, the heat transfer mechanisms begin to converge on those proposed within the literature.

For mist loading fractions between the above two cases, when non-continuous localised liquid films developed, a plateau in heat transfer coefficient was observed. It was postulated that this was due to competing heat transfer influences, with the films potentially damping

the influence of the droplet disturbances while not yet providing sufficient evaporation or convective flow to further enhance heat transfer. Further local analysis of the impingement surface is required to confirm this hypothesis however.

The effects of changes in mist jet Reynolds number and nozzle-to-plate spacing on the mist jet heat transfer coefficient were also examined; again the disturbances caused by the impingement of the liquid droplets were seen to be significant. At the higher Reynolds number examined, the shadowgraph data and high-speed surface imagery in chapter 6 showed that the surface behaviour was characterised by highly concentrated, intermittent impingements. This was reflected in the simultaneous temporal hot film sensor voltage and droplet detection distributions, with fluctuations in voltage of a greater magnitude than for the lower Reynolds number corresponding to these substantial impacts. Increasing the nozzle-to-plate spacing somewhat diminished the influence of the droplet impacts for both Reynolds numbers considered; this was attributed to the spreading of the mist jet resulting in a decrease in droplet concentration at impingement, consistent with the mist jet structure data in chapter 6.

While additional probing of the time-varying heat transfer and mist jet structure might further elucidate the different heat transfer mechanisms in play as the surface liquid regime evolves from discrete slugs to a continuous film, the current investigation strongly suggests that the disturbances caused by the impingement of the mist jet droplets are the dominant influence on dilute mist jet heat transfer. Thus, the ability of the mist jet to offer significant heat transfer enhancement with the addition of very small amounts of liquid is primarily due to this disturbance to the thermal boundary layer by high heat capacity droplets, rather than to evaporation or heating of the surface liquid film.

Chapter 8

Conclusions

An experimental investigation has been undertaken into the heat transfer mechanisms for an impinging mist jet. To this end, the flow structure and impingement behaviour of the mist jet have been examined, with simultaneous flow visualisation and heat transfer measurements being performed. The specific focus of this study is on the case of a dilute mist jet impinging on a surface held at a temperature below the saturation temperature of water.

Comprehensive reviews of the literature on the subjects of mist jet flow structure and heat transfer were performed. It was identified that no work has been reported on the flow characteristics and non-boiling impingement heat transfer of mist jets with very low liquid fractions. Likewise, there has been no attempt to link the flow structure to the heat transfer for those studies that have examined higher liquid fractions. To address these gaps in the literature, an experimental apparatus has been designed and built to perform simultaneous flow visualisation and temporal heat transfer measurements, while a second rig has been modified to perform time-averaged heat transfer measurements. These allow the mist jet to be examined for a range of parameters including jet Reynolds number, mist loading fraction and axial distance to an impingement surface.

The first apparatus allowed for flow visualisation to be performed using a combination of shadowgraph imaging and high-speed imagery. Results have been presented for

- the atomisation behaviour of the mist jet using high-speed imagery
- the flow structure in terms of the droplet sizes and velocities using shadowgraph imaging
- the impingement behaviour and surface liquid morphology using high-speed imagery.

The atomisation behaviour was seen to be highly chaotic, and dependent on the aerodynamic Weber number of the mist jet. The droplet properties showed that the mist jet was initially highly non-uniform in the atomisation region, but that it developed a more uniform structure

in terms of mean droplet sizes and velocities as it moved downstream. This downstream evolution varied depending on the atomisation process. The impingement behaviour of the mist jet was observed to vary with increasing mist loading fraction, f. Three regimes were identified to describe the impingement behaviour of the mist jet in terms of f; these can be described as:

1. Low f regime, characterised by discrete liquid slugs forming without complete surface wetting in the impingement region.

2. Intermediate f regime, with the discrete liquid slugs merging to form localised thin liquid films, though still without complete surface wetting.

3. High f regime, where a continuous film of liquid has developed in the impingement region that flows outwards under the action of the impinging droplets.

Thus, for the low mist fractions under investigation here the surface is not always completely wetted by the impinging mist jet. This is noteworthy as the heat transfer mechanisms proposed in the few studies published on mist jet heat transfer assumed the existence of a continuous liquid film.

The second experimental apparatus was used to characterise the mist jet heat transfer, with time-averaged heat transfer coefficient profiles presented for varying Reynolds number, mist loading fraction and nozzle-to-plate spacing. Although the heat transfer coefficient increased in general with mist loading fraction, the increase was not uniform across the range of parameters examined. The time-averaged data suggested that there was a strong link between the surface liquid behaviour and the heat transfer coefficient. To further elucidate this, simultaneous temporal flow visualisation and heat transfer testing was carried out. Significant high-speed fluctuations in the heat transfer signal were identified which correlated strongly with the detection of droplets in the simultaneous shadowgraph imagery. This indicated the importance of the thermal disturbances caused by the droplets striking the impingement surface, which were hypothesised to be the driving heat transfer mechanism in the low f regime. As the mist loading fraction increased, leading to the onset of localised films and then a continuous film, the contribution to the heat transfer from evaporation and from convective cooling by the liquid film increased. In the intermediate f regime, a plateau in heat transfer

coefficient was observed; this was attributed to competing influences at the impingement surface as evaporative and convective cooling by the film becomes more significant, while the influence of the impinging droplets is potentially damped by the developing film. The influence of the surface liquid behaviour on mist jet heat transfer was also consistent with the variation in the heat transfer coefficient with Reynolds number and nozzle-to-plate spacing, as changes in the surface morphology were observed when these parameters were varied. More highly concentrated intermittent droplet impacts were seen at the higher Reynolds number; this was reflected in the temporal heat transfer signal, with fluctuations of a greater magnitude than for the lower Reynolds number being observed. An increase in nozzle-to-plate spacing resulted in decreased heat transfer fluctuations, with the spreading of the mist jet diminishing the influence of the droplet impacts for both Reynolds numbers considered.

These flow visualisation and heat transfer findings indicate that, in contrast with mechanisms discussed in the available literature, for very low liquid fractions mist jet heat transfer is not dominated by evaporation and convective cooling from the film, but rather by the disturbances caused by the intermittent impingement of the mist jet droplets on the surface. The establishment of a continuous liquid film is necessary for the heat transfer mechanisms to begin to converge on those proposed within the literature.

8.1 Further Work

Flow visualisation using particle image velocimetry (PIV) has been used before to examine the flow field of the annular air jet [52]. The use of PIV may shed further light on the flow structure of the mist jet, in particular how the annular air jet structure is changed by the presence of the liquid droplets. However, the liquid droplets themselves hamper the use of the technique as they may result in scattering of the laser light used in the PIV technique. This could be addressed by the addition of Rhodamine B dye to the mist jet liquid, which absorbs light with a wavelength in the green spectrum, that of the laser light typically used, and emits light in the orange-red spectrum. Thus, by using appropriate filtering on the PIV camera, light flashes caused by scattering as the laser light hits droplets could be removed. Thus, the flow structure of the mist jet could be characterised in terms of both the air and liquid streams, thereby shedding further light on the heat transfer phenomena associated with the mist jet.

The importance of the surface liquid behaviour has been identified in this study. However, the surface temperature was kept constant at ~40 °C throughout the investigation. Simultaneous high-speed imagery of the surface and heat transfer measurements over a range of surface temperatures would be expected to shed light on how the surface morphology changes and the influence this has on the mist jet heat transfer.

Several different types of mist jet nozzle exist, as discussed in section 3.6.4. A study on the heat transfer performance of the different nozzles under identical operating conditions would be of interest, as currently it is difficult to compare results between studies, indicating that the nozzle geometry may be influential.

A refinement in the technique used to measure the high-speed heat transfer fluctuations is required in order to accurately quantify the magnitude of the heat flux variations. Current techniques for the use of the Senflex hot film sensor are only appropriate for the lower heat flux environment of an impinging air jet. An improvement in this area could shed further light on the relative importance of the heat transfer mechanisms observed. Similarly, an improvement in the lighting set-up for the shadowgraph and high-speed imaging is expected to improve the quality of the flow visualisation results. This is particularly important for the impingement surface imagery, as shadows cast by the surface can make the images difficult to interpret, and also prevent the shadowgraph imaging technique from being used close to the surface. It would be interesting to characterise the droplet distributions close to the surface, as both incident and ejected droplets could then be accounted for, as could the effect of the heated surface, as has been done for sprays [63, 122].

Bibliography

[1] T. S. O'Donovan, D. B. Murray, and A. A. Torrance. Jet heat transfer in the vicinity of a rotating grinding wheel. *Proc. Inst. Mech. Eng. Part C J. Mech. Eng. Sci.*, 220(6):837–845, 2006.

[2] B. R. Hollworth and M. Durbin. Impingement cooling of electronics. *J. Heat Transf.*, 114(3):607–613, 1992.

[3] D. Lytle and B. W. Webb. Air jet impingement heat transfer at low nozzle-plate spacings. *Int. J. Heat Mass Transf.*, 31(12):1687–1697, 1994.

[4] T. S. O'Donovan and D. B. Murray. Jet impingement heat transfer — part I: mean and root-mean-square heat transfer and velocity distributions. *Int. J. Heat Mass Transf.*, 50(17):3291–3301, 2007.

[5] D. W. Zhou and S.-J. Lee. Heat transfer enhancement of impinging jets using mesh screens. *Int. J. Heat Mass Transf.*, 47(10):2097–2108, 2004.

[6] R. J. Goldstein and A. I. Behbahani. Impingement of a circular jet with and without cross flow. *Int. J. Heat Mass Transf.*, 25(9):1377–1382, 1982.

[7] D T Vader, F P Incropera, and R Viskanta. Local convective heat transfer from a heated surface to an impinging , planar jet of water. *Int. J. Heat Mass Transf.*, 34(3):611–623, 1991.

[8] S. V. Garimella and R. A. Rice. Confined and submerged liquid jet impingement heat transfer. *J. Heat Transf.*, 117(4):871–877, 1995.

[9] J. W. Hodgson and J. E. Sunderland. Heat transfer from a spray-cooled isothermal cylinder. *Ind. & Eng. Chem. Fund.*, 7(4):567–572, 1968.

[10] R. L. Mednick and C. P. Colver. Heat transfer from a cylinder in an air-water spray flow stream. *AIChE J.*, 15(3):357–362, 1969.

[11] B. Horacek, K. T. Kiger, and J. Kim. Single nozzle spray cooling heat transfer mechanisms. *Int. J. Heat Mass Transf.*, 48(8):1425–1438, 2005.

[12] C. A. Hernández-Bocanegra, A. H. Castillejos E., F. A. Acosta-González, X. Zhou, and B. G. Thomas. Measurement of heat flux in dense air-mist cooling: part I — A novel steady-state technique. *Exp. Therm. Fluid Sci.*, 44:147–160, 2013.

[13] J. J. Nijdam, S. H. Stårner, and T. a. G. Langrish. An experimental investigation of droplet evaporation and coalescence in a simple jet flow. *Exp. Fluids*, 37(4):504–517, 2004.

[14] W. Jia and H.-H. Qiu. Experimental investigation of droplet dynamics and heat transfer in spray cooling. *Exp. Therm. Fluid Sci.*, 27(7):829–838, 2003.

[15] R. Chen, L. C. Chow, and J. E. Navedo. Optimal spray characteristics in water spray cooling. *Int. J. Heat Mass Transf.*, 47(23):5095–5099, 2004.

[16] M. Fabbri, S. Jiang, and V. K. Dhir. A comparative study of cooling of high power density electronics using sprays and microjets. *J. Heat Transf.*, 127(1):38, 2005.

[17] J. R. Rybicki and I. Mudawar. Single-phase and two-phase cooling characteristics of upward-facing and downward-facing sprays. *Int. J. Heat Mass Transf.*, 49(1):5–16, 2006.

[18] S. Freund, A. G. Pautsch, T. A. Shedd, and S. Kabelac. Local heat transfer coefficients in spray cooling systems measured with temperature oscillation IR thermography. *Int. J. Heat Mass Transf.*, 50(9):1953–1962, 2007.

[19] S. W. Chang and L. M. Su. Heat transfer of confined impinging air-water mist jet. *JSME Int. J. Ser. B*, 44(2):274–287, 2001.

[20] K. M. Graham and S. Ramadhyani. Experimental and theoretical studies of mist jet impingement cooling. *J. Heat Transf.*, 118(2):343–349, 1996.

[21] K. Oliphant, B. W. Webb, and M. Q. McQuay. An experimental comparison of liquid jet array and spray impingement cooling in the non-boiling regime. *Exp. Therm. Fluid Sci.*, 18(1):1–10, 1998.

[22] C. Engelbert, Y. Hardalupas, and J. H. Whitelaw. Breakup phenomena in coaxial airblast atomizers. *Proc. R. Soc. A: Math., Phys. Eng. Sci.*, 451(1941):189–229, 1995.

[23] J. C. Lahseras, E. Villermaux, and E. J. Hopfinger. Break-up and atomization of a round water jet by a high-speed annular air jet. *J. Fluid Mech.*, 357:351–379, 1998.

[24] A. Lefebvre. *Atomization and sprays*. CRC press, 1989.

[25] J Plateau. Statique expérimentale et théorique des liquides soumis aux seules forces moléculaires (Gauthier-Villars, Paris, 1873); Lord Rayleigh. *Proc. London. Math. Soc*, 10(4), 1878.

[26] Lord Rayleigh. On the instability of jets. *Proc. London Math. Soc.*, 10:4–13, 1878.

[27] C. Weber. Disintegration of liquid jets. *Z. Angew. Math. Mech*, 11(2):136–159, 1931.

[28] W. von Ohnesorge. Formation of drops by nozzles and the breakup of liquid jets. *Z. Angew. Math. Mech*, 16(4):355–358, 1936.

[29] R. D. Reitz. *Atomization and other breakup regimes of a liquid jet*. PhD thesis, Princeton, 1978.

[30] J. C. Lasheras and E. J. Hopfinger. Liquid jet instability and atomization in a coaxial gas stream. *Annu. Rev. Fluid Mech.*, 32(1):275–308, 2000.

[31] C. M. Varga, J. C. Lasheras, and E. J. Hopfinger. Initial breakup of a small-diameter liquid jet by a high-speed gas stream. *J. Fluid Mech.*, 497:405–434, 2003.

[32] S. Nukiyama. Experiments on the atomization of liquids in an air stream. *Trans. Soc. Mech. Eng. Jpn.*, 5:68–75, 1939.

[33] P. Marmottant and E. Villermaux. On spray formation. *J. Fluid Mech.*, 498:73–111, 2004.

[34] N. Chigier and Z. Farago. Morphological classification of disintegration of round liquid jets in a coaxial air stream. *Atom. Sprays*, 2(2), 1992.

[35] H. F. Liu, W. F. Li, X. Gong, X. K. Cao, J. L. Xu, X. L. Chen, Y. F. Wang, G. Suo Yu, F. C. Wang, and Z. H. Yu. Effect of liquid jet diameter on performance of coaxial two-fluid airblast atomizers. *Chem. Eng. Process.: Proc. Intensif.*, 45(4):240–245, 2006.

[36] A. A. Borisov, B. E. Gel'Fand, M. S. Natanzon, and O. M. Kossov. Droplet breakup regimes and criteria for their existence. *J. Eng. Phys.*, 40(1):44–49, 1981.

[37] J. O. Hinze. Fundamentals of the hydrodynamic mechanism of splitting in dispersion processes. *AIChE Journal*, 1(3):289–295, 1955.

[38] R. D. Reitz and F. V. Bracco. Mechanism of atomization of a liquid jet. *Phy. Fluids*, 25(10):1730–1742, 1982.

[39] S. P. Lin and R. D. Reitz. Drop and spray formation from a liquid jet. *Annu. Rev. Fluid Mech.*, 30(1):85–105, 1998.

[40] N. Sozbir, Y. W. Chang, and S. C. Yao. Heat transfer of impacting water mist on high temperature metal surfaces. *J. Heat Transf.*, 125(1):70–74, 2003.

[41] Zhen Zhang, Jia Li, and Pei-xue Jiang. Experimental investigation of spray cooling on flat and enhanced surfaces. *Appl. Therm. Eng.*, 51(1):102–111, 2013.

[42] K. J. Choi and S. C. Yao. Mechanisms of film boiling heat transfer of normally impacting spray. *Int. J. Heat Mass Transf.*, 30(2):311–318, 1987.

[43] O. F. P. Lyons, T. Persoons, and D. B. Murray. Particle sizing and flow measurements in an atomizing mist jet nozzle: A shadowgraphy approach. In *ILASS-Europe 2010, 23rd Annu. Conf. Liq. At. Spray Syst.*, pages 1–9, 2010.

[44] O. F. P. Lyons, C. Quinn, T. Persoons, and D. B Murray. Heat transfer and flow in an atomizing mist jet: a combined hot film and shadowgraph imaging approach. *J. Phys. Conf. Ser.*, 395:012173, 2012.

[45] K. Ichimiya. Heat transfer characteristics of an annular turbulent impinging jet with a confined wall measured by thermosensitive liquid crystal. *Heat Mass Transf.*, 39(7):545–551, 2003.

[46] H. Q. Yang, T. Kim, T. J. Lu, and K. Ichimiya. Flow structure, wall pressure and heat transfer characteristics of impinging annular jet with/without steady swirling. *Int. J. Heat Mass Transf.*, 53(19):4092–4100, 2010.

[47] J. S. Chin and A. H. Lefebvre. Some comments on the characterization of drop-size distribution in sprays. In *ICLASS-85; Proceedings of the Third International Conference on Liquid Atomisation and Spray Systems, London, England, July 8-10, 1985. Volume 2 (A87-13826 03-34)*, volume 2, 1986.

[48] T. Liu and J. P. Sullivan. Heat transfer and flow structures in an excited circular impinging jet. *Int. J. Heat Mass Transf.*, 39(17):3695–3706, 1996.

[49] N. W. M. Ko and W. T. Chan. Similarity in the initial region of annular jets: three configurations. *J. Fluid Mech.*, 84(4):641–656, 1978.

[50] W. T. Chan and N. W. M. Ko. Coherent structures in the outer mixing region of annular jets. *J. Fluid Mech.*, 89(3):515–533, 1978.

[51] N. W. M Ko and W. T. Chan. The inner regions of annular jets. *J. Fluid Mech*, 93(3):549–584, 1979.

[52] B. Patte-Rouland, G. Lalizel, J. Moreau, and E. Rouland. Flow analysis of an annular jet by particle image velocimetry and proper orthogonal decomposition. *Meas. Sci. Technol.*, 12(9):1404–1412, 2001.

[53] Z. Trávníček and V. Tesař. Hysteretic behaviour of annular impinging jets. In *5th Eur. Therm.-Sci. Conf.*, pages 186–187, 2008.

[54] V. Tesař and Z. Trávníček. Excitational metamorphosis of surface flowfield under an impinging annular jet. *Chem. Eng. J.*, 144(2):312–316, 2008.

[55] Z. Trávníček and V. Tesař. Hysteresis in annular impinging jets. *Exp. Therm. Fluid Sci.*, 44:565–570, 2013.

[56] Y. Hardalupas and J. H. Whitelaw. Characteristics of sprays produced by coaxial airblast atomizers. *J. Prop. Power*, 10(4):453–460, 1994.

[57] V. Ferrand, R. Bazile, J. Borée, and G. Charnay. Gas-droplet turbulent velocity correlations and two-phase interaction in an axisymmetric jet laden with partly responsive droplets. *Int. J. Multiph. Flow*, 29(2):195–217, 2003.

[58] A. A. Mostafa and H. C. Mongia. On the interaction of particles and turbulent fluid flow. *Int. J. Heat Mass Transf.*, 31(10):2063–2075, 1988.

[59] Wen-Long Cheng, Feng-Yun Han, Qi-Nie Liu, Rui Zhao, and Han-lin Fan. Experimental and theoretical investigation of surface temperature non-uniformity of spray cooling. *Energy*, 36(1):249–257, 2011.

[60] W.-L. Cheng, F.-Y. Han, Q.-N. Liu, and R. Zhao. Theoretical investigation on the mechanism of surface temperature non-uniformity formation in spray cooling. *Int. J. Heat Mass Transf.*, 55(19):5357–5366, 2012.

[61] D. Kalantari and C. Tropea. Spray impact onto flat and rigid walls: Empirical characterization and modelling. *Int. J. Multiph. Flow*, 33(5):525–544, 2007.

[62] D. Kalantari and C. Tropea. Phase Doppler measurements of spray impact onto rigid walls. *Exp. Fluids*, 43(2):285–296, 2007.

[63] I. V. Roisman and C. Tropea. Fluctuating flow in a liquid layer and secondary spray created by an impacting spray. *Int. J. Multiph. Flow*, 31(2):179–200, 2005.

[64] O. G. Engel. Waterdrop collisions with solid surfaces. *J. Res. Natl. Bur. Stand. (1934).*, 54(5):281–298, 1955.

[65] S. Chandra and C. T. Avedisian. On the collision of a droplet with a solid surface. *Proc. R. Soc. A Math. Phys. Eng. Sci.*, 432(1884):13–41, 1991.

[66] M. Rein. Phenomena of liquid drop impact on solid and liquid surfaces. *Fluid Dyn. Res.*, 12(2):61–93, 1993.

[67] A. L. Yarin. Drop impact dynamics: splashing, spreading, receding, bouncing.... *Annu. Rev. Fluid Mech.*, 38(1):159–192, 2006.

[68] R. Rioboo, C. Tropea, and M. Marengo. Outcomes from a drop impact on solid surfaces. *At. Sprays*, 11(2), 2001.

[69] P. Walzel. Zerteilgrenze beim tropfenprall. *Chemie Ingenieur Technik*, 52(4):338–339, 1980.

[70] C. D. Stow and M. G. Hadfield. An experimental investigation of fluid flow resulting from the impact of a water drop with an unyielding dry surface. *Proc. R. Soc. A: Math., Phy. Eng. Sci.*, 373(1755):419–441, 1981.

[71] C. H. R. Mundo, M. Sommerfeld, and C. Tropea. Droplet-wall collisions: experimental studies of the deformation and breakup process. *Int. J. Multiph. Flow*, 21(2):151–173, 1995.

[72] A. L. Yarin and D. A. Weiss. Impacts of drops on solid surfaces: self-similar capillary waves, and splashing as a new type of kinematic discontinuity. *J. Fluid Mech.*, 283:141–173, 1995.

[73] W. Samenfink, A. Elsäß er, K. Dullenkopf, and S. Wittig. Droplet interaction with shear-driven liquid films: analysis of deposition and secondary droplet characteristics. *Int. J. Heat Fluid Flow*, 20(5):462–469, 1999.

[74] I. V. Roisman and C. Tropea. Impact of a drop onto a wetted wall: description of crown formation and propagation. *J. Fluid Mech.*, 472:373–397, 2002.

[75] E. Berberović, N. P. Van Hinsberg, S. Jakirlić, I. V. Roisman, and C. Tropea. Drop impact onto a liquid layer of finite thickness: dynamics of the cavity evolution. *Phys. Rev. E*, 79(3), 2009.

[76] N. P. van Hinsberg, M. Budakli, S. Göhler, E. Berberović, I. V. Roisman, T. Gambaryan-Roisman, C. Tropea, and P. Stephan. Dynamics of the cavity and the surface film for impingements of single drops on liquid films of various thicknesses. *J. Colloid Interface Sci.*, 350(1):336–343, 2010.

[77] J. M. Kuhlman, N. L. Hillen, M. Dinc, and D. D. Gray. Liquid volume measurements

in the cavity formed by single droplet impacts into a thin, static liquid film. *Exp. Therm. Fluid Sci.*, 54:179–188, 2014.

[78] A. I. Fedorchenko and A. Wang. On some common features of drop impact on liquid surfaces. *Phys. Fluids*, 16(5):1349, 2004.

[79] A. B. Wang and C. C. Chen. Splashing impact of a single drop onto very thin liquid films. *Phys. Fluids*, 12(9):2155–2158, 2000.

[80] C. Josserand and S. Zaleski. Droplet splashing on a thin liquid film. *Phys. Fluids*, 15(6):1650–1657, 2003.

[81] G. E. Cossali, A. Coghe, and M. Marengo. The impact of a single drop on a wetted solid surface. *Exp. Fluids*, 22(6):463–472, 1997.

[82] N. L. Hillen, C. Menchini, G. Morris, M. Dinc, S. Taylor, D. D. Gray, and J. M. Kuhlman. Droplet impact time histories for a range of Weber numbers and liquid film thicknesses for spray cooling application. In *43rd AIAA Fl. Dyn. Conf., June 24-27, 2013, San Diego*, pages 1–22, 2013.

[83] Ilia V Roisman and C Tropea. Flow on a wall surface due to spray impact. In *ILASS-Europe 2002, September 9-11, 2002, Zaragoza*, 2002.

[84] C. Tropea and I. V. Roisman. Modeling of spray impact on solid surfaces. *Atom. Sprays*, 10(3), 2000.

[85] D. Sivakumar and C. Tropea. Splashing impact of a spray onto a liquid film. *Phys. Fluids*, 14(12):L85–L88, 2002.

[86] M. Sommerfeld and H. H. Qiu. Experimental studies of spray evaporation in turbulent flow. *Int. J. Heat Fluid Flow*, 19(1):10–22, 1998.

[87] A. A. Mostafa and S. E. Elghobashi. A two-equation turbulence model for jet flows laden with vaporizing droplets. *Int. J. Multiph. Flow*, 11(4):515–533, 1985.

[88] V. Ferrand, R. Bazile, and J. Borée. Measurements of concentration per size class in a dense polydispersed jet using planar laser-induced fluorescence and phase Doppler techniques. *Exp. Fluids*, 31(6):597–607, 2001.

[89] T. Guo, T. Wang, and J. L. Gaddis. Mist/steam cooling in a heated horizontal tube — part 1: experimental system. *J. Turbomach.*, 122(2):360–365, 2000.

[90] A. Berlemont, M. Grancher, and G. Gouesbet. On the Lagrangian simulation of turbulence influence on droplet evaporation. *Int. J. Heat Mass Transf.*, 34(11):2805–2812, 1991.

[91] X. Li, J. L. Gaddis, and T. Wang. Modeling of heat transfer in a mist/steam impinging jet. *J. Heat Transf.*, 123(6):1086–1092, 2001.

[92] J. Senda, K. Yamada, H. Fujimoto, and H. Miki. The heat-transfer characteristics of a small droplet impinging upon a hot surface. *JSME Int. J. . Ser. 2, Fluids Eng. Heat Transf. Power, Combust. Thermophys. Prop.*, 31(1):105–111, 1988.

[93] G. E. Cossali, M. Marengo, and M. Santini. Thermally induced secondary drop atomisation by single drop impact onto heated surfaces. *Int. J. Heat Fluid Flow*, 29(1):167–177, 2008.

[94] W. M. Healy and J. G. Hartley. On the validity of the adiabatic spreading assumption in droplet impact cooling. *Int. J. Heat Mass Transf.*, 44(20):3869–3881, 2001.

[95] Y. Tao, X. Huai, L. Wang, and Z. Guo. Experimental characterization of heat transfer in non-boiling spray cooling with two nozzles. *Appl. Therm. Eng.*, 31(10):1790–1797, 2011.

[96] Y. Wang, M. Liu, D. Liu, K. Xu, and Y. Chen. Experimental study on the effects of spray inclination on water spray cooling performance in non-boiling regime. *Exp. Therm. Fluid Sci.*, 34(7):933–942, 2010.

[97] A. A. O. Tay, S. S. T. Ang, and L. O. Lwin. An experimental study of slot-jet impingement and mist cooling of microprocessors. *Therm. Thermomechanical Proc. 10th Intersoc. Conf. Phenom. Electron. Syst. 2006. ITHERM 2006.*, pages 175–180, 2006.

[98] X. C. Li, J. Zhou, and K. Aung. On selection of reference temperature of heat transfer coefficient for complicated flows. *Heat Mass Transf.*, 45(5):633–643, 2008.

[99] J. Kim. Spray cooling heat transfer: the state of the art. *Int. J. Heat Fluid Flow*, 28(4):753–767, 2007.

[100] S. Lee, J. Park, P. Lee, and M. Kim. Heat transfer characteristics during mist cooling on a heated cylinder. *Heat Transf. Eng.*, 26(8):24–31, 2005.

[101] F. P. Buckingham and A. Haji-Sheikh. Cooling of high-temperature cylindrical surfaces using a water–air spray. *J. Heat Transf.*, 117(4):1018–1027, 1995.

[102] S. Deb and S.-C. Yao. Analysis on film boiling heat transfer of impacting sprays. *Int. J. Heat Mass Transf.*, 32(11):2099–2112, 1989.

[103] D. Babic, D. B. Murray, and A. A. Torrance. Mist jet cooling of grinding processes. *Int. J. Mach. Tools Manuf.*, 45(10):1171–1177, 2005.

[104] K. A Estes and I. Mudawar. Comparison of two-phase electronic cooling using free jets and sprays. *J. Electron. Packag.*, 117(4):323–332, 1995.

[105] C. F. Ma and Y. Q. Tian. Experimental investigation on two-phase two-component jet impingement heat transfer from simulated microelectronic heat sources. *Int. Commun. Heat Mass Transf.*, 17(4):399–408, 1990.

[106] S. L. Lee, Z. H. Yang, and Y. Hsyua. Cooling of a heated surface by mist flow. *J. Heat Transf.*, 116(1):167–172, 1994.

[107] N. Karwa, S. R. Kale, and P. M. V. Subbarao. Experimental study of non-boiling heat transfer from a horizontal surface by water sprays. *Exp. Therm. Fluid Sci.*, 32(2):571–579, 2007.

[108] W.-L. Cheng, F.-Y. Han, Q.-N. Liu, and H.-L. Fan. Spray characteristics and spray cooling heat transfer in the non-boiling regime. *Energy*, 36(5):3399–3405, 2011.

[109] M. Liu, Y. Wang, D. Liu, K. Xu, and Y. Chen. Experimental study of the effects of structured surface geometry on water spray cooling performance in non-boiling regime. *Front. Energy*, 5(1):75–82, 2011.

[110] S. S. Hsieh and C. H. Tien. R-134a spray dynamics and impingement cooling in the non-boiling regime. *Int. J. Heat Mass Transf.*, 50(3):502–512, 2007.

[111] A. K. Sleiti and J. S. Kapat. An experimental investigation of liquid jet impingement and single-phase spray cooling using polyalphaolefin. *Exp. Heat Transf.*, 19(2):149–163, 2006.

[112] B. Abbasi and J. Kim. Development of a general dynamic pressure based single-phase spray cooling heat transfer correlation. *J. Heat Transf.*, 133(5), 2011.

[113] R. H. Pereira, S. L. Braga, and J. A. R. Parise. Single phase cooling of large surfaces with square arrays of impinging water sprays. *Appl. Therm. Eng.*, 36:161–170, 2012.

[114] W.-L. Cheng, W.-W. Zhang, L.-J. Jiang, S.-L. Yang, L. Hu, and H. Chen. Experimental investigation of large area spray cooling with compact chamber in the non-boiling regime. *Appl. Therm. Eng.*, 80:160–167, 2015.

[115] J. L. Xie, R. Zhao, F. Duan, and T. N. Wong. Thin liquid film flow and heat transfer under spray impingement. *Appl. Therm. Eng.*, 48:342–348, 2012.

[116] R. J. Issa and S.-C. Yao. Numerical model for spray-wall impaction and heat transfer at atmospheric conditions. *J. of Therm. and Heat Trans.*, 19(4):441–447, 2005.

[117] R. Zhao, W. Cheng, Q. Liu, and H. Fan. Study on heat transfer performance of spray cooling: model and analysis. *Heat Mass Transf.*, 46(8):821–829, 2010.

[118] K. Yoshida, Y. Abe, T. Oka, Y. H. Mori, and A. Nagashima. Spray cooling under reduced gravity condition. *J. Heat Transf.*, 123(2):309, 2001.

[119] B. Abbasi, J. Kim, and A. Marshall. Dynamic pressure based prediction of spray cooling heat transfer coefficients. *Int. J. Multiph. Flow*, 36(6):491–502, 2010.

[120] J. L. Xie, Z. W. Gan, F. Duan, T. N. Wong, S. C M Yu, and R. Zhao. Characterization of spray atomization and heat transfer of pressure swirl nozzles. *Int. J. Therm. Sci.*, 68:94–102, 2013.

[121] I. Mudawar and K. A. Estes. Optimizing and predicting CHF in spray cooling of a square surface. *J. Heat Transf.*, 118(3):672, 1996.

[122] J. L. Xie, Z. W. Gan, T. N. Wong, F. Duan, S. C. M. Yu, and Y. H. Wu. Thermal effects on a pressure swirl nozzle in spray cooling. *Int. J. Heat Mass Transf.*, 73:130–140, 2014.

[123] B. Q. Li, T. Cader, J. Schwarzkopf, K. Okamoto, and B. Ramaprian. Spray angle effect during spray cooling of microelectronics: experimental measurements and comparison with inverse calculations. *Appl. Therm. Eng.*, 26(16):1788–1795, 2006.

[124] M. Visaria and I. Mudawar. Theoretical and experimental study of the effects of spray inclination on two-phase spray cooling and critical heat flux. *Int. J. Heat Mass Transf.*, 51(9):2398–2410, 2008.

[125] M. R. Pais, L. C. Chow, and E. T. Mahefkey. Surface roughness and its effects on the heat transfer mechanism in spray cooling. *J. Heat Transf.*, 114(1):211–219, 1992.

[126] N. Kumari, V. Bahadur, M. Hodes, T. Salamon, P. Kolodner, A. Lyons, and S. V. Garimella. Analysis of evaporating mist flow for enhanced convective heat transfer. *Int. J. Heat Mass Transf.*, 53(15):3346–3356, 2010.

[127] L. M. Su, S. W. Chang, C. I. Yeh, and Y. C. Hsu. Heat transfer of impinging air and liquid nitrogen mist jet onto superheated flat surface. *Int. J. Heat Mass Transf.*, 46(25):4845–4862, 2003.

[128] H. W. Coleman and W. G. Steele. *Experimentation, validation, and uncertainty analysis for engineers*. John Wiley & Sons, 3rd edition, 2009.

[129] T. Berg, J. Deppe, D. Michaelis, H. Voges, and S. Wissel. Comparison of particle size and velocity investigations in sprays carried out by means of different measurement techniques. In *ICLASS-2006, August 27-September 1, Kyoto*, 2006.

[130] LaVision. *ParticleMaster Shadow*. LaVision GmbH, Göttingen, Germany, 2008.

[131] A. A. Pavlova, K. Otani, and M. Amitay. Active performance enhancement of spray cooling. *Int. J. Heat Fluid Flow*, 29(4):985–1000, 2008.

[132] A. A. Pavlova, K. Otani, and M. Amitay. Active control of sprays using a single synthetic jet actuator. *Int. J. Heat Fluid Flow*, 29(1):131–148, 2008.

[133] G. Castanet, P. Dunand, O. Caballina, and F. Lemoine. High-speed shadow imagery to characterize the size and velocity of the secondary droplets produced by drop impacts onto a heated surface. *Exp. Fluids*, 54(3):1–17, 2013.

[134] J. B. Blaisot and J. Yon. Droplet size and morphology characterization for dense sprays by image processing: application to the Diesel spray. *Exp. Fluids*, 39(6):977–994, 2005.

[135] J. Klinner and C. Willert. Tomographic shadowgraphy for three-dimensional reconstruction of instantaneous spray distributions. *Exp. Fluids*, 53(2):531–543, 2012.

[136] A. Lecuona, P. A. Sosa, P. A. Rodríguez, and R. I. Zequeira. Volumetric characterization of dispersed two-phase flows by digital image analysis. *Meas. Sci. Technol.*, 11(8):1152–1161, 2000.

[137] H. Malot and J. B. Blaisot. Droplet size distribution and sphericity measurements of low-density sprays through image analysis. *Part. Part. Syst. Charact.*, 17(4):146–158, 2000.

[138] K. U. Koh, J. Y. Kim, and S. Y. Lee. Determination of in-focus criteria and depth of field in image processing of spray particles. *Atom. Sprays*, 11(4):317–333, 2001.

[139] J. S. Bendat and A. G. Piersol. *Random data: analysis and measurement procedures*. John Wiley & Sons, 4th edition, 2010.

[140] A. F. Mills and B. H. Chang. Error analysis of experiments, 2007. http://www.seas.ucla.edu/mae/Error_Analysis_of_Experiments.

[141] D. G. Holmberg and C. A. Womeldorf. Performance and modeling of heat flux sensors in different environments. *Proc. ASME, Heat Transf. Div.*, 364(4):71–77, 1999.

[142] D. E. Beasley and R. S. Figliola. A generalised analysis of a local heat flux probe. *J. Phys. E.*, 21(3):316–322, 1988.

[143] T. S. O'Donovan, T. Persoons, and D. B. Murray. High-resolution hot-film measurement of surface heat flux to an impinging jet. *Meas. Sci. Technol.*, 22(10), 2011.

[144] Dantec Dynamics. *StreamLine®/StreamWare® installation & user's guide*. Dantec Dynamics, Skovlunde, Denmark, 2004.

[145] T. S. O'Donovan. *Fluctuating heat transfer to an impinging air jet*. PhD thesis, University of Dublin, 2005.

Appendices

Appendix A

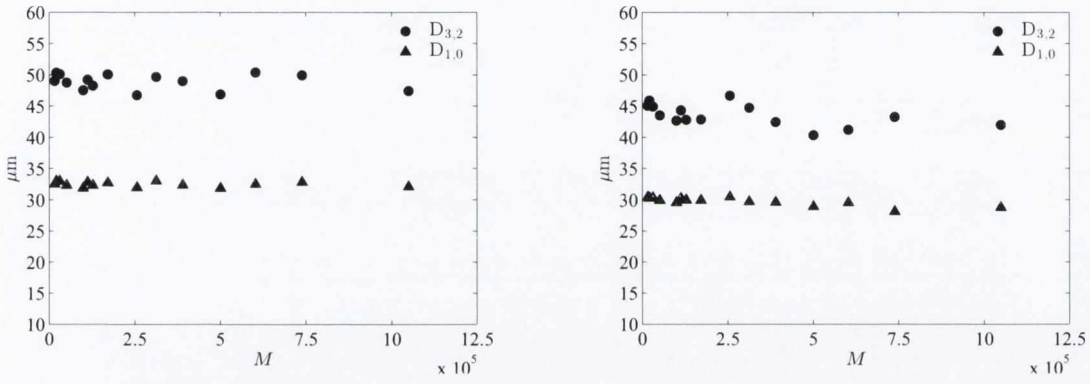

Figure A.1: Sauter mean and arithmetic droplet diameters as a function of momentum flux ratio at Re = 4500 and We = 146; (a) H/D = 5 and (b) H/D = 10

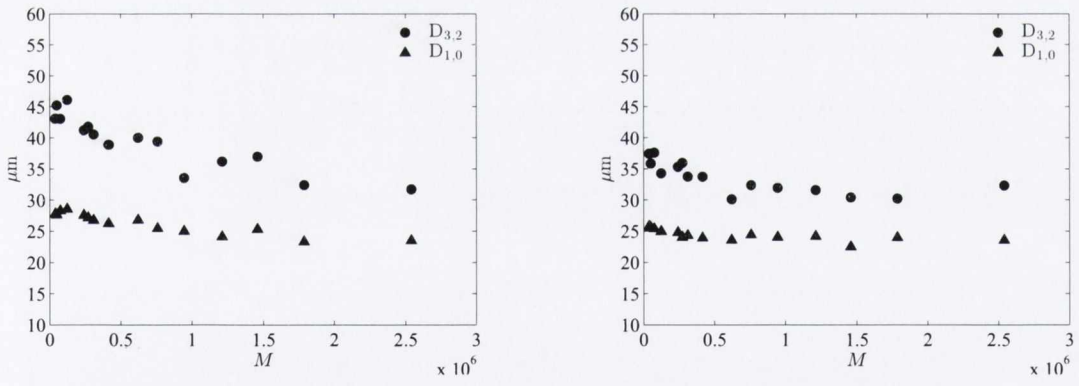

Figure A.2: Sauter mean and arithmetic droplet diameters as a function of momentum flux ratio at Re = 7800 and We = 353; (a) H/D = 5 and (b) H/D = 10

Appendix B

RdF Corporation
23 Elm Avenue
Hudson, New Hampshire 03051-0490
Tele: (603) 882-5195 1-800-445-8367
Fax: (603) 882-6925
E-mail: sensor@rdfcorp.com

ISO 9001 CERTIFIED

Q-116-01 REV B
Q-116-03 REV B
Q-116-13 REV B

MICRO-FOIL™ HEAT FLUX SENSOR

CALIBRATION

RdF PART NO. 27036-1

SERIAL NO. 0402907

HEAT FLUX SENSOR:

Output at 70°F: .185 μV/BTU/ ft² hr

Polarity: (For heat flow into the surface)
White - Positive (+)
Red - Negative (–)

Temperature Multiplication Factor: See Attached Graph

*Thermal Resistance: .003 °F/BTU/ft² hr (Typ)

*Heat Capacity: .01 BTU/ft² hr/°F (Typ)

Response Time: .020 sec (62% response to step function) (Typ)

THERMOCOUPLE:

ANSI TYPE	MATERIAL	POLARITY	COLOR
T	Copper	Pos. (+)	Blue
	Constantan	Neg. (–)	Red

Output per ANSI MC96.1-1975 and NBS Monograph 125

*Thermal resistance is the temperature difference between the front surface and rear mounting surface of the sensor per unit of heat flow through the sensor. Heat capacity is the amount of heat required to raise the mean temperature of the sensor 1°F. Typical values of these two properties are given primarily to indicate sensor capabilities and are required for heat flow calculations only in very rare instances.

BY: E C Tardy DATE: 2-23-04

RdF Corporation
Specialists in Temperature Measurement

RdF

ISO 9001 CERTIFIED

MICRO-FOIL HEAT FLUX SENSOR

OUTPUT MULTIPLICATION FACTOR VS RECEIVING SURFACE TEMPERATURE (70^0F)

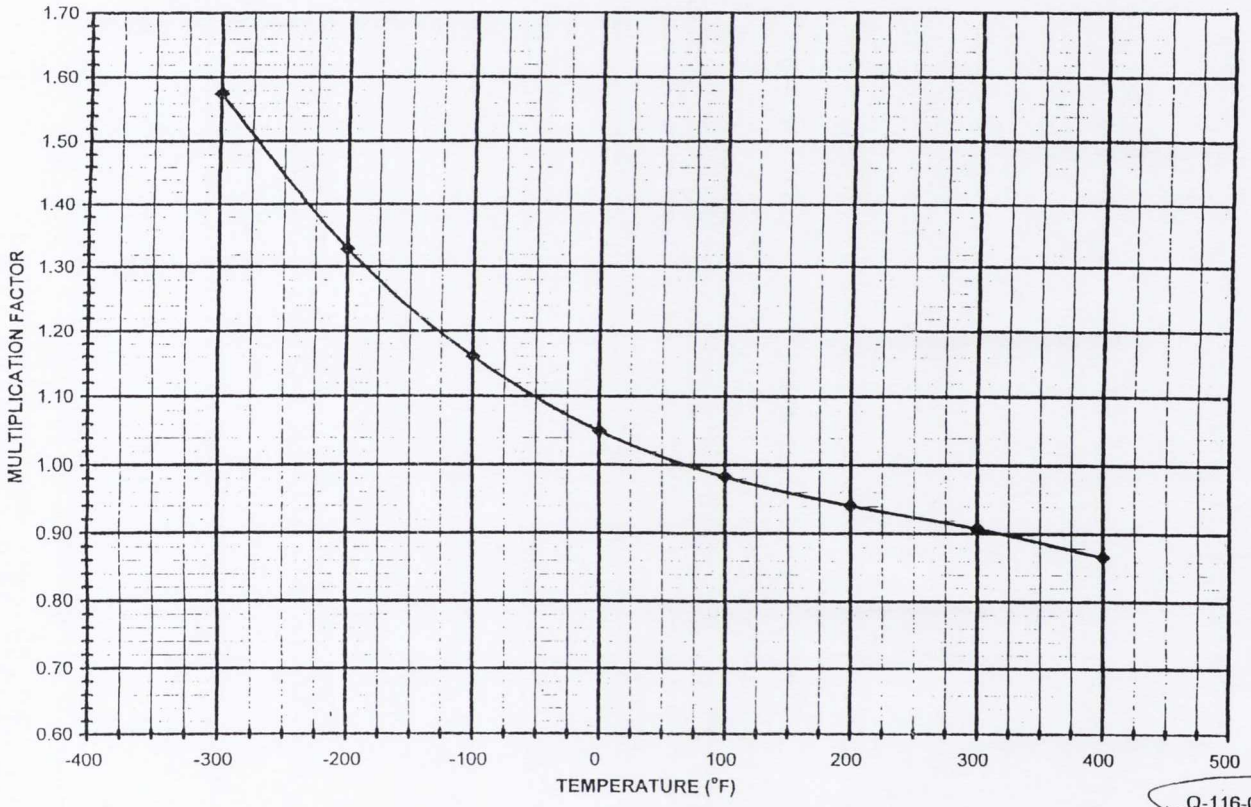

RdF Corporation
23 Elm Avenue
Hudson, NH 03051-0490
1-800-445-8367
INTERNET: sensor@rdfcorp.com

Q-116-03 REV A
Q-116-04 REV A
Q-116-08 REV A
Q-116-11 REV A
Q-116-12 REV A

OMEGA ENGINEERING LIMITED
ONE OMEGA DRIVE
RIVER BEND TECHNOLOGY CENTRE
NORTHBANK
IRLAM
MANCHESTER
M44 5BD
UNITED KINGDOM

Tel: +44 (0)161 777 6611
Fax: +44 (0)161 777 6622

FREEPHONE SALES 0800 488 488 (UK ONLY)

Website:

ISO 9002 REGISTERED COMPANY

NEWPORT® OMEGA® omega.co.uk

V.A.T. REG No. GB 620 0439 89 COMPANY REG No. 2564017

Certificate of Calibration

Certificate Number: M04481 **Issue Date:** 14-04-2003

Customer.: University of Dublin
Description.: RTD Probe **S. O. No.:** 09971
Type No.: PR-11-2-100-M30-200-1/10DIN **Serial No.:** 4

The above instrument has been calibrated. All measurements made were referenced to standards of the laboratory whose values are traceable to UK National Standards. Copies of tests performed are on file at Omega Engineering Limited, Irlam, Manchester and are available upon request.

STD Temperature °C	Recorded Probe Temperature °C	Uncertainty of Measurement °C
0.00	0.05	0.15
49.95	50.10	0.18
99.90	100.05	0.20
200.20	200.20	0.27
300.20	300.1	0.37

Test Conditions	Humidity	35 %
	Temperature	22 °C

Instruments Used:	OE01, OE204, OE52
Calibrated By:	S. C. Roach

Signed: Se[illegible]

Quality Manager

Ref: RTD.doc

The expanded uncertainties are based on the standard combined uncertainty multiplied by a coverage factor of K=2 providing a confidence probability of 95%